# Measurements and model development for flameless combustion in a lab-scale furnace

Huang, Xu

**DOI**
10.4233/uuid:209bd573-be15-46be-9bda-310d0e21d481

**Publication date**
2018

**Document Version**
Final published version

**Citation (APA)**
Huang, X. (2018). *Measurements and model development for flameless combustion in a lab-scale furnace*. [Dissertation (TU Delft), Delft University of Technology]. https://doi.org/10.4233/uuid:209bd573-be15-46be-9bda-310d0e21d481

**Important note**
To cite this publication, please use the final published version (if applicable).
Please check the document version above.

# MEASUREMENTS AND MODEL DEVELOPMENT FOR FLAMELESS COMBUSTION IN A LAB-SCALE FURNACE

# MEASUREMENTS AND MODEL DEVELOPMENT FOR FLAMELESS COMBUSTION IN A LAB-SCALE FURNACE

## Dissertation

for the purpose of obtaining the degree of doctor
at Delft University of Technology
by the authority of the Rector Magnificus Prof. dr. ir. T.H.J.J. van der Hagen
chair of the Board for Doctorates
to be defended publicly on
Tuesday 30 October 2018 at 10:00 o'clock

by

**Xu HUANG**

Master of Engineering in Aeronautic and Astronautic Science and Technology,
National University of Defense Technology, Changsha, China
born in Chongqing, China.

This dissertation has been approved by the promotors.

Composition of the doctoral committee:

| | |
|---|---|
| Rector Magnificus, | chairman |
| Prof. dr. D.J.E.M. Roekaerts, | Delft University of Technology, promotor |
| Dr. ir. M.J. Tummers, | Delft University of Technology, copromotor |

Independent members:

| | |
|---|---|
| Prof. dr. A.M. Kempf | University Duisburg-Essen |
| Prof. dr. H.B. Levinsy | University Groningen |
| Dr. ir. J.A. van Oijen | University of Technology Eindhoven |
| Dr. A. Gangoli Rao | Delft University of Technology |
| Prof. dr. ir. W. de Jong | Delft University of Technology |

The author of this thesis was financially supported by the China Scholar Council (CSC). The construction of the experimental setup was financially supported by Technology Foundation STW. The modelling work was sponsored by Netherlands Organization for Scientific Research (NWO) for the use of supercomputer facilities.




*Keywords:* Flameless Combustion, Experiments, Laser Diagnostics, Modelling, Flamelet Generated Manifolds, OpenFOAM

*Printed by:* to be determined



ISBN 000-00-0000-000-0

An electronic version of this dissertation is available at
http://repository.tudelft.nl/.

*To my parents*
*my wife & two little boys*

# CONTENTS

# SUMMARY

The technique called "flameless combustion", also denoted as "MILD" combustion, was developed to reduce the nitrogen oxides ($NO_x$) emission in the combustion process. The term "flameless" refers to the low visibility of the flame. The technique is particularly of interest when hot exhaust gas is used to preheat inlet air to high temperature. The combination of flameless combustion and exhaust gas heat recycling techniques simultaneously reduces the emission and increases the energy efficiency. Over the past few decades, flameless combustion has been successfully applied to industrial furnaces or tested at pilot scale setups in other applications. Nevertheless, despite the successful industrial application, many fundamental issues of flameless combustion are still unresolved. Detailed measurements of flameless combustion have been performed in jet-in-hot-coflow (JHC) flames, but it is unclear whether the findings can be related to the flameless combustion in a furnace because only part of the features of flameless combustion are mimicked in JHC flames. Concerning modelling, it is found that the existing combustion models are not suitable for numerical modelling of flameless combustion and new model development is needed.

The objective of this research is to characterize the flameless combustion in a lab-scale furnace that is simple enough to allow detailed measurements while keeping most relevant characteristics found in large scale furnaces. This thesis is divided into two parts, experimental measurements and model development and validation. The goal of experiments is to observe the flame behaviour and obtain detailed velocity and temperature data of flameless combustion in the furnace by means of high speed imaging and laser diagnostic techniques. The goal of the model development is to extend the Flamelet Generated Manifolds (FGM) method to take into account the effects of dilution by recirculated burnt gases. One of the databases of the Delft jet-in-hot-coflow (DJHC) flames and a new database obtained in a new lab-scale furnace are used for the model validation.

In the first part of this thesis (Chapters 2 to 4), flameless combustion has been experimentally studied in a lab-scale furnace. This new furnace has been designed and constructed at Delft University of Technology. The furnace consists of a WS REKUMAT 150 recuperative Flame-FLOX burner and a thermally insulated combustion chamber. The furnace allows for good optical access for detailed laser diagnostics. The present furnace configuration has been proved to offer stable combustion process at different optical accesses. All experiments were done using Dutch natural gas as fuel. The furnace was operated at a thermal input of 9 kW (fuel mass flow rate based) and studied in detail at three values of equivalence ratio, namely 0.7, 0.8 and 0.9. $NO_x$ emissions in the exhaust gas were below 1 ppmv for all three cases. The ignition and flame structure in the flameless regime were studied from OH* chemiluminescence images. Detailed velocity measurements were performed with Laser Doppler Anemometry (LDA) in a forward-scatter configuration. Temperatures were measured the with Coherent anti-Stokes Ra-

man Spectroscopy (CARS) technique.

The OH* chemiluminescence measurements show that autoignition sustains the combustion process in the furnace. There are three types of ignition behaviour, namely individual autoignition kernels, multiple autoignition kernels and ignition kernel clusters. The reaction zone (the zone with significant chemiluminescence) is a collection of these three autoignition structures together sustaining the combustion process in the furnace. This situation is referred to as "sustained combustion". This process guarantees continuous combustion in the furnace without presence of a stable local flame. Autoignition is local condition controlled, mainly depending on the flow, mixture composition and temperature. The latter two are determined by the amount of diluent and by the enthalpy loss in the diluent. It is found that there exists a dilution range where autoignition can be achieved in a wide range of flow conditions. This provides the best condition to sustain a stable flameless combustion process.

The combustion characteristics in the furnace are different at different equivalence ratios. Decreasing the equivalence ratio causes the reaction zone to shift upstream and reaction intensity becomes lower. The highly turbulent flow field plays an important role in preventing a locally stabilized flame. As the equivalence ratio is decreased the internal flow field becomes more turbulent, and the turbulent mixing and the entrainment of burnt gases into the jets of reactants are enhanced. Although the turbulent fluctuations in the three cases are similar, the reaction intensity and the position of the reaction zone change significantly.

The final mean temperature rise in the furnace due to combustion is less than 600K (compared to air inlet temperature). The instantaneous peak temperature is less than 1800 K, and the temperature samples which are larger than 1700 K is less than 1.5%. The low peak temperature greatly suppresses the formation of $NO_x$ emissions. Temperature histograms show that exothermic reactions are proceeding in the reaction zone, but there is no local stabilized flame front like structure present in the reaction zone. Large temperature fluctuations indicate that the combustion process is quite unsteady in the reaction zone. It also appears that the burner nozzle configuration is important to establish flameless combustion because it determines the flow field and therefore the burnt gases entrainment.

In the second part of this thesis (Chapters 5 to 7), an extended FGM model referred to as diluted air FGM (DAFGM) is developed for modelling flameless combustion. It includes the effects of dilution on flamelet structures. In the DAFGM model, the reactions in the reaction zone are treated as the fuel reacts with the diluted air. The corresponding lookup table stores the flamelets at different air dilution levels. With one control parameter named air dilution level, the corresponding flamelets can be indexed. To take into account the significant radiative heat transfer in the high temperature furnace, radiation is also coupled into the DAFGM model. The radiative properties of gases are modelled with a weighted-sum-of-grey-gas (WSGG) model which accounts for the local mole ratio between $CO_2$ and $H_2O$. In addition, a method to take into account turbulence-radiation interaction with DAFGM has also been developed. The models developed in this thesis have been implemented in the open source CFD package OpenFOAM-2.3.1 including a new algorithm for storage and retrieval with interpolation in two- to six-dimensional lookup tables.

The DAFGM model first has been applied to the case "DJHC-I Re=4100" of the DJHC burner database using both RANS and LES approaches. The results show that the predictions for the DJHC-I Re=4100 flame are not sensitive to the progress variable fluctuations, but that the surrounding air inlet velocity has effects on the predicted temperature profile at high axial locations. The turbulent flow field statistics and temperature predictions are in overall good agreement with experimental data. This is true for both RANS and LES results but the LES predicts better flow field statistics than those of RANS. In the LES results, it is clearly seen how air is mixed into the coflow by large vortices generated in the shear layer between coflow and air. At higher axial locations, the air is transported to the flame region and participates in the reactions.

Next the model is applied to the simulation of the new furnace, with the case at equivalence ratio $\phi = 0.8$ being selected as the validation case. It is found that in this case the model predictions are very sensitive to the fluctuations in progress variable. This is consistent with the observations in experiments that the combustion characteristics are sensitive to turbulence. The predicted final mean temperature rise in the reaction zone is close to the measured mean temperature rise. In the predicted flow field, it is seen that the dilution process can be divided into two phases, the direct dilution phase and the indirect dilution phase. The direct dilution phase occurs before the air jets interact with each other. Then all jets are independently diluted by entrained burnt gases. The indirect dilution phase occurs when the air jets are already interacting with each other. It is dominated by turbulent mixing which transports burnt gases from the recirculation zone to the inner region of the jets. This again confirms that the burner nozzle configuration is important for guiding the mixing between reactant jets and burnt gases.

The overall simulation results obtained with the proposed model are in good agreement with experimental data in both the DJHC-I flame and the furnace, demonstrating that the DAFGM model is capable of modelling flameless combustion.

Finally, the present study provides fundamental scientific knowledge and insight on the nature of flameless combustion. The experimental results not only show the combustion characteristics of flameless combustion in a furnace, but also provide a data base for numerical simulation validation. The DAFGM model and the turbulence-radiation interaction implementation in this thesis can provide good predictions of flameless combustion and can be useful in the design of clean and efficient combustion equipment.

# SAMENVATTING

De techniek genoemd "vlamloze verbranding", ook aangeduid met "MILD"verbranding, werd ontwikkeld om stikstofoxide ($NO_x$) emissies in verbrandingsproducten te verlagen. De term "vlamloos"verwijst naar de lage zichtbaarheid van de vlam. De techniek is in het bijzonder van belang wanneer hij gecombineerd wordt met lucht-voorverwarming tot hoge temperatuur door gebruik van warmte onttrokken aan de uitlaatgassen. De combinatie van vlamloze verbranding en recycling van warmte van de uitlaatgassen leidt tegelijkertijd tot verlaging van de emissie en verhoging van de energie efficiëntie. In de voorbije decennia werd vlamloze verbranding succesvol toegepast in industriële ovens of getest op piloot schaal opstellingen in andere toepassingen. Toch zijn, ondanks de succesvolle industriële toepassing, nog vele fundamentele vragen betreffende vlamloze verbranding niet opgehelderd. Er werden gedetailleerde metingen gedaan aan vlamloze verbranding in jet-in-hot-coflow (JHC) experimenten, maar het is niet duidelijke of bevindingen kunnen gerelateerd worden aan vlamloze verbranding in een oven, omdat slechts een deel van de karakteristieken van vlamloze verbranding nagebootst worden in JHC vlammen. Wat betreft modellering heeft men gevonden dat de bestaande verbrandingsmodellen niet geschikt zijn voor numerieke modellering van vlamloze verbranding en nieuwe modelontwikkeling is nodig.

De doelstelling van dit onderzoek is om vlamloze verbranding te karakteriseren in een oven op laboratoriumschaal. Dit systeem is eenvoudig genoeg om gedetailleerde metingen te kunnen doen terwijl toch de meeste relevante karakteristieken van fornuizen op grote schaal behouden zijn. Dit proefschrift is verdeeld in twee delen: enerzijds experimentele metingen en anderzijds modelontwikkeling en validatie. Het doel van de experimenten is om het vlamgedrag te observeren en gedetailleerde meet-data te verkrijgen van snelheid en temperatuur door middel van snelle camera's (highspeed imaging) en laserdiagnostische technieken. Het doel van de modelontwikkeling is om de Flamelet Generated Manifolds (FGM) methode uit te breiden om de effecten van verdunning door gerecirculeerd verbrandingsgas in rekening te brengen. Een van de experimentele databases van de Delft jet-in-hot-coflow (DJHC) brander en een nieuwe database verkregen in een nieuwe laboratorium schaal oven worden gebruikt voor modelvalidatie.

In het eerste deel van dit proefschrift (Hoofstukken 2-4) wordt vlamloze verbranding experimenteel bestudeerd in een laboratorium schaal oven. Deze oven werd in het kader van dit project ontworpen en gebouwd aan de Technische Universiteit Delft. De oven bestaan uit een WS REKUMAT 150 recuperatieve Flame-FLOX brander en een thermisch geïsoleerde verbrandingskamer. De oven is goed optisch toegankelijk voor gedetailleerde laserdiagnostiek. Deze oven configuratie biedt een stabiel verbrandingsproces bij verschillende wijzen van optische toegang. Alle experimenten werden uitgevoerd met Nederlands aardgas als brandstof. De oven werd ingesteld op een thermisch vermogen van 9 kW (gebaseerd op massastroom van de brandstof) en werd in detail bestudeerd voor drie waarden van equivalentieverhouding, namelijk 0.7, 0.8 en 0.9. $NO_x$ emissies in

de uitlaat waren voor alle drie gevallen lager dan 1 ppmv. Het ontstekingsgedrag en de vlam structuur in het vlamloze regime werden bestudeerd door middel van OH* chemiluminiscentie beelden. Gedetailleerde metingen van de snelheid werden uitgevoerd met Laser Doppler Anemometry (LDA) in een voorwaartse verstrooiing configuratie. Temperatuur werd gemeten met de Coherent anti-Stokes Raman Spectroscopy (CARS) techniek.

De OH* chemiluminescentiemetingen tonen aan dat het verbrandingsproces in de oven onderhouden wordt door zelfontbranding. Er zijn drie types van ontstekingsgedrag, namelijk een individuele zelfontbrandingskernen, meervoudige zelfontbrandingskernen en clusters van ontstekingskernen. De reactiezone (het gebied met significante chemiluminiscentie), is een verzameling van deze drie zelfontbranding structuren die tezamen het verbrandingsproces in de oven gaande houden. We noemen deze situatie de aanwezigheid van "sustained combustion". Dit proces garandeert continue verbranding in de oven zonder dat er een stabiele lokale vlam aanwezig is. Zelfontbranding wordt gecontroleerd door de lokale toestand, die voornamelijk afhangt van de stroming, de mengselsamenstelling en de temperatuur. De laatste twee worden bepaald door de mate van luchtverdunning (air dilution level) en enthalpieverlies in de verdunner. Het blijkt dat er een bereik van verdunning is waarbij zelfontbranding optreedt voor een breed bereik aan stromingscondities. Dit geeft de beste voorwaarde om stabiele vlamloze verbranding in stand te houden.

De verbrandingskarakteristieken in de oven zijn verschillend bij verschillende equivalentieverhouding. Vermindering van de equivalentieverhouding leidt tot een verschuiving van de reactiezone stroomopwaarts en een vermindering van de reactie-intensiteit. Het hoog turbulente snelheidsveld speelt een belangrijke rol in het beletten dat er een stabiele vlam zou zijn. Naarmate de equivalentieverhouding afneemt wordt het stromingsveld meer turbulent, en worden de turbulente menging en het inmengen (entrainment) van verbrandingsgassen in de jets van reactanten bevorderd. Alhoewel de turbulente fluctuaties in de drie gevallen gelijkaardig zijn, veranderen de reactie-intensiteit en de positie van de reactiezone op significante wijze.

De uiteindelijke stijging van de gemiddelde temperatuur in de oven door verbranding is minder dan 600 K, ten opzichte van de inlaattemperatuur van de lucht. De instantane piektemperatuur is lager dan 1800 K en minder dan 1.5% van de meetsamples is hoger dan 1700 K. De lage piektemperatuur onderdrukt de vorming van $NO_x$ emissies in hoge mate. Histogrammen van de temperatuurwaarden tonen aan dat er exotherme reacties optreden in de reactiezone, maar er zijn geen stabiele op een vlamfront lijkende structuren aanwezig in de reactie zone. Grote temperatuurfluctuaties zijn er een aanwijzing voor dat het verbrandingsproces nogal onregelmatig is in reactiezone. Ook blijkt dat de configuratie van het branderspruitstuk (nozzle) belangrijk is voor het realiseren van vlamloze verbranding omdat ze bepalend is voor het stromingsveld en voor de entrainment van verbrandingsgassen.

In het tweede gedeelte van dit proefschrift (hoofstukken 5-7), wordt een uitgebreid FGM model ontwikkeld, genoemd verdunde lucht FGM (diluted air FGM) DAFGM ontwikkeld. De effecten van verdunning op lokale condities worden hierbij meegenomen waardoor het model geschikt wordt om vlamloze verbranding te beschrijven. In het DAFGM model worden de reacties in de reactiezone behandeld als reacties van brand-

stof met verdunde lucht. In de corresponderende DAFGM opzoektabel zijn flamelets bij verschillende luchtverdunnings niveaus opgeslagen. Met een controle parameter genaamd, luchtverdunningsniveau (air dilution level), worden de flamelets geïndexeerd. Omwille van de significante warmteoverdracht door straling in de hoge temperatuur oven, wordt straling ook gekoppeld aan het DAFGM model. De stralingseigenschappen van gassen worden gemodelleerd door een gewogen-som-van-grijze-gassen model (WSGG) dat rekening houdt met de locale molaire verhouding tussen $CO_2$ en $H_2O$. Bovendien wordt ook een methode ontwikkeld om turbulentie-straling interactie in rekening te brengen in DAFGM. De modellen die in dit proefschrift zijn ontwikkeld zijn geïmplementeerd in de open source CFD software OpenFOAM-2.3.1, inclusief een nieuw algoritme voor het opslaan en opzoeken met interpolatie in twee tot zes-dimensionale opzoektabellen.

Het model is eerst toegepast op de case "DJHC-I Re=4100"van de DJHC brander database gebruik maken van zowel RANS als LES methoden. Het blijkt dat de resultaten voor deze vlam niet gevoelig zijn voor het al dan niet meenemen van fluctuaties in de voortgangsvariabele maar dat de beginsnelheid die wordt aangenomen voor de omgevingslucht wel enige invloed heeft op het voorspelde temperatuurprofiel op hogere hoogte boven de brander. De voorspelde statische eigenschappen van het turbulent snelheidsveld en van de temperatuur zijn grotendeels in goede overeenstemming met de experimentele resultaten. Dit geldt zowel voor RANS als voor LES, maar de voorspellingen door LES zijn wel nauwkeuriger dan die door RANS. In de LES resultaten is duidelijk te zien hoe lucht inmengt in de coflow door de grote vortices in de schuiflaag tussen beide. Daardoor wordt lucht hogerop getransporteerd tot in de vlam zone tussen brandstof en coflow en neemt daar deel aan de reacties.

Daarna is het model toegepast op de nieuwe oven. Het geval met equivalentieverhouding $\phi = 0.8$ werd gekozen voor de validatiestudie. Het blijkt dat de resultaten in de oven zeer gevoelig zijn voor de fluctuaties in de voortgangsvariabele. Dit is in overeenstemming met de waarneming dat de verbrandingskarakteristieken gevoelig zijn aan turbulentie. De gemiddelde eindtemperatuur bereikt in de reactiezone is dichtbij de gemeten waarde. Uit het voorspelde stromingsveld kan worden afgeleid dat het verdunningsproces opgedeeld kan worden in twee fasen, de directe verdunningsfase en de indirecte verdunningsfase. De directe verdunning gebeurt voordat de luchtjets met elkaar interageren. Alle jets worden dan onafhankelijk van elkaar verdund door entrainment van verbrandingsproducten. De direct verdunning gebeurt wanneer de jets al met elkaar reageren. De turbulente menging transporteert dan verbrandingsgassen vanuit de recirculatiezone naar het inwendige deel van de jets. Ook dit bevestigt dat het ontwerp van de brander nozzle configuratie belangrijk is voor het sturen van de sturing van menging van reactanten en verbrandingsgassen.

De rekenresultaten van het model zijn in goed overeenstemming met de experimentele data zowel voor de DJHC vlam als voor de oven. Dit toon aan dat het DAFGM goed geschikt is voor het modelleren van vlamloze verbranding.

Tot slot, deze studie levert fundamentele wetenschappelijk kennis en inzicht in de aard van vlamloze verbranding. De experimentele resultaten tonen de verbrandingskarakteristieken van vlamloze verbranding in een oven, en leveren ook een database voor validatie van numerieke modellen. Het DAFGM model en de implementatie van

turbulentie-straling interactie gepresenteerd in dit proefschrift kunnen goede voorspellingen leveren van vlamloze verbranding en kunnen van nut zijn bij het ontwerp van schone en efficiënte verbrandingsinstallaties.

# 1

# INTRODUCTION

1

## 1.1. ENERGY, COMBUSTION AND ENVIRONMENT

Humans need energy for daily life everywhere. Most of the energy used in our daily life originates from non-renewable sources. Once we have used these fuels, they are gone forever. Fortunately, thanks to technology development progress is being made towards increased use of renewable types of energy, e.g. solar and wind energy, hydro power, biomass, etc. and related techniques to use them. However, world energy consumption is projected to increase by 28%, according to the latest International Energy Outlook 2017 (IEO2017) from the US Energy Information Administration, and the challenge to combine this with transition to renewable sources is immense. As shown in Figure 1.1, through 2040, the outlook's reference case projects increased world consumption of marketed energy from all fuel sources, except for coal, demand for which is projected to remain essentially flat. Renewable energies are expected to be the fastest-growing energy source. Nuclear power is projected to be the world's second fastest-growing source of energy. Natural gas, which has a lower carbon intensity than coal and petroleum, is the fastest-growing fossil fuel in the outlook. Even though IEO2017 expects the nonfossil fuels–renewables and nuclear–to grow faster than fossil fuels, fossil fuels still account for more than three quarters of world energy consumption through 2040.

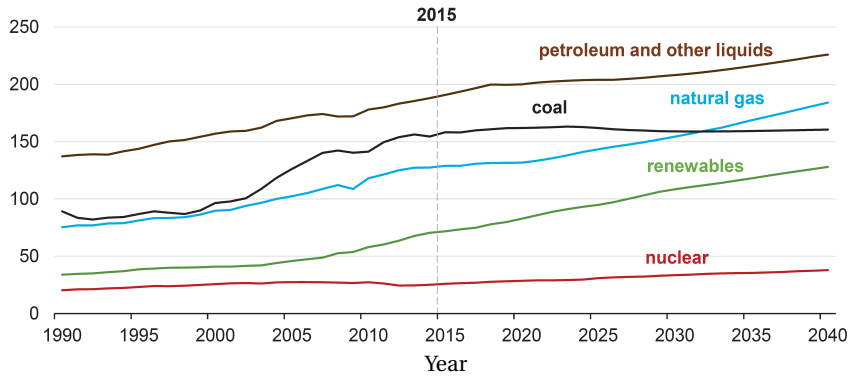


**Figure 1.1:** World energy consumption by energy source, unit: quadrillion British thermal unit (Btu*). Source: IEO2017.

Combustion is one of the greatest technologies in human history. It converts the chemical energy stored in fossil fuels in one or more steps towards directly usable forms of energy, primarily mechanical energy, electrical energy and heat energy. At present, eighty percent of energy from combustion is still produced by burning fossil fuels. Although increasing the comfort of life, wide spread use of combustion systems also has adverse effects on our environment, e.g. air pollution (particulate matter, $NO_x$, $SO_x$). and climate change (via release of greenhouse gases). Over the past twenty years, nearly three-fourths of these human-caused emissions came from burning fossil fuels. $NO_x$ is a generic term for the nitrogen oxides that are most relevant for air pollution, namely nitric oxide (NO) and nitrogen dioxide ($NO_2$). The most dominant source of $NO_x$ emissions is

* 1 Btu= 1055.0558526 J

combustion of fossil fuels. When released in the atmosphere $NO_x$ emissions can further react to produce photochemical smog, acid rain, as well as enhance tropospheric ozone production and stratospheric ozone depletion (Correa, 1993; Beér, 1994; Glassman and Yetter, 2008).

It is not feasible to switch the power source from fossil fuels to clean fuel source like solar and wind power in a short term. To reduce emissions also innovation of combustion technology to make it cleaner and more efficient is urgently needed. Emission regulations and growing awareness of the general public are also expected to bring forward the changes to more energy efficient and environment friendly technologies.

## 1.2. $NO_X$ EMISSIONS FROM COMBUSTION

Nitrogen oxides are formed when fuel is burned at high temperatures. They are emitted from automobiles, trucks and various non-road vehicles (e.g. construction equipment, boats, etc.) as well as industrial sources such as power plants, industrial furnaces, cement kilns, and turbines. Due to the role of $NO_x$ in combustion and their impacts on the environment, the chemical kinetics of their formation has been the subject of many studies (Zeldovich, 1946; Fenimore, 1971; Miller and Bowman, 1989; Ju and Niioka, 1997).

There are three predominantly mentioned sources of nitrogen oxides from combustion processes, namely thermal $NO_x$, prompt $NO_x$ and fuel-$NO_x$. The thermal NO formation mechanism described by the Zeldovich mechanism (Zeldovich, 1946) is dominant at high temperature and with sufficient oxygen available. It can cause considerable NO emissions in a time of a few seconds at temperature around 1873 K, or in a few milliseconds when temperature is above 2273 K (Wünning and Wünning, 1997). At 1800 K the NO formation rate doubles for every 35 K temperature rise (Beér, 1994). It has also been found that if temperatures does not exceed 1800 K thermal NO emissions are low (Chigier, 1981). Because of this strong temperature dependence, most NO-reducing techniques try to cut off peak temperatures, and keep the residence time in high temperature areas low and avoid high oxygen concentration in the reaction zone. These key factors as well as improved energy efficiency are the requirements for developing new combustion technologies.

## 1.3. FLAMELESS COMBUSTION

It is well known that thermal efficiency of combustion systems may be increased by preheating of the reactants with the energy recycled from exhaust gas (Weinberg, 1971; Hanby, 1994; Katsuki and Hasegawa, 1998). An immediate drawback of preheating techniques is that the increased peak flame temperature results in increased $NO_x$ emissions (Flamme et al., 1988). However, if a proper way for internal exhaust gas recirculation is used, reactants are diluted and a low oxygen content mixture is obtained in the furnace (Nishimura et al., 1997; Suzukawa et al., 1997; Choi and Katsuki, 2001; Tsuji et al., 2003). Combustion takes place at low fuel and oxygen concentration. The exhaust gas acts as an inert diluent which basically acts as additional thermal mass taking part of the heat released from reactions and flame temperature is lowered and $NO_x$ emission is reduced. In this way, energy efficiency is increased and $NO_x$ formation is to large ex-

tent suppressed at the same time. Together with the thermal efficiency also the carbon dioxide emission per unit of useful process heat delivered is reduced. The combination of using high temperature reactants and achieving highly diluted reactive mixture by internal recirculation in combustion system forms the basis of the flameless combustion technique.

Flameless combustion, also named Moderate or Intense Low-oxygen Dilution (MILD) combustion (de Joannon et al., 2000), colourless combustion (Weber et al., 2000) or high-temperature air combustion (HiTAC) (Tsuji et al., 2003), works on the principle of diluting reactants with recirculated combustion products slowing down the reactions. Reaction intensity becomes lower than the conventional combustion and peak flame temperature is reduced and thermal gradients in the reaction zone are lower. When the amount of inert introduced by the recirculation is sufficient to alter the structure of the reaction zone, the flameless combustion regime is reached (Mohamed et al., 2012). It is claimed that to achieve flameless combustion conditions the temperature prior to combustion must exceed the autoignition temperature of the mixture (Katsuki and Hasegawa, 1998; Choi and Katsuki, 2001). However, the exact definition of the amount of preheating and recirculation required to achieve flameless combustion is somewhat ambiguous.

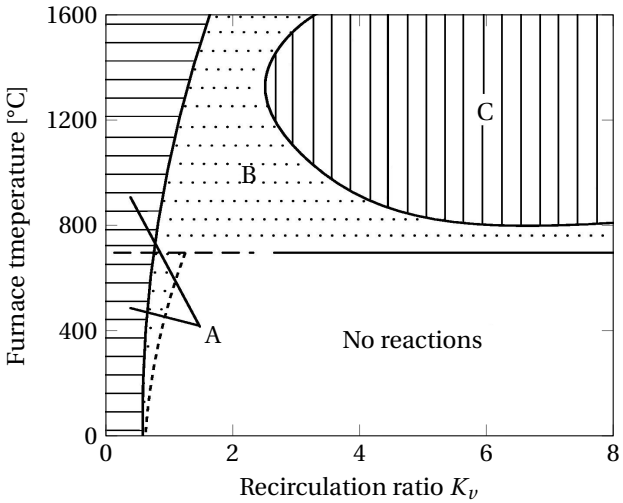


**Figure 1.2:** Schematic diagram of the stability limits for different combustion modes. Zone A: stable flames regime; zone B: unstable flames regime; zone C: flameless regime. Source: Wünning and Wünning, 1997.

The two basic conditions for flameless combustion mentioned above, namely high dilution and high preheat temperature of the reactants, are typically met by internal recirculation of the burnt gas into the reaction zone. While diluted by entrained burnt gases, fuel and air are both preheated. Entrainment of burnt gases into the combustion zone is very important for the initiation of flameless combustion (Özdemir and Peters, 2001). Wünning and Wünning (Wünning and Wünning, 1997) defined a parame-

ter named recirculation ratio to describe the characteristics of the recirculation. Different combinations of recirculation ratios and temperatures result in different combustion modes as shown in Figure 1.2. The recirculation ratio is defined as

$$K_v = \frac{\dot{m}_e}{\dot{m}_f + \dot{m}_a} \tag{1.1}$$

where $\dot{m}_e$, $\dot{m}_f$ and $\dot{m}_a$ are respectively mass flow rates of recirculated burnt gas, fuel and air. Stable flames (zone A) are achievable over the whole range of combustion chamber temperatures, but only in a narrow recirculation ratio window. As recirculation ratio is increased, the flames become unstable even extinguish if the temperature is below the autoignition temperature (the horizontal line), as seen in the "No reactions" zone. However, as long as the temperature is high (above the self-ignition temperature), stable reactions are sustained in the flameless regime even with very high burnt gas recirculation ratio (greater than 3).

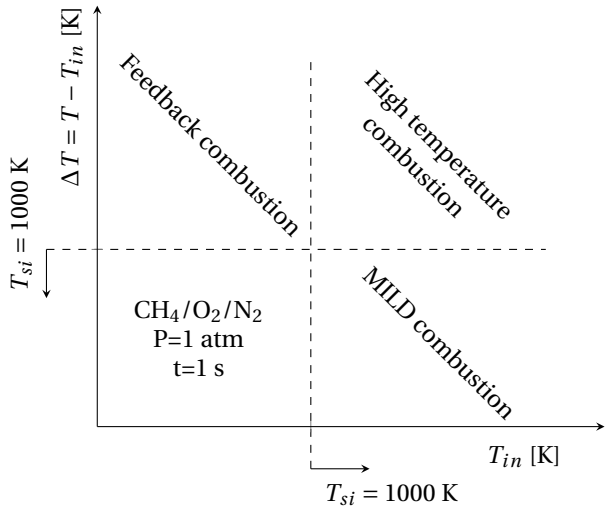


**Figure 1.3:** Combustion regimes defined with inlet temperature and temperature raise. Source: Cavaliere and de Joannon, 2004.

One most used definition of flameless combustion has been made by Cavaliere and de Joannon (2004): "A combustion process is named MILD when the inlet temperature of the reactant mixture is higher than mixture self-ignition temperature whereas maximum allowable temperature increase with respect to inlet temperature during combustion is lower than mixture self-ignition temperature." The resultant diagram is displayed in Figure 1.3. However, this definition is based on the theoretical analysis of a well-stirred reactor (WSR). It is easily applied to premixed combustion, whereas it is not straightforward for non-premixed systems (Minamoto et al., 2013). Because the inlet temperature of non-premixed systems is normally lower than the autoignition temperature. It is the mixing process with hot burnt gas that preheats the fuel and oxidizer to autoignition

temperature. Indeed, flameless (MILD) combustion can be achieved without air preheating (Kumar et al., 2002; Szegö et al., 2009).

One of the most directly evident features of flameless combustion is the change of luminous emission characteristics in the visible region of reaction zones as compared to traditional combustion processes (Ishiguro et al., 1998; Dally et al., 2002; Tsuji et al., 2003). By decreasing oxygen concentration and increasing preheating temperature the flame volume increases whereas the flame luminous emission decreases, by the combination of concentration and chemical effects (Cavaliere and de Joannon, 2004). The reactions are more distributed, in turn distributing the heat release. Although the heat release occurs over a larger volume, the total released energy is the same, implying that the heat release rate per unit volume is lower under flameless combustion conditions (Hasegawa et al., 1997). In the reaction zone, temperature peaks are avoided because of part of the heat from reactions is absorbed by recirculated flue gas, and thereby thermal NO formation is largely suppressed.

## 1.4. CURRENT STATE OF FLAMELESS COMBUSTION RESEARCH

As was highlighted in the previous section, flameless combustion has potentials in a number of practical applications, but this is limited by a lack of detailed understanding of its fundamental aspects. Extensive experimental and numerical work has been done to understand the fundamental aspects.

Flameless combustion has recently been experimentally studied on lab-scale setups because of its scientific challenges, environmental concerns and potential industrial applications. Such lab-scale setups enable a wide range of combustion parameters to be easily varied. Three levels of experimental setups are used to study flameless combustion. Those are jet-in-hot-coflow (JHC) burners, lab-scale furnaces and semi-industrial furnaces. To simplify the complexity of the recirculation of burnt gas in a confined furnace, JHC burners use hot coflows generated by a secondary burner or diluting air with $N_2$ or/and $CO_2$ to mimic the diluted air which is actually diluted by burnt gas entrainment in furnaces. The resultant lab-scale flame configuration is as simple as conventional jet flames and allows for detailed measurements with laser diagnostics for velocity, temperature and species. In addition, with the help of high-speed equipment, time-resolved visualization of flame structure and simultaneous scalar measurements on such burners have been obtained (Dally et al., 2002; Oldenhof et al., 2010; Duwig et al., 2012; Arndt et al., 2013). In this way, knowledge on the combustion under highly preheated and highly diluted air conditions was consolidated.

However, what is observed in these JHC flames represent only part of the phenomena in a furnace. How can these findings be related to the flames in a furnace is still unclear because of the lack of similar experimental measurements and observations in the furnace. Compared to the JHC burner, the internal recirculation patterns are represented more faithfully in a lab-scale furnace. And the configuration is still simple enough to make detailed laser diagnostic measurements, in contrast with the more complex (semi) industrial furnaces.

There are several past and ongoing investigations on lab-scale furnaces (Plessing et al., 1998; Cavigiolo et al., 2003; Lupant et al., 2007; Szegö et al., 2008; Veríssimo et al., 2011; Hosseini and Wahid, 2013). Operational conditions, including jet velocity, equiv-

alence ratio, air preheating temperature, burner configuration, have been varied. In all these studies, there is still no clear quantitative rule to define whether the furnace is working in flameless regime. Mostly the invisible flame and low $NO_x$ emission are used as key criteria. However, valuable results were obtained. Air jet(s) velocity or momentum was found of importance for establishing flameless combustion in all studies mentioned above, because it influences the internal recirculation of burnt gas which is decisive for flameless combustion. Therefore, attention should be paid to the factors which significantly affect the internal aerodynamics in the furnace, e.g. inlet velocities (or momentum) of air and fuel jets, air preheating temperature, equivalence ratio and burner configuration, etc. Although air preheating before entering the furnace was found not essential to establish flameless combustion (Szegö et al., 2009), it indirectly influences the air inlet velocity, and is also of interest for energy saving.

Due to the importance of internal aerodynamics in the furnace, non-intrusive methods like laser diagnostics are preferred to perform detailed measurements in a lab-scale flameless furnace. To clarify, both qualitatively and quantitatively, the relationships between flameless combustion and those factors (e.g. jets velocities, equivalence ratio, air preheating temperature and burner configuration) is a key objective for scientific research and also a fundamental issue for the development and optimization of flameless combustion technology.

Apart from the experimental approach, numerical modelling is also a powerful tool to understand the processes in flameless combustion. Several combustion models have been used for flameless combustion modelling: Laminar Flamelet Model (LFM) (Coelho and Peters, 2001; Christo and Dally, 2005), Eddy Dissipation Concept (EDC) model (Rebola et al., 2013; Lupant and Lybaert, 2015) and Transport Probability Density Function (TPDF) model (Christo and Dally, 2004; Sarras et al., 2014) and other. In the flameless conditions, the high dilution level significantly reduces the reaction rates and makes the interaction between chemistry and turbulence more important (Tabacco et al., 2002). In the modelling work for JHC flames, it was found that the LFM is inadequate. Although the EDC model gives reasonably good results, it incorrectly predicts the flame lift-off height (Christo and Dally, 2005; De et al., 2011). To obtain good results, modifying the model constants is needed. An extended EDC model, which determines the local model constants based on the local Damköhler number and turbulent Reynolds number, was proposed by Parente et al. (2016) to account for the specific features of flameless combustion. And a similar extended EDC model is developed by Bao (2017). Because the EDC model can incorporate detailed chemistry which is of importance in flameless combustion, it was applied in most of the simulation work in furnaces (Mi et al., 2010; Graça et al., 2013; Rebola et al., 2013; Li et al., 2014; Lupant and Lybaert, 2015). However, it becomes very computational expensive when large detailed chemistry mechanisms are used. In addition, the model constants are usually modified differently in different cases. Therefore, research has also continued towards using tabulated chemistry approaches like advanced flamelet concept based models–Flamelet Generated Manifolds (FGM) or Flamelet Progress Variable (FPV) approach (Ihme and See, 2011; Lamouroux et al., 2014; Locci et al., 2014; Abtahizadeh et al., 2017).

Although the flameless regime is often claimed to occur at Damköhler number ($Da$) of an order of unity where the flamelet concept is not valid, research has shown that

flamelet-like thin reaction structures are present in the reaction zone in flameless combustion. Experimental results especially PLIF images (Plessing et al., 1998; Özdemir and Peters, 2001; Dally et al., 2004) have shown the presence of local reaction zones in flameless combustion. Recent DNS (Direct Numerical Simulation) results also have shown that typical flamelet-like thin reaction zones do exist in flameless combustion (Minamoto and Swaminathan, 2014; Minamoto et al., 2014). Flamelet based models therefore could still be attractive for flameless combustion also because much less computational resources are required while incorporating detailed chemistry (Peters, 1984; van Oijen and de Goey, 2000). The challenge of modelling flameless combustion in furnaces with the FGM/FPV approach is to include the dilution effects of recirculated burnt gas in the tabulated flamelets library and find a proper way to relate the controlling parameters in the flow fields to the library. The related work will be reviewed in Chapter 5 and 7.

Another important factor in flameless combustion modelling in the furnace is radiation. Since fuel and air streams are highly diluted by recirculated burnt gas which contains carbon dioxide and water, these species increase the infrared radiative flux (Lallemant et al., 1996). Therefore, radiative heat transfer in flameless combustion processes can be significantly different from that in conventional combustion processes (Ruan et al., 2001; Wang and Niioka, 2001; Tsuji et al., 2003).

## 1.5. OBJECTIVES

The encouraging experimental observations from JHC flames actually call for further research in order to gain greater detailed understanding of flameless combustion in a furnace. Experimental studies are of course the first choice to get first hand information like flame behaviour, reaction zone structure, temperature, velocity and species. The more detailed the measurements are, the more useful they are for theoretical analysis and for formulation of proper mathematical models for the combustion process in both physical and chemical aspects.

To the author's knowledge, only few detailed non-intrusive measurements in flameless combustion chamber have been published, namely temperature measurements (Plessing et al., 1998; Özdemir and Peters, 2001; Kitagawa et al., 2003; Dally et al., 2004; Shimada et al., 2005) and flame structures (Plessing et al., 1998; Özdemir and Peters, 2001; Zhou et al., 2017) were reported. But velocity measurements in flameless combustion furnace were reported only in the Refs. (Özdemir and Peters, 2001; Szegö, 2010). A detailed review of the results including those in JHC flames will be presented in Chapter 3 and 4. To enrich the experimental data base, a well controlled lab-scale furnace which enables a fundamental study of the factors influencing flameless combustion is attractive, and is the main object of the study in this work.

On the other hand, detailed experimental observations collected in a data base are essential for new model development and model validation. With validated models, numerical simulation becomes an ideal tool to do further analysis due to the facts that it is normally cheaper than experiments, and more detailed information is available from the simulation results. Therefore model validation is also included in this work.

Flame structures in flameless combustion are very different from those in conventional flames. This brings difficulty in modelling of flameless combustion. There is

no existing model specifically for flameless combustion and most traditional combustion models failed in this job. New models are being developed and here is a common point for all the newly developed models, that is using tabulated chemistry methods. These models will be reviewed in the Chapter 6 and 7. When studying and applying the proposed methods, the author noticed the importance of the definition of the diluent stream and the chemistry tabulation method and this led to further developments to effectively and accurately account for the characteristics of thermochemical composition in flameless combustion.

The objective of this thesis is to study, experimentally and numerically, flameless combustion of Dutch natural gas in a lab-scale furnace which allows for detailed laser diagnostics. First, flame behaviour and flame structure will be captured using high-speed imaging system. Detailed measurements of velocity and temperature will be performed using Laser Doppler Anemometry (LDA) and Coherent Anti-stokes Raman Spectroscopy (CARS) techniques. The results will be analysed to deduced the essential characteristics of flameless combustion in a furnace. Next, appropriate CFD models will be developed and validated. The solver which contains the models will be implemented using the open source CFD platform OpenFOAM.

## 1.6. OUTLINE OF THIS THESIS

This thesis is a contribution towards the fundamental understanding of flameless combustion. A lab-scale furnace is chosen for both experimental and numerical study of flameless combustion. This thesis is structured in four parts: introduction, experiments, modelling and conclusions.

This chapter, Chapter 1, introduces the background information of this research, clarifies the motivation and objectives, and lists the outline of this thesis.

The part on experiments includes Chapter 2, 3 and 4. A detailed description of the lab-scale furnace and a brief description of the principles of measurements techniques are presented in Chapter 2. High-speed imaging was performed with an intensified camera. Flame behaviour and structure were examined by the analysis of OH* chemiluminescence images. LDA and CARS techniques were used for velocity and temperature measurements. Both techniques are pointwise technique. A flue gas analyser was employed to measure the $NO_x$ emission in the exhaust gas. Chapter 3 presents the observations of flame behaviour and flame structures and the theoretical analysis of the autoignition limit in highly diluted and highly preheated conditions. Detailed velocity and temperature measurements are presented in Chapter 4. A discussion of the effects of flow field on the reactions in the current furnace is given. Temperature statistics in the reaction zone and near the fuel nozzle exit are discussed.

The part on modelling includes Chapter 5, 6 and 7. A brief description of the theories that are involved in turbulent combustion modelling is presented in Chapter 5. The detailed descriptions of the combustion model–Diluted Air Flamelet Generated Manifolds (DAFGM), the method accounting for turbulence-radiation interaction (TRI), and the method of coupling radiation with DAFGM model are also presented in Chapter 5. Chapter 6 and 7 report the application of the DAFGM model developed in this thesis to the chosen target flames. Thanks to the general nature of the model, it is also capable to model the JHC flames. In Chapter 6, the DAFGM model is applied to Delft jet-in-

hot-coflow I Re=4100 flame for both RANS and LES modelling and the validation. In Chapter 7, the DAFGM model is applied to model flameless combustion in the lab-scale furnace used in this thesis. Radiation modelling and turbulence radiation interaction are included by using the methods developed in Chapter 5.

Finally, the main conclusions and findings of this study are summarized, suggestions and recommendations for future studies are made in Chapter 8.

# 2

# EXPERIMENTAL METHODS

*This chapter presents the lab-scale furnace and the measurement techniques used in this study. The furnace is designed such that it is able to operate in flameless combustion regime in a range of conditions. In the meantime, it should provide good optical access to enable the use of non-intrusive laser diagnostics. The furnace consists of a commercial WS REKUMAT 150 recuperative Flame-FLOX burner and an insulated combustion chamber. The burner and combustion chamber are mounted on a traversing system which allows three-dimensional movement of the furnace relative to the fixed optical setups. Mean and time resolved visualizations were performed with a high-speed imaging system. Measurements of the velocity and temperature were made by Laser Doppler Anemometry (LDA) and Coherent Anti-Stokes Raman Spectroscopy (CARS), respectively. $NO_x$ emissions were measured in the flue gas with a flue gas analyser.*

## 2.1. EXPERIMENTAL SETUP DESCRIPTION

The lab-scale flameless combustion furnace designed for this study is shown in Figure 2.1. The internal dimensions of the whole furnace are 320 mm×320 mm×1400 mm. The height of the combustion chamber is bounded by the internal top wall. A commercial WS REKUMAT 150 recuperative Flame-FLOX burner is mounted at the bottom of the combustion chamber. The REKUMAT 150 recuperative Flame-FLOX burner was made available by WS (Renningen, Germany) (WS). The burner (92 mm in diameter) is protruding 30 mm into the chamber, resulting in a distance of 600 mm from the nozzle tip to the internal top wall. This results in inner dimensions of the combustion chamber of 320 mm×320 mm×630 mm. The integrated setup is mounted on a traversing system. The combustion chamber can only be moved in the horizontal plane (x-y plane), and the burner and internal top wall can be moved both in the horizontal plane (x-y plane) and in the vertical (z) direction. The distance between the burner tip and the internal top wall is fixed at 600 mm thus keeping the same size of combustion chamber. This design allows for three dimensional measurements along the x, y and z directions with fixed optical probes. The burner nozzle (Figure 2.1(bottom right)) consists of one central fuel nozzle with a diameter of 4.5 mm and four air nozzles each having a diameter of 8.6 mm symmetrically located around the fuel nozzle. The distance between the fuel nozzle axis and each air nozzle axis is 21 mm. The side and bottom walls of combustion chamber are insulated with 50 mm thick ceramic foam layers. Furnace internal and external top walls are both 310 stainless steel plates, acting as a heat sink and not insulated. Decreasing or increasing heat extraction can be done by adding insulation on the external top wall or blowing cooling air on the external top wall. This cooling method is chosen because it causes less internal flow complexity than internal cooling tubes. Two side walls are equipped with quartz windows with size 280 mm×100 mm. The heat losses through these windows are large leading to different conditions in the furnace when the position of the burner and internal top wall is changed. Therefore, the windows are also insulated with ceramic foam except for a small opening allowing laser beams to pass through the furnace. The transmissivity of the quartz glass is above 90% within the wavelength 220~2000 nm, which also enable to collect OH* chemiluminescence around 308 nm.

The burner is able to operate in both flame and flameless modes. The flow control scheme is shown in Figure 2.2. In flame mode, fuel is supplied by a 200 millibar natural gas line. Fuel and air are premixed and injected into the furnace through the four air nozzles. Premixed flames stabilize on the four air nozzles and are used to preheat the furnace to 1123 K (850 °C). Once the temperature inside the furnace is above 1123 K, a switch to flameless mode is made automatically. Fuel is then supplied by a 2 bar natural gas line and injected through the central fuel nozzle, and pure preheated air is injected through the air nozzles. The flow rates of fuel and air are both controlled by Bronkhorst mass flow controllers with an inaccuracy of ±0.5% reading plus ±0.1% full scale. Flue gas leaves the combustion chamber through a 10 mm wide slit between the side walls and the bottom plate as shown in Figure 2.1 (right middle). The flue gas is then introduced into the recuperator of the burner to preheat air. The recuperator is able to preheat air up to ~973 K (700 °C).

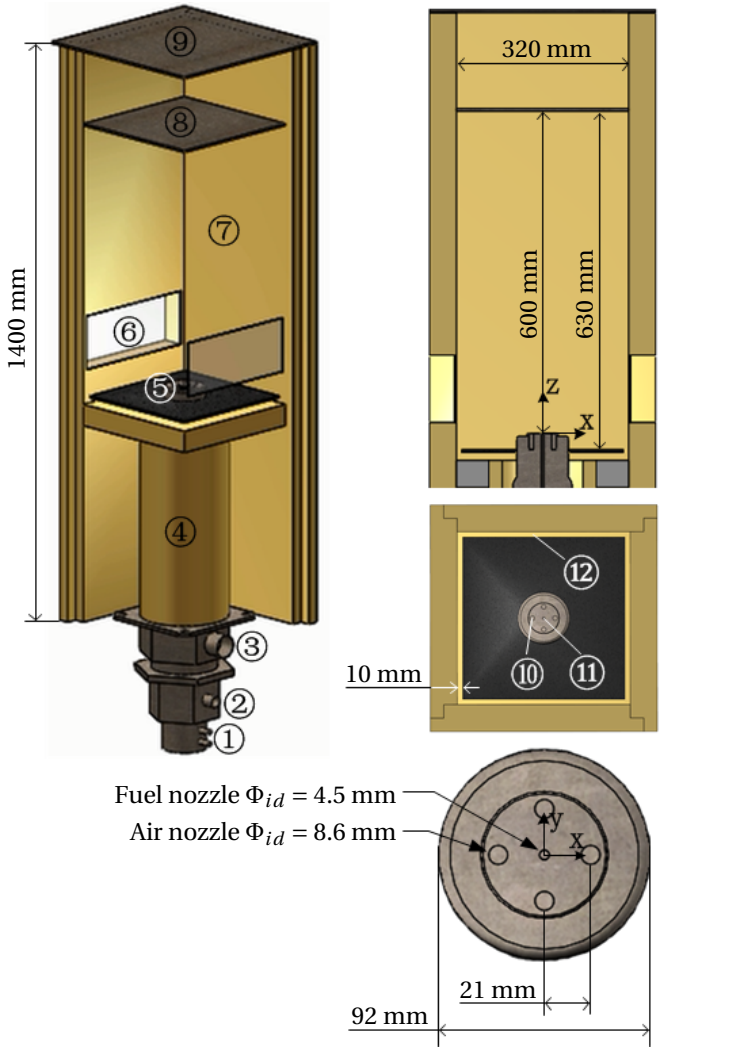


①:Fuel inlets
②:Air inlet
③:Flue gas exit
④:Recuperator
⑤:Burner nozzle
⑥:Quartz windows
⑦:Insulation walls
⑧:Internal top wall
⑨:External top wall
⑩:Air nozzles
⑪:Fuel nozzle
⑫:Outlet

**Figure 2.1:** Schematic of the lab-scale furnace (left), vertical cross section of combustion chamber (top right), top view (middle right) and burner nozzle (bottom right).

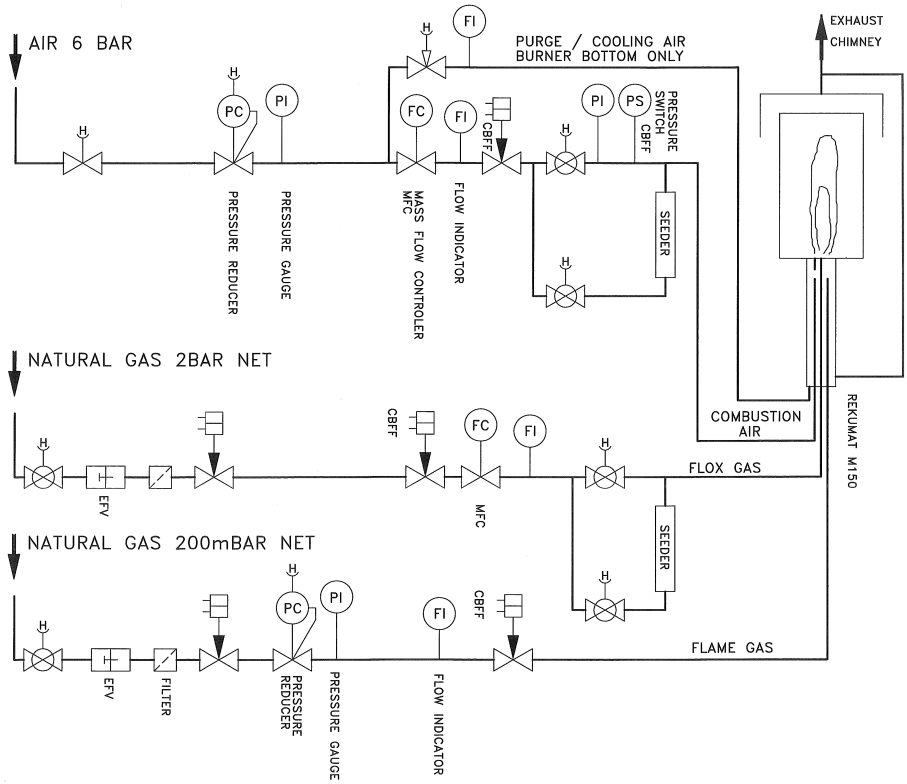


**Figure 2.2:** The flow control scheme used for the furnace operation .

## 2.2. MEASUREMENT TECHNIQUES

### 2.2.1. OH* CHEMILUMINESCENCE IMAGING

Flame chemiluminescence is the radiation emitted by electronically excited molecules in flames when these molecules return to a lower energy state. The wavelength of the radiation is characteristic for the particular molecule and the particular transitions the molecule undergoes. OH*, CH* and $C_2^*$ are examples of molecules exhibiting a simple spectrum with major peaks at 308 nm, 431 nm and 513 nm, respectively. Since these species are mainly produced in the reaction zone, chemiluminescence can be used as a marker of the reaction zone and heat release rate (Marques et al., 2001; Hardalupas and Orain, 2004; Stojkovic et al., 2005; Nori and Seitzman, 2008). It is also used to show dynamic behaviour of flames and to identify flame structure and flame stabilization mechanisms (Beyler and Gouldin, 1981; Paschereit et al., 1998; Song et al., 2016) in combustion research. Moreover, quantitative results such as Damköhler numbers (Ikeda et al., 2001) and heat release rate (Hardalupas et al., 2010) can be obtained. From a practical viewpoint, flame chemiluminescence detection is a simple method that can be used in many combustion systems. In this chapter, the chemiluminescence imaging technique

will be applied to identify flame characteristics in flameless combustion.

In flameless combustion, reactants are diluted. The reaction rate in the reaction zone is slowed down and reaction intensity is decreased. Compared to conventional flames, the chemiluminescence intensity from the reaction zone is orders of magnitude lower. The flame even becomes "invisible". In this study, OH* chemiluminescence images were collected by using a high-speed intensified camera (Lambert Instruments HI-CAM CR). The camera is equipped with a Nikkor UV 1:4.5, f=105 mm lens with a transmissivity exceeding 70% for wavelength between 220 nm and 900 nm. The CMOS sensor has 1280×1024 pixels. The maximum frame rate with full chip is 500 fps, and 1000 fps with half chip (1280×512 pixels). A bandpass UV filter was used to eliminate the furnace background light. The filter is centred at 308 nm wavelength with a FWHM (Full Width at Half Maximum) of 20 nm. The transmissivity is greater than 40%. Different settings were applied for time averaged and time resolved OH* chemiluminescence measurements. To obtain the time averaged OH* chemiluminescence of the whole reaction zone, the full chip was used and images were taken at low frame rate (50 Hz) to have longer averaging time. Due to the limited field of view of the camera, the images were taken at three different vertical positions and the total field is then reconstructed in data postprocess. To obtain the time resolved OH* chemiluminescence, half of the chip was used to achieve a higher frame rate (1000 Hz). The calibration for the field of view is done with a vertically hanging ruler.

### 2.2.2. LASER DOPPLER ANEMOMETRY (LDA)

Laser Doppler Anemometry is a widely used technique to measure velocity in gases and liquids. Its non-intrusive nature and directional sensitivity make it very suitable for measurements in highly turbulent flows with flow reversals, chemically reacting or high-temperature media, where physical sensors are difficult or impossible to use.

LDA measures the velocity of small tracer particles that move with the flow. When the particles are sufficiently small, it can be assumed that the velocity of the particles is equal to the velocity of the fluid. The physical principle used to measure the particle velocity is to measure the Doppler frequency of the light scattered by seeding particles. In practice a coherent light source such as a continuous laser is used to produce two crossing laser beams. At the intersection (the measurement volume) of the two laser beams, an interference pattern of alternating bright and dark fringes is formed. As a particle moves through the measurement volume, it scatters light when it crosses a bright fringe, and scatters no light when it passes a dark fringe. The distance $d_f$ between two consecutive lines of constant intensity in the interference pattern is given by

$$d_f = \frac{\lambda_0}{2\sin(\theta/2)}, \tag{2.1}$$

where $d_f$ is the fringe distance, $\lambda_0$ is the incident light wavelength and $\theta$ is the beam intersection angle. A small particle passing through the interference pattern with a velocity component $v_p$ in the direction perpendicular to the fringes, scatters light with an intensity that varies periodically in time. The frequency of these light intensity oscillations,

$f_D$, is proportional to the particle velocity, i.e.,

$$f_D = \frac{v_p}{d_f} = \frac{2\sin(\theta/2)}{\lambda_0} v_p, \tag{2.2}$$



where $f_D$ is known as the Doppler frequency, from which the velocity component can be derived.

The Doppler frequency defined in Equation (2.2) can be positive or negative depending on the sign of the velocity component $v_p$. However, in practice the Doppler frequency follows from the analysis of a photodetector output signal that oscillates with frequency $|f_D|$. As a result, it is not possible to determine the sign of the velocity component. To correct for this "directional ambiguity", one of the incident laser beam is frequency shifted by a known value, $f_s$. This causes the fringe pattern to move at speed $v_s = f_s d_f$. Particles crossing the measurement volume will now have a frequency either above or below $f_s$, depending on their direction. The photodector output signal now oscillates with frequency

$$f_D = f_s + \frac{v_p}{d_f} = f_s + \frac{2\sin(\theta/2)}{\lambda_0} v_p. \tag{2.3}$$

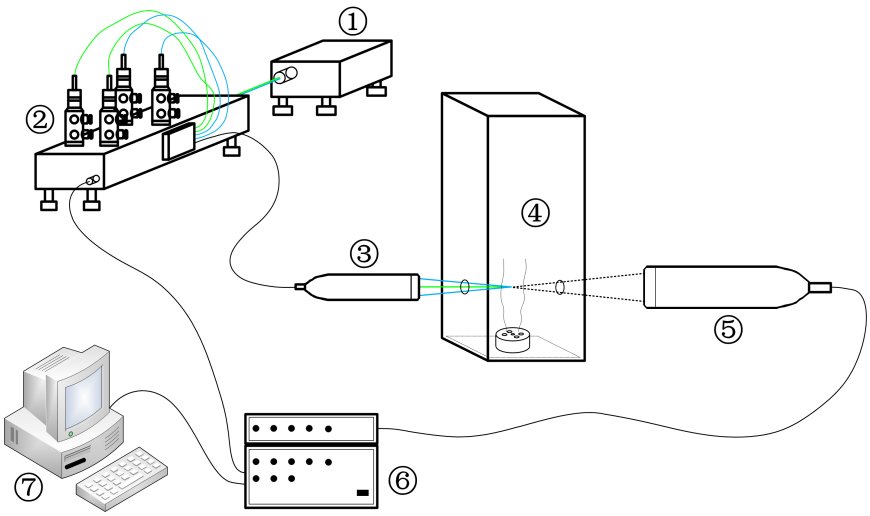


①:Laser
②:TSI Bragg Cell
③:Transmitting Probe
④:Lab-scale Furnace
⑤:Receiving Probe
⑥:Processor and Photo Detector
⑦:PC and Software

**Figure 2.3:** Schematic of the LDA system and main components.

The velocity measurements were performed with a two-component LDA system operating in a forward-scatter configuration. Aluminium oxide particles ($Al_2O_3$) with an

average diameter of 1 $\mu$m were added to the fuel and air by using two cyclone seeders. An illustration of the LDA system layout is displayed in Figure 2.3. A Dantec Doppler-Power DPSS laser producing a 1 W (maximum) blue line (488 nm) and a 1 W (maximum) green line (514 nm) was used to measure the vertical velocity component ($U_z$) and the horizontal velocity component ($U_x$). The blue beam and the green beam are each split in two beams of more or less equal intensity. One blue beam and one green beam were frequency pre-shifted over 40 MHz by a Bragg cell to enable the measurement of flow reversal. The transmitting probe had a lens with a focal length of 350 mm and yielded a measurement volume of 0.85 mm length and 0.12 mm diameter. The scattered light is collected in forward direction by placing the receiving probe on-axis and facing the transmitting probe. The photodiode output signals were electronically down-mixed, and subsequently fed to a FSA-3000 signal processor that was used to extract the two velocity components of the particles.

The calibration for this forward-scatter LDA system is done in three steps. Firstly, the transmitting probe and receiving probe are aligned on axis outside the furnace. The axis should be perpendicular to the furnace wall (or optical windows). Since the transmitting probe is self-aligned, the four beams are focused at one point. The receiving probe must be focused on the beam intersection (measurement volume). A little spray atomizer can be used to indicate the beam intersection. With the visualization of the intersection through the receiving probe, it is aligned and focused. Test measurements can be done using the spray atomizer. The rest steps should be done in a working furnace. When the furnace is stably working in flameless mode, the second step is to move the furnace and let the laser beams pass through the optical windows. Normally the receiving probe becomes slightly out of focus. One should adjust the position of the receiving probe to make it aligned again by using the seeding particles as an indicator. The last step is to align the measurement volume at the centre of the fuel jet. This must be done by moving the furnace in two directions (x and y direction as indicated in Figure 2.1). For example, when moving the furnace in x direction, one should find two jet shear layers where velocity gradients are quite large. The vertical velocities (in z direction) in each shear layer are denoted as $U_{z,x^-}$ (at $x^-$) and $U_{z,x^+}$ (at $x^+$ ). The jet centre can be zeroed at $0.5(x^- + x^+)$ where $U_{z,x^-} \approx U_{z,x^+}$. The same procedure should be done in y direction. The system is ready for measurements after these calibration procedures.

### 2.2.3. COHERENT ANTI-STOKES RAMAN SPECTROSCOPY (CARS)

CARS has been an attractive non-intrusive diagnostic technique for combustion processes over several decades since its application in flames (Tolles et al., 1977). The basic principle of the CARS thermometry is to derive the gas temperature from a comparison of the measured spectra to temperature dependent theoretical spectra. It is used to take temperature measurements in the present study. The detailed introduction of CARS theory can be found in the work of Eckbreth (1981) and Aldén et al. (1983), and a brief description on its working principle is giving below.

CARS is a four-wave-mixing and highly non-linear optical process in which three intense laser beams, one pump beam at frequency $\omega_p$, one Stokes beam at frequency $\omega_s$ and one probe beam at frequency $\omega_{pr}$ are focused into one probe volume, to generate a laser-like CARS beam at the anti-Stokes frequency $\omega_{as} = \omega_p + \omega_{pr} - \omega_s$ without chang-

ing the physical state of the probe. The anti-Stokes frequency $\omega_{as}$ is emitted only when $\omega_p - \omega_s$ is an allowed transition of the molecule.

Figure 2.4 illustrates the CARS process using an energy-level diagram. In order to obtain a temperature dependent CARS spectrum which includes all the transitions of a vibrational-rotational band of a particular molecule, e.g. $N_2$, a broadband Stokes laser is used. Thus, the CARS signal generated gives a complete spectrum containing temperature information. This allows single-shot instantaneous temperature measurements in turbulent combustion.

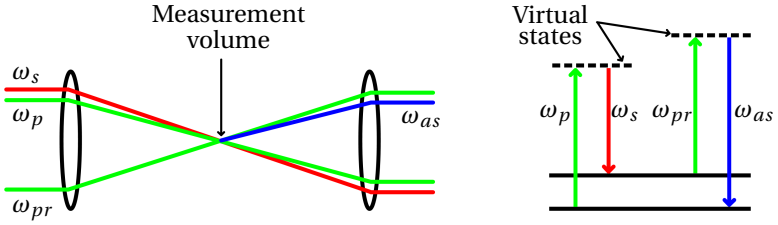


**Figure 2.4:** Illustration of Coherent anti-Stokes Raman spectroscopy optical arrangement (left) and corresponding energy level diagram for one isolated transition (right).

Typically, the probe beam comes from the same source as the pump beam and it has the same frequency $\omega_p$ and the same intensity as the pump beam. The anti-Stokes frequency becomes $\omega_{as} = 2\omega_p - \omega_s$. The intensity of the CARS signal at frequency $\omega_{as}$ is given by

$$I_{as} = \frac{\omega_{as}^2}{n_p^2 n_s n_{as} c^4 \epsilon_0^2} I_p^2 I_s \left|\chi_{CARS}^{(3)}\right|^2 L^2 \left(\frac{sin(\Delta kL)}{\Delta kL}\right)^2. \tag{2.4}$$

In the above equation, $I_*$ ("$_*$" represents "$as$", "$s$" or "$p$") are the beam intensities at frequencies $\omega_*$, respectively; $n_*$ are refractive indexes; $c$ is the speed of light; $\epsilon_0$ is permittivity of free space; $L$ is the length of probe volume; the third-order susceptibility $\chi_{CARS}^{(3)}$ is a complex quantity and detailed formulation can be found in the work of Tolles et al. (1977) and Boyd (2008); $\Delta k$ is phase mismatch of four beams. Based on Equation (2.4), the strongest CARS signal is obtained in the direction when phase matching is satisfied, that is, $\Delta k = 2\vec{k}_p - \vec{k}_s - \vec{k}_{as} = 0$. The easiest way to implement CARS is in collinear phase matching, but the spatial resolution is too low. BOXCARS, a crossed-beam phase matching technique (Eckbreth, 1978) greatly improves spatial resolution and this configuration is used in present study.

The schematic layout of the CARS system used in the current study is shown in Figure 2.5. This configuration yields a CARS probe volume of 0.7 mm length and 35 $\mu$m diameter. In the previous experiments, the single-shot imprecision of the system is 1%-4% over a range from 2000 K to 300 K. The inaccuracy is estimated to be 20 K (van Veen and Roekaerts, 2003, 2005). The reader is referred to the references for further information.

The calibration for the CARS system is similar to that for the LDA system. There are also three steps. Firstly, the optics are aligned outside the furnace to ensure strong CARS signal is generated and can be collected by the spectrometer. The axis of the focus lens should be perpendicular to the furnace wall (or optical windows). The second step is to

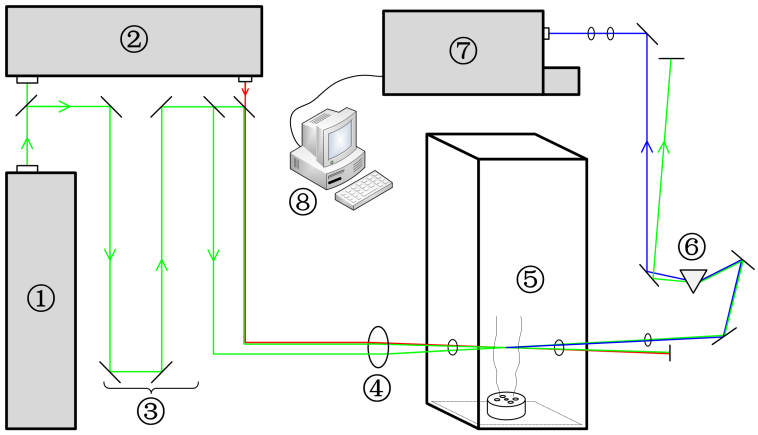


①:Nd: YAG Laser ④:Focus Lens ⑦:Spectrometer and CCD
②:Dye Laser ⑤:Lab-scale Furnace ⑧:PC and Software
③:Delay path ⑥:Receiving Optics

**Figure 2.5:** Schematic of the CARS system and main components.

move the stably working furnace and let the laser beams pass through the optical windows. Normally the CARS signal decreases sharply or disappears due to the laser beams become not focused. Slight adjustment is needed to refocus the beams to get the CARS signal back until maximum signal strength is obtained. The last step is also to align the measurement volume at the centre of the fuel jet. This is also done by moving the furnace in x and y directions (as shown in Figure 2.1). During the movement, one should pay attention to the spectrum change in the signal. Once methane passing through the measurement volume, its nonresonant spectrum would be noticed. The two points in each jet shear layers where the nonresonant spectrum of methane starts appearing are used to determine the centre in the direction. The same procedure should be done in the other direction. The system is ready for measurements after these calibration procedures.

### 2.2.4. FLUE GAS ANALYSER

Flue gas composition measurements were performed with a Testo 335 flue gas analyser which can be used for emission monitoring in industrial furnaces. It has a resolution of 1 ppm for both CO and $NO_x$. The inaccuracy for CO measurement is ±10 ppm of the reading at 0-200 ppm, ±5 ppm of the reading at 0-100 ppm for NO and ±10 ppm of the reading at 0-200 ppm for $NO_2$.

### 2.2.5. THERMOCOUPLES

Super OMEGACLAD$^{TM}$ XL sheathed ungrounded type K thermocouples were used for temperature control and wall temperature measurement. The sheath material is Nickel-Chrome based, which provides excellent oxidation resistance. The sheath can withstand

exposure to combustion gases or air at temperatures up to 1608K (1335°C). The temperature drift of the thermocouple is less than 5 K. For temperature control, one thermocouple is mounted at a corner of the combustion chamber to avoid disturbance of the flow, but the temperature data is not stored. Another thermocouple is also mounted at a corner of the combustion chamber and the temperature is stored as $T_{\text{check}}$. For wall temperature measurements, three thermocouples are used. One thermocouple is mounted at the internal top wall surface and the temperature is stored as $T_{\text{top}}$. Two thermocouples are fixed on one side wall surface and the temperature are stored as $T_{\text{mid}}$ and $T_{\text{mids}}$. The exact measurement positions for $T_{\text{top}}$, $T_{\text{mid}}$, $T_{\text{mids}}$ and $T_{\text{check}}$ can be found in Section 4.4. When the burner and the internal top wall moves vertically, the thermocouples effectively measure temperatures at the corresponding locations. The readings of $T_{\text{top}}$ and $T_{\text{check}}$ can also be used to check the furnace operating states from day to day and ensure all measurements are taken at the same conditions.

# 3

# FLAME BEHAVIOUR IN FLAMELESS COMBUSTION REGIME

*This chapter reports on the results of a study on the ignition and flame behaviour in flameless combustion in the lab-scale furnace. The ignition and flame behaviour have been studied by using high-speed chemiluminescence imaging. OH* chemiluminescence was chosen as a marker for reaction intensity and as a marker for the location of reaction zones. Both mean and time resolved OH* chemiluminescence images were taken in the flameless combustion regime at different equivalence ratios. Three types of ignition phenomena were observed, i.e., individual autoignition kernel, multiple autoignition kernels and autoignition kernel cluster. It is found that autoignition was responsible for sustaining the reactions in the flameless combustion regime. The reaction zone is a collection of those three types of autoignition phenomena, occurring frequently and sustaining the combustion process in the furnace. Autoignition calculations of laminar counterflow flames showed that autoignition is local conditions controlled, mainly depending on dilution level and enthalpy loss. It is also found that there exists a dilution range (or $O_2$ mass fraction range) in which autoignition can be achieved for a wide range of flow conditions. This range provides the best conditions to sustain a stable flameless combustion process. The burner nozzle configuration also limits the operating condition range for flameless combustion.*

Part of this chapter has been published as: X. Huang, M. J. Tummers, D.J.E.M. Roekaerts, MILD combustion in a lab-scale furnace: ignition and flame behaviour, Proceedings of the European Combustion Meeting, 2017.

## 3.1. INTRODUCTION AND LITERATURE REVIEW

Intensive research on flame visualization in conventional flames has been done, but there are not many studies that have reported on visualizations in flameless combustion. Some detailed measurements have been done in several JHC burners. Oldenhof et al. (2010) reported that the JHC flame is stabilized by autoignition kernels and visualized these with time-resolved flame luminescence imaging. By using high-speed flame luminescence imaging and OH-PLIF (planar laser induced fluorescence), it was found that the most upstream ignition location moved closer to the jet exit when jet velocity increased. This indicated that entrainment of hot oxidizer plays an important role in the formation of autoignition kernels and flame stabilisation (Oldenhof et al., 2011). The coflow temperature also has a significant effect on the flame lift-off height. When increasing the coflow temperature, the flame base moves closer to the burner exit and becomes more stable (Arndt et al., 2013). As the $O_2$ level in the coflow is reduced, the reaction zone becomes less intense leading to a greater degree of partial premixing in these flames (Medwell et al., 2007). Medwell et al. (2009) also concluded that large-scale vortices can lead to a weakening of the reaction zone or even local extinction leading to a form of partial premixing, and may contribute to the stabilization of the flameless combustion reaction zone. Arndt et al. (2016) recorded OH* chemiluminescence from two directions to determine the location of autoignition kernels. Combining this with high-speed planar Rayleigh scattering, it was found that autoignition occurs at the outmost periphery of the fuel jet at mixture fractions much leaner than the stoichiometric mixture fraction and at locations with low scalar dissipation rate. These locations are usually hot enough for autoignition kernel formation. It was also mentioned that the coflow temperature significantly influences flame characteristics, such as the flame lift-off height and ignition time.

Studying flameless combustion in industrial or semi-industrial scale furnaces with laser diagnostics is extremely difficult while detailed numerical simulations are computationally too expensive. However, flameless combustion can be studied in lab-scale furnaces that maintain the relevant internal flow patterns, but are simple enough to perform detailed optical measurements. There are several reports in literature on flame behaviour in lab-scale furnaces operating in the flameless combustion regime. Plessing et al. (1998) first reported on OH-PLIF measurements in a lab-scale furnace showing homogeneously distributed OH intensity in case of flameless combustion. Compared to highly turbulent premixed flames, OH intensity is significantly lower. Reaction zones composed of patches of distributed reaction zones approaching spatial uniformity were evidenced in subsequent work by Özdemir and Peters (2001) and Dally et al. (2004). Based on direct view of the flames in a furnace, Szegö et al. (2009) found that the flame becomes patchy and less luminous until it is no longer visible as the diluent mass fraction is increased in the fuel jet. The latter condition with nearly invisible flames can be considered as a stable flameless regime. Both flame luminescence and OH* chemiluminescence were used to determine flame behaviour at different operational conditions (Veríssimo et al., 2011, 2013a,b), such as thermal input, air inlet velocity and air preheat temperature. Zhou et al. (2017) used OH-PLIF and $CH_2O$-PLIF together with OH* chemiluminescence to characterise the different reaction zone structures from flame to flameless combustion in a laboratory combustor. They reported that the interplay between

turbulent mixing and the availability of oxygen from both the inlet air jet and recirculation is important for establishing flameless combustion. OH* chemiluminescence was also used to locate the reaction zone in a flameless furnace working with different low LHV (lower heating value) fuels by Lupant et al. (2010) and Mosca (2017).

In view of the above results, flame behaviour in JHC flames has received a lot of attention and people have reached common conclusions. They have laid a theoretical foundation of autoignition in flameless combustion and autoignition dominated flames which have been well studied in JHC flames. However, the question arises how these findings can be related to the flames in a furnace operating in flameless combustion regime. This is still unclear because of the lack of similar experimental observations in a furnace. OH* chemiluminescence was already found very suitable to capture flames or reaction zone structure in above studies. Besides, in flameless combustion, the formation of emitting species CH* and $C_2^*$ in traditional flames is suppressed (Cavaliere and de Joannon, 2004). The suppressed species chemiluminescence has been reported in the numerical study of de Joannon et al. (2000) and also has also been observed experimentally by Zhou et al. (2017). Therefore, in the present study, OH* chemiluminescence is selected as an indicator of reaction zones to study flame behaviour in a lab-scale furnace operated in flameless combustion mode.



## 3.2. CASE DESCRIPTION

Dutch natural gas was used as fuel in this study and its approximate composition is listed in Table 3.1. In the experiments, the furnace was operated at a thermal input of 9 kW (fuel mass flow rate based), and at equivalence ratios $\phi$ =0.7, $\phi$ =0.8 and $\phi$ =0.9. Table 3.2 summarizes the settings for the three cases.

**Table 3.1:** Composition of Dutch natural gas.

| Species | $CH_4$ | $C_2H_6$ | $N_2$ | Rest |
|---|---|---|---|---|
| [mole %] | 81.3 | 3.7 | 14.4 | 0.6 |

**Table 3.2:** Operating conditions for the three cases at different values of equivalence ratio $\phi$. P is the thermal input power; $\dot{V}_f$ and $\dot{V}_a$ are the fuel flow rate and air flow rate, respectively.

| Case | P (kW) | $\phi$ | $\dot{V}_f$ (nl/min) | $\dot{V}_a$ (nl/min) |
|---|---|---|---|---|
| 1 | 9 | 0.7 | 17.27 | 206.2 |
| 2 | 9 | 0.8 | 17.27 | 180.4 |
| 3 | 9 | 0.9 | 17.27 | 160.4 |

## 3.3. IMAGING METHOD AND SETTINGS

OH* chemiluminescence images of reaction region had to be composed from images taken at three vertical positions due to the limited size of the field of view of the camera in conjunction with the low chemiluminescence intensity in the flameless regime. The whole reaction region could be imaged via a quartz window in the side wall by vertically moving the burner and internal top wall, see Chapter 2 for details. As for time-averaged imaging, the full CMOS chip (1024×1280 pixels, horizontal×vertical) is used, corresponding to a field of view of 104 × 130 $mm^2$ in physical space. The resolution of the resulting image is approximately 10 pixels per millimeter. There is 104×40 $mm^2$ overlap between the fields-of-view of two adjacent positions. When constructing the mean OH* chemiluminescence distribution for the entire reaction region, strips with an area of 104×20 $mm^2$ were cut from the top and bottom of each image, resulting in an effective area of 104 × 90 $mm^2$ at each position and leading to 104 × 270 $mm^2$ for the whole reaction region. Three thousand images were taken at each position at a frame rate of 50 fps (at exposure time of 20 ms), resulting a relatively long measurement time of 60 seconds.

To capture the flame dynamics in flameless regime, a high speed imaging technique is used. When the frame rate of the camera is increased, the exposure time is reduced, hence the signal intensity is lowered. To compensate the intensity loss, the gain of the intensifier is increased to ensure sufficient signal intensity and without decreasing signal-to-noise ratio too much. Half of the CMOS chip (512×1280 pixels, horizontal×vertical) is used, corresponding to a field of view of 52 × 130 $mm^2$ (valid field of view is 52 × 120 $mm^2$) in physical space. Six thousand images were taken at each position at a frame rate of 1000 fps and at exposure time of 1 ms. The time-averaged images were taken from z=308 mm to z=578 mm (reconstructed region) above the burner nozzle. Time resolved images were taken from z=228 mm to z=548 mm above the burner nozzle.

## 3.4. IMAGE PROCESSING METHOD

Several considerations have to be taken into account when processing OH* chemiluminescence images recorded with the imaging system described in Chapter 2. First, OH* chemiluminescence intensity in flameless combustion is much lower than that in conventional flames. The reactions are distributed in space and reaction zones appear randomly in space and time due to longer chemical time scales and turbulence. The probability of flame presence at a fixed point is low. When thousands of images are averaged, the valid flame information is buried in background and noise. Second, the "vignetting effect" of the imaging system have to be considered. This means that when taking a picture of a uniform emitting target, one gets a nonuniform intensity distribution on the picture. This effect changes the spatial intensity distribution on the image hiding the real flame information in the images.

The procedure developed to solve the above mentioned problems is described as follows. Besides 3000 flame images taken at each position, a background image and an intensity image are also produced. The background image was constructed by averaging over 3000 images taken with the 308 nm bandpass filter on the lens, but in absence of combustion. The intensity image is constructed by averaging over 3000 images taken from a uniformly UV light illuminated flat target (white panel) with the 308 nm band-

pass filter mounted on the lens. Flame images at each position were averaged over 3000 frames. All the above mentioned images were taken with the same settings.

In a first processing step, the background image was subtracted from both the intensity image and the averaged OH* chemiluminescence image. A median filter of 8 × 8 pixels was then applied to reduce noise. To compensate for the vignetting effect, a scaling matrix is used to make the intensity of the intensity image uniform at its maximum value. This scaling matrix is called vignetting calibration matrix. It was then used to correct each image taken in flame measurements.

To detect the autoignition kernels and other reacting structures in the individual OH* chemiluminescence images, a boundary detection routine was made. Careful considerations are needed to distinguish reacting and non-reacting regions because the signal-to-noise ratio of the high-speed OH* chemiluminescence images is relatively low. Before doing that, brightness and contrast of each image were enhanced to increase the intensity gradient at the boundary between reacting and non-reacting region. Then the flame boundaries were determined based on an intensity threshold. Detected reacting or non-reacting regions with a size less than 10×10 pixels are considered as noise and are subsequently ignored.



## 3.5. RESULTS AND DISCUSSION

Before going into detailed analysis, a good prior understanding of the basic patterns in such a furnace is of help for drawing the conclusions in this chapter. It is well known that internal burnt gas recirculation is essential for establishing flameless combustion. Sufficient burnt gas has to be entrained by high momentum air and fuel jets, decreasing the oxygen concentration before reactions take place. In this furnace, internal recirculation is mainly driven by four high momentum air jets with a bulk velocity ranging from 40 to 50 m/s. The multi-jet configuration increases mixing between air and burnt gas thus better dilution is achieved. Fuel is supplied through a narrow central tube with a bulk velocity of about 35 m/s and the four air jets are symmetrically located 21 mm off the centre. The momentum of fuel jet is relatively high compared to a multi fuel jet system and the fuel jet is not easily influenced by stronger air jets. This delays the mixing between fuel and air, providing longer time for the entrainment of burnt gas. One would expect robust operation in flameless combustion regime in this furnace.

### 3.5.1. EFFECTS OF EQUIVALENCE RATIO

The equivalence ratio $\phi$ is an important parameter for operating a furnace. It is defined as the ratio of the actual fuel-air ratio ($f$) and the stoichiometric fuel-air ratio ($f_{st}$)

$$\phi = \frac{f}{f_{st}} = \frac{\left(\dot{m}_f/\dot{m}_a\right)_{actual}}{\left(\dot{m}_f/\dot{m}_a\right)_{st}}. \tag{3.1}$$

In some studies the air-fuel ratio $\lambda = 1/\phi$ is used instead.

Figure 3.1 shows the mean OH* chemiluminescence intensity distribution observed through the quartz window of the combustion chamber for three equivalence ratios. It is noted that the reaction zone is asymmetrical. This asymmetry is mainly due to the asymmetrical flow field which will be discussed in Section 4.3. The images were taken from a

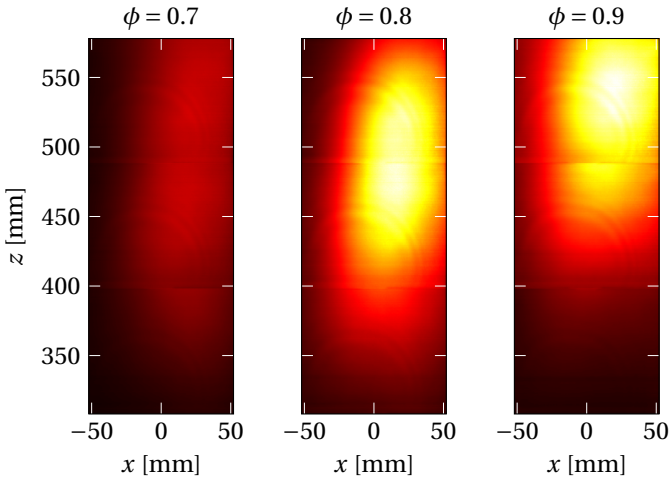


**Figure 3.1:** Mean OH* chemiluminescence intensity distribution at the middle cross section of combustion chamber between z=308 mm and z=578 mm. Fuel jet axis is at x=0 mm, and air jets axes locate at x=±21 mm. Left: case 1 with $\phi = 0.7$, middle: case 2 with $\phi = 0.8$, right: case 3 with $\phi = 0.9$.

direction normal to a plane crossing the fuel jet and two air jets. The z-coordinate indicates the height above the burner nozzle and the x-coordinate measures the offset from the central axis of the fuel tube. The mean OH* chemiluminescence intensity indicates the mean position of the reaction zone (Lee and Santavicca, 2003). As the equivalence ratio increases from $\phi = 0.7$ (for case 1) to $\phi = 0.9$ (for case 3), the reaction zone progressively moves further upward. The OH* chemiluminescence intensity for z>578 mm could not be measured because of limited optical access. This upward shift of the main reaction zone is due to the decrease in air jet momentum. This results in reduced turbulent mixing, which slows down the entrainment of burnt gas into the fresh air jets. Reactants need longer preheating time to be ignited in the furnace. Thus, at higher equivalence ratio, even if fuel and air meet with each other, the temperature of reactants are not high enough to initialize the reactions, which leads to ignition delay. It can be concluded that the current lab-scale furnace is quite robustly operating in flameless combustion regime for a wide range of equivalence ratios. The reaction intensity decreases because of intense dilution by entrained burnt gas and globally temperature decrease as equivalence ratio decreases, but a reaction zone is maintained.

### 3.5.2. EFFECTS OF BURNER CONFIGURATION

The upward shift of the reaction zone with increasing equivalence ratio that is reported in Section 3.5.1 is in contrast to the results reported by Veríssimo et al. (2011). The burner of their cylindrical furnace has a central tube of 10 mm inner diameter for air and sixteen fuel tubes of 2 mm inner diameter surrounding the air tube. Fuel and air are injected vertically downward into the furnace. They observed that the OH* chemiluminescence intensity started becoming higher locally and less evenly distributed when

the equivalence ratio is decreased to 0.67. When equivalence ratio is lower than 0.588, the OH* chemiluminescence distributions indicate the presence of a relatively narrow reaction zone (indicative for conventional combustion) located at the strong shear region between the central jet and the external recirculation zone. Moreover, they found that the values and variation of the $NO_x$ emissions are consistent with those expected for conventional lean combustion. The furnace-burner combination lead to a flameless combustion mode only under certain operating conditions.

The current furnace-burner combination is more robust in working in flameless combustion mode. No transition from flameless combustion to conventional combustion was observed when decreasing the equivalence ratio from 0.9 to 0.6 (by increasing air injection). On the contrary, the mean OH* chemiluminescence intensity becomes lower and more distributed indicating more flameless combustion like character when decreasing the equivalence ratio. For both furnaces, air injection plays an important role in the fluid dynamics inside the furnace, which affects the entrainment and recirculation of burnt gas. The way of injection, such as the number of jets, the velocity of the jets, the jet arrangement, determines the entrainment and recirculation of burnt gas. For the cylindrical furnace, the high speed air jet is at the centre, and 16 weak fuel jets around the central air jet act as a barrier between air and burnt gas, which causes fuel to be entrained strongly into the air jet before sufficient burnt gas is entrained, that is, less dilution. Fuel and air are well mixed in the shear layer due to strong local turbulence. Once ignition occurs, reactions are taking place at low dilution level which is not in favour of establishing flameless combustion. On the other hand, the outlet of the cylindrical furnace is on the opposite side as the burner. This leads to less recirculation of burnt gas inside the furnace. The outlet in the current furnace is at the same side as the burner helping generate strong recirculation inside the furnace. Fuel is injected through a central tube surrounded by multiple air jets. Using one fuel jet makes the fuel jet momentum higher compared to multiple small fuel jets, and multiple air jets provides more contact area with burnt gas. The current jets injection arrangement is beneficial to entrain more burnt gas for dilution before fuel and air mix with each other.



### 3.5.3. IGNITION BEHAVIOUR

Autoignition kernels were observed in all three cases along all heights in this study. The stabilized flames which are like the JHC flames were not present in the main reaction zone where mean OH* chemiluminescence intensity is highest. Intense narrow reaction zones were not observed in the main reaction zone, either. There are two reasons for these observations. First, the flame fronts are stretched by large scale vortices generated by the high speed jets, which has already been found in jet-in-hot-coflow flames (Medwell et al., 2009). Secondly, a propagating flame cannot survive in the current furnace. Mixing is too dynamic to allow a stabilized flame fed continuously by fuel and air mixture. Autoignition of fresh mixture dominates the start of reactions.

According to the OH* chemiluminescence images, three types of autoignition events are identified and these provide more insight into the ignition behaviour in the current furnace operating in the flameless regime. The first one is an individual autoignition kernel as shown in Figure 3.2. In Figure 3.2(a), an autoignition kernel has just formed, and it grows while being convected downstream as shown in Figure 3.2(b)-(e). It was

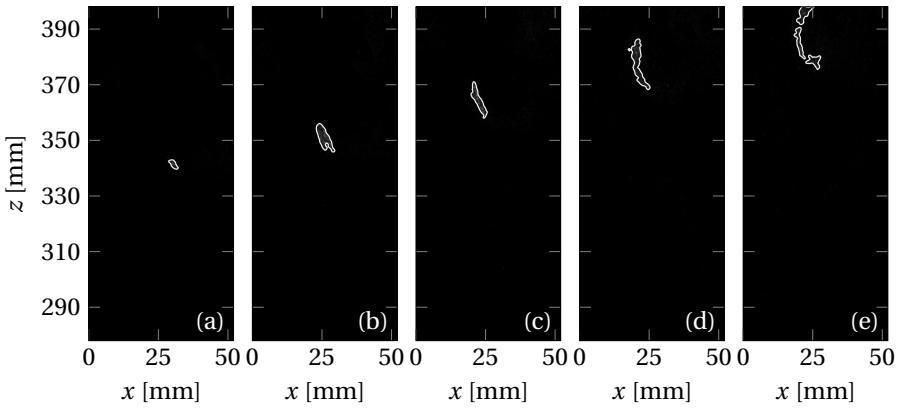


**Figure 3.2:** Sequential images taken from case 2 showing individual autoignition kernel development during one ignition event. Fuel jet axis is at x=0 mm, and air jet axis is at x=21 mm. Time interval between the images is 2 ms. The images were taken from 278~398 mm above the burner nozzle.

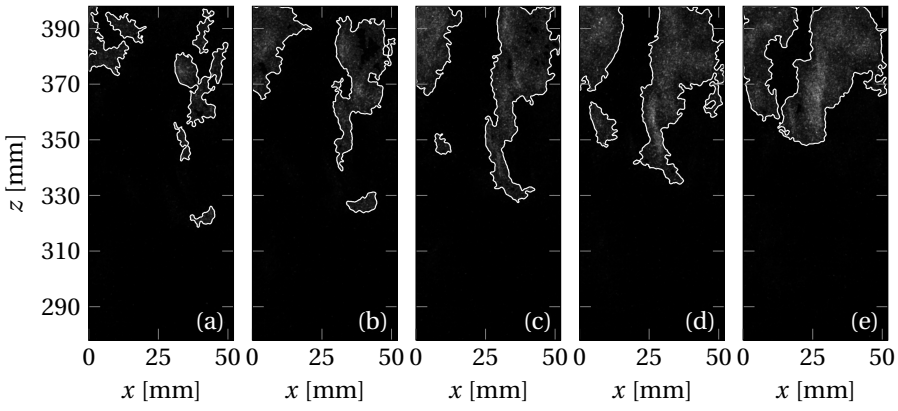


**Figure 3.3:** Sequential images taken from case 2 showing multiple autoignition kernel formation and development during ignition process. Fuel jet axis is at x=0 mm, and air jet axis is at x=21 mm. Time interval between the images is 1 ms. The images were taken from 278~398 mm above the burner nozzle.

observed that some of these individual autoignition kernels faded away and did not lead to intense reactions, but others did lead to intense reaction zone downstream. Locally, as long as the mixture of fuel and air becomes hot enough, the second type of ignition event, that is, multiple autoignition kernels would occur, as shown in Figure 3.3. In this type of ignition, multiple autoignition kernels appear in a region at nearly the same time (Figure 3.3(a)). They develop faster than individual kernels, and merge together thus leading to the formation of a large and intense reaction zone.

Both the individual and multiple autoignition kernels can develop into an autoigni-

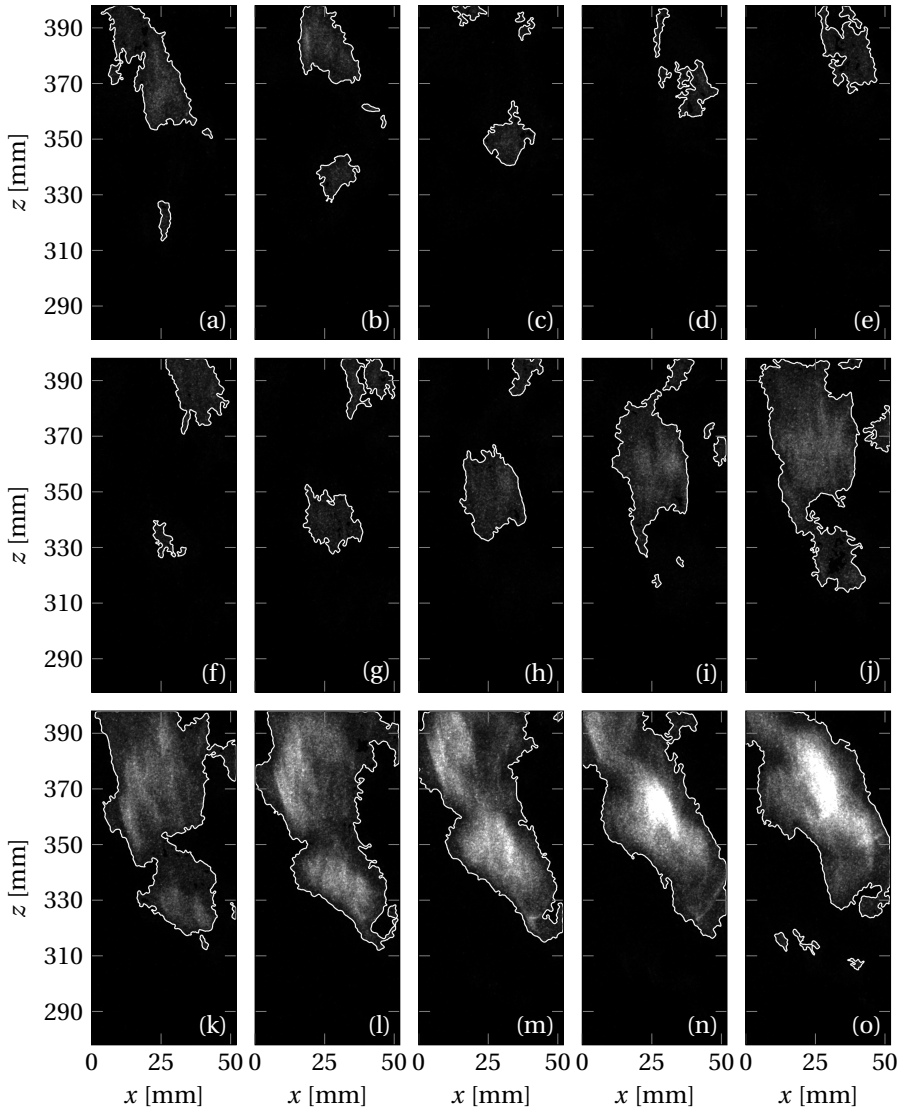


**Figure 3.4:** Sequential images taken from case 2 showing autoignition kernel cluster formation and development during ignition process. Fuel jet axis is at x=0 mm, and air jet axis is at x=21 mm. Time interval between the images (a)~(d) is 2 ms and the time interval for (e)~(o) is 1 ms. The images were taken from 278~398 mm above the burner nozzle.

tion kernel cluster, as shown in Figure 3.4. This is a very intense ignition process observed in the furnace. Autoignition kernels are continuously formed and move downstream and merge with the upper reaction zone. In Figure 3.4(a), there are two individual kernels appearing one after another. The upper one is shrinking, while the lower one is growing. The same phenomenon appears in the second row of the images in Figure 3.4(f)-(j). Finally, a large intense reaction zone is formed as shown in Figure 3.4(k)-(o). Heat release from such a region is significant which is helpful to sustain the reactions in the local region. It can be seen from Figure 3.4(o), several newly formed autoignition kernels are formed just below the high intensity region. As these are growing, they will merge with the high intensity zone and sustain the local reaction zone. These clustering autoignition kernels could form a flame in a stripe-like shape, but it exists only for a very short time (about 100 ms). The multiple autoignition kernels work in a similar way to cause autoignition kernel cluster and fusion with the high intensity zone formed in the local region.

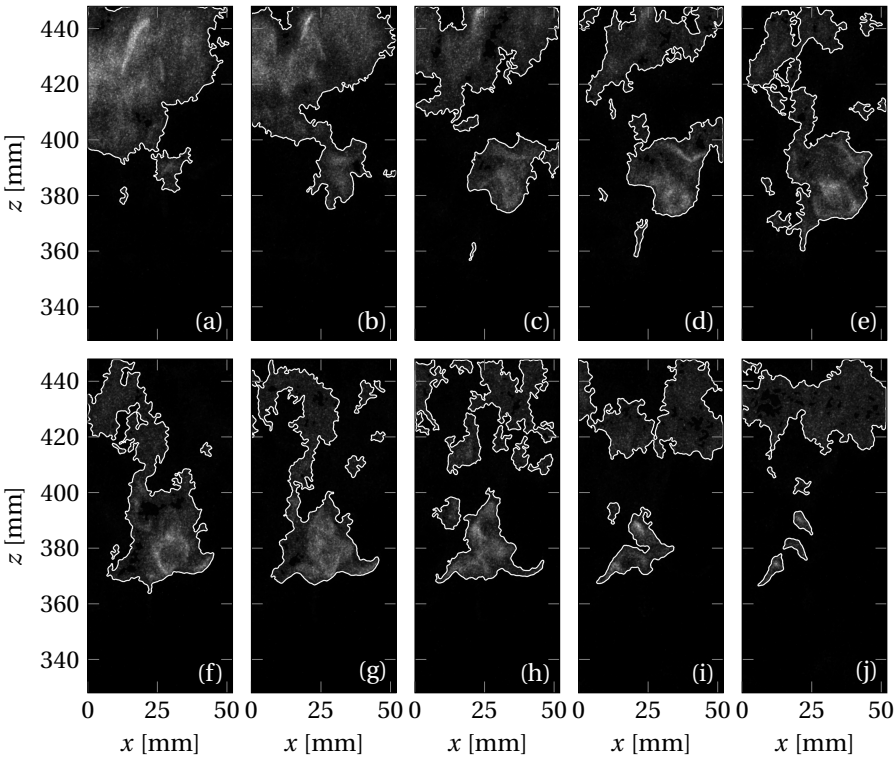


**Figure 3.5:** Sequential images taken from case 2 showing flame propagation behaviour. Fuel jet axis is at x=0 mm, and air jet axis is at x=21 mm. Time interval between above images is 1 ms. The images were taken from 328~448 mm above the burner nozzle.

Moreover, flame propagation was also observed following autoignition in all three cases, as shown in Figure 3.5. An autoignition kernel is formed in Figure 3.5(a). It grows

and its lower boundary moves upstream, but the upper large reaction region is moving downstream. This phenomenon occurs at higher positions in the furnace where fuel, air and burnt gas is well mixed. Reactions start once temperature is high enough. The flame can propagate outwards, even upstream, in such a flammable mixture, as the kernel does in Figure 3.5(b)-(e). Whereas, flame propagation stabilized flame depends very much on continuous fuel and oxidizer supply from upstream. The flammable mixture is pocket formed due to turbulence in the current furnace. Once the fuel near the kernel is consumed, the reactions are terminated, as shown in Figure 3.5(f)-(j). In the current furnace, flame propagation contributes only little to the flame stabilization or subsistence since the conditions allowing propagation are very critical in the current furnace. Autoignition is found taking place all the way along the flow until all fuel is consumed. The only difference between different regions is that autoignition kernels appear more frequently at higher position than that at lower position.



### 3.5.4. FLAME BEHAVIOUR

The ignition behaviour in the current furnace operating in flameless combustion regime has been discussed in the previous section. In this section, the flame behaviour in the main reaction zone will be addressed. Both OH* chemiluminescence and temperature, measured using Coherent Anti-Stokes Raman Spectroscopy (CARS), are used to interpret the flame behaviour. Figure 3.6 shows a set of the high-speed OH* chemiluminescence images ranging from z=428 mm to z=548 mm above the burner nozzle. In the sequential images, there is an individual autoignition kernel as marked by "①" in Figure 3.6(c) and (d); multiple autoignition kernels are marked by "②" in Figure 3.6(a), (q) and (r); the whole sequential images are an autoignition kernel cluster. In the main reaction zone, these flame behaviour were always observed. But in the ignition process at lower positions, the three ignition events occur much less frequent.

OH* chemiluminescence intensity histograms computed from 6000 high-speed images of case 2 are used to determine the probability of the presence of reactions at specific locations. The histograms in the main reaction zone between z=430 mm and z=545 mm above the burner nozzle are shown in Figure 3.7. Figure 3.7(a)-(f) pertain to the intensity histograms at x=0, 5, 10, 15, 20 and 25 mm. It can be seen that the intensity histograms are very similar, showing a high probability peak in the low intensity region and a long low probability tail in the high intensity region. For example, at x=0 mm the probability in low intensity region first decreases and then increases when going across the reaction zone (indicated in Figure 3.1) from z=435 mm to z=545 mm. On the other hand going into the centre of the reaction zone in horizontal direction from x=0 to x=25 mm at any z between 435 mm and 545 m, the probabilities of high intensity increase. This increase can be attributed to more frequent reactions or signal integration along the line of sight of the camera. However, the histogram shapes are hardly affected. It is noted from the histograms at a position in the reaction zone, most of the time there is no reaction present or very weak reactions. This suggests that the flame is dynamically spread in space since there is no high probability at high intensity levels. This universal shape of histograms in the reaction zone space shown in Figure 3.7 confirms that there is no stabilized flame in the furnace.

The flame behaviour was also partly described by temperature measurement in the

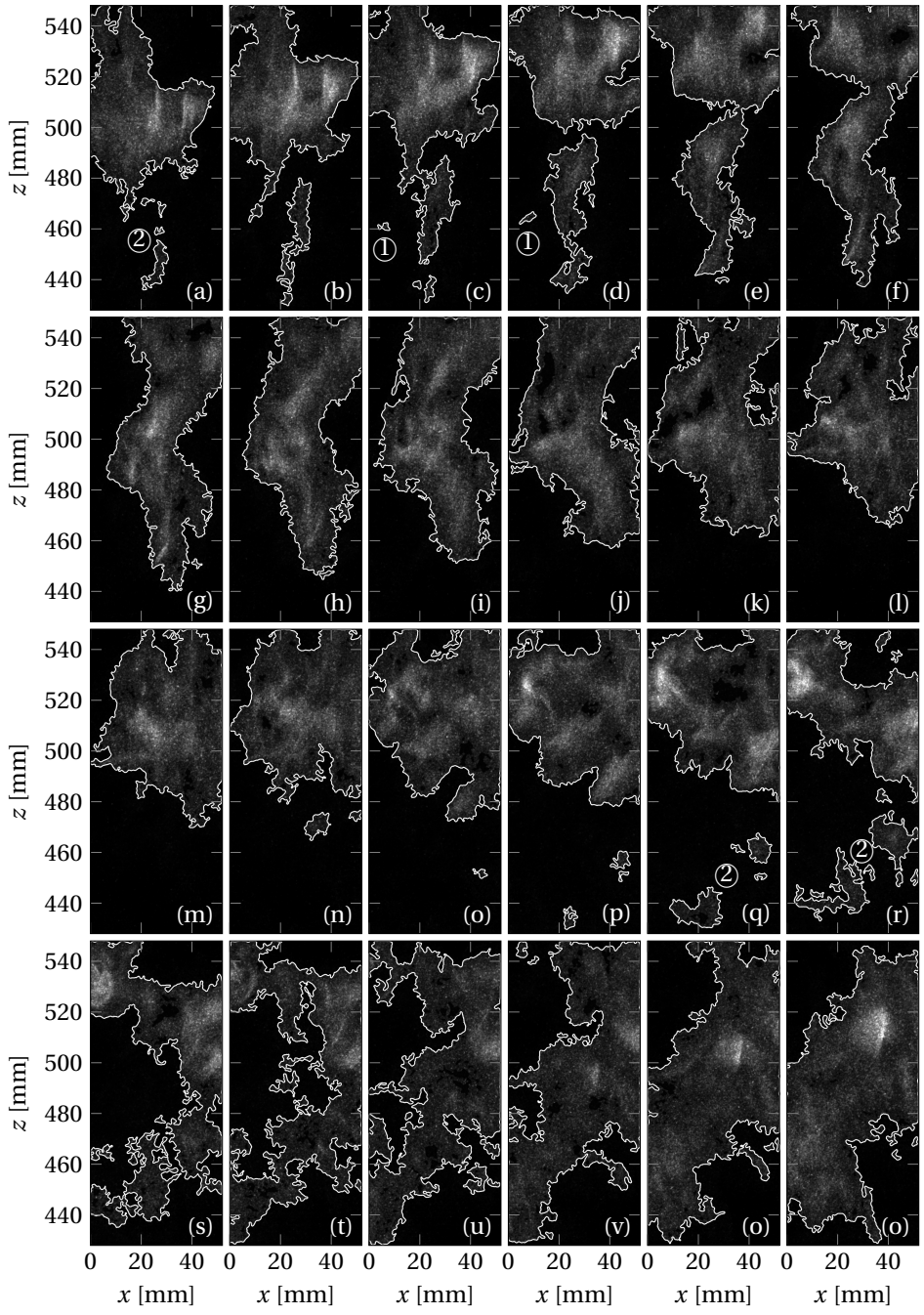


**Figure 3.6:** Sequential images taken from case 2 showing flame behaviour in the main reaction zone. Fuel jet axis is at x=0 mm, and air jet axis is at x=21 mm. Time interval between above images is 1 ms. The images were taken from 428~548 mm above the burner nozzle.

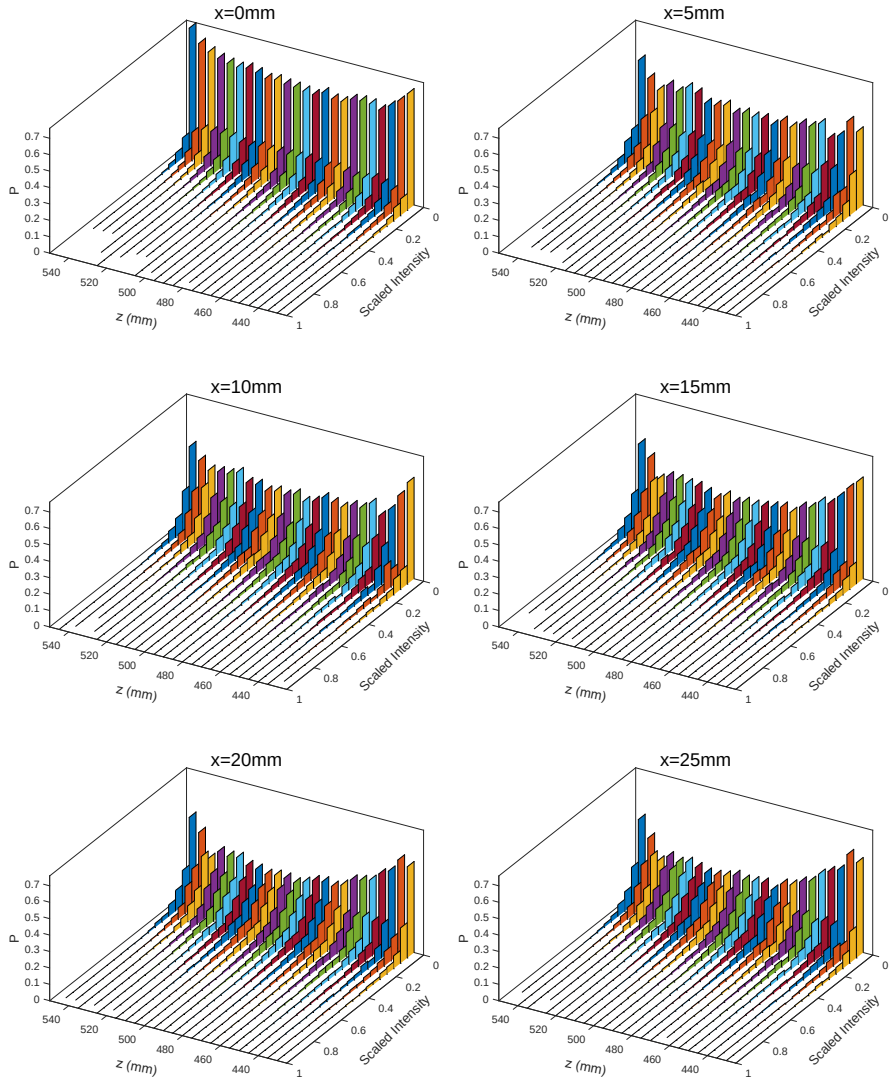


**Figure 3.7:** OH* chemiluminescence intensity histograms between 430 mm and 545 mm above burner nozzle for a furnace operating at 9 kW and at equivalence ratio $\phi = 0.8$. Along the vertical axis is the normalized probability and the horizontal axes are the height above burner nozzle, z, and the scaled OH* chemiluminescence intensity.

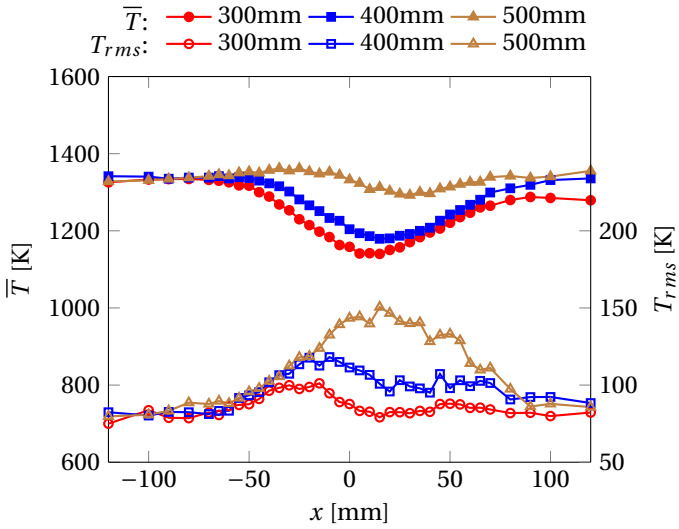


**Figure 3.8:** Mean temperature and temperature RMS values at different heights.

reaction zone. For each measuring point, 1600 single-shot CARS spectra were collected at 10 Hz. Temperature measurements were taken in the case 2. Mean temperatures and temperature root mean square (RMS) values in the main reaction zone which were obtained 300, 400 and 500 mm above the burner nozzle are shown in Figure 3.8. Mean temperatures at each height have a basin-shaped profile when going across the reaction zone. It is seen that mean temperature in that region increases with the height above the nozzle. The maximum mean temperature increase $\Delta T_{mean}$ between z=300 mm and z=400 mm is 63 K, but $\Delta T_{mean}$ = 134 K between z=400 mm and z=500 mm. At these heights, temperature increase by the entrainment of hot burnt gas becomes limited since the temperature difference between jet and surroundings is low and jet momentum is much smaller than that at lower height. Therefore, the temperature increase is mainly due to reactions. The maximum temperature RMS value is 24 K between 300 mm and 400 mm and 50 K between 400 mm and 500 mm. Turbulence intensity is higher at lower position, thus temperature fluctuations could also be higher due to turbulence. But an opposite result was observed because of significant effect of reactions. Autoignition takes place more frequently as height increases which results in larger temperature fluctuations. Note that the profiles of RMS values at 300 and 400 mm appear to be bimodal with two small peaks to the left and to the right of the centre. Referring to the work by Arndt et al. (2016), the location of the peaks probably is the edge of flammable mixture in which mixture fractions are much leaner than the stoichiometric mixture fraction and the temperatures there are high enough to allow autoignition. But at 500 mm the temperature RMS profile shows one broad envelope which indicates frequent autoignition is taking place throughout the reaction zone. Temperature histograms across the reaction zone are shown in Figure 3.9. Temperature ranges from 900 to 1800 K. The temperature histogram outside the reaction zone is narrowest, see at x=-60 mm for example. Going

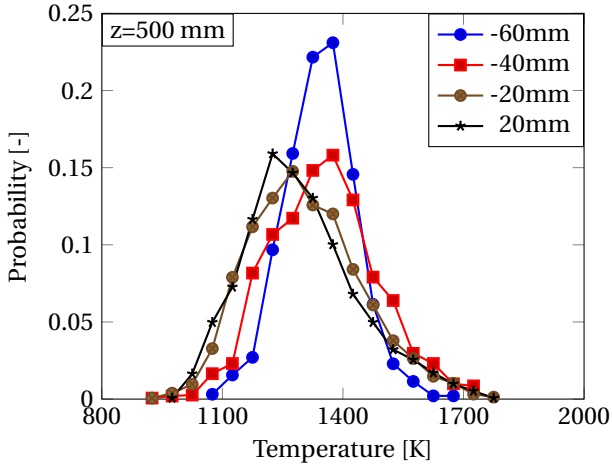


**Figure 3.9:** Normalized temperature histograms at 500 mm above the burner nozzle for four positions from outside the reaction zone to inside the reaction zone.

into the reaction zone, the temperature histogram becomes wider and lower. The location of the maximum of the distribution shifts towards lower values but also a tail of the distribution appears showing high values that can be attributed to reactions. Bimodal-shaped histogram as often seen in conventional flame were not observed in the reaction zone, indicating that an alternating presence of burnt mixture and cold reactants (flame front) is not the case.

Based on the discussions above, it is evident that autoignition is dominating flame stabilization in the current furnace. Flame stabilization is not an appropriate term for flame behaviour in the flameless regime. Here “sustained combustion” is proposed to describe the stability of the reactions in the current furnace. Actually, as long as a “sustained combustion” is achieved in the flameless regime, the furnace can operate properly, which means that no special flame stabilization strategies are necessary to have stabilized operation.

### 3.5.5. FLAME SUBSISTENCE

As concluded in the above section, a "sustained combustion" which is autoignition dominated is needed in the flameless regime. In this section, how to sustain the reactions in flameless regime will be discussed.

It is noted that whether autoignition occurs or not in conventional turbulent non-premixed flames is depending on local mixture fraction, strain rate and temperature (Mastorakos, 2009). However, these parameters appear again in another way in flameless combustion. Before fuel and air jets are mixing with each other, they are already diluted by entrained burnt gas and are also preheated to a certain temperature in the meantime. When they mix with each other, ignition of the mixture depends on local mixing state, local strain rate and temperature. The mixture fraction $Z$ based on pure fuel and air does not fully describe the mixing state, because here fuel and air are diluted by recirculated

burnt gas. Moreover, the mixture temperature also depends on the dilution.

Autoignition occurrence can be evaluated by introducing an autoignition indicator

$$A_o = A_o\left(Z,\alpha,\eta,a\right) = \begin{cases} 1 & \textbf{Autoignition occurs} \\ 0 & \textbf{Autoignition does not occur} \end{cases}, \tag{3.2}$$

which means that the probability of an autoignition event occurring depends on the local mixture faction $Z$, dilution level $\alpha$, enthalpy loss factor $\eta$, and strain rate $a$. The dilution level $\alpha$ and enthalpy loss factor $\eta$ are introduced to represent the mass fraction of diluent in the local mixture and enthalpy loss in the diluent. These two parameters $\alpha$ and $\eta$ play important roles in the model developed in Chapter 5.



It is known from Equation (3.2), that autoignition depends on the local mixture faction, dilution level, enthalpy loss and strain rate. In other words, it requires fuel-oxidizer mixture, high temperature and proper flow condition. Actually, in furnaces, they are not difficult to achieve. Fuel-oxidizer mixture must be present. The mixture is preheated by entrainment of hot burnt gas in the furnace. Flow condition is quite a local parameter that is affecting the reactions in a similar way as in flame propagation. Therefore, there must be a region in which autoignition can happen and out of which autoignition cannot occur, especially when air is preheated.

In this section, a method to determine that region is proposed. Considering a gas mixture which is combustible in the reaction zone, it could be classified as mixture of fuel+air, fuel+diluted air or fuel+diluent. Here the "diluent" will be considered as equilibrium products of combustion of fuel/air in a stoichiometric mixture ($Z_{st}$). The recirculated burnt gas is treated as a mixture of air and diluent if the furnace is working at lean condition. The mixture fraction of the mixture can be written as

$$Z = (1-\alpha)Z_0 + \alpha Z_{st}, \tag{3.3}$$

where $Z_0$ is the mixture fraction of the fresh fuel and air in the mixture excluding the diluent.

A one-dimensional laminar counterflow diffusion flame configuration is used to assess the characteristics of the flame in such a mixture. In the calculation setup, one side is pure fuel and the other side is air or diluted air. The diluted air is obtained by mixing air and diluent with heat loss. A mixture fraction $\xi$ based on fuel and diluted air is introduced and $\gamma$ is defined as mass fraction of diluent in the diluted air, namely air dilution level. According to Equation (3.3), one can find

$$\xi = (1-\alpha)Z_0 = Z - \alpha Z_{st}, \tag{3.4}$$

$$\gamma = \frac{\alpha}{1-\xi} = \frac{\alpha}{1-Z+\alpha Z_{st}}. \tag{3.5}$$

The local maximum enthalpy loss in the diluent is related to $\xi$ and $\gamma$

$$\Delta h_{maxlocal} = \gamma(1-\xi)\left(h^d_{\eta=1} - h^d_{\eta=0}\right). \tag{3.6}$$

The enthalpy loss factor $\eta$ can be determined by normalizing enthalpy loss $\Delta h$ by the maximum enthalpy loss at local dilution level which results in $\eta$, which gives

$$\eta = \frac{\Delta h}{\gamma(1-\xi)\left(h^d_{\eta=1} - h^d_{\eta=0}\right)} = \frac{h - h_{ad}}{\alpha\left(h^d_{\eta=1} - h^d_{\eta=0}\right)}, \tag{3.7}$$

where $h_{ad}$ is the adiabatic enthalpy at local mixture fraction

$$h_{ad} = Z h_f + (1 - Z)\, h_{ox}, \tag{3.8}$$

and $h^d_{\eta=1}$ and $h^d_{\eta=0}$ are respectively the enthalpy of diluent with maximum and minimum enthalpy loss. This approach using dilution level $\alpha$, air dilution level $\gamma$ and enthalpy loss factor $\eta$ will be elaborated further in Chapter 5 on modelling. The autoignition indicator $A_o$ is then characterised by

$$A_o = A_o\left(\xi, \gamma, \eta, a\right) = \begin{cases} 1 & \textbf{Autoignition occurs} \\ 0 & \textbf{Autoignition does not occur} \end{cases}.$$



The autoignition is detected by temperature rise compared to the mixing line, that is, if temperature increases, $A_o = 1$, otherwise $A_o = 0$. With a mesh grid of 11×14 in $\gamma$ and $\eta$, calculations were performed. The situations $\gamma = 0$ and $\gamma = 1$ correspond to $\eta = 0$ and no oxidizer, respectively. Therefore, 9×14+1 calculations are actually needed. The maximum enthalpy loss in the diluent is set at $2.341 \times 10^6 J/kg$ in the calculations.

**Table 3.3:** Fuel and air temperature and composition used in laminar counterflow flames calculations.

| | T[K] | Species[mole %] | | | |
|---|---|---|---|---|---|
| Fuel | 400 | $CH_4$(81.3 ) | $C_2H_6$(3.7) | $N_2$(14.4) | $CO_2$(0.06) |
| Air | 843 | $O_2$(21 ) | $N_2$(79) | | |

Composition and temperature of the fuel and air streams used in the calculations are listed in Table 3.3. To determine the diluted air needed as boundary condition for the transient counterflow flame condition, the following procedure is followed. Firstly, calculate the equilibrium state at stoichiometric mixture fraction with specified enthalpy loss and then mix air with the products to the specified dilution level. The calculations were done with the CHEM1D code developed at the Eindhoven University of Technology. Once the boundaries are determined, a counterflow mixing field is first calculated as an initial field for calculations with reactions on. In each calculation, strain rate was increased from a very small value until no ignition was achieved. With this critical strain rate ($a_{ci}$) and corresponding air dilution level ($\gamma$) and enthalpy loss factor $\eta$, the region where autoignition can occur was determined. Figure 3.10 shows the region where autoignition is taking place in the coordinates of $\gamma$, $\eta$ and $a_{ci}$. The surface represents the critical strain rate $a_{ci}$ above which no ignition occurs. The larger $a_{ci}$ is, the wider the range where autoignition takes place. Below this surface $A_o = 1$, and $A_o = 0$ above the surface. It is seen that ignition occurs in a wide strain rate range when enthalpy loss is small and ignition does not occur when enthalpy loss is too large. The oxygen mass fraction at the oxidizer side of the laminar counterflow is a constant for given dilution level. Increasing enthalpy loss, temperature decreases resulting in longer chemical time scale which does not allow ignition at high strain rate. On the other hand, at a fixed enthalpy

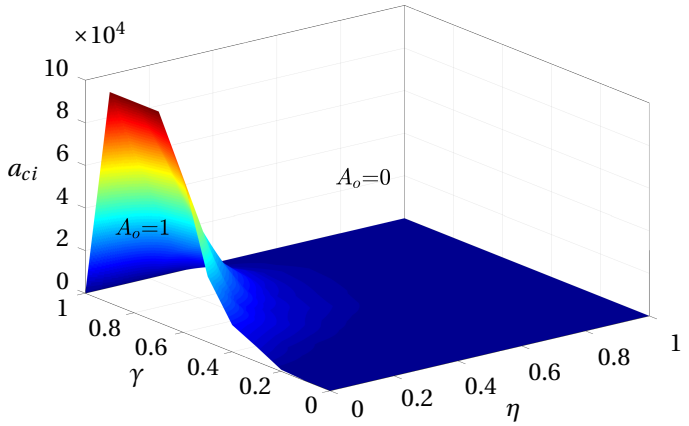


**Figure 3.10:** Autoignition region in the coordinates of air dilution level $\gamma$, enthalpy loss factor $\eta$ and critical strain rate $a_{ci}$. $A_o = 1$ indicates the region ignition take place and $A_o = 0$ not.

loss level, oxidizer temperature increases but oxygen mass fraction decreases when dilution level increases. In this situation, chemical time scale is affected by both temperature and oxygen mass fraction. At low air dilution level, oxygen is sufficient and has less effect on ignition, temperature plays an more important role. Chemical time scale becomes smaller when temperature increases, in other words, air dilution level increases. As oxygen mass fraction is decreasing to some point, chemical time scale increases even if oxidizer temperature continues increasing. Since low heat release at low oxygen level is not sufficient to sustain reactions at high strain rate. These are all observed from Figure 3.10. At a given $\gamma$, $a_{ci}$ decreases as increasing $\eta$, while given $\eta$, $a_{ci}$ first increases and then decreases as increasing $\gamma$.

Figure 3.11 shows the normalized strain rate (normalized by maximum $a_{ci}$ at a given $\eta$) profiles. It is noted that the maximum $a_{ci}$ is always located around dilution level $\gamma = 0.8$. Some maxima occur at $\gamma = 0.7$. However, the $a_{ci}$ are very close to those at $\gamma = 0.8$. Since at high air dilution level, the stoichiometric mixture fraction between fuel and diluted air is very small, at autoignition condition (lean), the mass of diluted air approximately equals the total mass of the mixture. The corresponding oxygen mass fraction in diluted air is estimated by $(1-\gamma)Y_{O_2,air}$, resulting in 6.99% and 4.66% respectively. It seems that there could be a small range of $O_2$ mass fraction from about 4.5% to 7% which is most favourable for autoignition, and this $O_2$ mass fraction does not depend on the inlet air temperature.

This result is in agreement with other criteria proposed in the literature, e.g., the gas recirculation ratio $K_v$ (Equation (1.1)) proposed by Wünning and Wünning (Wünning and Wünning, 1997). When temperature is sufficiently high and $K_v \geqslant 3$, the fuel can react in the very stable form of flameless oxidation (Plessing et al., 1998). $K_v = 3$ corresponds to a dilution level $\gamma \approx 0.75$ and $O_2$ mass fraction in oxidizer is approximate to 5.86%. They are located in the range where the maximum critical strain rates are found in the Figure 3.11.

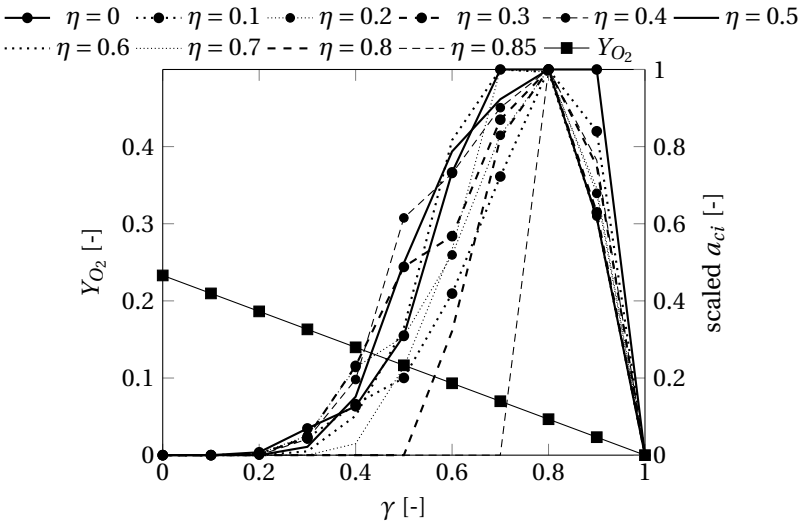


**Figure 3.11:** Normalized strain rates vary with air dilution level from minimum to maximum enthalpy loss. There is no ignition when $\eta \geqslant 0.9$. The maximum enthalpy loss in the diluent is $2.341 \times 10^6$ J/kg.

## 3.6. SUMMARY AND CONCLUSIONS

Flameless combustion in a lab-scale furnace has been studied. Mean and time resolved OH* chemiluminescence images at different equivalence ratios have been taken to study the flame behaviour in the flameless combustion regime.

Autoignition is found to be responsible for sustaining the combustion process in the flameless regime. Three types of ignition behaviour were observed, namely individual autoignition kernel, multiple autoignition kernels and autoignition kernel cluster. The reaction zone is a collection of these three autoignition type of phenomena, occurring very frequently sustaining the reactions in the furnace without any need for a flame stabilization strategy or mechanism. We call this situation presence of a "sustained combustion". Continuous combustion on the scale of the furnace is guaranteed by this process without presence of a stable local flame.

Autoignition occurrence is local condition controlled, mainly depending on dilution level and diluent enthalpy loss, or in other words, recirculation ratio and temperature. For Dutch natural gas, a critical air dilution level near 0.7~0.8 or $O_2$ mass fraction near 4.5% and 7% in oxidizer was obtained. One can also relate these conditions to recirculation ratio about 2.33~4. Autoignition can be achieved in a wide range of flow conditions near above condition. This provides the best condition to sustain a stable flameless combustion.

The combustion characteristics in the furnace are sensitive to equivalence ratio. Decreasing the equivalence ratio means higher air injection is leading to a shift of the reaction zone in upstream direction, which means that the ignition is earlier. A transition to conventional combustion is not observed. This observation is opposite to that in Ref.

(Veríssimo et al., 2011). The burner nozzle configuration (number and size, relative position) is determining the internal flow field, in particular in which range of equivalence ratio flameless combustion is realized.

# 4

# MEASUREMENTS OF VELOCITY AND TEMPERATURE IN FLAMELESS COMBUSTION

*This chapter reports the results of velocity and temperature measurements in a lab-scale furnace operating in the flameless combustion regime. The measurements were performed with laser based diagnostics (LDA and CARS) to avoid disturbing the internal flow. The measurements were done at a thermal input of 9 kW (fuel mass flow rate based) for equivalence ratios $\phi$=0.7, 0.8 and 0.9. Although the difference in turbulence statistics between the three cases is not large, the reaction intensity and the positions of the reaction zone are clearly different. Decreasing the equivalence ratio leads to a more turbulent flow field in the furnace, the reaction zone shifts upstream and reaction intensity becomes lower. The highly turbulent flow field plays an important role in the entrainment and internal recirculation of burnt gas, which is important for autoignition. However, the highly turbulent flow field also plays a role in preventing a stabilized flame. Temperature histograms in the reaction zone do show high temperature samples due to exothermic reactions. However, the temperature rise (compared to the air inlet temperature) in the mean temperature is less than 600 K, and the instantaneous peak temperature is less than 1800 K. The temperature samples above 1700 K is less than 1.5% of the total sample number at one measurement point. The low peak temperature greatly suppresses the formation of $NO_x$ emissions.*

## 4.1. INTRODUCTION AND LITERATURE REVIEW

Flameless combustion is a flow controlled combustion technique because it requires internal recirculation of burnt gas in the combustion chamber. The recirculation efficiency is commonly measured by the recirculation ratio $K_v$ defined as the ratio of recirculated mass flow of combustion products (before reaction) and the mass flow of the injected fresh reactants (Wünning and Wünning, 1997; Plessing et al., 1998). The injected fuel and air flows are the driving force for the in-furnace flow field. Detailed non-intrusive measurements of flow and temperature field are of great importance to understand the flameless combustion processes.

There are a number of studies that have reported on detailed measurements of velocity, temperature and species with laser diagnostics in flameless combustion furnaces. Most of these were carried out in the flames produced by injecting a fuel jet in a hot diluted coflow, that is, jet-in-hot-coflow (JHC) flames. Compared to flames in the furnace, these flames are simple, but remain certain physical processes of interest in flameless combustion. Reaction zone structures in JHC flames show common features. Simultaneous imaging of OH, $H_2CO$ and temperature in non-premixed $CH_4/H_2$ jet flames in highly diluted hot coflow by planar LIF and Rayleigh scattering showed reduced temperature in the reaction zone, a suppression of OH and a broadening of the OH layer (Medwell et al., 2007). The reaction zone weakened by large-scale vortices, and flame stretch lead to partial premixing which was evidenced by high $H_2CO$ levels (Medwell et al., 2009). Entrainment of coflow fluid into the fuel jet is essential for flame stabilization in JHC flames. The entrainment of coflow fluid into the turbulent fuel jet has been quantified by using the velocity and temperature data in the near-nozzle region (Oldenhof et al., 2011). It was concluded that hot coflow transport rate towards fuel jet edge was important for stabilizing the flames. Increasing the jet Reynolds number increases entrainment of the coflow so that reactions started earlier opposite to what happens in jet in cold coflow flames. Autoignition occurred at locations where temperature was sufficiently high, mixture fraction was much leaner than stoichiometric mixture fraction and scalar dissipation rate was low (Oldenhof et al., 2013; Arndt et al., 2016). Autoignition time also depended on coflow temperature and local strain rate (Arndt et al., 2013). The reaction layer was found thickened by the turbulent structures in a distributed and flameless combustion burner (Duwig et al., 2012).

The JHC flames have received adequate attention and valuable results have been obtained. However, due to the simplification of the combustion process, the results only reveal part of the important flow and combustion characteristics in a furnace. For enclosed combustors, some factors bring difficulties for detailed laser diagnostics, like limited optical access, beam steering in density varying environment, limited transmissivity of optical windows, etc. Detailed measurements have been conducted in a number of lab-scale furnaces operating in flameless combustion mode, such as the furnaces at RWTH Aachen (Plessing et al., 1998; Özdemir and Peters, 2001; Dally et al., 2004), University of Adelaide (Szegö et al., 2008, 2009; Szegö, 2010), Technical University of Lisbon (Veríssimo et al., 2011; Castela et al., 2012; Veríssimo et al., 2013a,b; Alves et al., 2013) and University of Mons (Lupant et al., 2010; Lupant and Lybaert, 2015; Mosca, 2017). All of these furnaces provide optical accesses to enable the use of laser diagnostics. The general characteristics of these furnaces are summarised in Table 4.1. OH-PLIF and Rayleigh

scattering measurements have been performed in the Aachen furnace. LDA measurements have been done in the furnaces of Aachen, Adelaide and Lisbon (non-reacting). OH- and $CH_2O$-PLIF measurements have been made in the Lisbon furnace. OH* chemiluminescence were performed in both the Lisbon and Mons furnaces.

**Table 4.1:** A summary of the differences in the representative furnaces.

| Furnace | Dimension | Burner | Power[kW] | Techniques |
|---|---|---|---|---|
| Aachen | Cuboid $250\times250\times485mm^3$ | WS REKUMAT | 5-10 | LDA<br>OH-PLIF<br>Rayleigh scattering |
| Adelaide | Cuboid $280\times280\times585mm^3$ | Self-built | 7.5-20 | LDA<br>Thermocouple<br>Gas analyser |
| Lisbon | Cylindrical $\pi 50\times50\times340mm^3$ | Self-built | 6-13 | LDA, OH*<br>OH- and $CH_2O$-PLIF<br>Thermocouple<br>Gas analyser |
| Mons | Cuboid $350\times350\times1000mm^3$ | Self-built | 30 | OH*<br>Thermocouple<br>Gas analyser |

Based on the reaction zone visualization by OH-PLIF and velocity measurements by LDA, Özdemir and Peters (2001) concluded that an aerodynamic design ensuring strong shear was of crucial importance to flameless combustion. High stretching rates prevented the formation of a conventional flame and provided sufficient time for the mixing of reactants and burnt gas. For the non-reacting case, Veríssimo et al. (2013b) conducted LDA measurements in a 100 mm diameter cylindrical combustor. A strong reverse flow zone generated by a high speed central air jet was observed. The authors claimed that the reverse flow zone was essential to establish flameless combustion in the their combustor. The internal recirculation was improved by placing the exhaust gas outlet at the same side of the inlets (Castela et al., 2012). The operating range for flameless combustion was extended compared to the previous one. The mixing pattern inside the furnace was also found to have strong influences on the structure of the reaction zone (Szegö, 2010). Mi et al. (2009) determined a critical value of the momentum rate of the initial reactants injection in the same furnace by using CFD method. Below the critical value flameless combustion does not occur, and no significant influences were observed above the critical value. The critical value should vary from furnace to furnace. Mi et al. (2011) also reported that increasing the fuel jet penetration distance is beneficial for establishing flameless combustion in their furnace. For application of flameless combustion in a gas turbine combustor, Arghode and Gupta (2011) reported that a configuration with large separation between air and fuel stream helps to promote entrainment of burnt gas before fuel and air mix. PIV measurements in non-reacting condition suggest that a recirculation zone is present and is entrained by the air jet (Arghode et al., 2012). This

allows favourable characteristics that are close to flameless combustion.

It can be concluded that compared to JHC flames which mimic only certain characteristics of flameless combustion characteristics, internal flow field is crucial for establishing flameless combustion in the furnace. Because it ensures sufficient burnt gas being recirculated and entrained into fresh fuel and air streams before reactions take place. Although some flow field measurements have been performed in non-reacting condition, there is a lack of detailed in-furnace measurements under reacting conditions due to the difficulties, e.g., the seeding particles deposit on the optical window reducing the transmissivity, thus less light signal is collected in both LDA and PIV measurements campaign (Arghode et al., 2012). In addition to velocity measurements, temperature information in reacting conditions is also essential to understand the interplay between flow and reactions in flameless combustion. However, most temperature measurements were done with thermocouples except for the measurements in the Aachen furnace (Plessing et al., 1998; Özdemir and Peters, 2001; Dally et al., 2004). The thermocouples not only disturb the flow, but also their responses are not fast enough to follow the temperature fluctuations in the turbulent reacting flows. In this study, LDA and CARS techniques are used to measure velocity and temperature. CARS technique has not been used for in-furnace measurement in flameless combustion regime. It is an accurate temperature measurement technique which provides instantaneous gas temperature in the measurement volume.

The remainder of this chapter is organised as follows. The experimental cases are described in Section 4.2, including the inlet boundary conditions measurements. Results of the velocity measurements are discussed in Section 4.3. Section 4.4 discusses the results of the temperature measurements. Finally, progress towards improved understanding of turbulence-chemistry interactions in flameless combustion is presented in Section 4.5.

## 4.2. CASE DESCRIPTIONS

### 4.2.1. MEASUREMENT SETTINGS

**Table 4.2:** Operating conditions for the three cases with different equivalence ratios. P is the thermal input; $\phi$ is the equivalence ratio; $\dot{V}_f$ and $\dot{V}_a$ are the flow rates for fuel and air , respectively, in unit of normal litres (calculated at 1.01325 bar and 273.15 K) per minute; $\dot{m}_f$ and $\dot{m}_a$ are mass flow rate for fuel and air, respectively.

| Case | P (kW) | $\phi$ | $\dot{V}_f$ (nl/min) | $\dot{V}_a$ (nl/min) | $\dot{m}_f$ (kg/s) | $\dot{m}_a$ (kg/s) |
|---|---|---|---|---|---|---|
| 1 | 9 | 0.7 | 17.27 | 206.2 | $2.37\times10^{-4}$ | $4.42\times10^{-3}$ |
| 2 | 9 | 0.8 | 17.27 | 180.4 | $2.37\times10^{-4}$ | $3.87\times10^{-3}$ |
| 3 | 9 | 0.9 | 17.27 | 160.4 | $2.37\times10^{-4}$ | $3.44\times10^{-3}$ |

Dutch natural gas was used as fuel. The thermal input of 9 kW was chosen by taking into account two considerations. The first is to avoid too high furnace temperatures which would damage the quartz windows that provide optical access. The second is to prevent

the main reaction zone from positioning itself too close to the top wall of the furnace, where the optical access is limited. The temperature in the furnace is determined by the balance between the thermal input and the heat loss. Passive cooling by radiation heat loss through furnace top wall was adopted in the experiments. It was found that the flames impinge on the top wall at 8 kW, while the temperature in the upper part in the furnace is too high for the quartz windows at 10 kW. Therefore, the measurements of velocity and temperature were performed at 9 kW (fuel mass flow rate based). The operating conditions for the three experimental cases are summarized in Table 4.2.

The results of the measurements are presented in the x-z coordinate system that is shown in Figure 2.1. The origin is located at the exit of the fuel nozzle, and the z-axis is measured in the vertical direction (jet flow direction). The x-axis is in the horizontal direction crossing the fuel jet and two air jets. The mean velocity components $\widetilde{U_z}$, $\widetilde{U_x}$ and the Reynolds stresses, $\widetilde{u_z'' u_z''}$, $\widetilde{u_x'' u_x''}$, $\widetilde{u_z'' u_x''}$ were measured with a two-component LDA system in forward scatter configuration. For each measurement point, 5000 samples were taken to compute the velocity statistics. The velocity statistics were computed as transit-time weighted averages to compensate for the effect of the velocity bias. Since the particle density is proportional to the gas density, the LDA measurements directly provide density weighted (Favre averaged) mean quantities.

The velocity profiles were measured at seven different heights, z = 3, 50, 100, 200, 300, 400 and 500 mm. LDA measurements were initially conducted using a back-scatter configuration. However, when taking measurements in flameless mode the signal-to-noise ratio of the Doppler bursts was very low resulting in very low data rates even at very high seeding particle density. The high seeding particle density led to a gradual deposition of seeding particles on the window which further reduced the quality of the signals. This problem was solved by using an LDA in forward scatter configuration. Even at low seeding particle density, a data rate of at least 50~100 Hz could be reached. Continuous measurements could be performed with this setting for several hours without encountering problems with deposition of seeding particles. In-furnace measurements did encounter problems due to beam steering. Beam steering reduced the data rate in time coincident mode. Therefore, time-coincident measurements were only taken in the jet regions where the seeding particle density was high enough and non-coincident data were acquired outside those regions.

Mean temperatures $\overline{T}$ and temperature root mean square (RMS) values $T_{rms}$ were determined with CARS. The measurements were performed at the same heights as the velocity measurements, except for z=25 mm instead of 50 mm. The CARS measurements at z=25 mm were used to check whether reactions between fuel and recirculated burnt gas take place. This could happen since the furnace was operating at lean conditions. For each measurement point, 1600 shots in the reaction zone (x=-55~55 mm, z=300~500 mm) and 1000 shots outside the reaction zone. The CARS spectra were taken at 10 Hz. Signal strength fluctuates with the actual temperature and also due to beam steering which sometimes results in unacceptable signal quality when the strength is comparable to background noise. A fitting quality parameter was used to select valid shots (van Veen and Roekaerts, 2003). As a result, at least 95% of the shots were valid. Temperature statistics (mean and RMS values) were computed from the valid shots. These statistics correspond to Reynolds averaged values.

### 4.2.2. INLET PROFILES

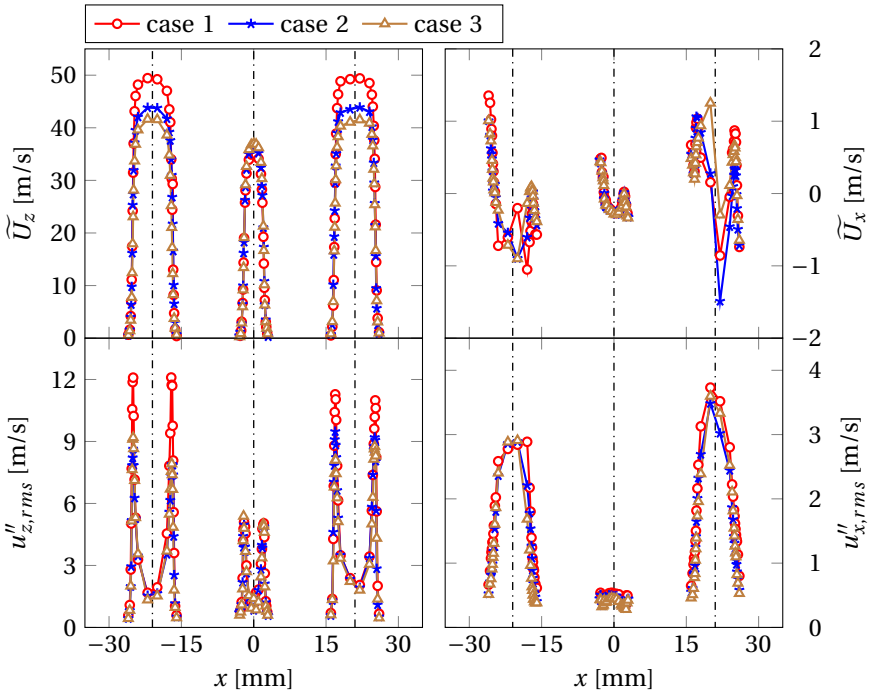


**Figure 4.1:** Fuel and air jets mean velocities and velocity RMS values measured at z=3 mm for the three cases. The fuel jet axis is at x=0 mm and the air jets axes are located at x=±21 mm. The axes of the different jets are marked by the dotted dashed lines.

Figure 4.1 shows the mean velocity and velocity RMS profiles at z=3 mm for the three cases. These profiles provide inlet boundary conditions for numerical simulations. At z=3 mm, measurements were only made above the nozzles because outside the jets the data rate is too low. The fuel jet is in the middle centred at x=0 mm and the two air jets are located 21 mm away from the centre. The mean velocity profiles for the fuel jets are nearly the same for the three cases as the equivalence ratio was varied by varying the air flow. The fuel jets have maximum velocity of $\widetilde{U_z}$ =35.2, 36.2 and 37.0 m/s in case 1, 2 and 3, respectively. As the equivalence ratio was increased (from case 1 to 3), the air preheat temperature increased due to the increased air residence time in the recuperator and increased flue gas temperature. The fuel temperature was also slightly affected and this led to a slight change in the fuel jet velocity. In all three jets, the positions where the horizontal mean velocity $\widetilde{U_x}$ switched from positive to negative values were not at the jet centres indicated by the dotted dashed lines. This shows that the jets were possibly not perfectly issuing in vertical direction.

The maximum mean velocity $\widetilde{U_z}$ of the air jets was the largest for case 1 with highest air mass flow rate. High values of $u''_{z,rms}$ are found at the jet boundaries due to high shear. Highest values of $u''_{z,rms}$ were also in case 1 due to highest velocity. Fluctuations

in the air jets are much larger than those in the fuel jet. The magnitude of $u''_{x,rms}$ in the fuel jet is around 0.5 m/s, but it is 3 m/s or larger in the air jets, about one-third of the maximum $u''_{z,rms}$. The profiles of the mean velocity in x-direction are complex. This may also be due to the jets supplying feature of the burner. Fuel was supplied through a long straight stainless steel pipe having a length of 800 mm. The fuel flow was consequently considered as a fully developed pipe flow. However, the air jets cannot be considered as fully developed pipe flows, because the length of the nozzles is only 28 mm. This is not long enough to have a fully developed flow. However, mean velocity in x-direction and velocity fluctuations were quite similar in all cases which indicates this is not statistical experimental error.

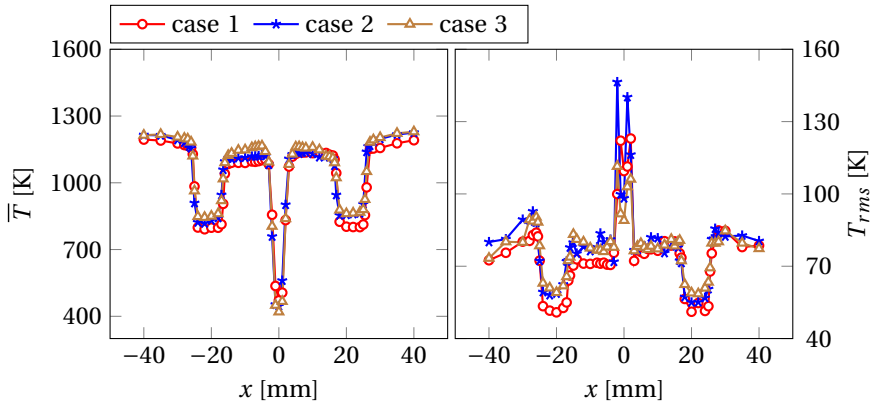


**Figure 4.2:** Fuel and air jets inlet mean temperatures (left) and temperature RMS values (right) measured at z=3 mm for the three cases.

Figure 4.2 shows the mean temperature and temperature RMS values at z=3 mm. The fuel temperature differs slightly in the three cases, and the maximum temperature difference was less than 50 K. However, the fuel temperature determination from CARS spectra was significantly affected by the nonresonant signal produced by the fuel. Uncertainty in these temperatures is not clear. The mean air temperature was, as expected, lowest in case 1 and highest in case 3. The maximum air temperature difference between the cases was less than 70 K. It was found that there is a slight temperature difference between the left and right air jets for each case. This difference might be attributed to non-uniform distribution of air in the recuperator leading to slightly non-uniform preheating. The measured mean velocity profiles together with the measured mass flow rates were used to calculate the bulk temperature of the air and fuel jets. This gives an impression of the uncertainties of the temperature measurements in the low temperature range and fuel rich region. The relation between mass flow rate $\dot{m}$ and axial velocity $U_z$ is as follows

$$\dot{m} = \int_A \rho U_z \, dA, \tag{4.1}$$

where $\rho$ is the density and $A$ is the nozzle area. Using the ideal gas equation of state and

**Table 4.3:** Comparison between measured and calculated jet inlet temperatures. $\overline{T}_*$ and $\overline{T}_{*,c}$ represent the the measured and the calculated temperatures, respectively. $\overline{T}_{*,c}$ was calculated at 1.01325 bar. Subscript "$_*$" represents either "$f$" or "$a$" which denotes fuel or air. $\Delta\overline{T}_* = \overline{T}_{*,c} - \overline{T}_*$.

| Case | $\overline{T}_f$ [K] | $\overline{T}_{f,c}$ [K] | $\overline{T}_a$ [K] | $\overline{T}_{a,c}$ [K] | $\Delta\overline{T}_f/\overline{T}_f$ | $\Delta\overline{T}_a/\overline{T}_a$ |
|---|---|---|---|---|---|---|
| 1 | 471 | 401 | 801 | 806 | -14.8% | 0.6% |
| 2 | 446 | 416 | 843 | 816 | -6.9% | -3.2% |
| 3 | 420 | 422 | 860 | 847 | 0.5% | -1.2% |



assuming ambient pressure and constant temperature, the equation above becomes

$$\dot{m} = \frac{p}{RT}\int_A U_z dA, \tag{4.2}$$

where $p$ is the pressure, $R$ is the gas constant and $T$ is the temperature. The comparison between measured temperatures and those determined by Equation (4.2) is shown in Table 4.3. The air temperature $\overline{T}_a$ shown in the table is the average of the two air jets. The calculated air temperature $\overline{T}_{a,c}$ is based on the average of the left and right mean velocity profiles of air jets. The differences between the calculated and measured fuel temperature are quite large. The measured fuel temperatures decrease from case 1 to 3, but the calculated fuel temperatures exhibit an opposite trend. This indicates large experimental uncertainties in the fuel rich region due to nonresonant signal. However, the differences in the calculated and measured air temperatures are quite small and are within the uncertainties given by van Veen and Roekaerts (2003).

## 4.3. VELOCITY STATISTICS

### 4.3.1. MEAN VELOCITY

The evolution of the mean velocity components $\widetilde{U_z}$ and $\widetilde{U_x}$ in the three cases are displayed in Figure 4.3. The corresponding RMS values $u''_{z,rms}$, $u''_{x,rms}$ and Reynolds shear stress $\widetilde{u''_z u''_x}$ are shown in Figure 4.4 and Figure 4.5, respectively. Between z=50 mm and z=500 mm, the peak of the mean velocity profile shifts by about 15~20 mm in the positive x-direction. Several factors may have caused this shift. First, the burner nozzle is mounted on the top of the recuperator which is not uniformly heated by flue gas and cooled by inlet air (resulting in slightly different air inlet temperatures as discussed in the previous section). The nozzle orientation may have been affected by the recuperator expansion. Secondly, the fact that the air jet located at the right-hand side (positive x-values) decays faster than the other one also contributes to the asymmetry. This difference in decay may have been caused by temperature difference. The temperature of the air jet on the right-hand side is higher but the velocity is similar to that of the left-hand side air jet. Therefore, the mass flow rate of the right-hand side air jet is smaller, resulting in less momentum thus causing faster decay. Another explanation could be a slight displacement of the jet orientation out of the xz plane.

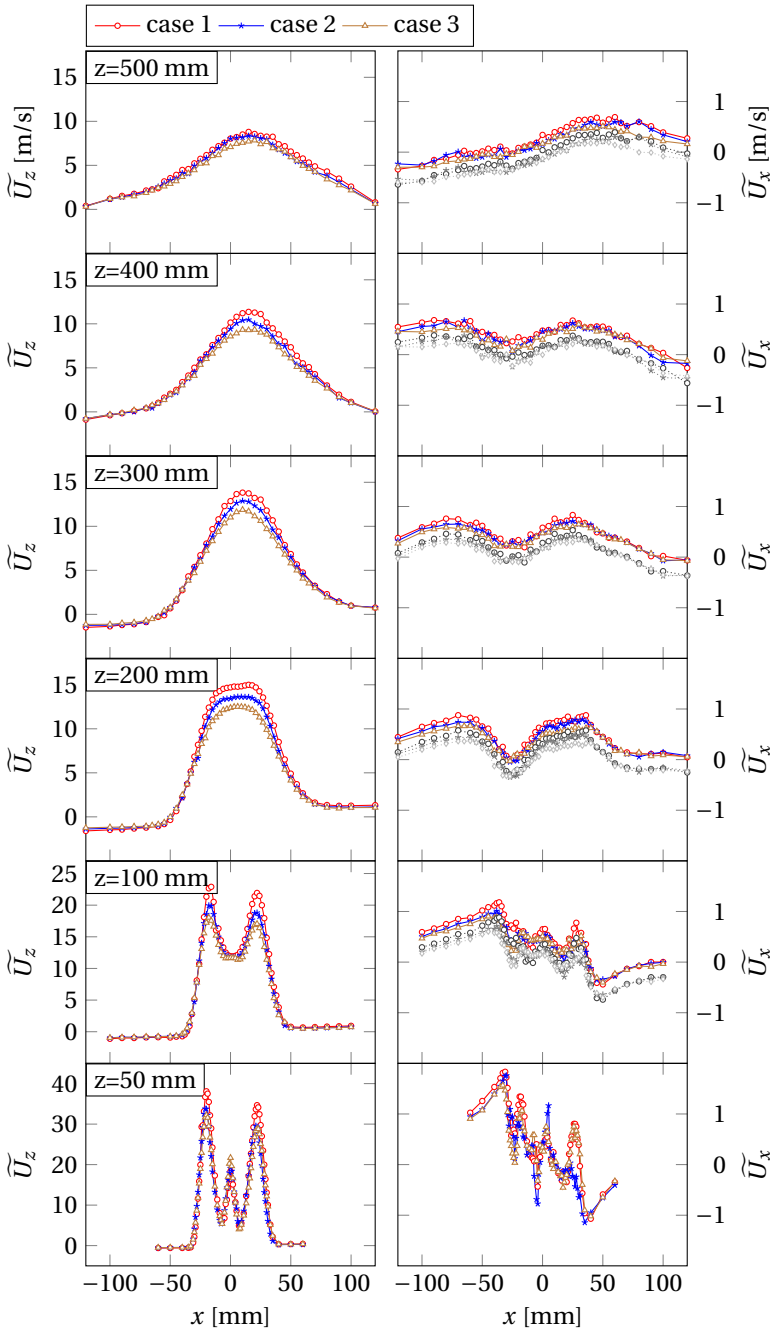


**Figure 4.3:** Mean velocity components $\widetilde{U_z}$ (left) and $\widetilde{U_x}$ (right) measured with LDA at z=50, 100, 200, 300, 400, 500 mm for the three cases. $\widetilde{U_x}$ compensated with -0.3 m/s are shown respectively in dark grey (case 1), grey (case 2), light grey (case 3).

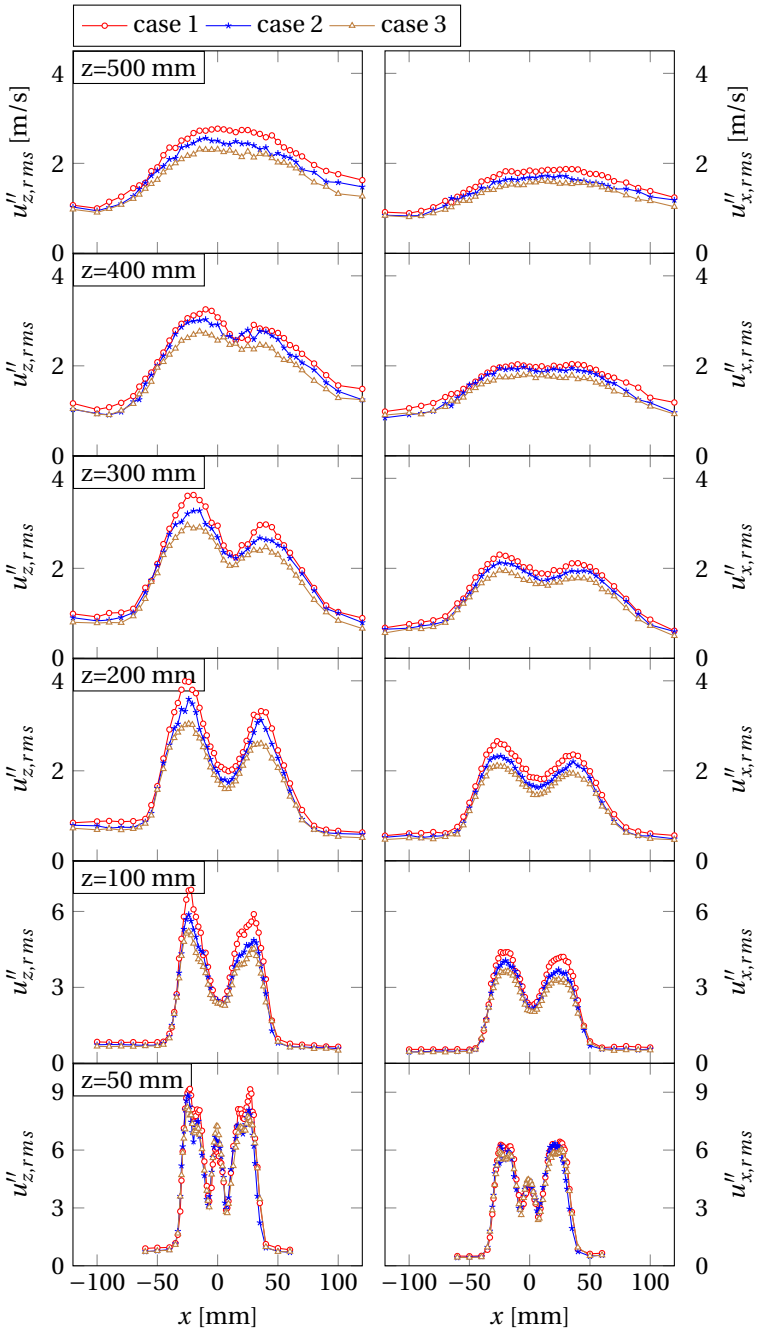


**Figure 4.4:** Velocity RMS values $u''_{z,rms}$ (left) and $u''_{x,rms}$ (right) measured with LDA at z=50, 100, 200, 300, 400, 500 mm for the three cases.

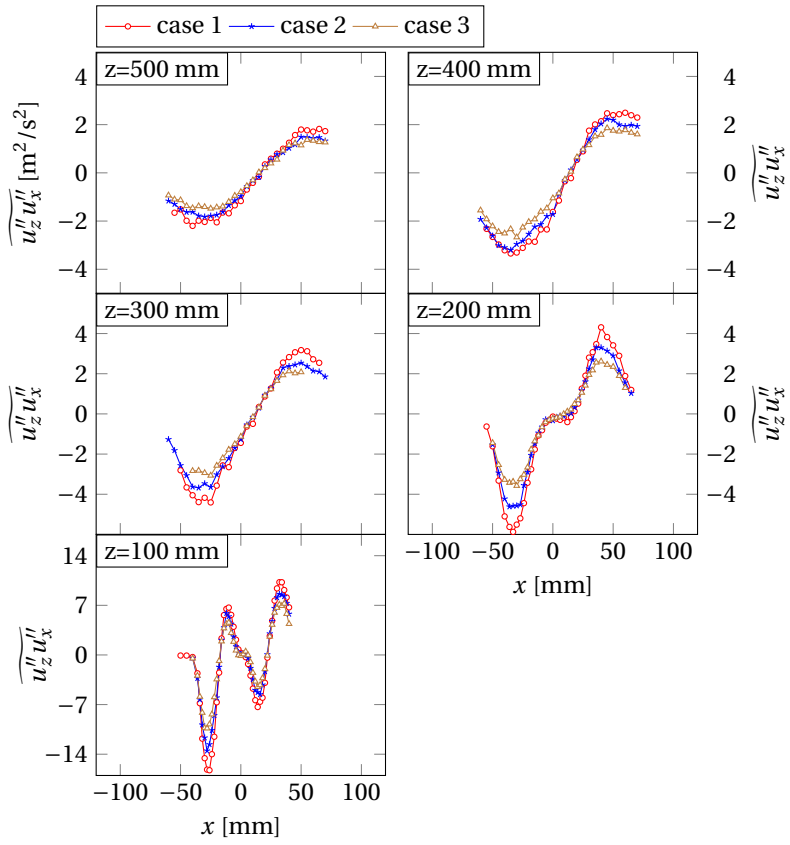


**Figure 4.5:** Reynolds shear stress $\widetilde{u_z''u_x''}$ measured with LDA at z=100, 200, 300, 400, 500 mm for the three cases .

Note that $\widetilde{U_x}$ is positive at most locations due to the shift in the positive x direction of the mean flow. In order to interpret it as in a symmetrical flow field, the $\widetilde{U_x}$ profiles for z=100 to z=500 mm are compensated by a constant value of -0.3 m/s and these shifted values are shown in grey colour. It can be seen in Figure 4.3 that, three distinct jets are still visible in the velocity profiles at z=50 mm with only the edges of the fuel jet slightly affected by the two air jets.

Further downstream at z=100 mm, the fuel jet has already merged with the air jets. A flat velocity profile of a width of about 16 mm is formed between two the air jets. The individual air jets can still be observed in the mean velocity profile. At larger distance from the centre, the mean velocity $\widetilde{U_z}$ is negative in the negative x region, but is still positive in the positive x region. The difference is quite small, so the main flow is not disturbed by the asymmetry.

At z=200 mm, the jets merged and the mean velocity $\widetilde{U_z}$ has a flat central region about 30 mm wide. At z=300 mm, the flat region in $\widetilde{U_z}$ is no longer present and the profile has

become bell-shaped with a full width at half maximum (FWHM) of about 80 mm. At z=400 mm, the general features are similar to those of the previous position. Velocity magnitudes are gradually decaying. The profile of $\widetilde{U_z}$ at 500 mm is similar to that at 400 mm, but the profile of $\widetilde{U_x}$ has significantly changed. As observed from the $\widetilde{U_x}$ profiles, the flow is radially outwards (negative velocity for negative x and positive velocity for positive x) towards the side walls because of the impingement on the top wall. The flow then starts its recirculation phase.

### 4.3.2. TURBULENCE FLUCTUATIONS

Velocity RMS values in terms of $u''_{z,rms}$, $u''_{x,rms}$ and the Reynolds shear stress $\widetilde{u''_z u''_x}$ are displayed in Figure 4.4 and Figure 4.5, respectively. Generally speaking, there is no essential difference in these turbulence quantities between the three cases. Turbulence quantities decrease from case 1 to case 3 mainly due to the lower air jet velocities.

In the early developing phase at z=50 mm, the differences in fluctuation levels between cases are small but one can still observe that the highest fluctuation level in the air jets occurs in case 1 and the highest fluctuation level in the fuel jet is found in case 3. In the jet regions, due to the presence of the fuel jet, the shear effect in these regions is lower than in the outer region leading to lower fluctuations. The peak value of $u''_{z,rms}$ at the air jets shear layers which are closer to the fuel jet accordingly is smaller. The fuel jet centre has been affected by the shear layer developed at the jet boundary due to the small initial jet diameter and only one peak in the centre is present at this height.

At z=100 mm, the differences in velocity fluctuations between the cases become larger. The $u''_{z,rms}$ peak of the fuel jet disappears and the double peaks in each air jet velocity fluctuation profiles become a single peak. According to the Reynolds stress $\widetilde{u''_z u''_x}$ measured at z=100 mm, the fuel jet is significantly influenced by the air jets. The shear stress in the fuel jet region is flattened, but two strong shear layers of each air jet are still clearly present since they have higher momentum. At z=200 mm, the shear stress peaks in the inner jet regions are flattened. Merging of air jets makes the overall flow start behaving like a single large jet with one velocity peak, two fluctuation peaks and two shear stress peaks. Turbulent fluctuations do not decay much from z=200 to 300 mm. The flat region in shear stress presented at z=200 mm disappears. Fluctuations continue decaying further downstream and the double peak profiles develop into a single wide envelope at z=500 mm.

## 4.4. TEMPERATURE STATISTICS

### 4.4.1. WALL TEMPERATURE

Wall temperatures were measured by the thermocouples whose tips are mounted at the wall surface. Two thermocouples are fixed to the side wall for the side wall temperature measurements, but these have different z positions when both the burner and the internal top wall are moving in vertical direction. The positions for side wall temperature measurements are located along the vertical line x=160 mm, y=0 mm and the line x=160 mm, y=80 mm at z= 3, 100, 200, 300, 400, 500 mm (The coordinate system used here is shown in Figure 2.1). The measurements are denoted as $T_{\text{mid}}$ and $T_{\text{mids}}$ respectively. A thermocouple is fixed to the centre of the internal top wall measuring the top wall tem-

perature $T_{top}$. A thermocouple is fixed at a corner of the combustion chamber (about 300 mm above the bottom plate) and moves together with the burner. It measures the temperature at the same location in the combustion chamber. The measured values are denoted by $T_{check}$.

The measured temperature values are not corrected for radiation heat loss. Besides, the thermal couples used here are ungrounded type. The junction of the thermocouple is shielded and it is not attached on the sheath. The measured temperatures do not represent the actual temperature of the wall, and the measured values are expected to be lower than the actual values. Although the uncertainty of these measured temperatures is not determined in this study, the measured temperatures can be used to show the qualitative variation of the side wall temperature and the stability of the furnace when the burner and internal top are moved vertically.

It can be seen from Figure 4.6 that the side wall temperature increases with increasing height. It should be pointed out that $T_{top}$ and $T_{check}$ are six measurements made when LDA or CARS measurements are performed at z= 3, 100, 200, 300, 400, 500 mm respectively. Although the whole combustion chamber moves vertically, the profiles of the measured temperature $T_{top}$ and $T_{check}$ are more or less flat. The temperature variations at these to locations are less than 20 K, indicating that the in-furnace condition is independent of the position of the optical window in the side wall.

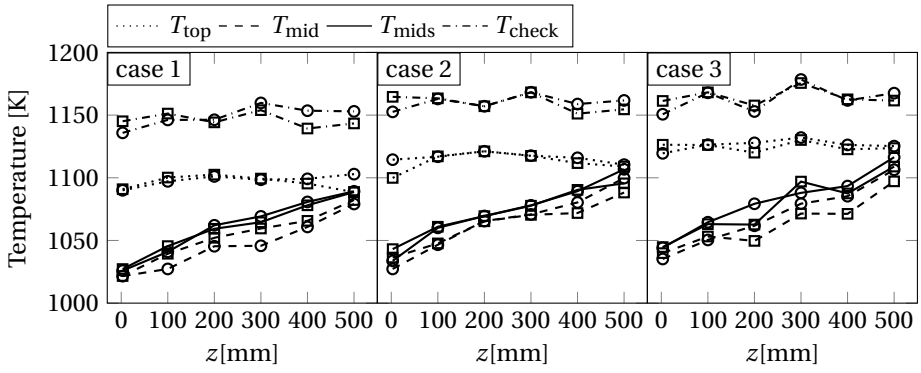


**Figure 4.6:** Wall temperatures at the top wall and along the side wall for the three cases. Circle and square markers denote two measurements, dotted line: $T_{top}$, dashed line: $T_{mid}$, solid line: $T_{mids}$.

### 4.4.2. MEAN TEMPERATURE AND TEMPERATURE FLUCTUATIONS

Figure 4.7 shows profiles of the mean temperature $\overline{T}$ (left) and temperature RMS values $T_{rms}$ (right) along the x-direction at six different heights. It should be pointed out that the first height above the inlet for the temperature measurements is at z=25 mm instead of z=50 mm in the velocity measurements. Temperature measurements at this height (z=25 mm) are important to determine whether reactions take place between fuel and oxygen left in recirculated burnt gas.

At z=25 mm, three low temperature jets are causing the three valleys in the mean temperature profiles for each case. From each jet centre to jet edge, temperature in-

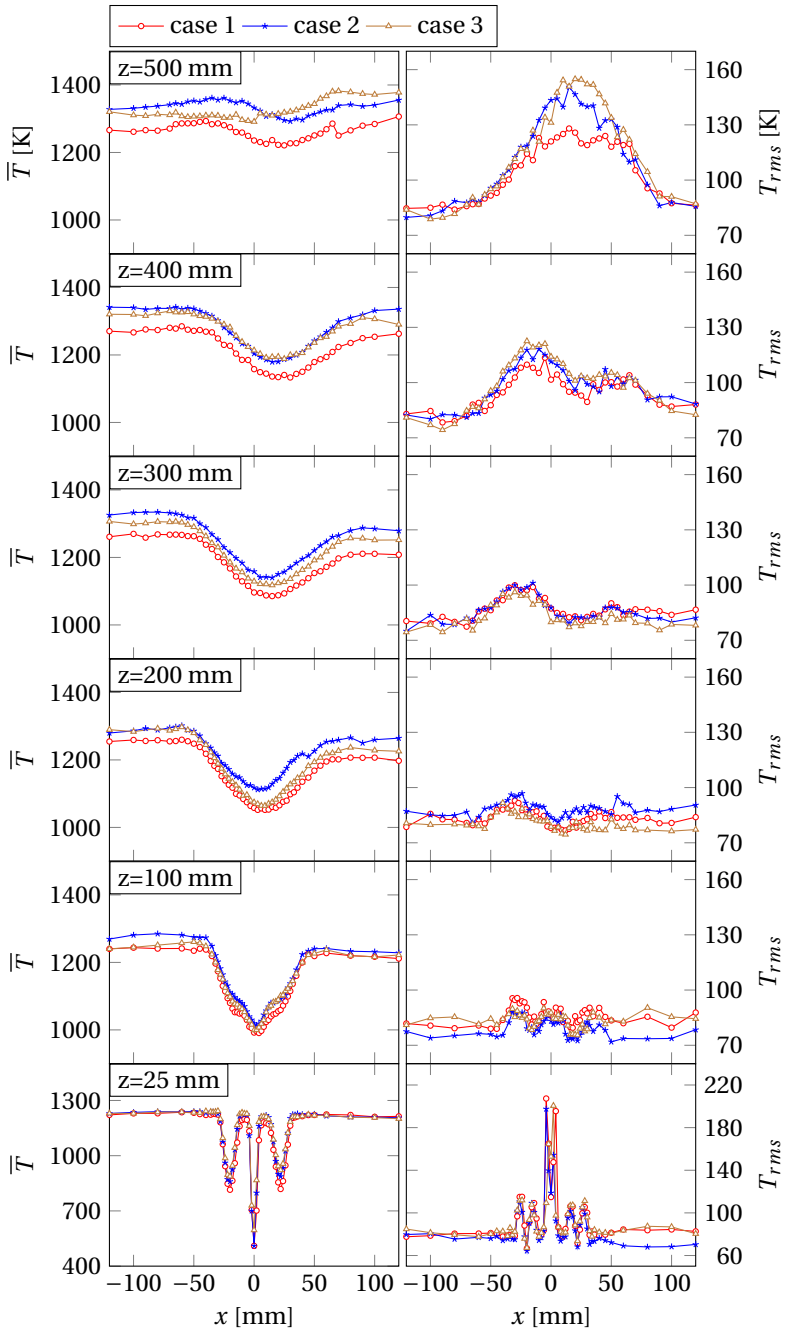


**Figure 4.7:** Mean temperatures (left) and temperature RMS values (right) at six heights. Temperature RMS fluctuations are derived from 1600 samples in the reaction zone (x=-55~55 mm, z=300~500 mm) and 1000 samples outside the reaction zone

creases due to mixing. The mean temperature profile in the regions away from the jets is flat for all cases. Double peak temperature RMS values can be seen at the shear layers at the jet edges at z=25 mm and these peak values are higher than those in Figure 4.2. However, it is not an effective way to determine whether reactions take place just based on mean temperature and corresponding RMS fluctuations. Inspection of temperature histograms would be more helpful and this will be discussed in Section 4.4.3.

According to the velocity measurements, the fuel and air jets are interacting with each other at z=100 mm and the individual fuel jet can hardly be observed in Figure 4.3 (left). The mean temperature profiles at this height also show that behaviour, see Figure 4.7 (left). The mean temperature levels slightly differ between the cases. Mean temperatures are generally the lowest for case 1 and the highest for case 2. Temperature in the central region is increasing to about 1000 K and the air jets are heated up to 1050~1100 K. Temperature fluctuations in the centre decrease sharply due to low temperature gradient. The double peak in fluctuations disappears and the fluctuation profiles exhibit three hills, one at each jet. The highest temperature RMS values are observed in case 1 and the maximum value is not more than 100 K.

Further downstream at z=200 mm, there is no trace of the individual jets. Mean temperature profiles exhibit a wide valley in the centre. Mean temperature is the highest for case 2 and lowest for case 1. Although a globally higher temperature could be reached in case 3, the temperature in the jet centre increases slowly in this case. It can also be seen from the overall temperature fluctuations that, case 3 has lowest temperature fluctuations due to less turbulent flow field and this agrees with the relatively slow rate of the change in the mean temperature profile. On the contrary, turbulent mixing rate is high in case 1 but temperatures in the air jets and burnt gas are lower, as a result of lower temperature in the combined jet central region. The three hills at the previous height disappear in the temperature fluctuation profiles, but wide envelopes appear between x=-50 and 0 mm and between x=10 and 60 mm for all cases. The turbulent mixing phenomena are sufficient to explain the trends in temperature fluctuations and clear effects of reactions are absent.

At z=300 mm, the overall mean temperature has increased compared to that at z=200 mm for all cases. The mean temperature in case 3 is catching up with case 2 but still a bit lower. Temperature fluctuations in the envelope regions observed at z=200 mm become larger. The reactions should contribute considerably to these fluctuations, because the mixing between the fuel, air and burnt gas are better than at the previous height and the contribution to the temperature fluctuations due to mixing should become less. Small temperature RMS peak values indicate that exothermic reactions at this height are still weak. At z=400 mm, the mean temperatures continue increasing in all cases. The mean temperatures of case 3 overlaps with those of case 2. Temperature RMS values become larger and fluctuations in case 3 exceed both case 1 and 2. This indicates that more frequent reactions take place there. Mean temperature profiles become more or less flat at z=500 mm due to reactions in the central region, showing a relatively uniform temperature field. Temperature fluctuates significantly in the central region due to the unsteady autoignition as observed in time resolved OH* chemiluminescence images (see Chapter 3 Section 3.5.3). The mean temperatures in the positive x part for case 3 become higher than those in case 2 and the corresponding temperature RMS fluctuations also exceed

those in case 2. Reactions are prominent in the central combined jet region. As seen from OH* chemiluminescence in Figure 3.1, the measurement line at z=500 mm goes across the main reaction zone in all cases.

It is concluded that reactions start reaching a level influencing temperature profiles at around z=300 mm. At lower height the injected fuel and air are continuously preheated and diluted by entrained hot burnt gas. The final mean temperature rise (compared to the air inlet temperature) due to combustion is less than 600 K which is much lower than that of conventional flames produced by direct combustion of fuel and air. The low temperature rises can be attributed to the fact that the diluent is taking part of the heat released from reactions. Large temperature fluctuations in the reaction zone indicate that the combustion process is quite unsteady. The low temperature also greatly reduces formation of $NO_x$ emissions.



### 4.4.3. TEMPERATURE HISTOGRAMS

Figure 4.8 displays the normalized temperature histograms at z=300, 400 and 500 mm for the three cases. A bin size of 50 K is set for all displayed histograms. The profiles are plotted by bin centre values and the corresponding probability. The total number of temperature samples for each histogram was 1600, except for x=-60 mm which is outside the reaction zone where the sample number is 1000.

It is seen that the temperature distributions range from 750 K to 1800 K. At z=300 mm, temperatures at x=-60 mm just in the back flow region are highest. Temperature histograms at x=-40 and -20 mm are wider while shifting to lower temperature range. Temperatures continue shifting to lower values at x=0 and 20 mm, but a small number of high temperature (above 1500 K) samples are measured in case 1 and case 2, indicating the start of considerable reactions. At z=400 mm, all temperature histograms shift slightly to a hotter range and the high temperature samples magnitudes also increase. This is certainly due to the heat released from the reactions. At the last measurement height z=500 mm, all histograms are largely overlapping. More high temperature samples are observed with larger magnitude. The shape of histograms at x=-60, -40 and -20 do not change much, but those at x=0 and 20 mm inside the reaction zone exhibit different shapes. In case 1, the profiles inside the reaction zone are highest and narrowest with less high temperature samples, while they are smallest and widest in case 3 with more high temperature samples.

As mentioned in Section 4.2.1, measurements at z=25 mm were used to check whether fuel reacts with recirculated burnt gas before air is introduced into the mixture when the furnace is working at lean conditions. The reactions between fuel and oxygen left in the burnt gas at lean combustion condition may result in a lifted flame similar to the jet flame in jet in hot coflow burners, which is not desired for a stable flameless combustion process.

Temperature histograms near the fuel jet (x=±4 and ±6 mm) at z=25 mm for all cases are shown in Figure 4.9. The profiles at x=-60 mm represent conditions far away from the jet and show temperature distributions in recirculated burnt gas and thus are used as a reference to represent burnt gas temperature. At x=-4 mm in case 1, there is a considerable number of low temperature samples representing presence of fuel. It should be noted that the magnitude and the sample number in the high temperature range above

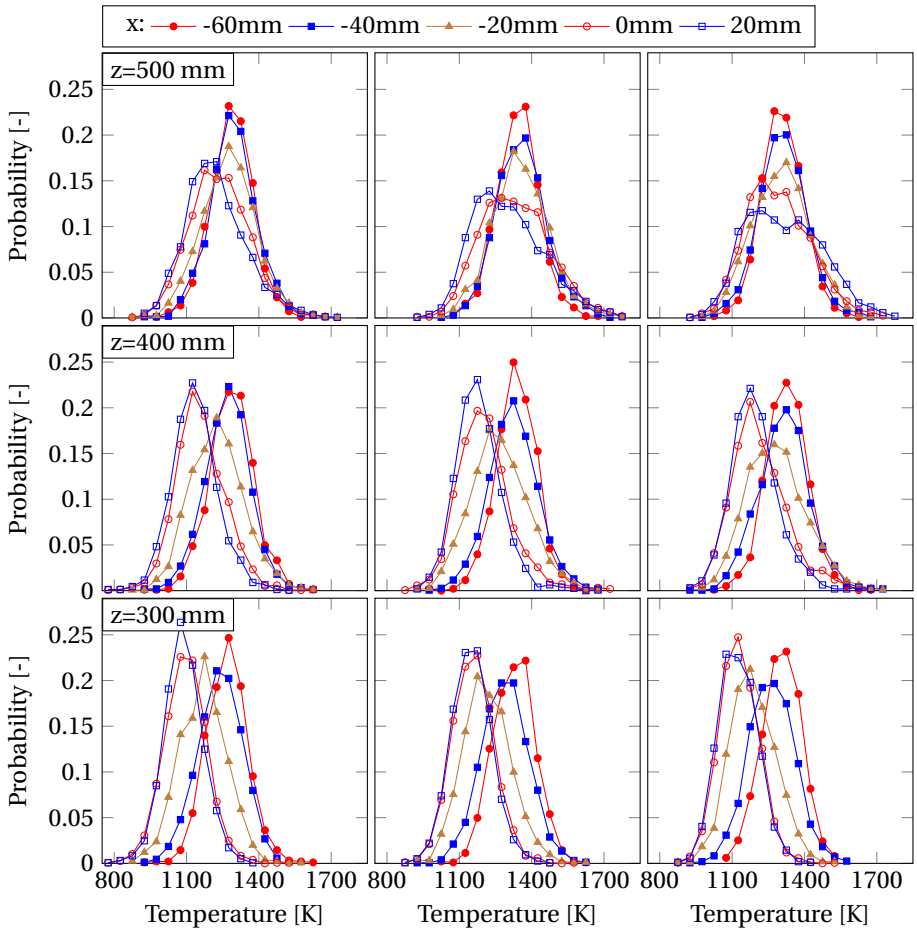


**Figure 4.8:** Temperature histograms at z=300 mm (third row), z=400 mm (second row) and z=500 mm (first row) for the three cases, from left to right: case 1, case 2 and case 3. Histograms are plotted from outside to inside the reaction zone, at x=-60, -40, -20, 0, 20 mm.

1400 K both exceed those at the reference position. It is fair to say that fuel indeed reacts immediately with oxygen in burnt gas. This is also observed in case 2 but not in case 3. In case 2, the profiles at ±4 mm are quite different, probably because the misalignment between the measurement probe and the fuel jet axis in the experiment. As equivalence ratio $\phi$ increases from 0.7 to 0.9, oxygen mass fraction in burnt gas decreases from 6.63% to 2.18%. For case 1 and case 2, oxygen mass fractions are respectively 6.63% and 4.39%, both are located in the range which is favourable for autoignition (see Chapter 3 Section 3.5.5). In case 3, profiles at ±4 mm are quite similar, but much less low temperature samples are present. This may be attributed to slightly higher temperature of fuel and burnt gas and also less turbulent flow field. Further investigations with OH-PLIF would be very helpful to clarify these features.

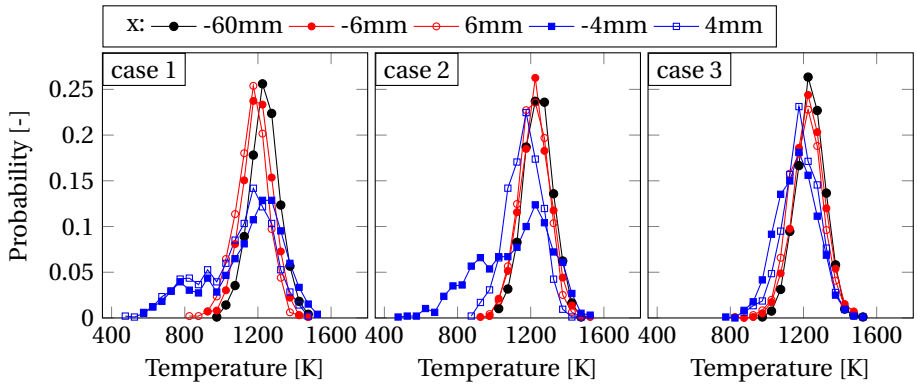


**Figure 4.9:** Temperature histograms at z=25 mm in the three cases, from left to right: case 1, case 2 and case 3. Histograms are plotted for fuel jet shear layers, at x=±4 and ±6 mm. The histogram at x=-60 mm is used as a reference in burnt gas.

The fuel jet in the current furnace is very similar to that in DJHC-I (Re=4100) case in the Ref. (Oldenhof et al., 2010). But the oxygen mass fractions in the burnt gas in the current furnace is lower than those in the coflow. In JHC burners, the turbulent flow field is driven by the fuel jet. However, for the current burner nozzle configuration, the fuel jet is surrounded by four air jets around it, thus the flow is much more turbulent than that in JHC burners at the location where a stabilized flame can be present in JHC burners. The flame in the current furnace is stretched to extinction. However, due to highly turbulent mixing rate, flammable mixture pockets are already formed in the furnace. Once sufficient burnt gas are mixed in the mixture, autoignition can be achieved. A stable lifted flame cannot be present in such a turbulent field.

### 4.4.4. HIGH TEMPERATURE SAMPLES

Since the reactants are diluted and distributed in a large space, reaction intensity is low and temperature increase by reaction is hardly noticeable although it is visible in the temperature RMS. In order to demonstrate the effects of the exothermic reactions in the reaction zone, the $T_{95}$ which is defined as the temperature where the cumulative density function exceeds 95% is used. Figure 4.10 shows the $T_{95}$ profiles at z=300, 400 and 500 mm where OH* chemiluminescence intensity becomes significant.

It is seen that the profiles for mean temperature $\overline{T}$ and $\overline{T}_{95}$ are quite similar at z=300 mm in all cases. The profiles are just shifted to higher magnitudes, which means reactions do not contribute much to the temperature increase. At z=400 mm, a region with elevated values appears in the $\overline{T}_{95}$ profiles between x=-50 and 0 mm. Temperature increase due to heat release from reactions becomes visible. However, it is not that obvious in the corresponding locations on the right-hand side. However, the $\overline{T}_{95}$ profiles become symmetrical with respect to the combined jet centre at z=500 mm. All $\overline{T}_{95}$ profiles change a shape from a concave curve to a convex curve. Temperature rises become quite significant. In case 1, the $\overline{T}_{95}$ profile is flatter than the other two which means reaction intensity is quite uniform over the reaction zone and it is consistent with the

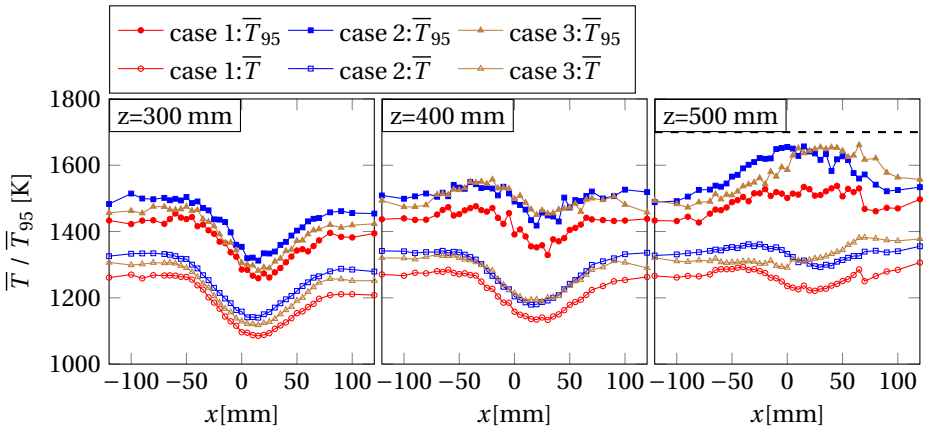


**Figure 4.10:** Mean value of high temperature samples $\overline{T}_{95}$ at z=300 (left), 400 (middle) and 500 (right) mm in the three cases.

OH* chemiluminescence images. Whereas the reaction intensity is higher in the reaction zone centre in case 2 and case 3. The overall temperature rise is quite low compared to conventional flames. In Figure 4.10, the horizontal dashed line at z=500 mm indicates temperature 1700 K. $\overline{T}_{95}$ values in all cases are below this line and the instantaneous peak temperature is less than 1800 K. Thus the thermal $NO_x$ formation is suppressed. For all cases, measured $NO_x$ emissions were below 1 ppmv.

## 4.5. SUMMARY AND CONCLUSIONS

In this chapter, detailed measurements of velocity and temperature were obtained and presented for a lab-scale furnace operating in flameless combustion regime. The furnace was working at 9 kW at three values of equivalence ratio, namely $\phi$=0.7, 0.8 and 0.9. Visible flames were not observed in the flameless combustion regime for all cases. It is found that the design (see Chapter 2) of the furnace can retain similar combustion conditions while providing good optical access to the inside furnace. This allows flexibility for measurements. The main findings based on the experimental results are as follows.

The highly turbulent flow field plays an important role in preventing a stabilized flame. The flow field in the furnace is mainly driven by air jets, more air injection results in a more turbulent internal flow field, enhancing turbulent mixing and accelerating internal burnt gas entrainment. These are sensitive factors that affects flameless combustion. Although the turbulent fluctuations in the three cases are similar and the difference in velocity fluctuations between case 1 and 3 is only around 10%~30% (based on case 1), the reaction intensity and the position of the reaction zone change obviously.

The mean temperature rise in the furnace due to combustion is low, and the high temperature samples and temperature histograms show exothermic reactions are indeed present in the reaction zone, but there is no locally stabilized lifted flame present in the reaction zone. The final mean temperature rise (compared to the air inlet temperature) due to combustion is less than 600 K which is much lower than that in conven-

tional combustion of fuel and air. The instantaneous peak temperature is less than 1800 K and the temperature samples above 1700 K is less than 1.5%. The low peak temperature greatly reduces the formation of $NO_x$ emissions. At lower height in the furnace the fuel and air are continuously mixing and diluted by entrained hot burnt gas. The reactions become visible (according to $T_{rms}$ and histograms) at around z=300 mm. Large temperature fluctuations in the reaction zone (z=400 and 500 mm) indicate that the combustion process is quite unsteady. The temperature in the reaction zone spans a quite wide range showing dynamic presence of reacting pockets.

The burner nozzle configuration is important to prevent locally stabilized flame and to establish flameless combustion. The temperature histograms above the nozzle exit at z=25 mm confirm that the fuel reacts immediately with the oxygen left in the burnt gas (similar to JHC flames). This consideration should be included in the burner design, especially for the distance between the fuel and the air nozzles. The larger the distance, the fuel and the air jets have more time to be diluted before mixing. But a lifted flame may be established before the fuel mixes with the air. In this case, the air jets are used to prevent the lifted flame and should be designed close to the fuel jet.

# 5

# THEORIES FOR NON-PREMIXED TURBULENT REACTING FLOWS

*In this chapter, the theories and models that are used in the following chapters are introduced and described. Firstly, the governing equations in turbulent combustion are introduced. Secondly, RANS and LES approaches for turbulent combustion modelling and the closure for the stresses and fluxes are introduced. Furthermore, the flamelet concept based FGM model for turbulent combustion modelling is introduced. Finally, the extended FGM model referred to as diluted air FGM (DAFGM) model is developed for flameless combustion. The dilution effects are included. In the DAFGM model, the reactions in the reaction zone are treated as the fuel reacts with the diluted air. The corresponding lookup table stores the flamelets at different air dilution levels. With one additional control parameter named air dilution level, the corresponding flamelets can be indexed. The radiative heat transfer in the high temperature furnace is significant, thus radiation is also coupled into the DAFGM model. The radiative properties of gases are modelled with a weighted-sum-of-grey-gas (WSGG) model which accounts for the mole ratio between $CO_2$ and $H_2O$. In addition, a method to take into account the turbulence-radiation interaction with DAFGM has also been developed. The models developed in this thesis have been implemented in the open source CFD package OpenFOAM-2.3.1 including a new table lookup scheme for two- to six-dimensional lookup tables and interpolations.*

## 5.1. GOVERNING EQUATIONS

The theory in this chapter partially follows references (Poinsot and Veynante, 2012; Peters, 2004; Pope, 2000). The equation for conservation of mass, or continuity equation for single phase flow can be written as follows:

$$\frac{\partial \rho}{\partial t} + \frac{\partial \rho u_i}{\partial x_i} = 0. \tag{5.1}$$

The equation of momentum is the same in reacting and non reacting flows:

$$\frac{\partial \rho u_j}{\partial t} + \frac{\partial}{\partial x_i}\left(\rho u_i u_j\right) = -\frac{\partial p}{\partial x_j} + \frac{\partial \tau_{ij}}{\partial x_i} + \rho \sum_{k=1}^{N} Y_k f_{k,j}. \tag{5.2}$$

In Equations (5.1) and (5.2), $\rho$ is density; $u$ is velocity; $p$ is pressure; $f_{k,j}$ is the volume force acting on species $k$ in direction $j$; the viscous tensor $\tau_{ij}$ is defined by

$$\tau_{ij} = \mu\left(\frac{\partial u_i}{\partial x_j} + \frac{\partial u_j}{\partial x_i}\right) - \frac{2}{3}\mu\frac{\partial u_k}{\partial x_k}\delta_{ij} = 2\mu\left(S_{ij} - \frac{1}{3}\delta_{ij}S_{kk}\right), \tag{5.3}$$

where

$$S_{ij} = \frac{1}{2}\left(\frac{\partial u_i}{\partial x_j} + \frac{\partial u_j}{\partial x_i}\right), \tag{5.4}$$

is the strain rate tensor; $\mu$ is the dynamic viscosity; $\delta_{ij} = 1$ if $i = j$, otherwise $\delta_{ij} = 0$.

The mass conservation equation for species k is written:

$$\frac{\partial \rho Y_k}{\partial t} + \frac{\partial}{\partial x_i}\left(\rho u_i Y_k\right) = -\frac{\partial}{\partial x_i}\left(\rho V_{k,i} Y_k\right) + \dot{\omega}_k, \quad k = 1, \cdots, N, \tag{5.5}$$

where $V_{k,i}$ is the $i$-component of the diffusion velocity $V_k$ of species $k$ and $\omega_k$ is the production rate of species k. The species laminar diffusion fluxes are generally modelled as:

$$V_{k,i} Y_k = -D_k \frac{\partial Y_k}{\partial x_i}, \tag{5.6}$$

where $D_k$ is the diffusion coefficient of species $k$. If equal diffusivity for all species is assumed, the balance equations for species become

$$\frac{\partial \rho Y_k}{\partial t} + \frac{\partial}{\partial x_i}\left(\rho u_i Y_k\right) = \frac{\partial}{\partial x_i}\left(\rho D \frac{\partial Y_k}{\partial x_i}\right) + \dot{\omega}_k, \quad k = 1, \cdots, N. \tag{5.7}$$

The conservation equation for the enthalpy $h$ is written as

$$\frac{\partial \rho h}{\partial t} + \frac{\partial}{\partial x_i}\left(\rho h u_i\right) = \frac{Dp}{Dt} - \frac{\partial q_i}{\partial x_i} + \Phi_v + \Phi_F + S_r, \tag{5.8}$$

where $q_i = -\lambda\frac{\partial T}{\partial x_i} + \rho\sum_{k=1}^{N} h_k Y_k V_{k,i}$ is the enthalpy flux and $\lambda$ is the thermal conductivity; $\Phi_v = \tau_{ij}\frac{\partial u_i}{\partial x_j}$ is the viscous heating source term; $\Phi_F = \rho\sum_{k=1}^{N} Y_k f_{k,i} V_{k,i}$ is the power produced by volume forces; $S_r$ represents heat transfer due to radiation. Effects of volumetric force and viscous heating are negligible compare to other terms in the enthalpy

equation. The pressure can be obtained from the equation of state for a mixture of ideal gases

$$p = \rho \frac{R_u T}{W}, \tag{5.9}$$

where $R_u$=8.314 J/(mol·K) is the universal gas constant and $W$ is the mean molecular weight given by

$$W = \left( \sum_{k=1}^{N} \frac{Y_k}{W_k} \right)^{-1}, \tag{5.10}$$

where $W_k$ is the molecular weight of species $k$. For subsonic combustion with low Mach numbers, the pressure can be assumed to be constant. Pressure changes are neglected in the equation of state, but kept in the momentum equation. Therefore, the change of pressure $Dp/Dt$ in Equation (5.8) may be negligible. In addition assuming unity Lewis number, the enthalpy equation becomes

$$\frac{\partial \rho h}{\partial t} + \frac{\partial}{\partial x_i}\left(\rho h u_i\right) = \frac{\partial}{\partial x_i}\left(\frac{\lambda}{c_p}\frac{\partial h}{\partial x_i}\right) + S_r. \tag{5.11}$$

Directly solving of the governing Equations (5.1), (5.2), (5.5) and (5.7) without any turbulence model is referred to as Direct Numerical Simulation (DNS). Since the large range of scales that have to be resolved in DNS, enormous computational resources are required. DNS is applicable to only simple geometries with low Reynolds number flows. DNS is therefore regarded as an unfeasible solution for industrial applications. However, instead of directly solving the governing equations, the averaged or filtered governing equations are solved in Reynolds Averaged Navier-Stokes (RANS) or Large Eddy Simulations (LES) approach.

## 5.2. REYNOLDS AVERAGED NAVIER-STOKES (RANS)

### 5.2.1. AVERAGED THE BALANCE EQUATIONS

Reynolds averaging splits any quantity into a mean and a fluctuating component as follows:

$$f = \overline{f} + f' \quad \text{with} \quad \overline{f'} = 0. \tag{5.12}$$

In density varying flows, Reynolds averaging introduces many unclosed correlations between any quantity $f$ and density $\rho$ fluctuations, $\overline{\rho' f'}$. Therefore Favre averaging (density-weighted averaging) (Favre, 1969; Kuo, 2005) is usually used to avoid this issue. The Favre averaged quantity is written as:

$$\widetilde{f} = \frac{\overline{\rho f}}{\overline{\rho}}. \tag{5.13}$$

Any quantity can be decomposed as follows:

$$f = \widetilde{f} + f'' \quad \text{with} \quad \widetilde{f''} = 0. \tag{5.14}$$

The Favre averaged balance equations become:
Mass:

$$\frac{\partial \overline{\rho}}{\partial t} + \frac{\partial \overline{\rho}\widetilde{u_i}}{\partial x_i} = 0, \tag{5.15}$$

Momentum:

$$\frac{\partial \overline{\rho}\widetilde{u_j}}{\partial t}+\frac{\partial}{\partial x_i}\left(\overline{\rho}\widetilde{u_i}\widetilde{u_j}\right)=-\frac{\partial \overline{p}}{\partial x_j}+\frac{\partial}{\partial x_i}\left(\overline{\tau_{ij}}-\overline{\rho}\widetilde{u_i''u_j''}\right), \tag{5.16}$$

Species:

$$\frac{\partial \overline{\rho}\widetilde{Y_k}}{\partial t}+\frac{\partial}{\partial x_i}\left(\overline{\rho}\widetilde{u_i}\widetilde{Y_k}\right)=\frac{\partial}{\partial x_i}\left(\overline{\rho D\frac{\partial Y_k}{\partial x_i}}-\overline{\rho}\widetilde{u_i''Y_k''}\right)+\overline{\dot{\omega}}_k,\quad k=1,\cdots,N, \tag{5.17}$$

Enthalpy:

$$\frac{\partial \overline{\rho}\widetilde{h}}{\partial t}+\frac{\partial}{\partial x_i}\left(\overline{\rho}\widetilde{u_i}\widetilde{h}\right)=\frac{\partial}{\partial x_i}\left(\overline{\rho D\frac{\partial h}{\partial x_i}}-\overline{\rho}\widetilde{u_i''h''}\right)+\overline{S}_r. \tag{5.18}$$

The remaining unclosed terms are: Reynolds stresses ($\widetilde{u_i''u_j''}$), species and enthalpy turbulent fluxes ($\widetilde{u_i''Y_k''}$ and $\widetilde{u_i''h''}$), mean laminar diffusive fluxes for species or enthalpy ($\overline{\rho D\frac{\partial Y_k}{\partial x_i}}$ and $\overline{\rho D\frac{\partial h}{\partial x_i}}$), and species chemical reaction rate ($\overline{\dot{\omega}}_k$), and mean radiative source term $\overline{S}_r$. They will be addressed in the following sub sections.

5

### 5.2.2. CLOSURE FOR RANS EQUATIONS

Reynolds stresses ($\widetilde{u_i''u_j''}$) are normally described using the Boussinesq's turbulent viscosity hypothesis (Pope, 2000).

$$\overline{\rho u_i''u_j''}=\overline{\rho}\widetilde{u_i''u_j''}=-\mu_t\left(\frac{\partial \widetilde{u_i}}{\partial x_j}+\frac{\partial \widetilde{u_j}}{\partial x_i}-\frac{2}{3}\delta_{ij}\frac{\partial \widetilde{u_k}}{\partial x_k}\right)+\frac{2}{3}\overline{\rho}k, \tag{5.19}$$

where $\mu_t$ is turbulent dynamic viscosity. The turbulence kinetic energy $k$ is defined as

$$k=\frac{1}{2}\sum_{i=1}^{3}\widetilde{u_i''u_i''}. \tag{5.20}$$

There are three types of approaches that can be used to close turbulent viscosity $\mu_t$ in RANS simulations, namely, zero-equation model, one-equation model and two-equations model. Here the two-equation $k-\epsilon$ model (Jones and Launder, 1972) is described as an example. The turbulent viscosity in $k-\epsilon$ is estimated as

$$\mu_t=\overline{\rho}C_\mu\frac{k^2}{\epsilon}, \tag{5.21}$$

where $C_\mu$ is a model constant.Turbulent kinetic energy $k$ and its dissipation rate $\epsilon$ are calculated by their modelled transport equations:

$$\frac{\partial \overline{\rho}k}{\partial t}+\frac{\partial}{\partial x_i}\left(\overline{\rho}\widetilde{u_i}k\right)=\frac{\partial}{\partial x_i}\left[\left(\mu+\frac{\mu_t}{\sigma_k}\right)\frac{\partial k}{\partial x_i}\right]+P_k-\overline{\rho}\epsilon, \tag{5.22}$$

$$\frac{\partial \overline{\rho}\epsilon}{\partial t}+\frac{\partial}{\partial x_i}\left(\overline{\rho}\widetilde{u_i}\epsilon\right)=\frac{\partial}{\partial x_i}\left[\left(\mu+\frac{\mu_t}{\sigma_\epsilon}\right)\frac{\partial \epsilon}{\partial x_i}\right]+C_{\epsilon 1}\frac{\epsilon}{k}-C_{\epsilon 2}\overline{\rho}\frac{\epsilon^2}{k}. \tag{5.23}$$

The model constants are

$$C_\mu = 0.09, \quad \sigma_k = 1, \quad \sigma_\epsilon = 1.3, \qquad C_{\epsilon 1} = 1.44, \quad C_{\epsilon 2} = 1.92. \tag{5.24}$$

The production term $P_k$ is given by:

$$P_k = -\overline{\rho}\widetilde{u_i'' u_j''}\frac{\partial \widetilde{u_i}}{\partial x_j}, \tag{5.25}$$

and can be rewritten using Equation (5.19).

Turbulent fluxes are generally closed using the classical gradient diffusion assumption

$$\overline{\rho}\widetilde{u_i'' Y_k''} = -\frac{\mu_t}{Sc_{kt}}\frac{\partial \widetilde{Y_k}}{\partial x_i}, \tag{5.26}$$

$$\overline{\rho}\widetilde{u_i'' h''} = -\frac{\mu_t}{Pr_t}\frac{\partial \widetilde{h}}{\partial x_i}, \tag{5.27}$$

where $Sc_t$ and $Pr_t$ are respectively turbulent Schmidt number and Prandtl number.

The molecular diffusion term are generally modelled as

$$\overline{\rho D\frac{\partial Y_k}{\partial x_i}} \approx \overline{\rho}\,\overline{D}\frac{\partial \widetilde{Y_k}}{\partial x_i}, \tag{5.28}$$

$$\overline{\rho D\frac{\partial h}{\partial x_i}} \approx \overline{\rho}\,\overline{D}\frac{\partial \widetilde{h}}{\partial x_i}. \tag{5.29}$$

The mean reaction rates $\overline{\dot{\omega}}_k$ in species balance equations can be modelled using different combustion models. The reader is referred to references (Poinsot and Veynante, 2012; Peters, 2004). For the closure models for the radiative source term, the reader is referred to (Coelho, 2007). The closures used in this work are presented in Section 5.5 and 5.6.

## 5.3. LARGE EDDY SIMULATION

### 5.3.1. FILTERED GOVERNING EQUATIONS

In LES, the large turbulent scales are resolved whereas the smaller ones are modelled using subgrid models. Spatial filtering is employed in LES to separate the resolved large scales from the unresolved small scales. Filtering of the balance equations leads to equations similar in form to the Reynolds averaged balance equations.

Mass:

$$\frac{\partial \overline{\rho}}{\partial t} + \frac{\partial}{\partial x_i}\left(\overline{\rho}\widetilde{u_i}\right) = 0, \tag{5.30}$$

Momentum:

$$\frac{\partial \overline{\rho}\widetilde{u_j}}{\partial t} + \frac{\partial}{\partial x_i}\left(\overline{\rho}\widetilde{u_i}\widetilde{u_j}\right) = -\frac{\partial \overline{p}}{\partial x_j} + \frac{\partial}{\partial x_i}\left[\overline{\tau}_{ij} - \overline{\rho}\left(\widetilde{u_i u_j} - \widetilde{u_i}\widetilde{u_j}\right)\right], \tag{5.31}$$

Species:

$$\frac{\partial \overline{\rho}\widetilde{Y_k}}{\partial t}+\frac{\partial}{\partial x_i}\left(\overline{\rho}\widetilde{u_i}\widetilde{Y_k}\right)=\frac{\partial}{\partial x_i}\left[\overline{\rho D\frac{\partial Y_k}{\partial x_i}}-\overline{\rho}\left(\widetilde{u_iY_k}-\widetilde{u_i}\widetilde{Y_k}\right)\right]+\overline{\dot{\omega}}_k,\quad k=1,\cdots,N, \tag{5.32}$$

Enthalpy:

$$\frac{\partial \overline{\rho}\widetilde{h}}{\partial t}+\frac{\partial}{\partial x_i}\left(\overline{\rho}\widetilde{u_i}\widetilde{h}\right)=\frac{\partial}{\partial x_i}\left[\overline{\rho D\frac{\partial h}{\partial x_i}}-\overline{\rho}\left(\widetilde{u_ih}-\widetilde{u_i}\widetilde{h}\right)\right]+\overline{S}_r. \tag{5.33}$$

The subgrid scale (SGS) fluxes $\overline{\rho}\left(\widetilde{u_iY_k}-\widetilde{u_i}\widetilde{Y_k}\right)$ and $\overline{\rho}\left(\widetilde{u_ih}-\widetilde{u_i}\widetilde{h}\right)$ are unresolved and can be closed in a similar way as in RANS using the gradient diffusion assumption. Laminar diffusion fluxes can also be modelled similarly as in RANS. The unclosed unresolved Reynolds stresses $\overline{\rho}\left(\widetilde{u_iu_j}-\widetilde{u_i}\widetilde{u_j}\right)$ will be discussed in the following section.

### 5.3.2. CLOSURE FOR SGS STRESSES

For density variable flows, the Favre filtered subgrid-scale stresses $R_{ij}$ in LES are modelled based on the Boussinesq assumption:

$$R_{ij}=\overline{\rho}\left(\widetilde{u_iu_j}-\widetilde{u_i}\widetilde{u_j}\right)=-2\mu_{sgs}\left(\widetilde{S}_{ij}+\frac{1}{3}\widetilde{S}_{kk}\right)+\frac{1}{3}R_{kk}\delta_{ij}, \tag{5.34}$$

where $\mu_{sgs}$ is the SGS viscosity.

#### SMAGORINSKY MODEL

The Smagorinsky model was first proposed by Smagorinsky (Smagorinsky, 1963). In the this model, the subgrid viscosity is modelled by

$$\mu_{sgs}=\overline{\rho}\left(C_S\Delta\right)^2\left(2\widetilde{S}_{ij}\widetilde{S}_{ij}\right)^{1/2}, \tag{5.35}$$

where $\Delta$ is the local grid scale and $C_S$ is the model constant called the Smagorinsky model constant. It is not a universal constant and it is flow dependent, with different values typically in the range $C_S$=0.05~0.25 (Lilly, 1966; Deardorff, 1970; Piomelli et al., 1988). This is the most serious shortcoming of this simple model.

#### DYNAMIC SMAGORINSKY MODEL

To improve the performance of Smagorinsky model, Germano et al. (Germano et al., 1991) proposed a procedure in which the Smagorinsky model constant $C_S$ is dynamically computed based on the information provided by the resolved scales of motion.

The basic idea of the dynamic procedure is to apply a second filter (called the test filter) to the equations of motion. The new filter size is larger than the grid filter size. Both filters produce a resolved flow field. The difference between the two resolved fields is the contribution of the small scales whose size is between the grid filter size and the test filter size. The information related to these scales is used to compute the model constant. For detailed derivation and formulations, the readers are referred to reference (Germano et al., 1991; Moin et al., 1998; Pino Martín et al., 2000).

### 5.3.3. CLOSURE FOR SCALAR FLUXES

The SGS scalar fluxes are usually modelled using the gradient diffusion assumption.

$$\overline{\rho}\left(\widetilde{u_i Y_k} - \widetilde{u_i}\widetilde{Y_k}\right) = -\frac{\mu_{sgs}}{Sc_{sgs}}\frac{\partial \widetilde{Y_k}}{\partial x_i}, \tag{5.36}$$

$$\overline{\rho}\left(\widetilde{u_i h} - \widetilde{u_i}\widetilde{h}\right) = -\frac{\mu_{sgs}}{Pr_{sgs}}\frac{\partial \widetilde{h}}{\partial x_i}, \tag{5.37}$$

where $Sc_{sgs}$ and $Pr_{sgs}$ represent subgrid Schmidt and Prandtl number respectively. They are normally set as a constant near unity.

## 5.4. COMBUSTION MODELLING

In both RANS and LES, the reaction source terms in Equations (5.17) and (5.32) have to be closed with combustion models. There are combustion models available for handling this issue, e.g. finite rate model, eddy dissipation model (EDM) and eddy dissipation concept (EDC) model. In order to have a good prediction of flame structure, using a detailed reaction mechanism is preferred. However, the computational cost increases significantly when transport equations for many reacting species are used, for example incorporating with EDC model. The flamelet model (Peters, 1984) and its extension provides a closure that handle detailed chemistry at acceptable cost.



### 5.4.1. FLAMELET AND FGM MODEL

The turbulent diffusion flame can be viewed as consisting of an ensemble of stretched laminar flames also called flamelets. Mixture fraction $Z$ is a very important quantity for the description of non-premixed combustion. It is defined as the local mass fraction of mass originating from the fuel stream in the mixture, that is, in fuel stream $Z = 1$ and $Z = 0$ in oxidizer stream. The local flame structure in a laminar counterflow diffusion flame configuration only depends on time and mixture fraction, and can be calculated using the flamelet equations given below:

$$\rho\frac{\partial \Phi}{\partial t} = \dot{\omega}_\Phi + \frac{1}{2}\rho\chi\frac{\partial^2 \Phi}{\partial Z^2}, \tag{5.38}$$

where $\Phi$ represents species $Y_k$ and temperature $T$. The scalar dissipation rate $\chi$ is defined by:

$$\chi = 2D\left(\frac{\partial Z}{\partial x_i}\frac{\partial Z}{\partial x_i}\right). \tag{5.39}$$

Here $D$ is the diffusion coefficient that in this formulation is assumed to be the same for all species. For steady flamelet approximation, Equation (5.38) becomes

$$-\frac{1}{2}\rho\chi\frac{\partial^2 \Phi}{\partial Z^2} = \dot{\omega}_\Phi. \tag{5.40}$$

The above flamelet equations can be entirely solved in mixture fraction space with the knowledge of $\chi$. Different scalar dissipation rates result in different flame structures.

Scalar dissipation rate quantifies the departure from equilibrium. The flame structure in turbulent flames can be retrieved from laminar flamelets by specifying mixture fraction and scalar dissipation rate. The scalar dissipation rate at stoichiometric condition, $\chi_{st}$, is normally used together with mixture fraction, $Z$, to characterize a flamelet

$$\Phi = \Phi\left(Z, \chi_{st}\right). \tag{5.41}$$

Therefore, one only needs to find the value of $Z$ and $\chi_{st}$ in the simulation instead of solving individual species transport equations. Species and temperature can be retrieved from the flamelets library. Influence of turbulence on the flame structure can be determined from the joint probability density function (PDF) of $Z$ and $\chi_{st}$

$$\widetilde{\Phi} = \int_0^{+\infty} \int_0^1 \Phi(Z, \chi_{st}) \widetilde{p}(Z, \chi_{st}) dZ d\chi_{st}, \tag{5.42}$$

where $\widetilde{p}(Z, \chi_{st})$ is the joint PDF of $Z$ and $\chi_{st}$. The mean density, $\overline{\rho}$, is also of interest. One can take the Favre average of $\rho^{-1}$ to obtain it:

$$\widetilde{\rho^{-1}} = \frac{1}{\overline{\rho}} = \int_0^{+\infty} \int_0^1 \frac{1}{\rho} \widetilde{p}(Z, \chi_{st}) dZ d\chi_{st}. \tag{5.43}$$

Mixture fraction and scalar dissipation rate are often assumed statistically independent

$$\widetilde{p}(Z, \chi_{st}) = \widetilde{p}(Z)\widetilde{p}(\chi_{st}) \tag{5.44}$$

Flamelet Generated Manifolds (FGM) (van Oijen and de Goey, 2000) method or Flamelet Progress Variable (FPV) (Pierce and Moin, 2004) approach is conceptually very similar to flamelet model in the sense that local flame structure can be obtained from precalculated laminar flames library. To fully describe the flamelet structure, a progress variable $Y_c$ is introduced in FGM approach. The reaction progress can be described by a scaled progress variable $C$ from 0 in the unburnt gas to 1 in the fully burnt gas. $Y_c$ is normally defined as a combination of mass fractions of typical products, e.g. $CO_2$ and CO, and the relation between $Y_c$ and $C$ is as follows:

$$C = \frac{Y_c - Y_c^u}{Y_c^b - Y_c^u}, \tag{5.45}$$

where $Y_c^u$ and $Y_c^b$ are the progress variable in unburnt state and burnt state respectively. They are both functions of mixture fraction. The progress variable $Y_c$ can be solved by its transport equation.

In this thesis, laminar flamelets are computed using the CHEM1D code developed in Eindhoven University of Technology. The laminar diffusion counterflow flame configuration is used to generate a flamelets library, as shown in Figure 5.1. In CHEM1D, the corresponding flames are first solved in physical space and then transformed to mixture fraction space, which is different from Equation (5.38). In this way, different diffusion coefficients of species can be taken into account.

Similarly, with the joint PDF for both mixture fraction and scaled progress variable, species and temperature at local flame structure are retrieved from the FGM library. Although $Y_c$ depends on mixture fraction, $C$ can be assumed statistically independent of

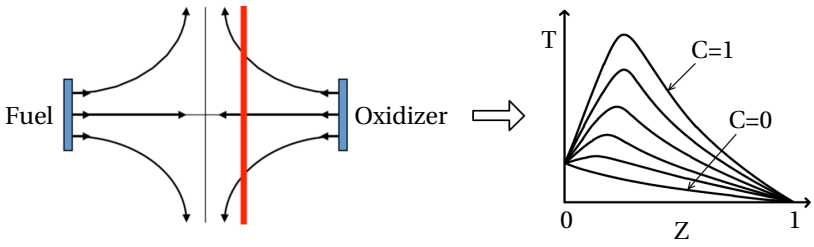


**Figure 5.1:** Laminar diffusion counter flow flame (left) and generated flamelets library (right).

mixture fraction, and a mean value can be calculated using

$$\widetilde{\Phi} = \int_0^1 \int_0^1 \Phi(Z,C)\widetilde{p}(Z,C)dZdC = \int_0^1 \int_0^1 \Phi(Z,C)\widetilde{p}(Z)\widetilde{p}(C)dZdC. \tag{5.46}$$

### 5.4.2. PRESUMED PDF SHAPE METHOD



The influence of turbulence on combustion is accounted for presuming a certain shape for the PDFs of mixture fraction and scaled progress variable distributions. The $\beta$-function based on $\widetilde{Z}$ and $\widetilde{Z''^2}$ is widely used for mixture fraction distribution (Janicka and Peters, 1982; Girimaji, 1992). The $\delta$-function was used for $C$ in the Ref. (Pierce and Moin, 2004). Ihme and Pitsch (2008b) commented that this model was mainly developed for applications to stably burning flame configurations without strong turbulence/chemistry interaction, for which a $\delta$-function as presumed PDF for $C$ gave good results. For the distribution of a reactive scalar has frequently been modelled by a $\beta$ distribution (Cha and Pitsch, 2002; Ihme et al., 2005). There are also other methods to evaluate the joint PDF for $Z$ and $C$, e.g. the statistically most likely distribution (SMLD) model (Ihme and Pitsch, 2008a; Coclite et al., 2015), the top-hat distribution (only in LES) (Floyd et al., 2009; Olbricht et al., 2010, 2012) and transported PDF methods (Avdić et al., 2016). Since the $\beta$-PDF is the most widely used method, in this thesis, mixture fraction $Z$ will be assumed to have a PDF which is a $\beta$-function, and the PDF for $C$ will be assumed to be a $\delta$-function or $\beta$-function. Determination of the parameters in $\beta$-function requires the values of mean and variance. Using the gradient diffusion assumption, the averaged/filtered transport equations for mixture fraction and progress variable in RANS/LES can be written as

$$\frac{\partial \overline{\rho}\widetilde{Z}}{\partial t} + \frac{\partial}{\partial x_i}\left(\overline{\rho}\widetilde{u_i}\widetilde{Z}\right) = \frac{\partial}{\partial x_i}\left[\overline{\rho}\left(\overline{D} + D_t\right)\frac{\partial \widetilde{Z}}{\partial x_i}\right], \tag{5.47}$$

$$\frac{\partial \overline{\rho}\widetilde{Y_c}}{\partial t} + \frac{\partial}{\partial x_i}\left(\overline{\rho}\widetilde{u_i}\widetilde{Y_c}\right) = \frac{\partial}{\partial x_i}\left[\overline{\rho}\left(\overline{D} + D_t\right)\frac{\partial \widetilde{Y_c}}{\partial x_i}\right] + \overline{\dot{\omega}}_{Y_c}, \tag{5.48}$$

where the source term $\overline{\dot{\omega}}_{Y_c}$ in the progress variable transport equation is also tabulated in the FGM library. The diffusion coefficient $D$ is modelled as

$$\overline{\rho}\overline{D} = \frac{\mu}{Sc}, \tag{5.49}$$

and $D_t$ in RANS and LES can be respectively written as:

$$\overline{\rho} D_t = \frac{\mu_t}{Sc_t}, \tag{5.50}$$

and

$$\overline{\rho} D_t = \frac{\mu_{sgs}}{Sc_{sgs}}, \tag{5.51}$$

where $\mu$ is the laminar viscosity, and $\mu_t$ and $\mu_{sgs}$ are respectively turbulent viscosity and subgrid scale viscosity; $Sc$ is the laminar Schmidt number, and $Sc_t$ and $Sc_{sgs}$ are respectively the turbulent Schmidt number and the subgrid scale Schmidt number. Here it is assumed that mixture fraction and progress variable have the same Schmidt number.

The mean value of scaled progress variable, $\widetilde{C}$, is obtained with $\widetilde{Y_c}$

$$\widetilde{C} = \frac{\widetilde{Y_c} - \widetilde{Y_c^u}}{\widetilde{Y_c^b} - \widetilde{Y_c^u}}. \tag{5.52}$$

The transport equations for mixture fraction and progress variable variances used in this thesis are written as follows:

$$\frac{\partial \overline{\rho}\widetilde{Z''^2}}{\partial t} + \frac{\partial}{\partial x_i}\left(\overline{\rho}\widetilde{u_i}\widetilde{Z''^2}\right) = \frac{\partial}{\partial x_i}\left[\overline{\rho}\left(\widetilde{D} + D_t\right)\frac{\partial \widetilde{Z''^2}}{\partial x_i}\right] + 2\overline{\rho} D_t \left(\frac{\partial \widetilde{Z}}{\partial x_i}\right)^2 - \overline{\rho}\widetilde{\chi}_Z, \tag{5.53}$$

$$\begin{aligned}\frac{\partial \overline{\rho}\widetilde{Y_c''^2}}{\partial t} + \frac{\partial}{\partial x_i}\left(\overline{\rho}\widetilde{u_i}\widetilde{Y_c''^2}\right) = \frac{\partial}{\partial x_i}\left[\overline{\rho}\left(\widetilde{D} + D_t\right)\frac{\partial \widetilde{Y_c''^2}}{\partial x_i}\right] + 2\overline{\rho} D_t \left(\frac{\partial \widetilde{Y_c}}{\partial x_i}\right)^2 - \overline{\rho}\widetilde{\chi}_{Y_c} \\ + 2\left(\overline{Y_c \dot{\omega}_{Y_c}} - \widetilde{Y_c}\overline{\dot{\omega}}_{Y_c}\right).\end{aligned} \tag{5.54}$$

The turbulent scalar dissipation rate for mixture fraction and progress variable variance, $\overline{\rho}\widetilde{\chi}_Z$ and $\overline{\rho}\widetilde{\chi}_{Y_c}$ in Equations (5.53) and (5.54), will be discussed in Chapter 6. And the conversion from $\widetilde{Y_c''^2}$ to $\widetilde{C''^2}$ follows the formula below:

$$\widetilde{C''^2} = \frac{\widetilde{Y_c''^2} - \left(\widetilde{Y_c}\right)^2 - \widetilde{\left(Y_c^u\right)^2} - 2\widetilde{C}\left[\widetilde{Y_c^u Y_c^b} - \widetilde{\left(Y_c^u\right)^2}\right]}{\left(\widetilde{Y_c^b} - \widetilde{Y_c^u}\right)^2} - \widetilde{C}^2, \tag{5.55}$$

where $\left(\widetilde{Y_c}\right)^2$, $\widetilde{\left(Y_c^u\right)^2}$ and $\widetilde{Y_c^u Y_c^b}$ are pre-integrated and tabulated as functions of mean mixture fraction $\widetilde{Z}$ and its variance $\widetilde{Z''^2}$ (Albrecht et al., 2008; van Oijen et al., 2016).

With mean values and variances for mixture fraction, the corresponding PDF can be calculated as

$$\widetilde{p}(Z) = \frac{1}{B(a,b)} Z^{a-1}(1-Z)^{b-1} = \frac{\Gamma(a+b)}{\Gamma(a)\Gamma(b)} Z^{a-1}(1-Z)^{b-1}, \tag{5.56}$$

where $B(a,b)$ and $\Gamma$ function are respectively defined as

$$B(a,b) = \int_0^1 Z^{a-1}(1-Z)^{b-1}\, dZ, \tag{5.57}$$

$$\Gamma(x) = \int_0^{+\infty} e^{-t} t^{x-1} dt. \tag{5.58}$$

The PDF parameters $a$ and $b$ are determined by

$$a = \widetilde{Z}\left[\frac{\widetilde{Z}\left(1-\widetilde{Z}\right)}{\widetilde{Z''^2}} - 1\right], \quad b = \frac{a}{\widetilde{Z}} - a. \tag{5.59}$$

The PDF for scaled progress variable is also calculated in the same way.

In practice, to simplify the table construction, the variances of mixture fraction and scaled progress variable are normally scaled using following expressions:

$$S_Z = \frac{\widetilde{Z''^2}}{\widetilde{Z}(1-\widetilde{Z})}, \tag{5.60}$$

$$S_C = \frac{\widetilde{C''^2}}{\widetilde{C}(1-\widetilde{C})}. \tag{5.61}$$

Therefore, mean values are stored in a four-dimensional flamelets library

$$\widetilde{\Phi} = \Phi\left(\widetilde{Z}, S_Z, \widetilde{C}, S_C\right). \tag{5.62}$$



### 5.4.3. NON-ADIABATIC CONSIDERATION

The flamelets library generation discussed in the previous section is for adiabatic cases. The enthalpy is linearly related to the mixture fraction. However, enthalpy loss exists due to heat transfer through furnace walls and radiative heat loss. In the non-adiabatic cases, the non-adiabatic effects on the flames structures should be taken into account in flamelets library generation. The enthalpy becomes one more independent control parameter for the flamelets library, and the flamelets library needs to be extended.

Bray and Peters (Bray and Peters, 1994), Giordano et al. (Giordano and Lentini, 2001) and Marracino et al. (Marracino and Lentini, 1997) have suggested solving a transport equation for enthalpy with radiation source term.

$$\frac{\partial \overline{\rho}\widetilde{h}}{\partial t} + \frac{\partial}{\partial x_i}\left(\overline{\rho}\widetilde{u_i}\widetilde{h}\right) = \frac{\partial}{\partial x_i}\left(\alpha_{eff}\frac{\partial \widetilde{h}}{\partial x_i}\right) + \overline{S}_r, \tag{5.63}$$

where the effective thermal diffusivity $\alpha_{eff}$ in RANS and LES can be respectively written as

$$\alpha_{eff} = \frac{\lambda}{c_p} + \frac{\mu_t}{Pr_t}, \tag{5.64}$$

and

$$\alpha_{eff} = \frac{\lambda}{c_p} + \frac{\mu_{sgs}}{Pr_{sgs}}. \tag{5.65}$$

The source term $\overline{S}_r$ for enthalpy is calculated by a radiation model but is unclosed. Its closure will be addressed in Section 5.6.

A new parameter called "enthalpy loss factor", $\eta$, is introduced to characterize the flamelet structure with non-adiabatic effects. The enthalpy loss is

$$\Delta h = h - h_{ad}, \tag{5.66}$$

where $h_{ad}$ is the adiabatic enthalpy which is linearly related to the mixture fraction. The enthalpy loss factor is given by

$$\eta = \frac{\Delta h}{h_{min} - h_{ad}}, \tag{5.67}$$

where $h_{min}$ is the enthalpy which corresponds to the maximum enthalpy loss in flamelets generation.

In this thesis, a statistical independence between the three parameters ($Z$, $C$, and $\eta$) has been assumed and a presumed PDF approach has been adopted. A $\delta$-function has been assumed for enthalpy loss, which means that the fluctuations are neglected, $\widetilde{\eta} \equiv \eta$. Therefore, the mean values depend on five parameters

$$\widetilde{\Phi} = \Phi\left(\widetilde{Z}, S_Z, \widetilde{C}, S_C, \widetilde{\eta}\right). \tag{5.68}$$

There are three types of methods that can be used to couple non-adiabatic effects in flamelets library. "Type 1", freezing the species in adiabatic flamelets, temperature is re-calculated with the enthalpy, as done in ANSYS Fluent (ANSYS, 2015). "Type 2", The temperature at flamelet boundaries are reduced according to certain enthalpy loss levels and a set of flamelets are calculated. The combined flamelets form the non-adiabatic library (Marracino and Lentini, 1997). "Type 3", solving flamelet equations with source term taking into account the heat loss (Stöllinger and Roekaerts, 2013; Frank and Pfitzner, 2015). In this thesis, the second method is adopted for flamelets library generation.

## 5.5. DILUTED AIR FGM (DAFGM) MODEL

### 5.5.1. APPLICATION BACKGROUND

The combustion in a furnace can be considered as a three-stream problem, with combustible mixture consisting of fuel, air and recirculated flue gas. Flamelets based on only fuel and air as inflow do not take into account the dilution effects by burnt gas on the chemical reactions. But these effects can be relevant. Figure 5.2 shows the effect of dilution on fuel consumption and product formation at different dilution levels when burning Dutch natural gas in a counterflow flame between fuel and diluted air. It can be seen that although reactants and products for large $Y_c$ converge to the final near equilibrium state, fuel consumption and products formation both follow different reaction paths at different dilution levels. Moreover, the source term of progress variable $Y_c$ in Figure 5.2 differs significantly at a fixed mixture fraction, e.g. $Z_{st}$. This means flame structures are different at different dilution conditions. Therefore, dilution effects have to be taken into account in flameless combustion. The standard FGM model only tabulates reactions based on pure fuel and oxidizer in laminar diffusion counterflow flames, that is, the profiles at $\gamma = 0$. These flame structures do not well represent the flames in flameless condition where reactants are diluted by recirculated burnt gas.

### 5.5.2. FLAMELETS LIBRARY WITH DILUTION

The dilution effects on the flamelets were studied in the Ref. (Abtahizadeh et al., 2012). The dilution level has been found as a dominant parameter to control chemical effects using the laminar counterflow flame configuration using both fuel and air diluted and preheated, or either fuel or air diluted and preheated by burnt gas. To account for the

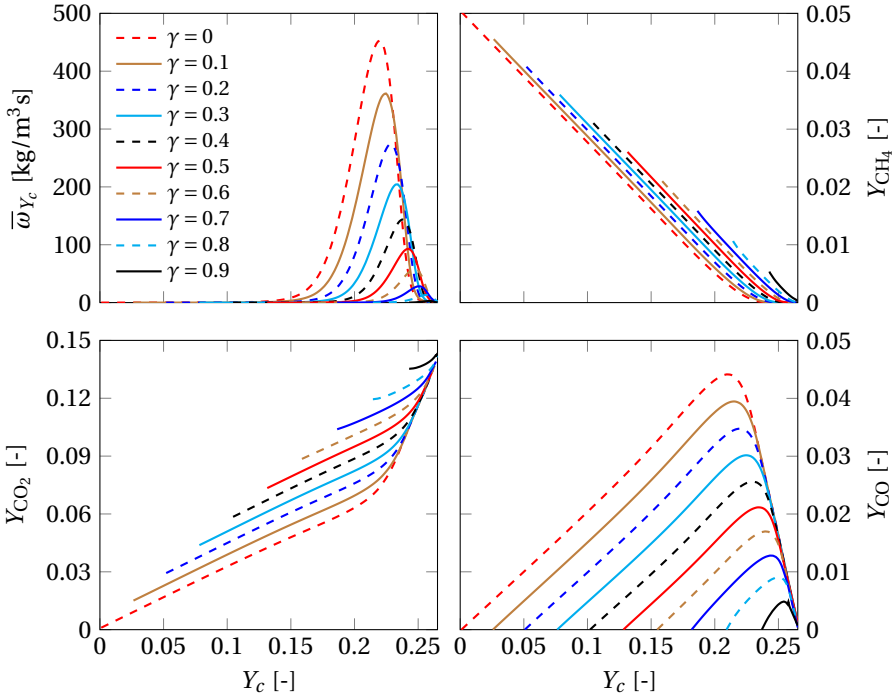


**Figure 5.2:** Properties of counterflow flame of fuel and diluted air at stoichiometric mixture fraction $Z_{st}$. The results are calculated with fuel at 430 K, air at 293 K, and burnt gas at 1564 K. The source term of $Y_c$, mass fraction of $CH_4$, $CO_2$ and CO are plotted as functions of progress variable $Y_c$. The $\gamma$ in the figure denotes the mass fraction of burnt gas at stoichiometric mixture fraction in oxidizer (diluted air).

dilution effects of recirculated burnt gas in a numerical simulation, it is important to determine locally how much diluent (dilution level, that is, the mass fraction of diluent) is present in the reactive mixture. A dilution variable is then used for this purpose (Lamouroux et al., 2014; Locci et al., 2014, 2015). Lamouroux et al. proposed a tabulated chemistry model to account for dilution and heat loss effects. The library was generated by laminar counterflow flames using diluted fuel and diluted air. Locci et al. used diluted homogeneous reactors to capture the autoignition trajectories triggered by the dilution at different dilution levels and enthalpy losses. In the case of homogeneous reactor, residence time is playing a role similar to (instead of) scalar dissipation rate in a counterflow flame. In order to account for the three-stream mixing that occurs between air, fuel and burnt gas, a two-dimensional flamelet equation was proposed by Colin and Michel (Colin and Michel, 2016). The enthalpy loss is included in the model as a supplementary parameter, because enthalpy loss in burnt gas has a crucial impact on the mixture reactivity.

Here we give a brief comparison between the methods in the Ref. (Lamouroux et al., 2014) and Ref. (Locci et al., 2014, 2015). There are two remarkable differences in these

studies. The first difference is the way to determine the dilution level. In the Ref. (Lamouroux et al., 2014), a transport equation for a dilution variable $Y_d = Y_{CO_2} + Y_{CO}$ is solved to obtain the evolution of diluent stream. The dilution level is equal to the ratio $Y_d / Y_d^{Dil}$, where $Y_d^{Dil}$ is the dilution variable in the pure diluent stream. Whereas, in the Ref. (Locci et al., 2014, 2015), the dilution level is divided into non-reactive and reactive parts. In non-reactive part it is directly deduced from progress variable and in reactive part it is set to a critical dilution level representing all reactive trajectories. They also suggest solving a transport equation for the mean dilution level, which can be more accurately representing the local dilution levels and the effects of different dilution levels on the reactions can be represented locally. The second difference is the way to generate the lookup tables. The library in the Ref. (Lamouroux et al., 2014) is generated by laminar counterflow flames using the diluted fuel and the diluted air. Locci et al. (2014; 2015) used the diluted homogeneous reactors (DHR) to capture the autoignition trajectories as a function of mixture fraction, temperature, dilution level, progress variable and enthalpy loss. However the DHR does not include the convective and diffusive effects in the flow.



The common point in the above methods is that the diluent stream is defined as the burnt gas at global equivalence ratio determined by the furnace operation. However, we conclude that this is not a good option for furnace operating at lean conditions ($\phi < 1$). Two reasons can be given for this. Firstly, the fuel may react with the hot air left in the burnt gas immediately before it mixes with the fresh air stream in a furnace operating at $\phi < 1$. In the tabulation method in the Ref. (Lamouroux et al., 2014), both the fuel and the air are diluted. The fuel and the air are first mixed with diluent. The mass fractions of the diluent in the diluted fuel and the diluted air are the same. The flamelets library is generated using the diluted fuel and the diluted air. In this way, only the mixing state between fuel and diluent is tabulated in the table. The reactions between the fuel and the air left in the recirculated burnt gas are not included. Moreover, the mixing and reacting states between the fuel and a mixture in which the oxygen mass fraction is lower than that in burnt gas are not included in the library, either.

In order to avoid the above mentioned problems, a new chemistry tabulation method is proposed in this thesis. The physical problem in the furnace is treated as fuel is injected into to an environment of diluted oxidizer. The dilution condition varies in the furnace due to internal recirculation. Taking the advantages in the above methods, a transport equation is also solved for a dilution variable to account for the dilution levels. The flamelets library is also generated by laminar counterflow flames using the fuel and the air at different dilution levels to cover the states at all dilution levels. Air dilution level becomes one controlling dimension in the final library. The details of the proposed method are as follows.

#### DEFINITION OF DILUENT

The local instantaneous gas mixture in the furnace giving rise to a flame is treated as a mixture of fuel, air and burnt gas. A schematic of representative mixture components is shown in Figure 5.3(a). For a furnace operating at complete reaction condition or global equivalence ratio $\phi = 1$, the burnt gas recirculated to reaction zone is the products at stoichiometric mixture fraction $Z_{st}$ corresponding to chemical equilibrium due to long

residence time in the furnace. In this case, there is no excess air left in the burnt gas. The burnt gas is actually the diluent. However, when a furnace is operating at lean condition or global equivalence ratio $\phi < 1$, excess air is left in the burnt gas and can take part in reactions later. Therefore, the burnt gas at $\phi < 1$ is not only diluent, but also contains oxidizer. It is reasonable to consider the burnt gas as a mixture of excess air and the products at stoichiometric mixture fraction $Z_{st}$. That is, the products at $Z_{st}$ are defined to be the diluent.

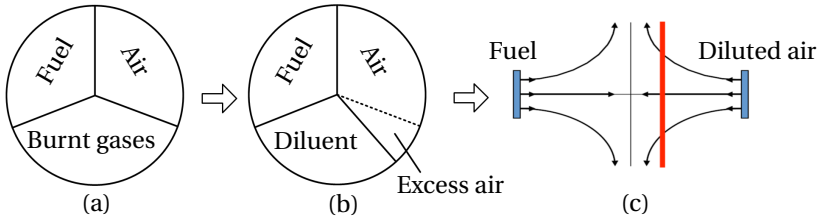


**Figure 5.3:** Schematic of representative mixture components in the furnace with strong internal recirculation. (a) and (b) illustrate the definition of diluent; (c) illustrate the addition of diluent in a counterflow flame configuration.



#### WHERE TO ADD DILUENT

In this way, the "mixture before reaction" is then divided into three parts, fuel, air (fresh air + excess air) and diluent, as shown in the schematic in Figure 5.3(b). As mentioned earlier, the basic concept is to treat the reactions in the mixture as fuel reacts with diluted air. A second mixture fraction $\xi$ based on pure fuel and diluted air is introduced to describe the mixing between fuel and diluted air. An air dilution level $\gamma$ is used to measure the mass fraction of diluent in the diluted air. Therefore, flamelets are calculated using the laminar diffusion counterflow configuration in Figure 5.3(c) with the following boundaries:

$$\Phi(\xi = 1) = \Phi_f, \tag{5.69}$$

$$\Phi(\xi = 0) = \Phi_{ox}(\gamma), \tag{5.70}$$

where $\Phi_f$ and $\Phi_{ox}$ are respectively pure fuel state and diluted air state. The FGM library now becomes three-dimensional, namely the mean properties are depending on $\xi$, $C$ and $\gamma$:

$$\Phi = \Phi(\xi, C, \gamma). \tag{5.71}$$

Determination of air dilution level $\gamma$ will be addressed in the Section 5.5.4.

### 5.5.3. NON-ADIABATIC FLAMELETS LIBRARY WITH DILUTION

To take into account enthalpy loss effects, enthalpy loss is introduced in the diluent. That is, air is diluted by an amount of burnt gas at $Z_{st}$ with enthalpy loss $dh$. This $dh$ includes both enthalpy loss due to radiation and heat transfer to the cold walls. Since diluent is only present in air side, enthalpy loss is only imposed on the diluted air side

when computing flamelets using laminar counterflow flames. Boundary conditions for counterflow flamelets now read:

$$\Phi(\xi = 1) = \Phi_f, \tag{5.72}$$

$$\Phi(\xi = 0) = \Phi_{ox}(\eta, \gamma), \tag{5.73}$$

where $\eta$ is the normalized enthalpy loss, $\eta = 0$ and $\eta = 1$ corresponding respectively to minimum and maximum enthalpy loss. The thermochemical state-space can be written as

$$\Phi = \Phi(\xi, C, \eta, \gamma). \tag{5.74}$$

Determination of air enthalpy loss factor $\eta$ will be described in the Section 5.5.4.

### 5.5.4. LOOKUP PROCEDURE

When dilution effects and enthalpy loss are taken into account, the tabulated library becomes four-dimensional. Controlling parameters, $\xi$, $C$, $\eta$ and $\gamma$ must be determined for table lookup. They are not solved immediately from transport equations, but can be derived from other variables. It is noted that the control parameters, $\xi$, $C$, $\eta$ and $\gamma$ are all related to dilution conditions. Therefore, the first step is to find out how much diluent is present in the local mixture, that is, to find out the value of the dilution level $\alpha$ which represents the mass fraction of the diluent in the mixture.

#### DETERMINATION OF DILUTION LEVEL $\alpha$

An additional scalar, namely dilution variable $Y_d$, defined as a combination of typical species in the diluent stream, e.g. $Y_d = Y_{CO_2} + Y_{H_2O}$, is introduced here to find out the dilution level $\alpha$. The relation between $Y_d$ and $\alpha$ is given by

$$\alpha = \frac{Y_d}{Y_d^{Dil}}, \tag{5.75}$$

where $Y_d^{Dil}$ is the dilution variable in diluent which is the burnt gas at stoichiometric mixture fraction $Z_{st}$.

The dilution variable $Y_d$ is solved by one additional transport equation, for example in RANS simulation.

$$\frac{\partial \overline{\rho}\widetilde{Y_d}}{\partial t} + \frac{\partial}{\partial x_i}\left(\overline{\rho}\widetilde{u_i}\widetilde{Y_d}\right) = \frac{\partial}{\partial x_i}\left[\overline{\rho}\left(\widetilde{D} + D_t\right)\frac{\partial \widetilde{Y_d}}{\partial x_i}\right] + \overline{\dot{\omega}}_{Y_d}. \tag{5.76}$$

The source term of dilution variable used in this study is as follows:

$$\overline{\dot{\omega}}_{Y_d} = \frac{1}{\Delta t}\overline{\rho}\left(\widetilde{Y_d^b} - \widetilde{Y_d}\right) H(\widetilde{C} - 0.99), \tag{5.77}$$

where $\Delta t$ is the simulation time step, $\widetilde{Y_d^b}$ is the mean dilution variable in local burnt gas. Noting that $\widetilde{Y_d^b}$ is related to local mixture fraction, it is also stored in the lookup table with less dimensions, $\widetilde{Y_d^b} = Y_d^b\left(\widetilde{\xi}, S_\xi, \widetilde{\eta}, \widetilde{\gamma}\right)$ at $\widetilde{C} = 1$. The $H$ function is a unit step function which is used to activate the source term only in fully burnt states. The dilution variable is zero at the inlet boundaries and is initially set as zero in the furnace. Its source term $\overline{\dot{\omega}}_{Y_d}$ nearly instantaneously transforms burnt gas into diluent stream when reaction is completed. Here $\widetilde{C} \geqslant 0.99$ is set for this purpose.

### DETERMINATION OF THE SECOND MIXTURE FRACTION $\xi$ AND AIR DILUTION LEVEL $\gamma$

The mass fraction of the fuel and air streams in the mixture is $1-\alpha$. The mixture fraction $Z$ of the local instantaneous gas mixture is then given by

$$Z = (1-\alpha)Z_0 + \alpha Z_{st}, \tag{5.78}$$

Here $Z$, $Z_0$ and $Z_{st}$ ar all mixture fractions based on pure fuel and pure air. Considering a mixture of fuel, air and diluent, $Z_{st}$ is the mixture fraction of the diluent, $Z_0$ is the mixture fraction of fuel-air mixture and $Z$ is the mixture fraction of the total mixture.

The derivations of second mixture fraction $\xi$ and air dilution level $\gamma$ are based on their definitions. Actually $\xi$ represents the mass fraction of the fuel stream in local gas mixture, therefore,

$$\xi = (1-\alpha)Z_0 = Z - \alpha Z_{st}, \tag{5.79}$$

and the mass fraction of diluent in diluted air, that is air dilution level

$$\gamma = \frac{\alpha}{1-\xi} = \frac{\alpha}{1-Z+\alpha Z_{st}}. \tag{5.80}$$



### DETERMINATION OF ENTHALPY LOSS FACTOR $\eta$

Once air dilution level is obtained, enthalpy loss factor $\eta$ can be determined. Enthalpy loss $\Delta h$ is normalized by the maximum tabulated enthalpy loss at local dilution level which results in $\eta$. The local maximum enthalpy is $\gamma(1-\xi)\left(h^d_{\eta=1} - h^d_{\eta=0}\right)$. $\eta$ is therefore expressed as

$$\eta = \frac{\Delta h}{\gamma(1-\xi)\left(h^d_{\eta=1} - h^d_{\eta=0}\right)} = \frac{h - h_{ad}}{\alpha\left(h^d_{\eta=1} - h^d_{\eta=0}\right)}, \tag{5.81}$$

where $h_{ad}$ is the adiabatic enthalpy at local mixture fraction

$$h_{ad} = Z h_f + (1-Z)\, h_{ox}, \tag{5.82}$$

and $h^d_{\eta=1}$ and $h^d_{\eta=0}$ are respectively the enthalpy of diluent with maximum and minimum enthalpy loss. The minimum enthalpy loss usually is zero, and the maximum enthalpy loss has to be specified based on the information of the specific application. To calculate the value of $\eta$, the value of $Z$ (entering $h_{ad}$) and $h$ are needed. The mean value $\widetilde{\eta}$ is obtained by averaging over the PDF of $Z$.

### DETERMINATION OF SCALED PROGRESS VARIABLE $C$

The incoming stream at the oxidizer side consists of diluted air and contains the species taken into account in the definition of the progress variable. Therefore, scaled progress variable $C$ must be determined at each air dilution level and enthalpy loss level. With the information of dilution and enthalpy loss, progress variable is evaluated. Progress variable is defined as the sum of several typical species mass fraction

$$Y_c = \sum_{k=1}^{N_{Y_c}} Y_k. \tag{5.83}$$

The main condition on progress variable definition is that in a flamelet it defines the combustion unambiguously.

In the application worked out in Chapter 6 and 7, the following choice is made

$$Y_c = Y_{CO_2} + Y_{CO} + Y_{H_2O} + Y_{H_2}. \tag{5.84}$$

Scaled progress variable is written as

$$C = \frac{Y_c - Y_c^u(\xi,\eta,\gamma)}{Y_c^b(\xi,\eta,\gamma) - Y_c^u(\xi,\eta,\gamma)}, \tag{5.85}$$

where $Y_c^u$ and $Y_c^b$ are respectively the value of $Y_c$ in unburnt state and burnt state.

### SUMMARY

In summary, four controlling parameters $\xi$, $C$, $\eta$ and $\gamma$ are defined by Equation (5.79), (5.85), (5.81) and (5.80) respectively. With the solutions from the transport equations discussed above

$$\widetilde{\alpha} = \frac{\widetilde{Y_d}}{Y_d^{Dil}}, \tag{5.86}$$

$$\widetilde{\xi} = \widetilde{Z} - \widetilde{\alpha} Z_{st}, \tag{5.87}$$

$$\widetilde{\gamma} = \frac{\widetilde{\alpha}}{1-\widetilde{\xi}}, \tag{5.88}$$

$$\widetilde{\eta} = \frac{\widetilde{h} - \widetilde{h}_{ad}}{\widetilde{\alpha}\left(h^d_{\eta=1} - h^d_{\eta=0}\right)}, \tag{5.89}$$

$$\widetilde{C} = \frac{\widetilde{Y_c} - \widetilde{Y_c^u}}{\widetilde{Y_c^b} - \widetilde{Y_c^u}}. \tag{5.90}$$

The mean quantities in the DAFGM library are then indexed using Equation (5.92), where $S_C$ is also estimated with the quantities at corresponding to air dilution level and enthalpy loss factor. The mean properties can be calculated based on the joint PDF of $\xi$, $C$, $\eta$ and $\gamma$, and it is assumed that they are statistically independent:

$$\tilde{\Phi} = \int_0^1\int_0^1\int_0^1\int_0^1 \Phi(\xi,C,\eta,\gamma)\widetilde{P}(\xi)\widetilde{P}(C)\widetilde{P}(\eta)\widetilde{P}(\gamma)d\xi dC d\eta d\gamma. \tag{5.91}$$

Presuming $\beta$ PDF for $\xi$ and $C$, $\delta$ PDF for $\eta$ and $\gamma$, a six-dimensional library is constructed in which

$$\widetilde{\Phi} = \Phi\left(\widetilde{\xi}, S_\xi, \widetilde{C}, S_C, \widetilde{\eta}, \widetilde{\gamma}\right). \tag{5.92}$$

$S_\xi$ is determined by assuming no fluctuations for $Y_d$, and therefore $\alpha$ is not fluctuating. Using Equations (5.79) and (5.87), the following equations are obtained.

$$\widetilde{\xi''^2} = \widetilde{Z''^2}, \tag{5.93}$$

$$S_\xi = \frac{\widetilde{\xi''^2}}{\widetilde{\xi}(1-\widetilde{\xi})} = \frac{\widetilde{Z''^2}}{(\widetilde{Z} - \widetilde{\alpha} Z_{st})(1 - \widetilde{Z} + \widetilde{\alpha} Z_{st})}. \tag{5.94}$$

$S_C$ can also be determined similarly by using Equations (5.55) and (5.61).

The governing equations are solved by a pressure-based solver developed in OpenFOAM (version 2.3.1). The solver is based on Pressure-Implicit with Splitting of Operators (PISO) pressure-velocity coupling scheme. The transport equations for the independent variables are solved after the velocity prediction, and then the controlling parameters for table lookup are derived.

## 5.6. RADIATION MODELLING

### 5.6.1. TURBULENCE-RADIATION INTERACTION (TRI)

Including radiation effects in combustion modelling is very important to achieve good predictions in combustion systems where radiation heat transfer plays a significant role. In turbulent reacting flows, radiative transfer is influenced by turbulent scalar fluctuations and vice versa (Coelho, 2007). This is so-called TRI. Traditionally, turbulence and radiation are treated independently using mean properties to calculate radiative heat transfer. This may result in very large errors in reactive flows. A better modelling of thermal radiation, taking TRI into account, may improve the prediction of the temperature field, flame structure, and pollutants emission (Coelho, 2012).



The radiation effects in DAFGM model are considered by introducing enthalpy loss. The radiation source term in Equation (5.63) is calculated using the Discrete Ordinate Method (DOM) to solve the radiative transfer equation (RTE). It requires the data exchange between combustion model and radiation model. The scattering effect is negligible in a gas fired furnace, and the RTE for an absorbing, emitting, and non-scattering medium (Modest, 2003) can be used:

$$\frac{\mathrm{d}I_\nu(\mathbf{r},\mathbf{s})}{\mathrm{d}s} = -\kappa_\nu(\mathbf{r})I_\nu(\mathbf{r},\mathbf{s}) + \kappa_\nu(\mathbf{r})I_{b\nu}(\mathbf{r}). \tag{5.95}$$

In the above equation, $I_\nu(\mathbf{r},\mathbf{s})$ is the spectral radiation intensity at point $\mathbf{r}$ and direction $\mathbf{s}$, $I_{b\nu}$ is the spectral blackbody radiation intensity, $\kappa_\nu$ is the spectral absorption coefficient of the medium. In this thesis, the DOM model in OpenFOAM is used for radiation modelling. Each octant of the angular space $4\pi$ at any spatial location is discretized into 2×2 solid angles. Then the RTE in each solid angle direction is solved. A total of 32 directions are solved. The details of DOM will not be presented here. The readers are referred to reference (Fiveland, 1984).

Conservation of radiative energy may be expressed as

$$\nabla\cdot\mathbf{q} = \int_0^{+\infty} \kappa_\nu\left(4\pi I_{b\nu} - G_\nu\right)d\nu = \kappa\left(4\pi I_b - G\right), \tag{5.96}$$

where the second equality only holds in the case of a grey medium. Here, $\mathbf{q}$ is the radiative heat flux vector, and $G$ is the incident radiation given by

$$G = \int_0^{+\infty}\int_{4\pi} I_\nu d\Omega d\nu = \int_{4\pi} I d\Omega. \tag{5.97}$$

The term $-\nabla\cdot\mathbf{q}$ can be directly substituted into the enthalpy Equation (5.63) to account for heat sources (or sinks) due to radiation. In this thesis, the grey gas approximation is

used in the RTE equations but the grey gas absorption coefficient is calculated from a weighted-sum-of-grey-gas (WSGG) model.

In general, turbulent flows are numerically simulated using RANS or LES. Then the time averaged or filtered RTE is required. In a RANS simulation, the time-averaged form of the RTE (Equation (5.95)) for non-scattering media is written as follows

$$\frac{\mathrm{d}\bar{I}_\nu}{\mathrm{d}s} = -\overline{\kappa_\nu I_\nu} + \overline{\kappa_\nu I_{b\nu}}. \tag{5.98}$$

According to the optically thin fluctuation approximation (OTFA) (Kabashnikov and Kmit, 1979), the above equation is simplified as follows

$$\frac{\mathrm{d}\bar{I}_\nu}{\mathrm{d}s} = -\bar{\kappa}_\nu \bar{I}_\nu + \overline{\kappa_\nu I_{b\nu}}, \tag{5.99}$$

which means that the absorption coefficient and intensity are assumed to be statistically uncorrelated. In the above equation, the time-averaged terms $\overline{\kappa_\nu}$ and $\overline{\kappa_\nu I_{b\nu}}$ are affected by species and temperature fluctuations. They cannot be calculated directly by the mean quantities, for the reason that both terms $\kappa$ and $\kappa I_b$ depend non-linearly on species and temperature, e.g.,

$$\overline{\kappa I_b} = \frac{\sigma}{\pi}\overline{\kappa T^4} \neq \frac{\sigma}{\pi}\bar{\kappa}\bar{T}^4. \tag{5.100}$$

The way to account for TRI in RANS based methods to a large extent depends on the combustion and radiation models employed, as well as on the radiative properties model. A comprehensive review of these methods is available (Coelho, 2007). In this thesis a joint PDF used in combustion modelling is also applied for TRI and will be addressed in Section 5.6.3.

In the framework of LES, the RTE equation must be spatially filtered. Notice that the overline in the Equation (5.98) denotes a spatially filtered quantity, rather than a time averaged quantity in the RANS. When performing LES in combustion systems, the subgrid-scale (SGS) TRI effects are normally ignored (Amaya et al., 2010; Paul and Paul, 2010; Poitou et al., 2011; Ghosh and Friedrich, 2015; Ghosh et al., 2015). However, some works addressed on the influence of SGS-TRI have also been done (Coelho, 2009; Chandy et al., 2009; Roger et al., 2010). These works suggest that SGS TRI is less important in LES than TRI in RANS but may be non-negligible at typical temperatures and fluctuation levels found in combustion systems and for filter sizes commonly used in practical simulations (Coelho, 2012). The reader is referred to the above references for more details.

### 5.6.2. ABSORPTION COEFFICIENT

The solution of the time-averaged RTE requires knowledge of the absorption coefficient $\kappa$ of the medium. The Weighted-Sum-of-Grey-Gases (WSGG) model is often used in combustion modelling. The basic assumption of the WSGG model proposed by Hottel and Sarofim (Eckert, 2004) is that the total emissivity $\varepsilon$ over the distance $s$ can be presented as

$$\varepsilon = \sum_{j=0}^{J} a_j \left[1 - \exp\left(-\kappa_j p s\right)\right], \tag{5.101}$$

where $a_j$ denote the emissivity weighting factors for the $j$-th grey gas as based on gas temperature, $T$. $\kappa_j$ is the absorption coefficient for $j$-th grey gas; $p$ is the sum of the partial pressures of the absorbing gases. $s$ is the mean beam length. The absorption coefficient for clear gas $j = 0$ is zero.

In Ansys Fluent, the coefficients values proposed by Smith et al. (1982) and Coppalle and Vervisch (1983) are used. Here, the modified WSGG model with four grey gases and one clear gas is used (J=4). The coefficients proposed by R. Johansson et al. (Johansson et al., 2011) are adopted to account for various ratios of $H_2O$ to $CO_2$ concentrations. Both the absorption coefficients and the weights depend on mole ratio, while only the weights depend on temperature.

$$a_j = \sum_{i=1}^{3} c_{j,i} \left( \frac{T}{T_{ref}} \right)^{i-1}, \quad \text{with} \quad T_{ref} = 1200K, \tag{5.102}$$

$$\kappa_j = K1_j + K2_j \frac{X_{H_2O}}{X_{CO_2}}, \tag{5.103}$$

$$c_{j,i} = C1_{j,i} + C2_{j,i} \frac{X_{H_2O}}{X_{CO_2}} + C3_{j,i} \left( \frac{X_{H_2O}}{X_{CO_2}} \right)^2, \tag{5.104}$$

where $X_{H_2O}$ and $X_{CO_2}$ are mole fraction in the medium. The values for coefficients $K1_j$, $K2_j$, $C1_{j,i}$, $C2_{j,i}$ and $C3_{j,i}$ can be found in reference (Johansson et al., 2011). The weighting factor for the clear gas are given by

$$a_0 = 1 - \sum_{j=1}^{4} a_j, \tag{5.105}$$

and makes the sum of the weights equal to unity. The total absorption coefficient is then estimated by

$$\kappa = -\frac{\ln(1-\varepsilon)}{s}, \tag{5.106}$$

where the mean beam length is computed according to the domain based method recommended by Hottel and Sarofim (Eckert, 2004),

$$s = \frac{3.6V}{A} \tag{5.107}$$

where $V$ is the volume of the domain and $A$ the corresponding surface area.

Due to the non-linear dependency of absorption coefficient and emissivity, this way of calculation of a grey absorption coefficient is not accurate. A possible improvement leading to a more accurate prediction of heat flux and radiative source term would be to solve RTE for each of the grey gases.

### 5.6.3. COUPLING RADIATION WITH COMBUSTION

To calculate the absorption coefficient using the WSGG model discussed above, temperature and mole fractions of $CO_2$ and $H_2O$ are needed as input parameters for the radiation model. Radiation intensity is then solved and radiation source term is calculated. Instead of only storing mean temperature and mean mole fraction for $CO_2$ and

$H_2O$, the mean higher orders of temperature are needed to account for TRI. But including more parameters results in a huge library which requires large amount of memory. An approach to solve this problem is proposed in this section.

The radiation source term in enthalpy equation is computed by DOM. The DOM model requires the solution of the RTE for a number of discrete directions. Using WSGG model for absorption coefficient with the DOM leads to the time-averaged form of the discrete ordinates equations which under the OTFA may be written as follows for non-scattering medium (Coelho, 2007, 2012)

$$\frac{\mathrm{d}\overline{I^m}}{\mathrm{d}s} = -\overline{\kappa}\,\overline{I^m} + \overline{\kappa I_b}, \tag{5.108}$$

where the superscript $m$ stands for one of the directions resulting from the angular discretization, and $I^m$ is the mean radiation intensity for direction $m$.

The mean values of the absorption coefficient and radiative emission required to account for the TRI may be obtained by pre-integrating flamelets values as (Coelho, 2012)

$$\overline{\kappa} = \overline{\rho}\int_0^1\int_0^1\int_0^1\int_0^1 \frac{\kappa(\xi,C,\eta,\gamma)}{\rho(\xi,C,\eta,\gamma)}\widetilde{P}(\xi,C,\eta,\gamma)\,d\xi\,dC\,d\eta\,d\gamma, \tag{5.109}$$

$$\overline{\kappa I_b} = \frac{\overline{\rho}\pi}{\sigma}\int_0^1\int_0^1\int_0^1\int_0^1 \frac{\kappa(\xi,C,\eta,\gamma)T^4(\xi,C,\eta,\gamma)}{\rho(\xi,C,\eta,\gamma)}\widetilde{P}(\xi,C,\eta,\gamma)\,d\xi\,dC\,d\eta\,d\gamma. \tag{5.110}$$

Therefore, only these two additional terms need to be tabulated and not the mean mole fractions and mean powers of temperature. During the simulation, controlling parameters for library lookup are obtained as discussed before, and the above two terms are then retrieved from the library. Finally, the radiation intensities in each discrete ordinate direction are solved and the radiation source term is

$$\nabla\cdot\mathbf{q} = 4\pi\overline{\kappa I_b} - \sum_{m=1}^{M}\omega_m\overline{I^m}, \tag{5.111}$$

where $\omega_m$ is the weight for the $m$th direction. The term $-\nabla\cdot\mathbf{q}$ can be directly substituted into the enthalpy equation accounting for enthalpy loss.

The boundary condition of Equation (5.108) is for the case of a grey, diffuse surface given by (Coelho, 2012)

$$\overline{I}_w = \varepsilon_w\overline{I}_{bw} + \frac{1-\varepsilon_w}{\pi}\sum_{\substack{m=1\\ \mathbf{s}\cdot\mathbf{n}<0}}^{M}\omega_m|\mathbf{s}\cdot\mathbf{n}|\overline{I^m}, \tag{5.112}$$

where $\varepsilon_w$ is the emissivity of the boundary, and $I_{bw}$ is the black body intensity at the temperature of the boundary.

## 5.7. SUMMARY

First, a brief introduction to the modelling approach and basic theories in non-premixed combustion simulation used in the present work was presented in this chapter (Section 5.1~5.4). Next, an extended FGM model referred to as DAFGM model (Section 5.5) was

developed for combustion with dilution effects, e.g. flameless combustion. Finally, a method to couple radiation and turbulence-radiation interaction with DAFGM model was developed (Section 5.6). The data exchange between radiation and combustion and the consideration of turbulence effects on combustion and radiation were explained.

The models developed in this chapter have been implemented in the open source CFD package OpenFOAM-2.3.1. The extensions are made based on the "FGMFoam" developed by Ma (2015, in Chapter 6). The FGM model is replaced by DAFGM model, and a new table lookup scheme was developed that can be used for two- to six-dimensional table lookup and interpolations. This scheme is also easily extended for higher dimensional lookup tables. The value of $\overline{\kappa}$ and $\overline{\kappa I_b}$ needed in the radiation model are also stored in the lookup table.

# 6

# APPLICATION OF THE DAFGM MODEL TO A DELFT-JET-IN-HOT-COFLOW FLAME

*In this chapter, the DAFGM model developed in Chapter 5 is applied to the DJHCI Re=4100 flame studied experimentally at Delft University, which mimics flameless combustion. The flame is produced from a jet of natural gas injected into a coflow of lean combustion products. The coflow has a non-uniform distribution of species and temperature. The DAFGM model can handle the non-uniformity of the coflow boundary inlet with the assist of the dilution variable. For the coflow boundary condition, a mismatch was noticed between the integrated oxygen flux over the coflow inlet and the oxygen flux following from the mass flow rate. A modified oxygen concentration profile was used in the simulation. It is found in the results that the predicted results are not sensitive to the progress variable fluctuations, but the air stream inlet velocity has effects on the predicted temperature profile at high axial locations. Turbulent flow field statistics and temperature predictions are in overall good agreement between experimental data and both RANS and LES results. The LES predicts overall better velocity and temperature fields than RANS. In the LES results, it is clear that air is entrained by the large vertices generated in the shear layer between coflow and air. At higher axial locations, the air is transported to the flame region and participates in the reactions.*

## 6.1. INTRODUCTION AND LITERATURE REVIEW

Lab-scale setups e.g. jet-in-hot-coflow (JHC) burners are commonly used to mimic burnt gas recirculation process in furnace. The configuration of these burner flames is simple and it is very suitable for detailed measurements. The produced comprehensive database is of great importance for model development and validation. Two existing experimental datasets have been widely used to for this purpose, the Adelaide jet-in-hot-coflow flames (Dally et al., 2002) and the Delft-Jet-in-Hot-Coflow (DJHC) flames (Oldenhof et al., 2010, 2011).

For the model validation with the datasets mentioned above, intensive work has been done. Christo and Dally (2004; 2005) assessed the performance of different combustion models by modelling the JHC flames in the Ref. (Dally et al., 2002), including the steady flamelet model, the eddy dissipation concept (EDC), and transported probability density function (PDF) model, and concluded that the EDC model produced better results than the flamelet model. De et al. (2011) found that the EDC combustion model predicts too early ignition and under-predicts lift-off height. However it accurately captured the sensitivity of the lift-off height with respect to Reynolds number. With modified model constants, early ignition can be avoided. Kim et al. (2005) used a conditional moment closure (CMC) model to predict the flame structure and NO formation. In this work, a new approach was proposed to describe three stream mixing in terms of a single mixture fraction, but it is not accurate at downstream where interaction between fuel and fresh air becomes significant in a JHC flame. Ihme and See (2011) proposed a flamelet-model for application to three-stream combustion systems. The oxidizer split was introduced as an additional scalar to predict the mixing between two oxidizer streams and the fuel stream and used to identify flamelets of different mixture composition. It was concluded that this approach significantly improved predictions for the flame structure and the flow field in the JHC burner system compared to the single-mixture-fraction FPV model. This model was further applied to higher dilution levels and good agreement with experimental data was obtained (Ihme et al., 2012). A similar approach was also used in the Ref. (Kulkarni and Polifke, 2013), but the turbulence-chemistry interaction in this work was taken into account by solving a set of stochastic differential equations, instead of using a presumed $\beta$-PDF for mixture fraction. Similar method was also applied to DJHC flames (Bhaya et al., 2014). Recently, conditional source-term estimation (CSE) method was also applied to two DJHC flames (Labahn et al., 2015; Labahn and Devaud, 2016), and overall good agreement with experimental data was obtained.

According to the above studies, a tabulated chemistry approach like FGM could still be attractive for flameless combustion because it is requiring less computational resources while incorporating detailed chemistry. In the case of JHC/DJHC, the dilution is created by a secondary burner producing a stream consisting of combustion products and air. In the case of perfect mixing of the coflow, the JHC flames are jet flames of fuel in a diluted air environment. The challenge of modelling flameless combustion with the FGM approach is to include the dilution effects. Although the DAFGM model described in Chapter 5 Section 5.5 is developed for flameless combustion in a furnace, it can also be applied to JHC/DJHC flames. The coflow is therefore defined as a mixture of air and diluent, and it is even able to handle non-uniform coflow compositions. In this chapter, the DAFGM model will be applied to model one DJHC flame using both RANS and LES

approaches, case DJHC-I at Re=4100 (Oldenhof et al., 2011).

## 6.2. DESCRIPTION OF DJHC DATABASE

### 6.2.1. DJHC-BURNER

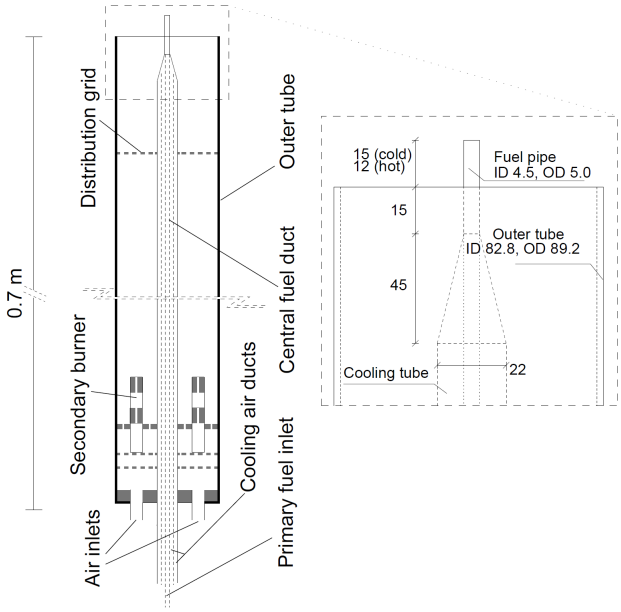


**Figure 6.1:** Schematic design of the Delft JHC burner (Oldenhof et al., 2011).

Figure 6.1 shows a sketch of the configuration of the DJHC burner. Detailed measurements of the flames on this burner have been performed by Oldenhof et al. (2010; 2011). The design of the burner is similar to the Adelaide burner (Dally et al., 2002). This DJHC burner is designed to create axi-symmetric flames with a high temperature coflow carrying low oxygen concentration to mimic important characteristics of flameless combustion. Photographs illustrating the burner design and the flame structure can be found in the Appendix of the work of De et al. (2011). The fuel for the jet is supplied via a 900 mm long vertical tube with an inner diameter of 4.5 mm. During burner operation, the central fuel pipe is continuously cooled by flushing air through the cooling ducts surrounding the fuel pipe. This prevents excessive heat transfer from the surrounding hot coflow to the fuel. The coflow of containing hot combustion products is generated by the secondary burner positioned in an annulus of diameter 82.8 mm. The secondary burner is designed to allow for addition of seeding particles in the air flow needed for LDA and PIV measurements. It consists of rich partially premixed flames forming a ring burner. A small part of the air (24 nl/min) is fed to the ring burner flame, the rest of the air is injected via the air inlets at the bottom and bypasses the ring-burner (at the inner side and at the outer side). When unconfined, the flame created by the secondary burner has a length of about 0.4 m. But in the burner they are confined by the outer wall and

a redistribution grid placed horizontally in the coflow annulus. This grid is located 0.11 m upstream of the burner exit. It keeps the fuel pipe centred and plays an essential role in reducing the temperature of the coflow via convective and radiative heat loss. The profiles at the height where the coflow leaves the burner were measured using LDA for velocity, CARS for temperature and probes for composition (oxygen). The design of the secondary burner has a direct consequence on temperature and species distributions at that location. The single redistribution grid is not sufficient to create a radially uniform coflow. But good axisymmetrical flames are realized by the design. Due to the heat loss to the air cooling duct wall and to the outer tube wall, the temperature has a maximum in the middle of coflow, away from the walls. But in that region the oxygen concentration has a minimum. This will be explained further when addressing the inlet boundary conditions in numerical simulations.

### 6.2.2. CASE DESCRIPTION

**Table 6.1:** Experimental settings for the case DJHC-I Re=4100. $\dot{V}_{*,co}$ represent volume flow rates of fuel (denoted by subscript "$f$") and air (denoted by subscript "$a$") for the secondary burner; $T_f$ is the fuel temperature at primary burner fuel jet exit; $T_{max,co}$ and $Y_{O_2}$ are maximum coflow temperature and the mass flux weighted average oxygen mass fraction between r=2.5 mm and r=35 mm at z=3 mm; $Z_{co}$ is the mean mixture fraction based on fuel/air flow rates.



| Case | $Re_{jet}$ [-] | $\dot{V}_{f,co}$ [nl/min] | $\dot{V}_{a,co}$ [nl/min] | $T_f$ [K] | $T_{max,co}$ [K] | $Y_{O_2}$ [mass%] | $Z_{co}$ [-] |
|---|---|---|---|---|---|---|---|
| DJHC-I | 4100 | 16.1 | 224 | 430 | 1540 | 7.6 | 0.044 |

Velocity and temperature were measured at 3, 15, 30, 60, 90, 120 and 150 mm downstream above the fuel jet exit of the primary burner. Favre averaged velocity statistical quantities were measured using LDA. Temperature was measured using the CARS technique. Oxygen concentration was measured using a probe based gas analyser (Testo 335). The axial velocity, temperature and oxygen mole fraction profiles at z=3 mm above the primary fuel jet exit are shown in Figure 6.2. They were used as inlet boundary conditions for the simulation.

## 6.3. MODEL DESCRIPTION

### 6.3.1. COMPUTATIONAL DOMAIN AND MESH

The simulations were performed using both RANS and LES. In RANS simulations, the mean flow and flame were considered axisymmetric. Therefore, a 2D grid was used. The computational domain starts 3 mm downstream of the jet exit and extends up to 225 mm in the axial direction, as used in the Refs. (De et al., 2011; Sarras et al., 2014; Labahn et al., 2015; Labahn and Devaud, 2016). The radial direction of the grid extends up to radial distance 80 mm in order to include the air entrainment in the simulation. The grid consists of 300 ×215 cells, in axial and radial directions, respectively, refined in the centre and the jet shear layer. This grid has been proven to be fine enough for this study according to the grid independence study in the Refs. (De et al., 2011; Sarras et al., 2014). In LES

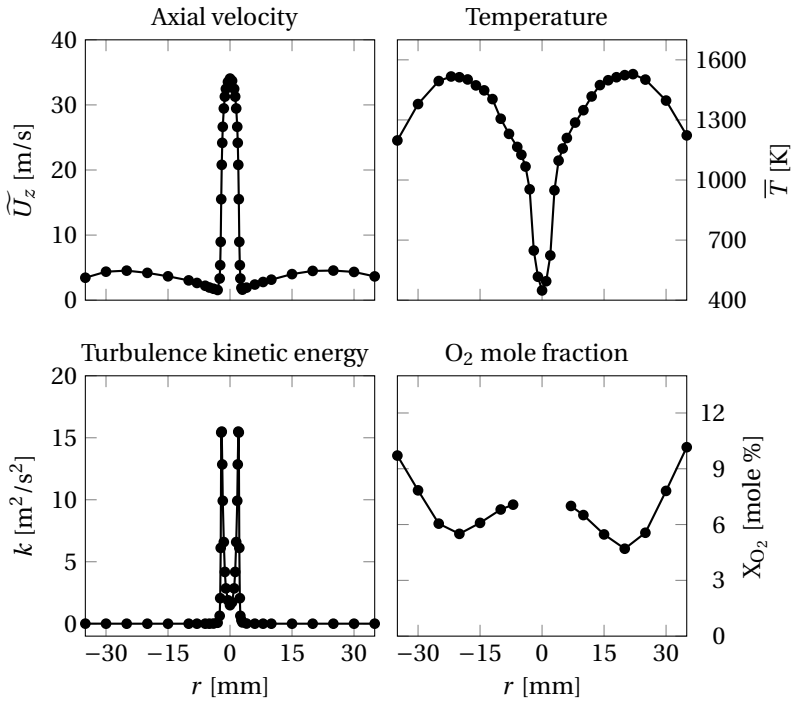


**Figure 6.2:** Measurements along the radial direction at z=3 mm. Upper left: mean axial velocity, upper right: mean temperature, bottom left: mean turbulence kinetic energy and bottom right: mean oxygen mole fraction for case DJHC-I Re=4100 (Oldenhof et al., 2011).

simulations, the full 3D domain with the same dimensions as RANS setup was used. The computational domain becomes a cylinder with a radius of 80 mm and extends 225 mm in the axial direction. A hexahedral structured mesh was used. The grid includes approximately 2.5 million cells and is non-uniform with a higher density of cells near the nozzle and close to the centreline. At large radial position, cell size in circumferential direction becomes larger. Therefore staged refinement in circumferential direction was applied to maintain acceptable aspect ratio. The first refinement was at radius $r$=8 mm, and the second refinement was at $r$=20 mm. In order to properly capture the entrainment of ambient air, the grid was also refined near the interface between air and coflow. This results in cell size between 0.2~0.4 mm in the jet region. Schematics of both computational domains are presented in Figure 6.3 and 6.4.

### 6.3.2. TURBULENT COMBUSTION MODEL

In the DAFGM model discussed in Chapter 5, the diluent is defined as combustion products at stoichiometric mixture fraction at equilibrium state. As will be shown below, this model can be applied to modelling of jet-in-hot-coflow flames, even with coflow having non-uniformly distributed temperature and species. The coflow is considered as a mixture of air and diluent. For every radial position in the coflow from the measured mean

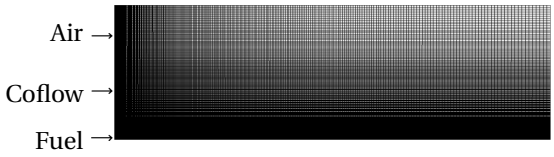


**Figure 6.3:** The mesh used in RANS simulation for case DJHCI Re4100.

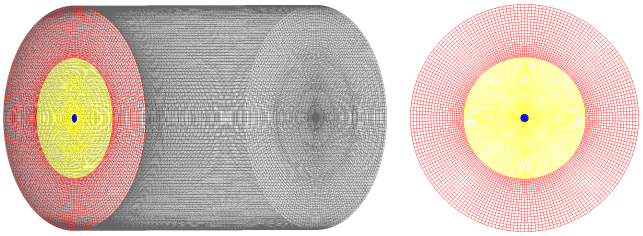

**Figure 6.4:** The mesh used in LES for case DJHCI Re4100. Blue: fuel inlet, yellow: coflow inlet, red: air inlet.



temperature and oxygen concentration, assuming equilibrium and neglecting turbulent fluctuations, a unique combination of dilution variable and enthalpy loss can be found corresponding to the measurements. With the combination of these control parameters, a coflow condition, e.g. temperature, $O_2$, can be represented. In this way, the three streams, fuel, coflow and air can be well defined. The progress variable in this study is defined as a combination of mass fractions of several species as follows:

$$Y_c = Y_{CO_2} + Y_{CO} + Y_{H_2O} + Y_{H_2} \tag{6.1}$$

In the RANS or LES simulations, in addition to continuity and momentum equations, the following Favre-averaged equations or filtered equations are solved under the unit Lewis number assumption.

Mixture fraction

$$\frac{\partial \overline{\rho}\widetilde{Z}}{\partial t} + \frac{\partial}{\partial x_i}\left(\overline{\rho}\widetilde{u_i}\widetilde{Z}\right) = \frac{\partial}{\partial x_i}\left[\overline{\rho}\left(\widetilde{D}+D_t\right)\frac{\partial \widetilde{Z}}{\partial x_i}\right], \tag{6.2}$$

Progress variable

$$\frac{\partial \overline{\rho}\widetilde{Y_c}}{\partial t} + \frac{\partial}{\partial x_i}\left(\overline{\rho}\widetilde{u_i}\widetilde{Y_c}\right) = \frac{\partial}{\partial x_i}\left[\overline{\rho}\left(\widetilde{D}+D_t\right)\frac{\partial \widetilde{Y_c}}{\partial x_i}\right] + \overline{\dot{\omega}}_{Y_c}, \tag{6.3}$$

Dilution variable

$$\frac{\partial \overline{\rho}\widetilde{Y_d}}{\partial t} + \frac{\partial}{\partial x_i}\left(\overline{\rho}\widetilde{u_i}\widetilde{Y_d}\right) = \frac{\partial}{\partial x_i}\left[\overline{\rho}\left(\widetilde{D}+D_t\right)\frac{\partial \widetilde{Y_d}}{\partial x_i}\right] + \overline{\dot{\omega}}_{Y_d}, \tag{6.4}$$

Enthalpy

$$\frac{\partial \overline{\rho}\widetilde{h}}{\partial t} + \frac{\partial}{\partial x_i}\left(\overline{\rho}\widetilde{u_i}\widetilde{h}\right) = \frac{\partial}{\partial x_i}\left[\overline{\rho}\left(\widetilde{D}+D_t\right)\frac{\partial \widetilde{h}}{\partial x_i}\right] + \overline{S}_r, \tag{6.5}$$

Mixture fraction variance

$$\frac{\partial \overline{\rho}\widetilde{Z''^2}}{\partial t}+\frac{\partial}{\partial x_i}\left(\overline{\rho}\widetilde{u_i}\widetilde{Z''^2}\right)=\frac{\partial}{\partial x_i}\left[\overline{\rho}\left(\widetilde{D}+D_t\right)\frac{\partial \widetilde{Z''^2}}{\partial x_i}\right]+2\overline{\rho}D_t\left(\frac{\partial \widetilde{Z}}{\partial x_i}\right)^2-\overline{\rho}\widetilde{\chi}_Z, \tag{6.6}$$

Progress variable variance

$$\begin{aligned}\frac{\partial \overline{\rho}\widetilde{Y_c''^2}}{\partial t}+\frac{\partial}{\partial x_i}\left(\overline{\rho}\widetilde{u_i}\widetilde{Y_c''^2}\right)=&\frac{\partial}{\partial x_i}\left[\overline{\rho}\left(\widetilde{D}+D_t\right)\frac{\partial \widetilde{Y_c''^2}}{\partial x_i}\right]+2\overline{\rho}D_t\left(\frac{\partial \widetilde{Y_c}}{\partial x_i}\right)^2-\overline{\rho}\widetilde{\chi}_{Y_c}\\&+2\left(\overline{Y_c\dot{\omega}_{Y_c}}-\widetilde{Y_c}\overline{\dot{\omega}}_{Y_c}\right).\end{aligned} \tag{6.7}$$

In the RANS approach, the turbulent scalar dissipation rate for mixture fraction and progress variable variance $\overline{\rho}\widetilde{\chi}_Z$ and $\overline{\rho}\widetilde{\chi}_{Y_c}$ in Equations (6.6) and (6.7) are respectively modelled as follows (Poinsot and Veynante, 2012):

$$\widetilde{\chi}_Z=C_{Zv}\frac{\epsilon}{k}\widetilde{Z''^2}, \tag{6.8}$$

and

$$\widetilde{\chi}_{Y_c}=C_{Y_cv}\frac{\epsilon}{k}\widetilde{Y_c''^2}, \tag{6.9}$$

where $k$ and $\epsilon$ are turbulence kinetic energy and corresponding dissipation rate which are calculated by a turbulence model. Here the $k-\epsilon$ model is used. $C_{Zv}$ and $C_{Y_cv}$ are two model constants and are both set to a value of 2. The diffusion coefficients are modelled by Equations (5.49) and (5.50), with the laminar Schmidt number and turbulent Schmidt number both 0.7.

In the LES approach, the SGS part of the scalar dissipation rate in Equations (6.6) and (6.7) can be modelled by linear relaxation models (Domingo et al., 2008; Rittler et al., 2015):

$$\widetilde{\chi}_Z=C_{Zv}D_t\frac{\widetilde{Z''^2}}{\Delta^2}, \tag{6.10}$$

and

$$\widetilde{\chi}_{Y_c}=C_{Y_cv}D_t\frac{\widetilde{Y_c''^2}}{\Delta^2}, \tag{6.11}$$

in which $\Delta$ is the LES filter size, $C_{Zv}$ and $C_{Y_cv}$ are two model constants and are both set to a value of 2. The diffusion coefficients are modelled by Equations (5.49) and (5.51), with the laminar Schmidt number and subgrid scale Schmidt number both 0.7.

For the evaluation of source terms in Equations (6.3), (6.4), (6.5) and (6.7), $\overline{\dot{\omega}}_{Y_c}$, $\overline{\dot{\omega}}_{Y_d}$ and $\overline{Y_c\dot{\omega}_{Y_c}}$ are tabulated in the lookup table and radiation source term in the enthalpy equation is neglected. The source term $\overline{\dot{\omega}}_{Y_d}$ for dilution variable needs to be modelled. This term accounts for transforming burnt gas to the dilution stream. The detailed tabulation and transformation procedures have been described in Chapter 5 Section 5.5.

During the simulations, the DAFGM lookup table control parameters can be derived from $\widetilde{Z}$, $\widetilde{Y_c}$, $\widetilde{Y_d}$, $\widetilde{h}$, $\widetilde{Z''^2}$ and $\widetilde{Y_c''^2}$ by solving Equations (6.2)~(6.7). Procedures and scaling methods of Chapter 5 were used to obtain the second mixture fraction $\widetilde{\xi}$ and its scaled variance $S_z$, scaled progress variable $\widetilde{C}$ and its scaled variance $S_C$, air dilution level $\widetilde{\gamma}$ and normalized enthalpy loss factor $\widetilde{\eta}$.

### 6.3.3. BOUNDARY CONDITIONS

The known overall fuel and air flow rates in Table 6.1 determine the overall mixture fraction of the coflow. This coflow here is considered to be a stream of non-adiabatic equilibrium products of combustion of Dutch natural gas. It is locally treated as a mixture of excess air and equilibrium products of stoichiometric combustion. The local mean oxygen mole fraction and measured temperature together determine the mean mixture fraction and enthalpy loss in the Ref. (De et al., 2011; Sarras et al., 2014). Taking into account the enthalpy loss the corresponding equilibrium composition is calculated using the TU Delft FLAME code (Peeters, 1995). However, for the simulations reported here, the reported measured oxygen mole fraction profile was not adopted unchanged, because a mismatch was noticed between the mass flux weighted mean mixture fraction based on the measured oxygen mole fraction and the mixture fraction following from the mass flow rates in the coflow. This can be due to inaccuracy of the measurements or the uncertainty whether the considered sample were dry or wet. The oxygen measurements were not adopted in this study. Nevertheless, its basic shape with low concentration at half radius of outer tube and higher concentration on both sides was taken into account when reconstructing the oxygen profile. We started with calculating overall mean mixture fraction at the coflow boundary by Equation (6.12). Its value should be in agreement with the value $Z_{co}$ obtained from the mass flow rates in Table 6.1.

$$Z_{mean} = \frac{\int_A \rho U Z_{ass} dA}{\int_A \rho U dA}, \tag{6.12}$$

where $Z_{mean}$ is mass flux weighted mean mixture fraction, $Z_{bc}$ is the mixture fraction specified at coflow boundary, density $\rho$ is calculated at atmosphere pressure and measured temperature, and $U$ is the measured velocity at coflow boundary. The integration is performed over the area of coflow annulus. Instead of using the measured oxygen profile, we assume an oxygen profile or equivalently we assume a profile ($Z_{ass}$) for $Z_{bc}$. The assumed oxygen profile and mixture fraction profile are shown in Figure 6.5. The $Z_{mean}$ based on the $Z_{ass}$ profile results in a difference less than one percent compared to $Z_{co}$. The $Z_{ass}$ profile leads to a mass flux weighted average oxygen mass fraction 8.8% in the coflow.

Once the local mixture fraction in the coflow is defined, based on the following calculation, the local mean temperature profile, the local enthalpy loss in the coflow can be determined. Enthalpy at the coflow boundary inlet is defined by

$$h = (h_f - h_{ox})Z + h_{ox} - \Delta h.$$

Using the Equation (5.78),

$$Z = (1-\alpha)Z_0 + \alpha Z_{st},$$

because the coflow consists of diluent and air, $Z_0$=0, the dilution level $\alpha$ at the coflow boundary is obtained, $\alpha = Z/Z_{st}$. Using Equation (5.75),

$$\alpha = \frac{Y_d}{Y_d^{Dil}}.$$

$Y_d$ at the coflow boundary inlet is defined. We also note that in the absence of fuel, $\alpha = \gamma$ (see Equation (5.80)). So far, boundary conditions for mixture fraction, enthalpy, and

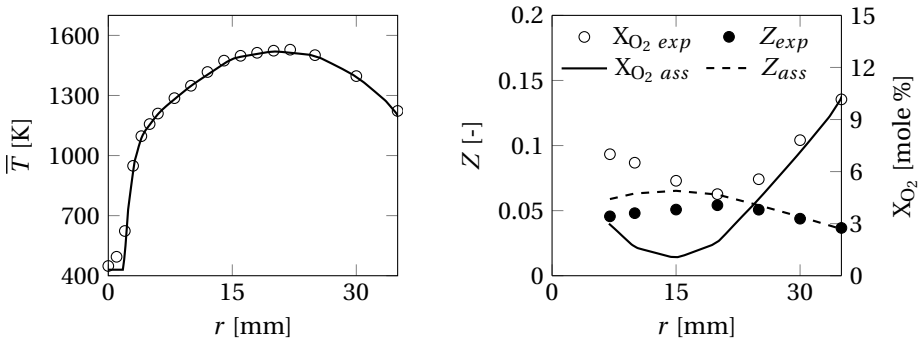


**Figure 6.5:** Comparison between the experimental measurements and specified boundary conditions at z=3 mm. Left: temperature, right: mixture fraction and $O_2$ mole fraction. $X_{O_2\ exp}$ and $X_{O_2\ ass}$ are the measured and assumed $O_2$ mole fraction, respectively. The corresponding mixture fractions are $Z_{exp}$ and $Z_{ass}$, respectively.

dilution variable have been well defined. Progress variable, $Y_c$, was specified as $Y_{c,min}$ corresponding to local mixture fraction, enthalpy and air dilution level, and obtained from the DAFGM library (see Section 6.3.4).

Furthermore, the following the boundary conditions at fuel and air inlet were applied.

| **fuel inlet** | **coflow inlet** | **air inlet** |
|---|---|---|
| $\widetilde{Z} = 1$ | $\widetilde{Z} = \widetilde{Z}(r)$ | $\widetilde{Z} = 0$ |
| $\widetilde{Y_c} = \widetilde{Y}_{c,f}$ | $\widetilde{Y_c} = \widetilde{Y_c}(r)$ | $\widetilde{Y_c} = 0$ |
| $\widetilde{Y_d} = 0$ | $\widetilde{Y_d} = \widetilde{Y_d}(r)$ | $\widetilde{Y_d} = 0$ |
| $\widetilde{h} = \widetilde{h_f}$ | $\widetilde{h} = \widetilde{h}(r)$ | $\widetilde{h} = \widetilde{h}_{air}$ |

It is assumed that there are no fluctuations in the mixture fraction and progress variable at the boundaries which means $\widetilde{Z''^2} = 0$ and $\widetilde{Y_c''^2} = 0$.

It is important to point out that the new $O_2$ mole fraction profile is quite different from the original $O_2$ mole fraction from the experimental data, as shown in Figure 6.5. The $O_2$ mole fraction is calculated by assuming equilibrium state at the new mixture fraction and measured temperature profiles. Apart from the factors mentioned earlier, the assumption that the coflow is in chemical equilibrium could also be one reason for this difference in $O_2$ mole fraction. The argument for this is that the measured mean temperature in the coflow increases from z=15 mm to z=30 mm which seems incompatible with chemical equilibrium.

In the RANS simulation, standard $k-\epsilon$ was used. The turbulence kinetic energy $k$ at the inlet boundary is calculated from the measured axial and radial velocity fluctuations and assuming the azimuthal component to be equal to radial one. It is assumed that the turbulence production is equal to dissipation, and thus turbulence dissipation rate $\epsilon$ at

the inlet is calculated using the measured Reynolds shear stress and axial mean velocity:

$$\epsilon = -\widetilde{u''v''}\frac{\partial \widetilde{U}}{\partial r}.$$

In LES simulation, turbulence at the inlet is generated using the synthetic turbulence method developed in the Ref. (Kornev and Hassel, 2007; Kornev et al., 2008) based on prescribed mean velocity profiles, the corresponding Reynolds stress tensor and integral length scales. No turbulent fluctuations for enthalpy and dilution variable are included at the inlet.

The axial and radial velocities in the jet and coflow are set based on the experimental measurements in both RANS and LES. The velocity in the air region is set to a small value in the range 0.1 to 0.5 m/s as will be discussed later.

### 6.3.4. NON-ADIABATIC DAFGM LIBRARY GENERATION

Due to fuel tube cooling and radiation heat loss by the outer tube and the distribution grid, an enthalpy loss occurs in the secondary burner leading to a non-adiabatic enthalpy profile at the coflow inlet. For the considerations of these non-adiabatic effect in the simulation, the non-adiabatic DAFGM library was generated in the way discussed in Chapter 5 Section 5.5.3. To construct the non-adiabatic DAFGM library, a counterflow laminar diffusion flame is solved in physical space with CHEM1D. The enthalpy loss effect is imposed by decreasing diluent temperature. Therefore, when air is diluted, boundary temperature (enthalpy) at the oxidizer side is reduced. A commonly used method to construct a 2D-FGM library is first to calculate steady flamelet equations with strain rate (or scalar dissipation rate in other package, e.g. Flamemaster) increasing from a very small value to the critical value where flame quenches. Second, an unsteady solution of the counterflow equations is attained describing extinction starting at the critical strain rate towards to the mixing state. The steady flamelets and the unsteady extinguishing flamelet are then together mapped in mixture fraction and progress variable space (Chrigui et al., 2012). This method is commonly referred as "extinguishing flamelets" and is used in the present study.

In counterflow laminar flame settings, boundary conditions at the fuel side are fixed by fuel composition and temperature. At the oxidizer side, it starts with pure air at ambient temperature and then it is replaced by diluted air. The diluted air was calculated by using the TU Delft FLAME code (Peeters, 1995) at mixture fraction $Z_{st}\gamma$ at given enthalpy loss. Note that, $Z$ and $Y_c$ are in general not statistically independent, whereas $Z$ and $C$ come close to being statistically independent. Therefore, $Z$ and $C$ are used as controlling parameters for tabulation with presumed $\beta$-function for $Z$ and $\beta$ or $\delta$-function for $C$.

Figure 6.6 shows some examples of flamelets generated at air dilution level $\gamma$=0.1, 0.5 and 0.9, and enthalpy loss factor $\eta$=0, 0.5 and 1. $\eta$=0 corresponds to no enthalpy loss in diluent and $\eta$=1 represents maximum enthalpy loss in diluent. In this study, maximum enthalpy loss is set as $2 \times 10^6$ J/kg. The flamelets are plotted as temperature versus mixture fraction based on fuel and pure air. With diluted air, the starting point of flamelets gradually shifts up to stoichiometric mixture fraction $Z_{st}$ as air dilution level increases to 1. According to Equation (5.78), the relationship between mixture fraction $Z$ and the

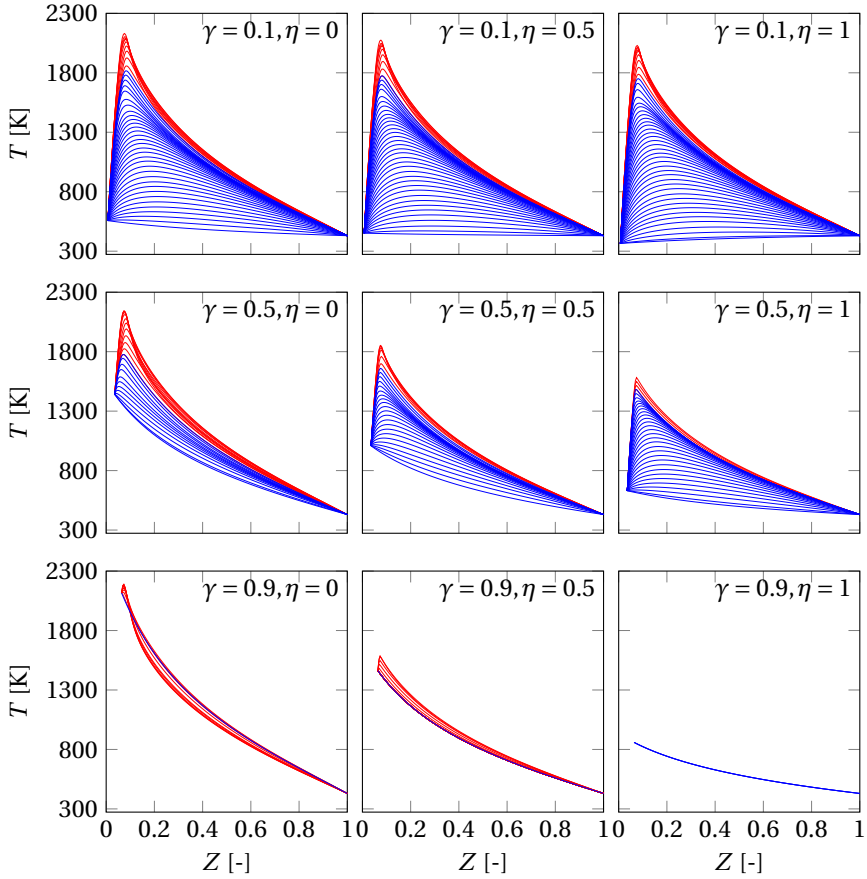


**Figure 6.6:** Flamelets calculated at different air dilution level $\gamma$ and enthalpy loss factor $\eta$. Red lines represent steady flamelets and blue lines represent unsteady extinguishing flamelets.

second mixture fraction $\xi$ is given by

$$Z = \xi + (1-\gamma)\xi Z_{st}.$$

It can be seen that at low air dilution level, enthalpy loss in diluent has only little effect on the flame temperature, but the influence becomes significant as air dilution level increases. Temperature rise also decreases with increasing air dilution level. This is consistent with the concept of flameless combustion. Due to highly diluted reactants, the temperature rise is very limited and peak temperature is therefore lowered by sufficient enthalpy loss in the recirculated burnt gas. Finally, the temperature in the reaction zone is below the temperature at which $NO_x$ is efficiently formed.

The progress variable source term in $(Z, C)$ space is shown in Figure 6.7. Differences in source term magnitudes are obvious. Lower air dilution level and lower enthalpy loss in diluent result in larger progress variable source term. The progress variable source

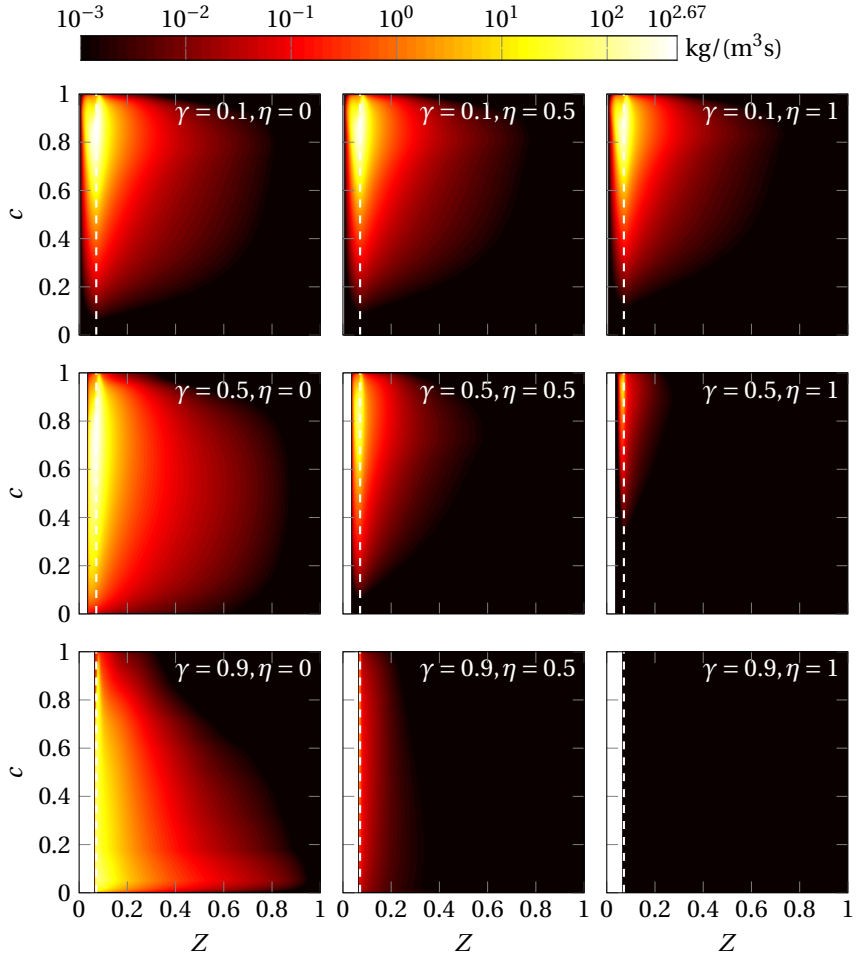


**Figure 6.7:** Progress variable source term in $(Z, C)$ space at different air dilution level $\gamma$ and enthalpy loss factor $\eta$ corresponding to the flamelets in Figure 6.6. The white dashed line represents the position of stoichiometric mixture fraction for fuel and undiluted air.

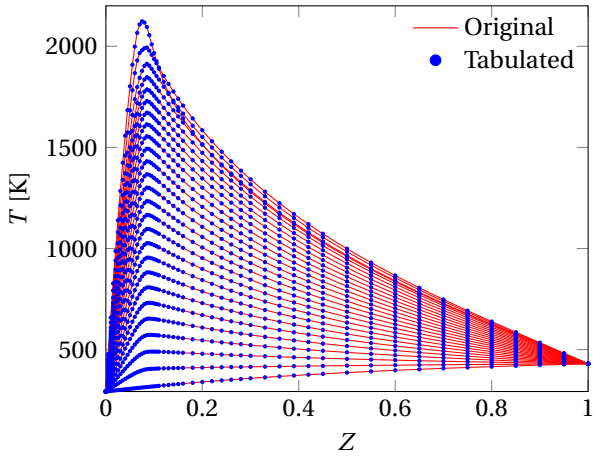


**Figure 6.8:** Tabulated $Z$ and $C$ (51×51) vs original source data (201×201).

term decreases with increasing air dilution level and enthalpy loss. This means that dilution and enthalpy loss make the mixture less reactive.

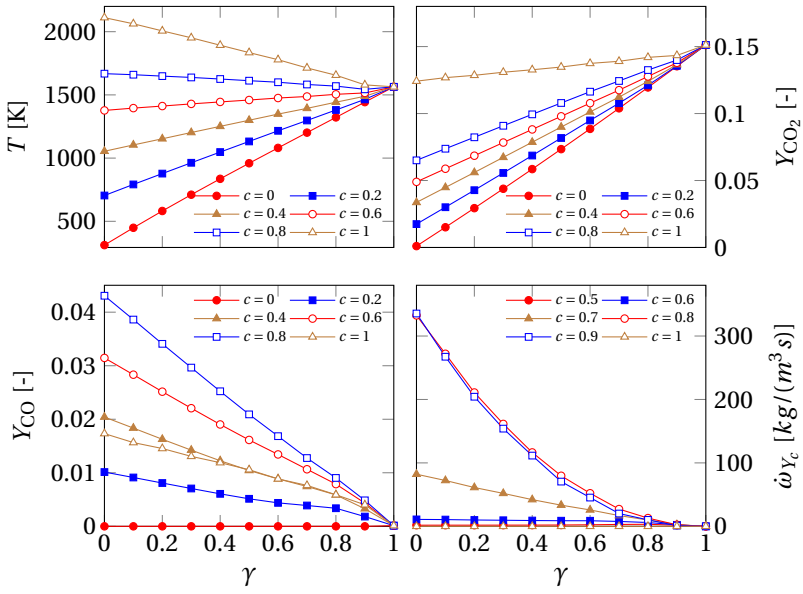


**Figure 6.9:** Variations of variables as a function of air dilution level $\gamma$ at $\eta$=0.5, $Z_{st}$ and at different $C$.

It should be pointed out that the library size increases linearly with the number of grid points in the control parameter space, hence number of grids points should be minimized. For $Z$ and $C$, it is found that a $51 \times 51$ grid is accurate enough for linear inter-

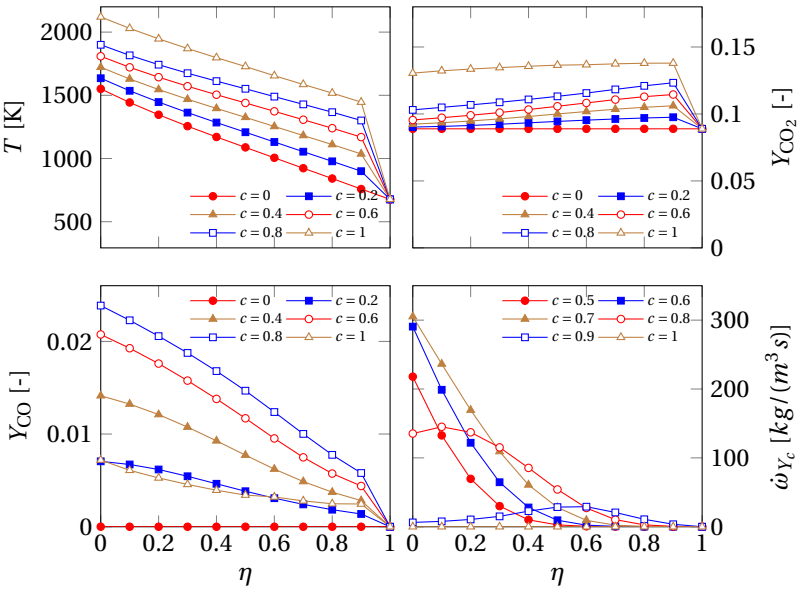


**Figure 6.10:** Variations of variables as a function of enthalpy loss factor $\eta$ at $\gamma$=0.6, $Z_{st}$ and at different $C$.

6

polation. In $Z$ dimension, fine grid points are set between 0 and 0.16. Grid points in $C$ dimension are evenly distributed. The tabulated temperature as an example is shown in Figure 6.8. Tabulated temperatures are overlapping with original source data which is attained on a 201×201 grid. Grid points for $Z$ make the tabulated temperature capture quite well the variation near $Z_{st}$ and temperature changes nearly linearly with $C$. This shows that the allocated grid points for $Z$ and $C$ is sufficient for the tabulation. Since the DAFGM library differs with different dilution and enthalpy loss levels, it is necessary to also check whether the tabulated grids in these two dimensions are sufficient before they can be applied to the simulation. Figure 6.9 and 6.10 display the variations of several selected variables as function of $\gamma$ and $\eta$ respectively. According to these plots, temperature and main product species fractions change almost linearly with $\gamma$ and $\eta$. Progress variable source term can be assumed changing piecewise-linearly with $\gamma$ and $\eta$. It can be concluded that as long as sufficient layers are stored for $\gamma$ and $\eta$, e.g. eleven layers for $\gamma$ and eleven layers for $\eta$, linear interpolation between these layers provides acceptable properties for simulation. In the DAFGM library construction, the 11 grid points for both $\gamma$ and $\eta$ are uniformly distributed from 0 to 1. So far, it is concluded that a tabulation grid of 51×51×11×11 is sufficient for the DAFGM library construction. These libraries are used in both RANS and LES simulations.

It is noted that no enthalpy loss occurs when dilution is zero. Therefore, 10×11 laminar counterflow flame cases with dilution and enthalpy loss plus one case without dilution and enthalpy loss are to be calculated. As a result, a 4D-DAFGM library is obtained from the combination of these 2D-FGM libraries.

## 6.4. RESULTS AND DISCUSSIONS

In this section, the results of RANS and LES simulations are compared to experimental measurements for velocity and temperature statistics. First, the sensitivity of progress variable variance and the effect of air inlet velocity on air entrainment are examined using RANS approach. It was found that the standard $k-\epsilon$ (SKE) model and the realizable $k-\epsilon$ (RKE) model predict similar flow field in the case DJHC-I Re=4100 (De et al., 2011), and SKE was also used in the results shown below. For LES, dynamic Smagorinsky model implemented in OpenFOAM was applied for closing the sub-grid scale (SGS) stress terms and SGS scalar fluxes with the SGS eddy viscosity.

Figure 6.11 shows the comparison between the predicted mean scalar ($\widetilde{Z}$, $\widetilde{Y_c}$, $\widetilde{Y_d}$ and $\widetilde{h}$) fields by RANS and LES. It can be seen that obvious differences exist in the results. The detailed comparison will be discussed in the following subsections.

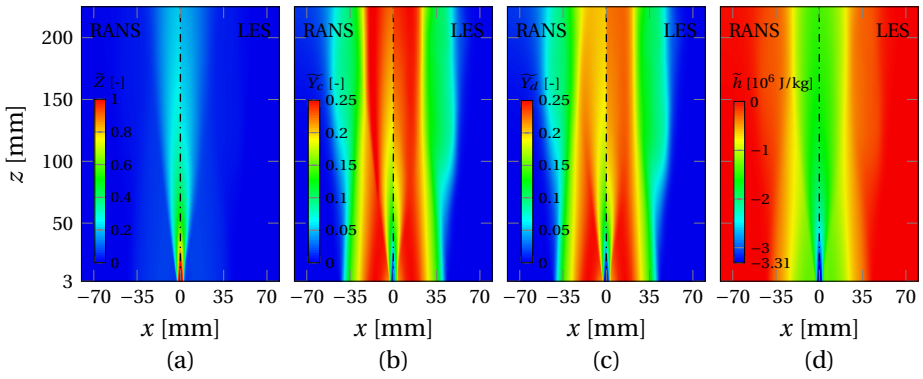


**Figure 6.11:** Comparison between the predicted mean scalar fields by RANS and LES. The results of RANS and LES are separated by the dash-dotted line. (a): mean mixture fraction; (b): mean progress variable, (c): mean dilution variable; (d): mean enthalpy.

### 6.4.1. PROGRESS VARIABLE VARIANCE

Two dimensional RANS simulations were used to give an idea on the influence of progress variable variance. The results at z=15, 60 and 120 mm are plotted in Figure 6.12 for comparison. Firstly, two cases with and without consideration of progress variable variance and with the same air inlet velocity $U_{air}$ = 0.5 m/s are compared. They are denoted as $5DU_{air}$ = 0.5 for without progress variable variance and $6DU_{air}$ = 0.5 for with progress variable variance. The corresponding solid and dashed lines are nearly overlapping in both axial mean velocity and mean temperature profiles. This indicates that progress variable variance is not having relevant influence in this case. Therefore, progress variable variance was also ignored in the following simulations, because this leads to significantly reduced lookup table size (from about 3000 MB to 225 MB).

### 6.4.2. AIR STREAM INLET VELOCITY

According to the coflow spreading rate and the measured temperature, significant influence from the entrainment of ambient air into the coflow was observed at z=60 mm and

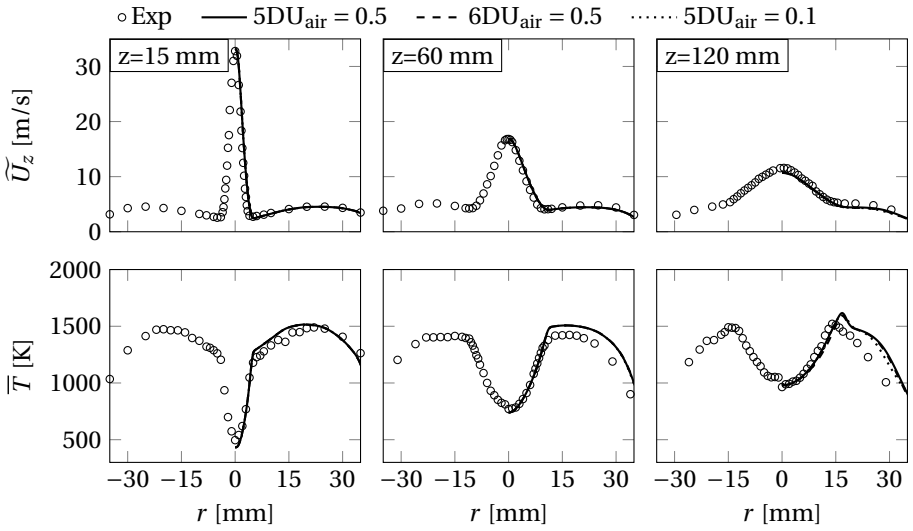


**Figure 6.12:** RANS results comparison between cases with and without progress variable variance, and with 0.5 m/s and 0.1 m/s air inlet velocity.



higher. Therefore, the imposed inlet air stream velocity is of importance to correctly predict the development of the coflow-air mixing layer. A low velocity is preferred because the laboratory air is coming from stationary surrounding. From the experimental data, the last velocity measurement is at $r$ = 40 mm and axial velocity magnitude is around 1 m/s. In the present study, air inlet velocity at 0.5 and 0.1 m/s were compared. A case without progress variable variance and $U_{air}$ = 0.1 m/s was calculated. This case is denoted as $5DU_{air}$ = 0.1 and the results are also plotted in Figure 6.12 by dotted lines for comparison. It is seen that at lower position both velocity and temperature are overlapping with the other two cases, but at z=120 mm, the difference becomes obvious. Although the difference in velocity is unnoticeable due to the plot scale, an effect of cold air inlet velocity on temperature at large radius region is evident. In the simulations presented below for both RANS and LES, air inlet velocity was set at 0.1 m/s.

### 6.4.3. TURBULENT FLOW FIELD PREDICTIONS

The success of predicting combustion physics depends on the quality of flow field prediction, because flow controls the fuel and oxidizer mixing. In this section, the predicted turbulent flow statistics including mean velocity, turbulence kinetic energy and velocity fluctuations are compared to experimental measurements. The mean properties of transient RANS and LES results discussed below were time averaged over 0.3 seconds. Instantaneous results at each time step were all taken into account and weighted by the corresponding time step.

The radial profiles of mean axial velocity $\widetilde{U_z}$ and mean radial velocity $\widetilde{U_r}$ at different axial locations are shown in Figure 6.13 and compared with available LDA experimental data (Oldenhof et al., 2011). As can be seen from the mean axial velocity profiles,

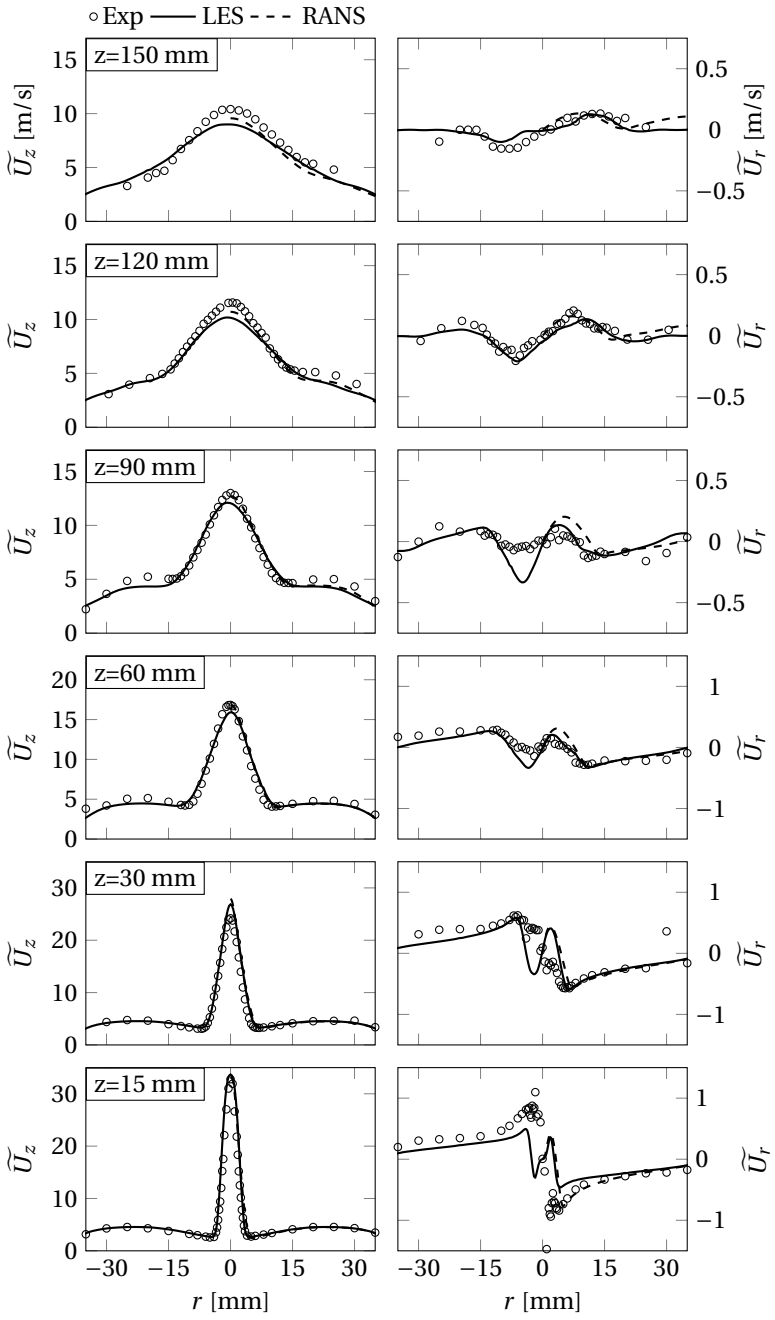


**Figure 6.13:** Mean axial and radial velocity profiles in radial direction at various axial locations above the fuel jet exit.

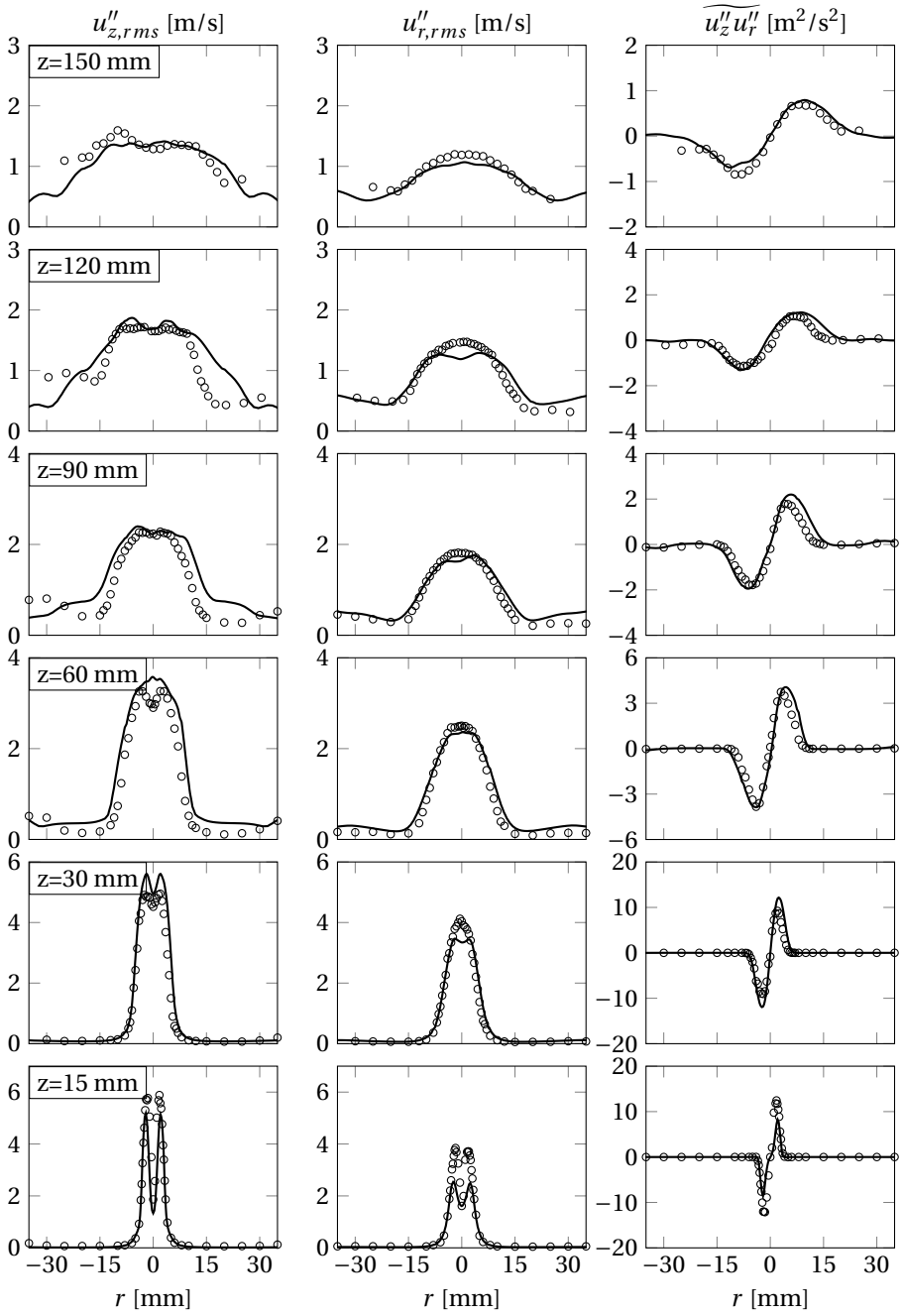


**Figure 6.14:** Mean axial, radial velocity fluctuations and mean shear stress profiles in radial direction at various axial locations above the fuel jet exit.

from axial location z=15 mm to z=90 mm, the predicted velocity profiles by RANS and LES are both in very good agreement with the experimental data. In mean radial velocity, results predicted by RANS show better entrainment of coflow at z=15 mm, but show higher outwards radial velocity at z=60 and 90 mm. This is a generally known weakness of SKE model. It over predicts spreading rate of a round jet. Further downstream, above the 90 mm, mean axial velocity predicted by RANS and LES both show faster decay than experimental data. The under prediction of centreline velocity in LES are respectively 7.2%, 11.6% and 13.5% for axial locations at 90, 120 and 150 mm. In RANS, these under predictions are less than half of those in LES. The turbulent flow prediction in LES is sensitive to the turbulence inlet boundary conditions, especially to the fuel jet inlet. It should be responsible for the larger discrepancies comparing to RANS. By using the synthetic turbulence method (Kornev and Hassel, 2007) for turbulence generation at the inlet, mean velocity, Reynolds stress tensor and integral length scale are needed. The first two properties are easily obtained from experimental data, but the length scale is unknown. When the integral length scale is taken as large as half of the fuel tube diameter, it was observed the mean axial velocity decays too fast and mixing between fuel and coflow is stronger according to the predicted temperature profiles. While the length scale is an order smaller than the fuel tube diameter, axial velocity is very much over predicted at z=30 mm. Therefore, a non-uniformly distributed integral length scale was applied in the present study. The length scale is taken half of the fuel tube diameter in the fuel axis and 10% of the fuel tube diameter at fuel boundary edge. The length scale is linearly reducing from the fuel axis to the edge.



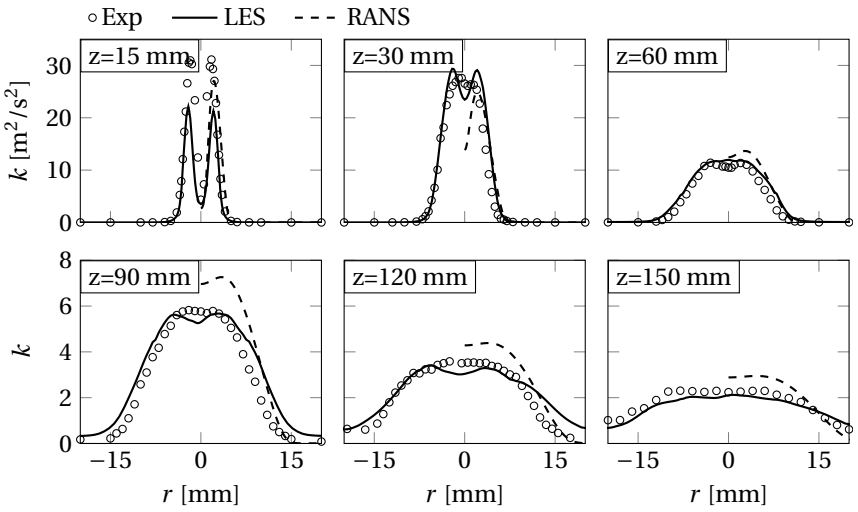


**Figure 6.15:** Mean turbulence kinetic energy profiles in radial direction at various axial locations above the fuel jet exit.

The mean turbulent fluctuations $u''_{z,rms}$, $u''_{r,rms}$ and shear stress $\widetilde{u''_z u''_r}$ are presented and compared with experimental data in Figure 6.14. The predicted axial velocity fluctuation $u''_{z,rms}$ is underestimated at 15 mm, but over predicted at 30 mm. Above 60 mm, the

shape of the axial velocity fluctuation profile is captured. Although the values at larger radius are over predicted, centreline axial velocity fluctuation is well predicted. As for radial velocity fluctuations, it is up to 32% underestimated in shear layers at 15 mm and up to 18% underestimated in the centre at 30 mm. The rest of the profiles all show good agreement with experimental data. The shear stresses are overall well captured. Shear stress peak locations are well predicted at all axial locations. The maximum discrepancy is observed at 15 mm, which is an approximately 30% underestimation.

Mean turbulence kinetic energy $k$ profiles are shown in Figure 6.15. The experimental turbulence kinetic energy is calculated by assuming the the normal stress orthogonal to the measurement plane to be equal to the radial normal stress. The numerical results for turbulence kinetic energy in RANS were directly obtained by solving $k$ equation, while in LES the turbulence kinetic energy is determined by extracting $\widetilde{u_z''u_z''}$, $\widetilde{u_x''u_x''}$ and $\widetilde{u_y''u_y''}$ during the simulation. Due to the underestimated velocity fluctuations at 15 mm, turbulence kinetic energy at this location is also underestimated. Above 30 mm (including 30 mm), both the shape and the magnitude of turbulence kinetic energy are well predicted by LES. Although turbulence kinetic energy prediction in RANS is better at 15 mm, it is about 50% under predicted in the jet centre at 30 mm and over predictions are observed at all downstream locations.

In conclusion, turbulent flow fields are predicted satisfactorily in both RANS and LES. LES shows its superiority in turbulence quantities prediction. This makes us confident to further discuss temperature predictions in the next section.

6

### 6.4.4. TEMPERATURE PREDICTIONS

A comparison of the mean temperature and temperature RMS values for flame DJHC-I Re=4100 is shown Figure 6.16. Good agreements are observed at z=15 and z=30 mm for both RANS and LES. An overall over prediction of temperature is observed at z=60 mm. It should be noted that the peak mean temperature reached in the simulations is hardly different between the heights z=15 mm, z=30 mm and z=60 mm. This is different from what is observed in the experiments. The experimental results for the highest mean temperatures reached in the coflow show a remarkable trend. Rounding experimental mean temperature to multiples of 5 K the following is observed. At the inflow boundary the maximum is about 1515 K and 1540 K at the two sides of the axis (see Figure 6.2). At z=15 mm the values are 1475 K and 1490 K. At z=30 mm the values both are 1500 K and at z=60 mm, the values are 1415 K and 1425 K. These maxima are reached away from the mixing layer with fuel and away from the mixing layer with air and should reflect the temperature evolution of the incoming mixture of lean combustion products. The variation with distance seems to contradict the model assumption that the coflow is in chemical equilibrium. The observed temperature increase between z=15 mm and z=30 mm possibly could be explained by a heat release effect, either directly (progress of reaction in the coflow stream) or indirectly (progress of reaction after a progress of radial mixing of enthalpy and oxygen). Thus, a more detailed experimental study on the coflow properties and also simulations of the flow inside the coflow annulus might be needed to explain these observations.

Based on the experimental $T_{rms}$ data in the right column in Figure 6.16, temperature RMS fluctuations in unaffected coflow are of the same magnitude at all heights. Accord-

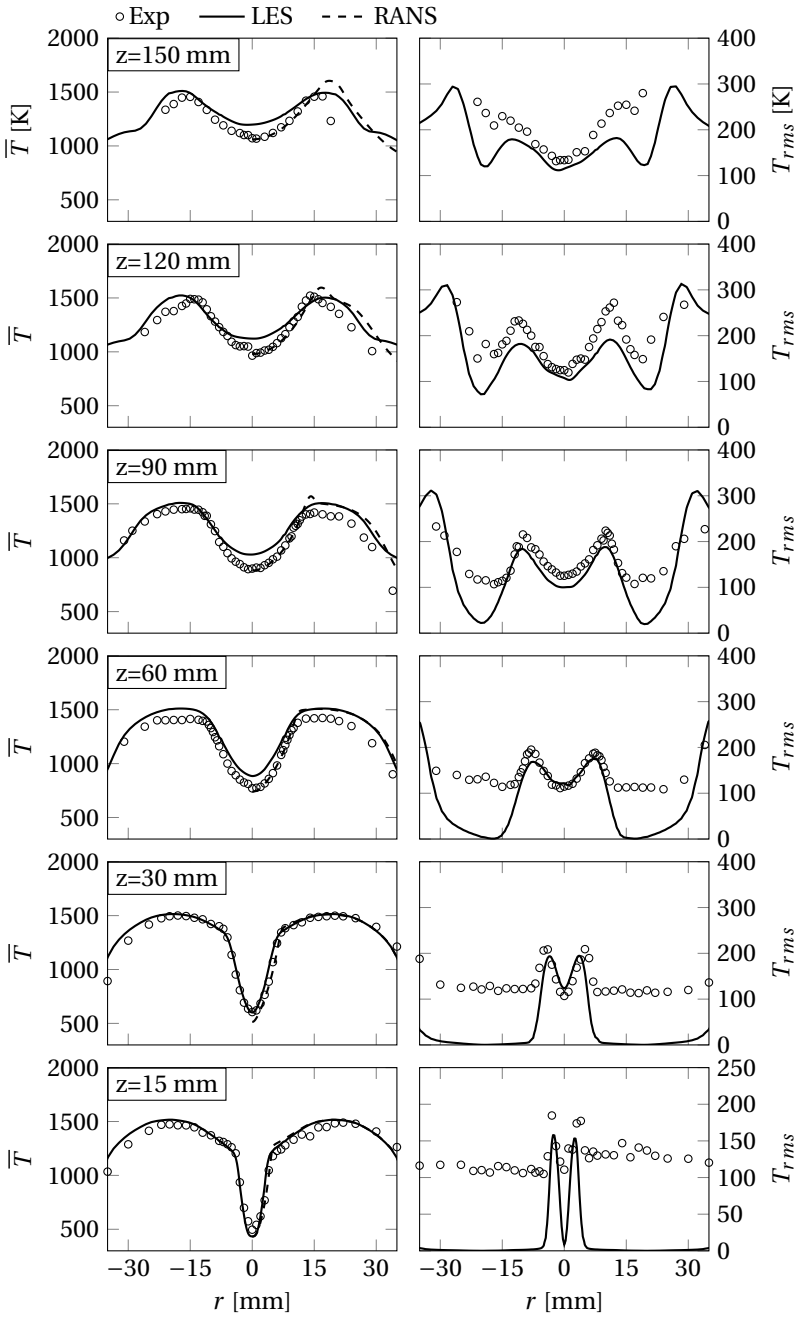


**Figure 6.16:** Mean turbulence kinetic energy profiles in radial direction at various axial locations above the fuel jet exit.

ing to experimental data at axial location z=60 mm, it is seen that the fuel coflow mixing extends up to radius 13 mm and the cold air penetrates to radius 30 mm which are indicated by an increase in temperature RMS values. At z=90 mm, the temperature RMS fluctuations still show a small flat region (few millimetres wide) which keeps the same magnitude as those of unaffected coflow. Above this location, mixing and cold air entrainment both affect the temperature fluctuations. It is also of interest to know whether entrained air takes part in the reactions. This will be analysed in the next subsection. In the simulations, absence of fluctuations of mixture fraction was imposed at the inlet boundary condition due to lack of mixture fraction information and also no temperature fluctuations are included. Therefore, the predicted temperature fluctuations in coflow are expected to be smaller than experimental values until coflow is affected by cold air entrainment and fuel-coflow mixing. As fuel and coflow mixing rate is quite large due to turbulence in the shear layer, predicted temperature RMS fluctuations in the shear layers match closely the experimental data at axial locations from 15 to 60 mm. The RMS values away from the fuel jet are significantly underpredicted at these locations. At higher axial locations, the general shape of the temperature RMS fluctuation profiles are well captured, but the values are underpredicted. It is noticed that the measured temperature RMS fluctuations in the coflow are about 50% higher than those in the recirculated burnt gas region in the furnace studied in Chapter 4. In conclusion, including the scalar fluctuations at the coflow inlet is of importance for further improvement in the LES results. The importance of including scalar fluctuations at the coflow boundary was also noticed by Sarras et al. (2014) in the framework of simulation using transported PDF method.



### 6.4.5. FLAME AND FLOW INTERACTION

It is interesting to point out that although luminous flames were observed in the experiments (Oldenhof et al., 2010, 2011), no temperature peak appears in the measured mean temperature profiles across the flame region. But from Figure 6.14 and Figure 6.16, we see that both the velocity and temperature RMS fluctuations are increased in some areas. This indicates that turbulent structures there have significant influence on the flame structure.

Figure 6.17 presents sequential snapshots for temperature extracted from the LES simulation. The white contour line indicates stoichiometric mixture fraction $Z_0$ based on unburnt fuel and air in the mixture and the black line represents the highest coflow temperature 1540 K in experiments. It should be noted that this black line does not start from coflow boundary because the coflow temperature at the boundary is about 1520 K, and it is the average temperature of the negative and positive $r$ from experimental data. It can be seen in Figure 6.17 that a vortex is generated at axial location around 60~70 mm in the shear layer between coflow and air. As it grows, air is entrained into the vortex and mixes with coflow and oxygen mass fraction in these locations is increased. However, these locations are still far away from the flame, thus the oxygen from the air stream should not be present in the mixing layer between fuel and coflow. The black temperature contour line can be used to indicate the presence of flame. Flame is mostly present above 80 mm. The flame fronts between 100 and 120 mm are stretched outwards by the large vortex. Further downstream, the outer vortex becomes larger and the region

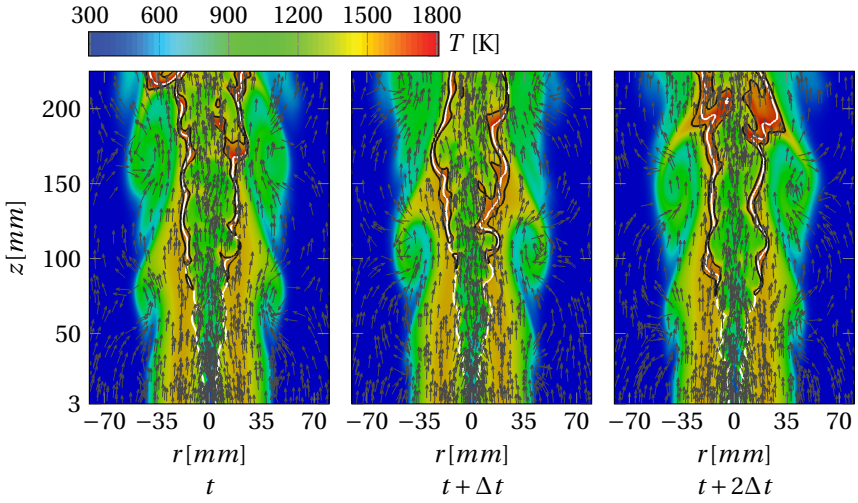


**Figure 6.17:** Sequential snapshots for temperature extracted from the LES simulation, $\Delta t = 0.02s$. White line indicates stoichiometric mixture fraction of unburnt fuel and air, black line represents maximum coflow temperature.



affected by the vortex extends to radius $r$ = 20 mm at axial location z=150 mm. The passage for coflow is narrowed by the outer vertices. The air entrained into the vortices is well mixed with coflow and is transported to the fuel-coflow mixing layer by the vortices. At these locations, air also participates in the reactions.

## 6.5. SUMMARY AND CONCLUSIONS

Both RANS and LES simulations of the DJHC-I 4100 flame were performed in this chapter. Flamelet Generated Manifold (FGM) method was extended to account for dilution effects on reactions in flameless combustion. The tabulated library consists of a series of flamelets calculated between fuel and diluted/undiluted air. Non-adiabatic effect was taken into account by reducing the diluent temperature in diluted air.

In the RANS simulations, the comparison between the results with progress variable variance and without progress variable variance indicate that the results are not sensitive to progress variable variance in this flame. Comparison between the results with different air inlet velocity shows that air stream inlet velocity has effects on the predicted temperature profile at high axial locations. Low air inlet velocity provides a better prediction of air entrainment effects on the flame structure.

Turbulent flow field statistics and temperature predictions are in overall good agreement between experimental data and both RANS and LES results. For the flow field statistics the LES predicts overall better results than RANS. This indicates that the current LES implementation incorporating with DAFGM model well captures the turbulent flow field and flame structure. The effect of air entrainment is significant at higher axial locations which is indicated by both experimental data and numerical predictions. In the LES results, it is clear to see that air is entrained by the large vortices generated in

the shear layer between coflow and air. At higher axial locations, the air is transported to the flame region and participates in the reaction. For better prediction of the flame structures, those effects should be taken into account.

# 7

# APPLICATION OF THE DAFGM TO FLAMELESS COMBUSTION IN A FURNACE

*In this chapter, the DAFGM model is applied to model the flameless combustion in the lab-scale furnace. RANS approach is used since LES approach is computationally expensive. Radiation and turbulence-radiation interaction are included in the RANS simulation. The predicted mean velocity, temperature and turbulence kinetic energy by the model are in good agreement with the experimental data when the progress variable fluctuation is included in the simulation. The predicted temperature rise in the reaction zone is 615 K which is close to the measured 600 K. It is seen from the predicted flow field that the dilution process can be divided into two phases, the direct dilution phase and the indirect dilution phase. In the direct dilution phase, all jets are diluted independently by the entrainment of burnt gas before the air jets interact with each other. The indirect dilution phase is dominated by turbulent mixing which transports burnt gas from recirculation zone to inner jets region. It can be concluded that the burner nozzle configuration is important for burnt gas entrainment.*

## 7.1. INTRODUCTION AND LITERATURE REVIEW

As discussed in Chapter 5, the modelling of turbulent reacting flows is one of the most challenging problems. The difficulty of the problem is due to the simultaneous presence of different physical phenomena, such as turbulence, combustion, thermal radiation, and to their interactions (Chun Sang et al., 2005). Compared to the jet-in-hot-coflow flames, flameless combustion in the furnace is more complex in terms of flow field, combustion characteristics and heat transfer. In the furnace, the flameless combustion is sustained by continuously entrainment of recirculated burnt gas into the fuel and the air streams. The dilution level varies over space which results in different combustion characteristics in space. Radiative heat transfer in the furnace is significantly affected by the high temperature walls and also has to be taken into account.

The dilution effects in flameless combustion modelling is one of the challenges. Using a detailed chemistry mechanism is preferred. The EDC model was applied in most of the simulation work in furnaces because it can be used with detailed chemistry and is relatively straightforward. But it is very computationally expensive. Moreover, the predicted results can be improved by adjusting the model constants, but there is no theoretical reason to support the quantitative changes on a general basis (Graça et al., 2013; Rebola et al., 2013). It is also concluded that the use of the EDC model for flameless combustion modelling requires further analysis (Lupant and Lybaert, 2015).

In the mean while, the FGM/FPV model is also being extended for flameless combustion modelling because of the efficiency of incorporating detailed chemistry in combustion modelling. For the flameless combustion in a furnace, it becomes a three-stream problem including fuel, air and recirculated burnt gas. To characterize the local combustion characteristics, the dilution effects have to be taken into account. In Section 5.5, the methods used in the Refs. (Lamouroux et al., 2014; Locci et al., 2014, 2015) have been reviewed. It is concluded in the Section 5.5.2 that the methods need to be improved in terms of the definition of diluent and lookup table generation.

On the other hand, the radiative heat transfer in the furnace is important. In a turbulent flow field, turbulence influences radiation and vice versa. Turbulence-radiation interaction (TRI) plays an important role in combustion systems when and where turbulent fluctuations and the radiative heat source are large and radiative emission is important (Coelho, 2012). In such a case, the temperature field is influenced by TRI, as well as all quantities (e.g. species) that are affected by temperature. Therefore, consideration of the temperature self-correlation alone is not sufficient to determine turbulence-radiation interactions (Li and Modest, 2003; Habibi et al., 2007). For the temperature sensitive reactions like the predictions of NO formation under the strong turbulence-chemistry interaction condition can only be performed when radiation is accounted for with full TRI (Habibi et al., 2007).

In this chapter, the DAFGM model is applied to the numerical simulation of the furnace studied in this thesis. The method described in Section 5.5.2 and 5.5.3 is used for chemistry tabulation accounting for the dilution effects. The TRI is included by the method developed in Section 5.6. In the method, the complete absorption coefficient-Planck function correlation is considered. And it is coupled with the DAFGM model. The case 2 in which the furnace was operated at equivalence ratio $\phi$=0.8 was chosen for numerical simulation validation.

## 7.2. CASE DESCRIPTION

The flame in the case 2 studied in the Chapter 3 and 4 is selected as the validation case for the numerical modelling study in this chapter. The Dutch natural gas is used as fuel and its composition can be found in Table 3.1. The detailed settings of the case 2 are summarized in the Table 4.2. Detailed velocity and temperature experimental measurements can be found in Section 4.2~4.4. They are used to validate the numerical results.

## 7.3. NUMERICAL DETAILS

### 7.3.1. COMPUTATIONAL DOMAIN

The simulations were performed using the RANS approach. The computational domain covered the complete volume of the furnace box. Its size is 320×320×630 mm$^3$, with a burner protruding 30 mm into the combustion chamber. The diameter of the burner is 92 mm. At cold conditions, the length of the four orifices on the nozzle is 28 mm. Considering the thermal expansion, they are extended to 30 mm long in mesh generation. Other details of the furnace can be found in Chapter 2. Since small round orifices are combined with a large cuboid, a multi-blocking strategy was used to obtain good quality mesh. O-grid method was used to handle the round orifices. The resulting blocking for the burner and the corresponding mesh for inlets are shown in Figure 7.1. The grids in jets region were refined. As grid edges radiate outwards, cell length in circumferential direction becomes larger. Therefore staged refinement in circumferential direction was applied. Two different mesh sizes with 2.5 and 9.5 million hexahedral cells are compared. The coarse mesh gives nearly the same results as the fine one. Therefore, the coarse mesh is used in the following.



### 7.3.2. TURBULENT COMBUSTION MODEL

Although only fuel and air streams are injected into the furnace, it becomes a three-stream problem when recirculated burnt gas is entrained into fuel and air streams. Unlike jet-in-hot-coflow flames, diluent stream in the furnace is generated inside the combustion chamber. No diluent is injected through the inlets. The diluent is defined as combustion products at stoichiometric mixture fraction at equilibrium state. Burnt gases are treated as a mixture of air and diluent at lean ($\phi < 1$) conditions.

The progress variable in this study is defined as a combination mass fraction of several species as follows:

$$Y_c = Y_{CO_2} + Y_{CO} + Y_{H_2O} + Y_{H_2}. \tag{7.1}$$

In the simulation, apart from continuity and momentum equations, the following Favre-averaged equations for mixture fraction $\widetilde{Z}$, progress variable $\widetilde{Y_c}$, dilution variable $\widetilde{Y_d}$, enthalpy $\widetilde{h}$, mixture fraction variance $\widetilde{Z''^2}$ and progress variable variance $\widetilde{Y_c''^2}$ are solved

$$\frac{\partial \overline{\rho}\widetilde{Z}}{\partial t} + \frac{\partial}{\partial x_i}\left(\overline{\rho}\widetilde{u_i}\widetilde{Z}\right) = \frac{\partial}{\partial x_i}\left[\overline{\rho}\left(\widetilde{D}+D_t\right)\frac{\partial \widetilde{Z}}{\partial x_i}\right], \tag{7.2}$$

$$\frac{\partial \overline{\rho}\widetilde{Y_c}}{\partial t} + \frac{\partial}{\partial x_i}\left(\overline{\rho}\widetilde{u_i}\widetilde{Y_c}\right) = \frac{\partial}{\partial x_i}\left[\overline{\rho}\left(\widetilde{D}+D_t\right)\frac{\partial \widetilde{Y_c}}{\partial x_i}\right] + \overline{\dot{\omega}}_{Y_c}, \tag{7.3}$$

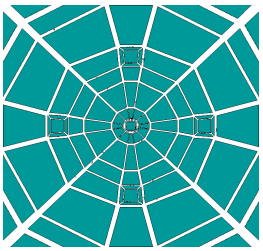

Blocking

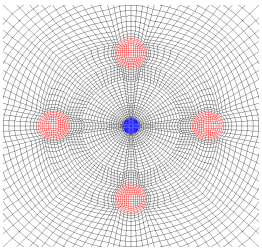

Inlets mesh

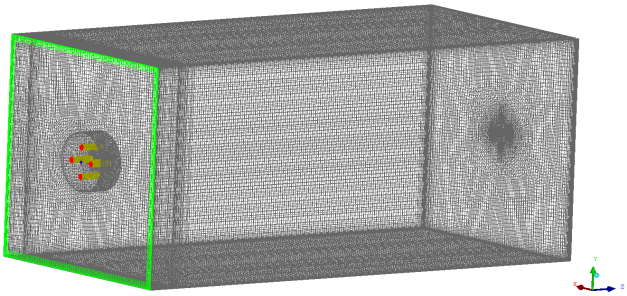

Furnace mesh

**Figure 7.1:** Illustration of the meshing strategy for furnace inlets.



$$\frac{\partial \overline{\rho}\widetilde{Y_d}}{\partial t}+\frac{\partial}{\partial x_i}\left(\overline{\rho}\widetilde{u_i}\widetilde{Y_d}\right)=\frac{\partial}{\partial x_i}\left[\overline{\rho}\left(\widetilde{D}+D_t\right)\frac{\partial \widetilde{Y_d}}{\partial x_i}\right]+\overline{\dot{\omega}}_{Y_d}, \tag{7.4}$$

$$\frac{\partial \overline{\rho}\widetilde{h}}{\partial t}+\frac{\partial}{\partial x_i}\left(\overline{\rho}\widetilde{u_i}\widetilde{h}\right)=\frac{\partial}{\partial x_i}\left[\overline{\rho}\left(\widetilde{D}+D_t\right)\frac{\partial \widetilde{h}}{\partial x_i}\right]+\overline{S}_r, \tag{7.5}$$

$$\frac{\partial \overline{\rho}\widetilde{Z''^2}}{\partial t}+\frac{\partial}{\partial x_i}\left(\overline{\rho}\widetilde{u_i}\widetilde{Z''^2}\right)=\frac{\partial}{\partial x_i}\left[\overline{\rho}\left(\widetilde{D}+D_t\right)\frac{\partial \widetilde{Z''^2}}{\partial x_i}\right]+2\overline{\rho}D_t\left(\frac{\partial \widetilde{Z}}{\partial x_i}\right)^2-\overline{\rho}\widetilde{\chi}_Z, \tag{7.6}$$

$$\frac{\partial \overline{\rho}\widetilde{Y_c''^2}}{\partial t}+\frac{\partial}{\partial x_i}\left(\overline{\rho}\widetilde{u_i}\widetilde{Y_c''^2}\right)=\frac{\partial}{\partial x_i}\left[\overline{\rho}\left(\widetilde{D}+D_t\right)\frac{\partial \widetilde{Y_c''^2}}{\partial x_i}\right]+2\overline{\rho}D_t\left(\frac{\partial \widetilde{Y_c}}{\partial x_i}\right)^2-\overline{\rho}\widetilde{\chi}_{Y_c} +2\left(\overline{Y_c\dot{\omega}_{Y_c}}-\widetilde{Y_c}\overline{\dot{\omega}}_{Y_c}\right). \tag{7.7}$$

The turbulent scalar dissipation rate for mixture fraction and progress variable variances $\overline{\rho}\widetilde{\chi}_Z$ and $\overline{\rho}\widetilde{\chi}_{Y_c}$ in above equations are modelled using (6.8) and (6.9) with the same model constants.

The source terms in Equations (7.3), (7.4) and (7.7), $\overline{\dot{\omega}}_{Y_c}$, $\overline{\dot{\omega}}_{Y_d}$ and $\overline{Y_c\dot{\omega}_{Y_c}}$ are tabulated in the lookup table. The source term $\overline{\dot{\omega}}_{Y_d}$ for dilution variable accounts for transforming burnt gas into the diluent stream. The radiation source term in the enthalpy equation (7.5) is calculated by the radiation model. During the simulations, lookup table

control parameters can be derived from $\widetilde{Z}$, $\widetilde{Y_c}$, $\widetilde{Y_d}$, $\widetilde{h}$, $\widetilde{Z''^2}$ and $\widetilde{Y_c''^2}$ by solving Equation (7.2)~(7.7). Feedbacks from reactions on temperature, density and viscosity, etc. are then retrieved from library.

### 7.3.3. COUPLING COMBUSTION AND RADIATION

The radiation source term in the Equation (7.5) is calculated by solving the RTE with the fvDOM and using WSGG radiative properties. Using the approach developed in Chapter 5 Section 5.6, only two additional quantities need to be tabulated in the library, that is, $\overline{\kappa}$ and $\overline{\kappa I_b}$ needed in the time-averaged RTE (5.99).

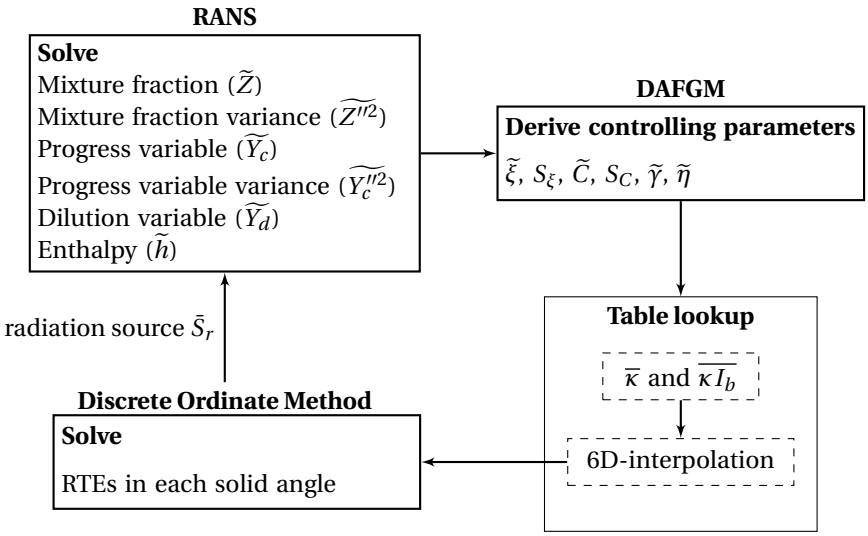


**Figure 7.2:** Schematic of the data exchange between radiation model (DOM) and RANS codes.

The complete coupling strategy is depicted in Figure 7.2 which is represented in the form of a flow diagram. In order to reduce the total computational time, a simulation was first made without radiation modelling. Once a converged combustion field was obtained, radiation was then switched on. The source term $S_r$ in the enthalpy equation is computed by integrating the solutions of the RTE over all directions. With continuously updated enthalpy equation, all fields are updated until the steady fields are obtained. Radiation is normally updated every 10 iterations of the flow solver.

### 7.3.4. BOUNDARY CONDITIONS

The known overall fuel and air flow rates for case 2 in the Table 4.2 were used to set the mass flow rate at the inlets of fuel and air. The calculated temperatures of fuel and air in Table 4.3 are used as inlet temperatures. Further, the following boundary conditions at

fuel and air inlet were applied.

| **fuel inlet** | **air inlet** |
|---|---|
| $\widetilde{Z} = 1$ | $\widetilde{Z} = 0$ |
| $\widetilde{Y_c} = Y_{c,f}$ | $\widetilde{Y_c} = 0$ |
| $\widetilde{Y_d} = 0$ | $\widetilde{Y_d} = 0$ |
| $\widetilde{h} = h_f$ | $\widetilde{h} = h_{air}$ |

where $Y_{c,f}$ is the value of progress variable computed from the fuel composition, $h_f$ and $h_{air}$ are the enthalpy in fuel and air stream respectively. The variances for mixture fraction and progress variable at boundary are both set at zero, $\widetilde{Z''^2} = 0$ and $\widetilde{Y_c''^2} = 0$.

The side wall temperature is set to be by 60 K lower than the averaged temperature at x=±120mm measured by CARS. Linear interpolation is used to calculate the temperature in between the heights $z$ where CARS data are available. The top wall and the bottom wall have uniform temperature and are respectively set at the highest temperature and lowest temperature of the side wall. It is assumed that the mixture fraction at walls is the mixture fraction at global equivalence ratio. With the temperature and mixture fraction, the enthalpies at walls are determined using the TU Delft FLAME code. The walls are treated as grey diffusive walls in radiation modelling. The emissivity is 0.8 for all walls.

### 7.3.5. NON-ADIABATIC DAFGM LIBRARY GENERATION

Due to the heat transfer through the furnace walls and significant radiative heat transfer in the furnace, non-adiabatic effects have to be included in the simulation. A non-adiabatic DAFGM library was generated in the way described in Section 5.5.3. The construction for the non-adiabatic DAFGM library in this chapter follows the same procedures used in Chapter 6. A series of laminar diffusion counterflow flames are solved in physical space with CHEM1D. Boundary conditions for counterflow flames are pure fuel at fuel side and pure or diluted air at the oxidizer side. The diluted air was calculated by using TU Delft FLAME code (Peeters, 1995) at the mixture fraction $Z = \gamma Z_{st}$ at given enthalpy losses. In this way, diluted air is the equilibrium products at mixture fraction $\gamma Z_{st}$. Here $\gamma$ is the air dilution level which represents the mass fraction of diluent in the diluted air. $\gamma$ is related to the dilution level $\alpha$ and $Z$ by Equation (5.80). Here $\alpha$ represents the mass fraction in the local mixture.

The differences compared to Chapter 6 are temperatures of fuel and air, and the maximum enthalpy loss in diluent. The determination for this value is based on the wall temperature measurements by thermocouples. Thermocouple data underpredict temperature due to unknown radiation effects, therefore the temperatures measured by thermocouples uncorrected for radiation loss can be directly used to determine the maximum enthalpy loss. The way to determine the maximum enthalpy loss is as following. The mixture fraction at wall surface is assumed to be equal to the mixture faction $Z_\phi$ at global equivalence ratio. In TU Delft FLAME code, gradually increasing enthalpy loss $\Delta h_\phi$ to calculate the equilibrium temperature at $Z_\phi$ until the lowest temperature is reached. Note that the enthalpy loss value $\Delta h_{\phi,max}$ obtained is the total enthalpy loss in the mixture. The enthalpy loss in the diluent accordingly equals $\Delta h_{\phi,max}/\gamma$.

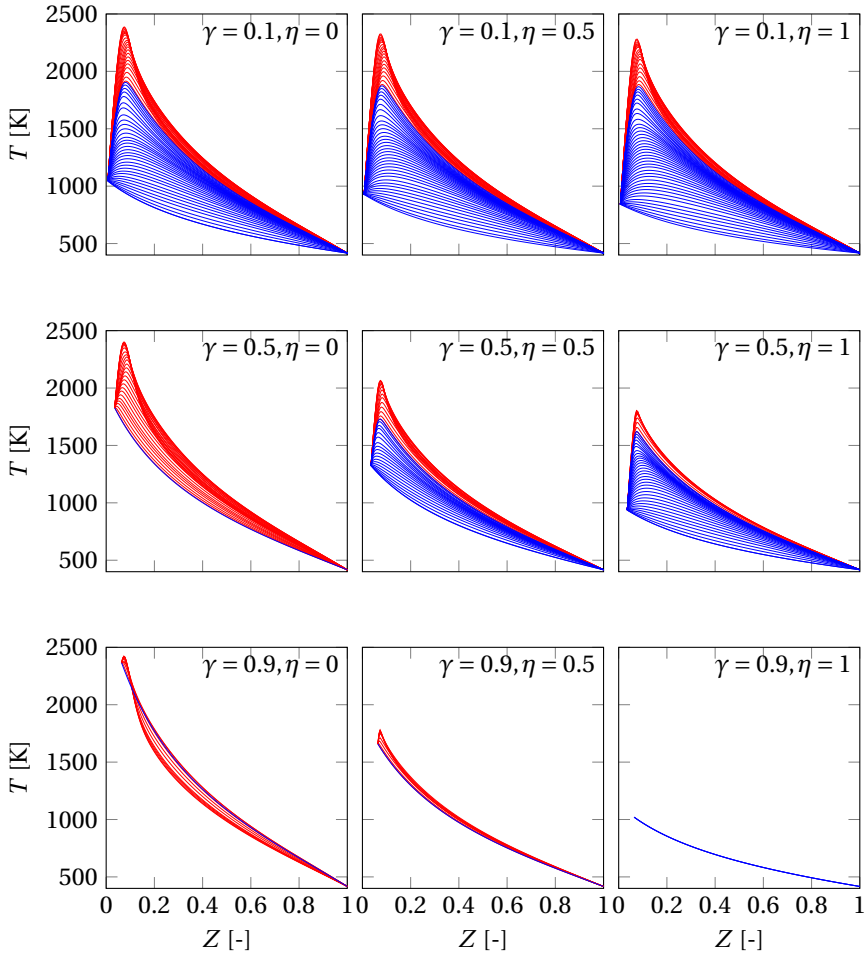


**Figure 7.3:** Flamelets calculated at different air dilution level $\gamma$ and enthalpy loss factor $\eta$. Red lines represent steady flamelets and blue lines represent unsteady extinguishing flamelets.

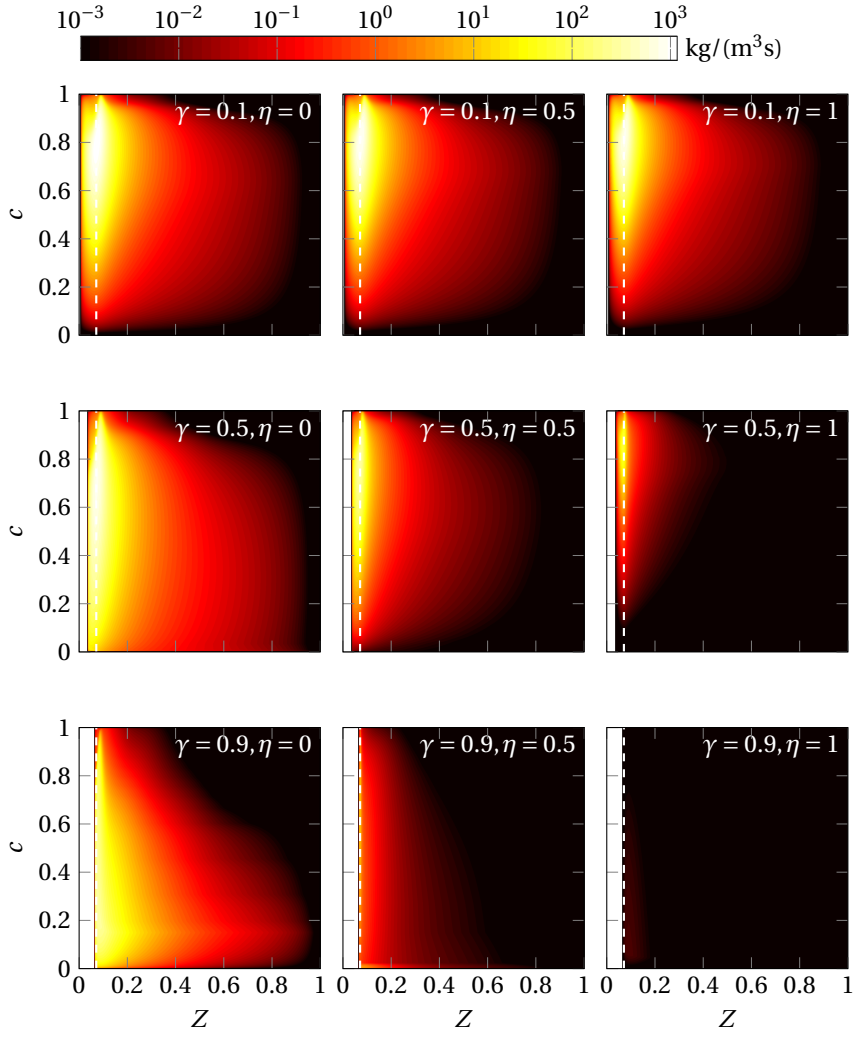


**Figure 7.4:** Progress variable source term in $(Z, C)$ space at different air dilution level $\gamma$ and enthalpy loss factor $\eta$ corresponding to the flamelets in Figure 7.3. The white dashed line represents the position of stoichiometric mixture fraction for fuel and undiluted air.

The FGM library constructed from steady flamelets covering the range of strain rate from a small value until extinction and unsteady extinguishing flamelet to cover the range from extinction to mixing state. The chemistry is described with the GRI 3.0 reaction mechanism. Figure 7.3 shows some examples of flamelets generated at air dilution level $\gamma$=0.1, 0.5 and 0.9, and enthalpy loss factor $\eta$=0, 0.5 and 1. $\eta$=0 corresponds to no enthalpy loss in diluent and $\eta$=1 represents maximum enthalpy loss in diluent. The corresponding progress variable source terms in each condition are plotted in Figure 7.4. In this study, maximum enthalpy loss is set to $2.341 \times 10^6$ J/kg. The flamelets are plotted as temperature versus mixture fraction $Z$ based on fuel and pure air. With diluted air, the starting point of flamelets at the oxidizer side gradually shifts towards to stoichiometric mixture fraction $Z_{st}$ as air dilution level increases to 1.

## 7.4. RESULTS AND DISCUSSIONS

### 7.4.1. INFLUENCE OF RADIATION AND PROGRESS VARIABLE FLUCTUATION

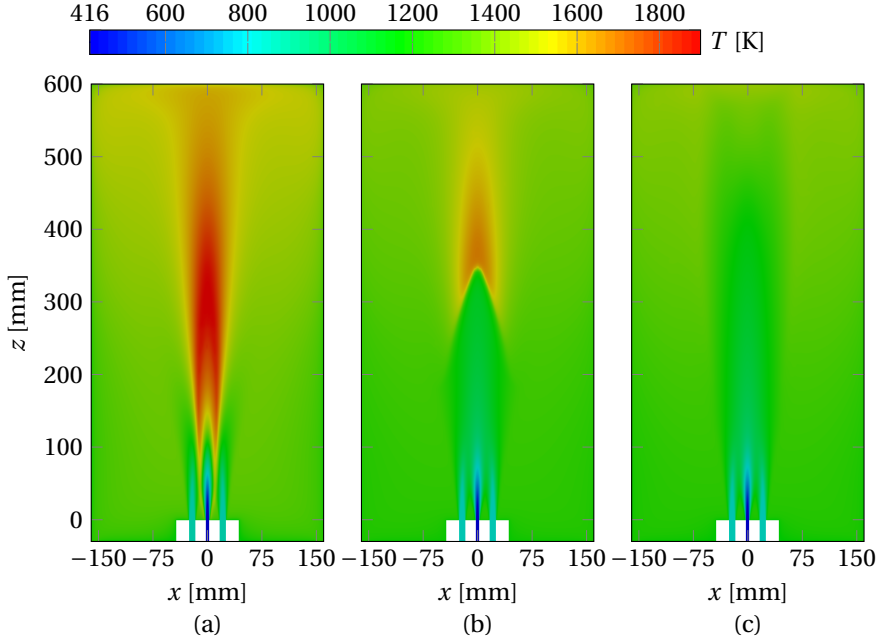


**Figure 7.5:** Predicted temperature fields on the vertical cross section parallel to the side wall: (a)excluding radiation and progress variable variance, (b)including radiation and excluding progress variable variance, (c)including radiation and progress variable variance.

It was mentioned that radiation plays an important role in the furnace. The contour plots in Figure 7.5(a) and (b) show respectively the results of simulations excluding and including radiative heat transfer and both excluding progress variable fluctuation. It is seen that the predicted temperature fields are quite different. The peak temperature in the reaction zone is as high as 1900 K without radiation consideration, and it is reduced

to 1677 K when radiation is taken into account. Without radiation, the reactions start very early, below z=100 mm, and reactions take place in the jets mixing layers. Whereas, the reaction zone is lifted up to z=300 mm when radiation is included. Due to local radiation heat loss, reactions are delayed. Therefore, radiation indeed significantly influences the results and has to be included.

It should be noted that in Figure 7.5(a) weak reactions are present in fuel jet shear layers near the nozzle exit. The ability of predicting reactions between fuel and recirculated burnt gas is one of the advantages of defining diluent as the equilibrium products at stoichiometric condition. The temperature profiles at 10, 20, 30 and 50 mm above the nozzle exit are displayed in Figure 7.6. Two temperature peaks at the fuel jet boundaries were observed in each profile due to reactions. The temperatures at the peaks increase and the peak moves outwards as the fuel jet develops from z=10 mm to z=30 mm. Further away from the nozzle at z=50 mm, these reactions are influenced by air jets. However, these reactions were not observed in the results when radiation effects were included in the simulations. According to the measured temperature shown in Figure 4.9 for case 2, the temperature samples which indicate the presence of reactions are very few. Their contribution to the mean is not visible. In RANS simulation only the mean values are predicted, a LES approach should be applied to see these temperature variations.

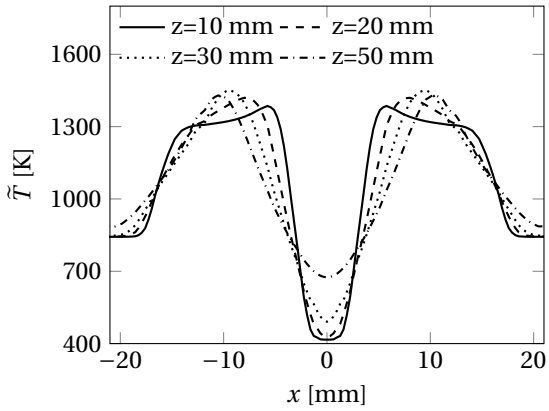


**Figure 7.6:** Predicted temperature profiles near fuel jet exit excluding both radiation and progress variable variance.

Figure 7.5(b) and (c) show the results of simulations including radiation and respectively excluding and including progress variable fluctuation. The predicted peak mean temperature in the furnace is reduced to 1430 K when progress variable fluctuation is taken into account by a presumed $\beta$-PDF. The temperature increase in the reaction zone is quite limited which is getting close to flameless combustion characteristics. We therefore conclude that the results are sensitive to progress variable fluctuation and these have to be considered. A detailed comparison between predicted and measured mean temperature is provided in Section 7.4.3.

Figure 7.7 shows the predicted mean fields of $\widetilde{Z}$, $\widetilde{Y_c}$, $\widetilde{Y_d}$ and $\widetilde{h}$ in the case where both radiation and progress variable fluctuation are included. The difference between $\widetilde{Y_c}$ and

$\widetilde{Y_d}$ in the range between z=400 mm and z=600 mm is quite clear. The increase of dilution variable is delayed compared to progress variable, and this is true according to the method to model dilution stream. As noticed in the OH* chemiluminescence images, the reactions mainly take place in this region. Therefore, progress variable increases, and when complete reaction is reached, dilution variable starts increase.

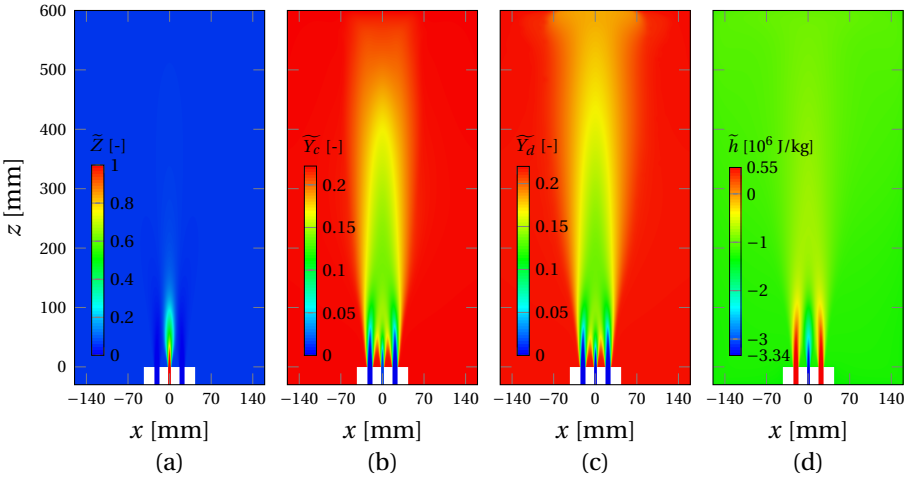


**Figure 7.7:** Predicted mean scalar fields in the furnace. (a): mean mixture fraction; (b): mean progress variable, (c): mean dilution variable; (d): mean enthalpy.

7

### 7.4.2. VELOCITY PREDICTION

To get better understanding of the mixing between fuel, air and burnt gas, numerical results are of great help since they can provide very detailed information. Figure 7.8 shows the flow fields on the middle plane (across fuel jet and two air jets) and the diagonal plane. The flow patterns are different on these two planes. On the middle plane, there are two recirculation zones in the upper part of the furnace shown by the white solid lines. While on the diagonal plane, the recirculation zones go through the furnace from top to bottom. With this comparison, we conclude that burnt gas mainly goes down through the four corners of the combustion chamber. The lowest positions of red solid lines on the diagonal plane indicate the location where the adjacent air jets start interacting with each other. Below this position, five jets develop independently and are diluted directly by entrained burnt gas. This phase is called direct dilution phase. Above this position, fuel jet is totally surrounded by air jets which blocks direct burnt gas entrainment by fuel jet. Further dilution can only be achieved by turbulent mixing which transport burnt gas from air jets outer boundaries to the inner region. This phase is called indirect dilution phase. Both dilution phases are important. There are two essential factors to establish flameless combustion with this burner nozzle configuration. One is high turbulence which is able to prevent an attached flame. The other is dilution. Dilution is achieved by internal recirculation driven by jets. For the direct dilution phase, the amount of burnt gas joining the jets flow depends on the jets momentum and the air jets arrangement

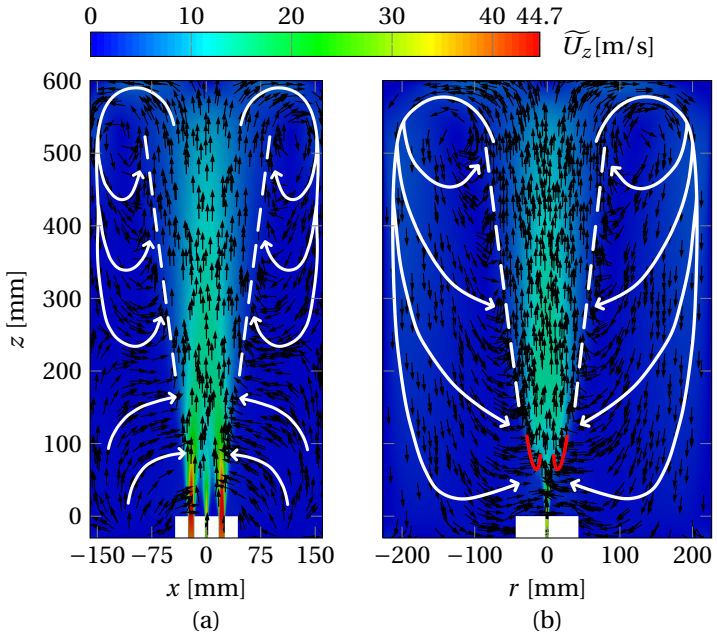


**Figure 7.8:** Predicted mean flow field in the furnace. (a): middle plane across fuel and two air jets; (b): diagonal plane, $r$ is the distance to fuel centre.



which determine the physical location where direct dilution phase ends. For example, with larger distance between fuel and air jets, the position shifts higher and away from the centre. This provides better condition for direct dilution in both time and space. However, one should also ensure the mixing between fuel and air to achieve complete combustion before recirculation starts.

Figure 7.9 shows the comparison between predicted velocity (solid lines) and measured velocity (symbols). It should be point out that velocity data from z=100 to 500 mm presented here is shifted for the convenience of comparison. The velocity $\widetilde{U}_z$ is shifted by a distance z·tan$\theta$ towards negative x direction. The angle $\theta$ is determined by the position where shear stress $\widetilde{u_z''u_x''} = 0$, and here tan$\theta \approx 0.03$. The velocities $\widetilde{U}_x$ used here are the shifted values suggested in Chapter 4. The velocity on the middle plane obtained from simulation is in good agreement with measurements. The mean velocity $\widetilde{U}_z$ at nozzle exit is in excellent agreement with experimental data. As flow develops, the velocities are over predicted at z=50 and 100 mm. This is similar to the simulation results of DJHC in Chapter 6, where the mean flow velocity was also over predicted at lower positions. But at higher positions from z=200 to 500 mm, the overall mean flow velocity predicted with $k-\epsilon$ model is quite good. As for the velocity in x direction, the overall trends are captured and the turning points on the profiles are also well captured. But the peak values at some turning points on the profiles of z=50 and 100 mm are mispredicted.

Figure 7.10 displays the turbulence kinetic energy predicted by the standard $k-\epsilon$ model. The experimental data is also shifted in the same way as for velocity. It is seen that

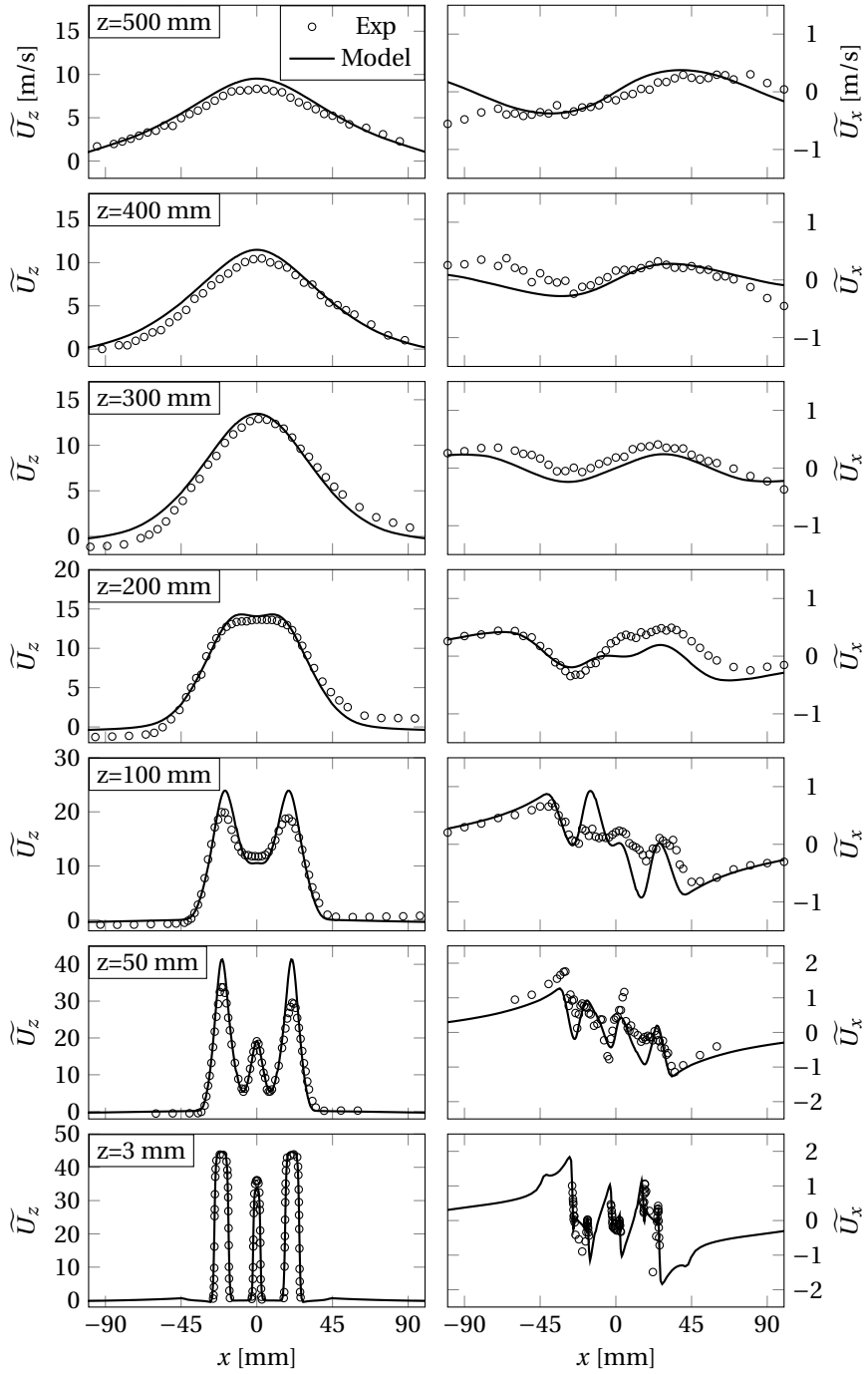


**Figure 7.9:** Comparison between predicted and measured mean velocity.

the turbulence kinetic energy is under predicted at the beginning, but is over predicted at z=100 and 200 mm. Satisfactory predictions start from z=300 mm. The variation of under prediction-over prediction-satisfactory prediction is observed in both simulations for DJHC and furnace using $k-\epsilon$ model. According to the LES results from the DJHC case, LES showed much better ability to capture turbulence kinetic energy since large turbulent scales are resolved. It can be a good choice for further investigation.

### 7.4.3. TEMPERATURE PREDICTION

A comparison between the predicted and the measured mean temperature is shown in Figure 7.11. The measured temperatures are also shifted. Good agreement is observed. Near the nozzle exit, the mean temperature is very well predicted at z=25 mm. But the temperature in jets region are under predicted from z=100 to 300 mm. This is due to the discrepancy in the turbulence prediction. The turbulence kinetic energy is under predicted below z=100 mm which means the turbulent mixing rate is under estimated in that region. Therefore mixing between burnt gas, fuel and air streams are slowed down. Less burnt gas is mixed and predicted local temperature is lower than measured temperature. But the turbulence kinetic energy is over predicted at z=100 and 200 mm. High turbulent mixing rate accelerates the mixing process and predicted temperature is getting closer to measured temperature from z=200 to 300 mm. Further downstream, mixing is

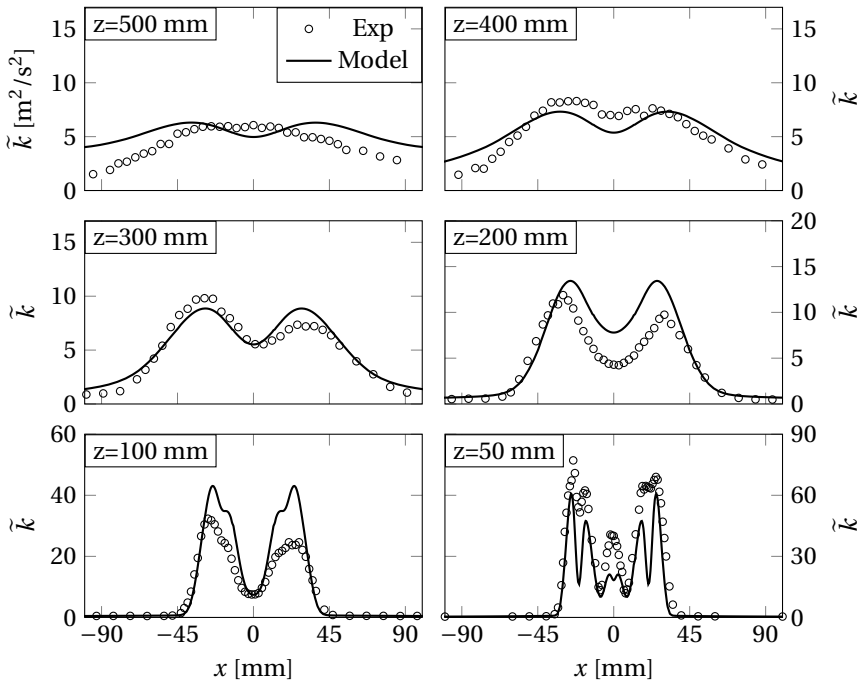


**Figure 7.10:** Comparison between predicted mean and measured turbulence kinetic energy.

well developed, the difference between predicted and measured temperature becomes smaller. The temperature increase from z=400 to 500 mm is due to reactions. The maximum temperature increase is about 136 K. The predicted overall temperature increase from air temperature to burnt state is less than 615 K. This detailed analysis confirms that good level of agreement is obtained only when both radiation and progress variable fluctuation are included in the model.

Figure 7.12 presents the temperature, dilution level $\alpha$ and air dilution level $\gamma$ profiles along the fuel tube axis. The temperature profile along the line may be divided into 3 stages. The first stage is below z=100 mm and is corresponding to the direct dilution phase; the second stage is from z=100 to 400 mm and is corresponding to the indirect dilution phase; the third one is the combustion stage. The first stage can be divided into two subphases. Below z=50 mm, it is fuel mixing with burnt gas, air dilution level $\gamma$ is flat and temperature along the central line increases very fast. Above z=50 mm, the central region starts being slightly influenced by the air stream. Temperature rise slows down slightly. This is indicated by the decrease in air dilution level from z=50 to 100 mm. Although the diluent mass fraction $\alpha$ is still increasing, it reaches a peak at z≈100 mm. The diluent present has come from the direct entrainment by the jets near the nozzle exit. However, as the air jets develop, the inner part which is much less diluted starts

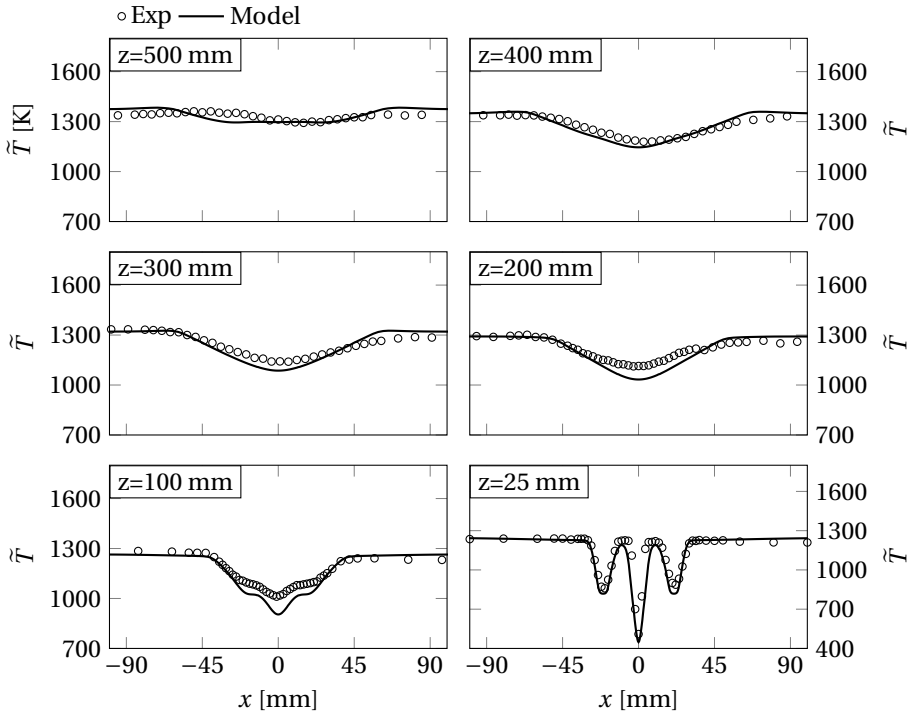


**Figure 7.11:** Comparison between predicted and measured mean temperature.

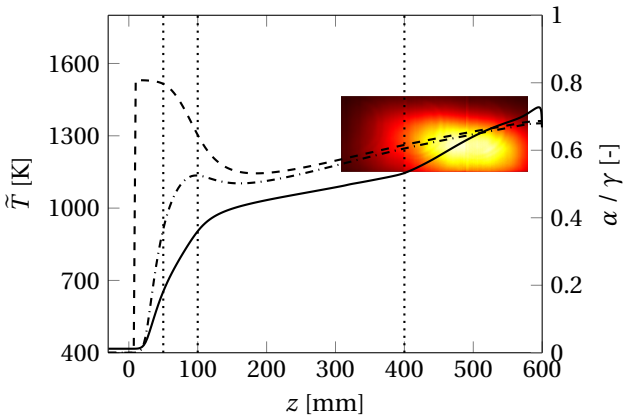


**Figure 7.12:** Predicted parameter profiles along the central line. solid line: mean temperature $\widetilde{T}$, dashed line: air dilution level $\gamma$, dash-dotted line: dilution level $\alpha$.

affecting the central region, the dilution level accordingly decreases, and temperature rise becomes very slow due to the relatively low air temperature. That is, the indirect dilution phase starts. Further downstream, more diluent from the recirculation region is transported into the central region by turbulent mixing, thus the dilution level starts increasing again. In the combustion stage, temperature increase is accelerated above z=400 mm due to the heat release from reactions. This prediction is consistent with the position of the reaction zone indicated by experimentally observed OH* chemiluminescence.

7

## 7.5. SUMMARY AND CONCLUSIONS

A numerical simulation of flameless combustion in a lab-scale furnace has been made using a RANS approach. The DAFGM model which extends the FGM method to account for dilution effects on reactions in flameless combustion was applied. The tabulated library consists of a series of flamelets calculated between fuel and pure or diluted air with non-adiabatic effects included. TRI was also included.

It is found that radiation and progress variable fluctuation both have significant influences on the results. Reactions between fuel and burnt gas were only observed in the results excluding effects of radiation and progress variable variance. The flame becomes lifted and total temperature rise in the reaction zone is not more than 615 K, which is close to the experimental temperature rise (600 K) reported in Chapter 4 and showing flameless combustion characteristics.

Based on the analysis of the flow field, it is found that the distance between fuel and air jets determines the relative importance of the direct dilution phase and the indirect dilution phase. The direct dilution phase occurs before air jets interact with each other. Then all jets are diluted independently by entrainment of burnt gas. The indirect dilution phase occurs when the air jets are already interacting with each other and is dominated by turbulent mixing, transporting burnt gas from recirculation zone to inner region of

the jets. Good predictions for mixing and dilution process before combustion takes place is important because they provide the initial state for combustion. Therefore the choice of proper turbulence model is of importance. RANS is found to perform well.

Overall, the simulation results obtained with the proposed model are in good agreement with experimental data, demonstrating the ability to capture the effects of dilution and enthalpy loss on the flameless combustion in the furnace. However, LES simulation is suggested to obtain more accurate prediction of the velocity and temperature fluctuations.

# 8

# Conclusions and Recommendations

## 8.1. SUMMARY AND CONCLUSIONS

In this thesis flameless combustion in a furnace has been studied experimentally and numerically. The investigation was carried out for the case of a lab-scale furnace using a commercial burner and confinement by insulation walls. This configuration is more representative for industrial scale furnaces than the often studied flameless combustion systems employing jet-in-hot-coflow burners but at the same time sufficiently small to allow accurate detailed experiments in contrast with the industrial scale furnaces. Experimental data obtained on lab-scale combustion setups can be valuable for the validations of numerical models with a wide range of applicability. A summary of the investigations is given in this Chapter, first for the experiments and then for the modelling, and final conclusions are given.

### 8.1.1. EXPERIMENTS

In Chapter 2, the design and construction of the lab-scale furnace has been explained. The furnace consists of a WS REKUMAT 150 recuperative Flame-FLOX burner and an insulated combustion chamber. By the presence of a quartz window, the furnace allows optical access for detailed laser diagnostics. It is not easy to move the spatial position of optical measurement probe volumes. Therefore the choice has been made to move the furnace volume instead. In order to do so the positions of the burner and the internal top wall of the furnace are moving relative to the side wall containing the windows for optical access. The amount of heat extracted from the combustion process in the furnace and the overall temperature control were realized by the amount of cooling through the external top wall. This is a top wall fixed to the side wall above the moving internal wall. It has been checked using thermocouples that for different relative positions of burner and optical window, the mean temperature at fixed locations in the furnace (relative to the burner) is less than 20 K. This shows that the procedure does not create unwanted bias.

Three operating conditions have been studied in detail. The furnace was operated using Dutch natural gas as fuel at the thermal input 9 kW (fuel mass flow rate based), at equivalence ratio $\phi$=0.7, $\phi$=0.8 and $\phi$=0.9, respectively. The ignition and flame behaviour in the flameless regime have been studied by the mean and time resolved OH* chemiluminescence images at different equivalence ratios. Detailed measurements of velocity and temperature have also been performed, respectively using LDA and CARS. Problems due to beam steering and seeding particle deposition were addressed. Due to the short beam path inside the furnace and the low thermal gradient in the furnace, the beam steering has little influence. By using a forward scatter LDA system, the signal strength was significantly improved although the seeding particles deposits on the optical window reducing the transmissivity.

It was found that the combustion characteristics in the furnace are sensitive to equivalence ratio. For the current burner nozzle configuration, decreasing the equivalence ratio causes a shift of the reaction upstream and also makes the combustion more having the characteristics of “flameless combustion”. This trend with change in equivalence ratio is opposite to that observed in the Ref. (Veríssimo et al., 2011) where a different nozzle configuration was used. Indeed, the burner nozzle configuration directly influences the internal flow field. The flow field with strong hot burnt gas entrainment is best to es-

tablish flameless combustion. It was found that the combustion process in the furnace is sustained by autoignition. In the chemiluminescence measurements three types of ignition behaviour were observed, namely individual autoignition kernel, multiple autoignition kernels and autoignition kernel cluster. The reaction zone is a collection of these three autoignition structures, occurring very frequently and sustaining the reactions in the furnace without any need for another flame stabilization strategy or mechanism. We call this situation presence of a "sustained combustion". By this process the heat release by combustion in the furnace proceeds continuously without presence of a stabilized local flame.

Autoignition is controlled by local conditions, mainly depending on the flow, mixture composition and temperature. The latter two are determined by the air dilution level and the enthalpy loss in the diluent. The autoignition occurrence boundary with respect to these parameters was found by a series of calculations of laminar counterflow flames. For Dutch natural gas, the critical air dilution level range was found to be from 0.7 to 0.8, which corresponds to a range of $O_2$ mass fraction in the oxidizer from 4.5% to 7% in oxidizer. This range of conditions can be related to a recirculation ratio about 2.33 to 4. At the indicated range, autoignition can be achieved in a wide range of flow conditions. Working in this range provides the best condition to sustain a stable flameless combustion process.

It is noted that the flow field plays important roles in internal recirculation and preventing locally stabilized flames. The internal flow field is driven by high momentum air jets. It becomes more turbulent as the equivalence ratio is decreased, enhancing turbulent mixing and accelerating internal burnt gas entrainment. Although the turbulent fluctuations in the three cases are similar and the difference in velocity fluctuations between $\phi$=0.8 and $\phi$= 0.9 is only around 10% to 30% (based on $\phi$= 0.7), the reaction intensity and the position of the reaction zone clearly change.

The final mean temperature rise in the furnace due to combustion is low but the high temperature samples and temperature histograms show that exothermic reactions are indeed present in the reaction zone, but there is no locally stabilized flame front like structure present in the reaction zone. The mean temperature rise compared to the air inlet temperature is less than 600 K, which is much lower than in the case of conventional combustion of fuel and air. The instantaneous peak temperature is lower than 1800 K and less than 1.5% of the samples is higher than 1700 K. The reactions become visible (according to Trms and histograms) at around the height z=300 mm below which the fuel and air are continuously mixing and diluted by entrained hot burnt gas. Large temperature fluctuations in the reaction zone (z=400 and 500 mm) indicate an unsteady combustion process. The low peak temperature greatly reduces the formation of $NO_x$. For all considered operating conditions the $NO_x$ emissions was below 1 ppmv.

Occurrence of reactions between the fuel and the oxygen left in the burnt gas are confirmed by the temperature histograms above the nozzle exit at z=25 mm. This suggests that the distance between the fuel and the air nozzles should be considered an important factor in the burner design. A large distance is good to provide sufficient time for the dilution process of air jets and fuel. But the air jets also play a role in suppressing direct combustion of fuel with the oxygen contained in the burnt gas. Therefore there should be a minimal distance between air and fuel to allow the air jets to play this role. This

issue is also addressed in the simulation results of the flow field in the modelling part.

### 8.1.2. MODELLING

The challenge of modelling flameless combustion is to include the dilution effects on reactions. Although the EDC model is available and is often applied to flameless combustion modelling, the model constants need to be modified in different situations. Besides, its computational cost is very high when using a detailed chemistry mechanism. It has been reported in the literature that the flamelet structure is observed also in the flameless combustion. Therefore, a tabulated chemistry approach like FGM is still attractive for flameless combustion because it is requiring less computational resources while incorporating detailed chemistry. But the dilution effects have to be included in the model. An extended FGM model referred to as DAFGM model was developed for combustion with dilution effects. In the model, it is proposed to treat the reactions in the furnace as non-premixed combustion of fuel with diluted air. The diluted air conceptually is divided in diluent and air. The diluent is defined as the combustion products at stoichiometric mixture fraction of combustion of fuel with air, $Z_{st}$ . Using the above, the tabulated library can cover all relevant states and has advantages compared to the methods in the Refs. (Lamouroux et al., 2014; Locci et al., 2014, 2015).

A method to couple radiation with DAFGM has been developed. For this, enthalpy had to be introduced as additional independent variable. The radiative properties of gases are modelled with a weighted-sum-of-grey-gas (WSGG) model which accounts for the mole ratio between $CO_2$ and $H_2O$. To use the DAFGM in turbulent flow a table of PDF integrated quantities is created. Turbulence-radiation interaction is included in the DAFGM by also storing in the table of PDF averaged quantities for the absorption coefficient and the correlation between absorption coefficient and black body emissivity. The models have been implemented in the open source CFD package OpenFOAM-2.3.1 including a new table lookup scheme for 2 to 6 dimensional lookup table and interpolations.

The approach has been applied to two situations, the Delft jet-in-hot coflow flame DJHC-I Re=4100 (referred to as DJHC-I in the following) and the case $\phi$= 0.8 of the lab-scale furnace. In the first case both RANS and LES turbulence modelling were used and radiation did not have to be taken into account. In the second case, RANS modelling was used and taking into account radiation is essential. The application of DAFGM with LES well captures the turbulent flow field and the flame structure of DJHC-I flame. Turbulent flow field statistics and temperature predictions are in overall good agreement with experimental data for both RANS and LES results. But the LES predicts overall better velocity and temperature fields than RANS. In the LES results, it is clearly seen that the surrounding air mixes with the coflow through the action of large vortices, and then reaches the reaction zone between fuel and coflow at high axial locations. The assumed inlet velocity of surrounding air has effects on the predicted temperature profile at high axial locations. Low air inlet velocity provides a better prediction of air entrainment effects on the flame structure. It is found that the results in DJHC-I are not sensitive to whether or not the progress variable fluctuation are taken into account, but on the contrary in the case of the furnace taking into account the progress variable fluctuation is important to obtain good agreement with experiments. Then the mean temperature is

predicted very well. The highest temperature rise reached in the upper part of the furnace compared to inflow air temperature is not more than 615 K, which agrees with the measured temperature rise, which is 600 K.

The simulation provides detailed insight in the phenomena in the near burner zone. Good predictions for mixing and dilution processes before combustion takes place are important because these processes provide the initial state for flameless combustion to proceed. Therefore the choice of proper turbulence model is of importance. RANS is found to perform well. It is seen that the distance between fuel and air jets determines the relative importance of the direct dilution phase and the indirect dilution phase. The direct dilution phase covers the region before the air jets interact with each other. Then all jets are being diluted by entrainment of product gas independently from each other. The indirect dilution phase covers the range when the air jets are already mixing with each other while being further diluted with products. Turbulent mixing creates the mixture of fuel, air and products which then is successfully described by the DAFGM based on fuel, air and products of stoichiometric combustion. The overall simulation results obtained with the proposed model are in good agreement with experimental data in both the DJHC-I flame and the furnace, demonstrating the ability to capture the dilution and enthalpy loss effects on flameless combustion.

## 8.2. RECOMMENDATIONS

Significant progress towards the understanding of the reacting flow structure of flameless combustion has been made in this study. There remains however some issues which could be further investigated both from experimental and from modelling point of view. The following recommendations are made to advance this field beyond the stage reached in this thesis.

### EXPERIMENTAL MEASUREMENTS

In this experimental study, the reaction zone imaging and high-speed visualizations of OH* chemiluminescence were performed with a single camera. The signal obtained is integrated along the view direction. Therefore it cannot reveal the 3D spatial structure of the reaction zone. However, it has been found that the flameless combustion in the furnace is sustained by autoignition which is controlled by local conditions. Further measurements like imaging of the OH or the $CH_2O$ radical (simultaneously with flow field measurements, e.g. PIV) would provide more information to clarify the autoignition structure.

In this work the velocity and temperature are measured separately with single-point measurement techniques. These experimental data provide valuable information on the flow and reaction characteristics. However, the instantaneous interactions between the flow and reactions are still not clear. In the flameless combustion regime, the reactions are relatively slow, and the flame structure development depends on both flow and chemistry. Simultaneous imaging of flow field using PIV and temperature field with two-dimensional Rayleigh imaging or radical imaging (OH-PLIF, $CH_2O$-PLIF) would provide both qualitative and quantitative information of the flame-flow interactions. With more detailed measurements, the influence of different nozzle configurations including nozzle diameter, number of air nozzles and the distance between the fuel and the air nozzles

can be better understood.

### NUMERICAL MODELLING

As is observed in both the JHC flames and the current furnace, autoignition is found to be responsible for sustaining the combustion process in the flameless combustion regime. When creating an FGM it could be more representative to use igniting flamelets instead of extinguishing flamelets. Also it may be important to include the effect of strain on the ignition process by including flamelets of different strain rates. This would lead to an additional dimension in the lookup table. Of course, including more information in the lookup table may be good, but it also means that the size of the table would become very large. A large amount of memory is needed to store the lookup table during the simulation and this may cause a problem on parallel computing platforms (using MPI, every core reads a copy of the lookup table and the memory per core is limited). In this study, the simulations were run on the Dutch supercomputer Cartesius. It is found that the five-dimensional table (about 225 MB) is fine on the thin nodes (24 cores, 64 GB memory) and the six-dimensional table (about 3000MB) case can only run on the fat node (32 cores, 256 GB memory). The memory usage is also related to the mesh size. An effective way to reduce the memory used to store the lookup tables is to use MPI-3 which allows for a shared memory allocation. The table could be stored in the shared memory and every core in one node could access the lookup table. Thus, each node only stores one copy of the lookup table. Another way is to reduce the dimension of the table. In this study, the presumed PDF method is used. Then variances of mixture fraction and of progress variable appear as extra dimensions of the table. Using other presumed PDFs (e.g., top-hat PDF (only for LES)) to reduce dimensionality of look-up tables could be effective. This can also be avoided when transported PDF methods (in a Lagrangian or an Eulerian approach) are used. Then the joint one-point statistical fluctuations of the variables ($Z$, $Y_c$, $Y_d$, $h$) are evaluated online and only a lower-dimensional table of instantaneous properties is needed. However, it leads to increase in computational cost, and the increase could be significant. A balance needs to be defined. Finally, for the prediction of $NO_x$ emissions, because its process of formation is slow compared to the time-scales taken into account in the flamelets, an additional independent transport equation for mean $NO_x$ mass fraction should be solved with the source term of $NO_x$ formation included in the DAFGM table.

# REFERENCES


Abtahizadeh, E., de Goey, P., van Oijen, J., 2017. LES of Delft jet-in-hot coflow burner to investigate the effect of preferential diffusion on autoignition of $CH_4/H_2$ flames. Fuel 191, 36–45.

Abtahizadeh, E., van Oijen, J., de Goey, P., 2012. Numerical study of MILD combustion with entrainment of burned gas into oxidizer and/or fuel streams. Combustion and Flame 159 (6), 2155–2165.

Albrecht, B. A., Zahirovic, S., Bastiaans, R. J. M., van Oijen, J. A., de Goey, L. P. H., 2008. A premixed flamelet-PDF model for biomass combustion in a grate furnace. Energy & Fuels 22 (3), 1570–1580.

Aldén, M., Edner, H., Svanberg, S., 1983. Coherent anti-stokes raman spectroscopy (CARS) applied in combustion probing. Physica Scripta 27 (1), 29.

Alves, M., Rosa, C., Costa, M., 2013. Effect of the oxidizer composition on the co and nox emissions from a laboratory combustor operating under oxy-fuel conditions. Energy & Fuels 27 (1), 561–567.

Amaya, J., Collado, E., Cuenot, B., Poinsot, D. T., 2010. Coupling LES, radiation and structure in gas turbine simulations. In: CTR, Proceedings of Summer Program. pp. 239–249.

ANSYS. Ansys fluent 16.2 theory guide.

Arghode, V. K., Gupta, A. K., 2011. Investigation of reverse flow distributed combustion for gas turbine application. Applied Energy 88 (4), 1096–1104.

Arghode, V. K., Gupta, A. K., Bryden, K. M., 2012. High intensity colorless distributed combustion for ultra low emissions and enhanced performance. Applied Energy 92, 822–830.

Arndt, C. M., Papageorge, M. J., Fuest, F., Sutton, J. A., Meier, W., Aigner, M., 2016. The role of temperature, mixture fraction, and scalar dissipation rate on transient methane injection and auto-ignition in a jet in hot coflow burner. Combustion and Flame 167, 60–71.

Arndt, C. M., Schießl, R., Gounder, J. D., Meier, W., Aigner, M., 2013. Flame stabilization and auto-ignition of pulsed methane jets in a hot coflow: Influence of temperature. Proceedings of the Combustion Institute 34 (1), 1483–1490.

Avdić, A., Kuenne, G., Janicka, J., 2016. Flow physics of a bluff-body swirl stabilized flame and their prediction by means of a joint eulerian stochastic field and tabulated chemistry approach. Flow Turbulence & Combustion 97 (4), 1–26.

Bao, H., 2017. Development and validation of new eddy dissipation concept (EDC) model for MILD combustion. Master's thesis, Delft University of Technology.

Beér, J. M., 1994. Minimizing $NO_x$ emissions from stationary combustion; reaction engineering methodology. Chemical Engineering Science 49 (24, Part A), 4067–4083.

Beyler, C. L., Gouldin, F. C., 1981. Flame structure in a swirl stabilized combustor inferred by radiant emission measurements. Symposium (International) on Combustion 18 (1), 1011–1019.

Bhaya, R., De, A., Yadav, R., 2014. Large eddy simulation of MILD combustion using PDF-based turbulence-chemistry interaction models. Combustion Science and Technology 186 (9), 1138–1165.

Boyd, R., 2008. Nonlinear optics, Third Edition. Academic Press, Burlington.

Bray, K., Peters, N., 1994. Laminar flamelets in turbulent reacting flows, In: Libby, P., Williams, F. (Eds.), Turbulent Reacting Flows. Academic, London.

Castela, M., Veríssimo, A. S., Rocha, A. M. A., Costa, M., 2012. Experimental study of the combustion regimes occurring in a laboratory combustor. Combustion Science and Technology 184 (2), 243–258.

Cavaliere, A., de Joannon, M., 2004. MILD combustion. Progress in Energy and Combustion Science 30 (4), 329–366.

Cavigiolo, A., Galbiati, M., Effuggi, A., Gelosa, D., Rota, R., 2003. MILD combustion in a laboratory-scale apparatus. Combustion Science and Technology 175, 1347–1367.

Cha, C. M., Pitsch, H., 2002. Higher-order conditional moment closure modelling of local extinction and reignition in turbulent combustion. Combustion Theory and Modelling 6 (3), 425–437.

Chandy, A. J., Glaze, D. J., Frankel, S. H., 2009. A hybrid large eddy simulation/filtered mass density function for the calculation of strongly radiating turbulent flames. Journal of Heat Transfer 131 (5), 051201–051201–9, 10.1115/1.3082405.

CHEM1D. A one-dimensional laminar flame code, Eindhoven University of Technology.

Chigier, N. A., 1981. Energy, combustion, and environment. McGraw-Hill Inc. US.

Choi, G.-M., Katsuki, M., 2001. Advanced low $NO_x$ combustion using highly preheated air. Energy Conversion and Management 42 (5), 639–652.

Chrigui, M., Gounder, J., Sadiki, A., Masri, A. R., Janicka, J., 2012. Partially premixed reacting acetone spray using LES and FGM tabulated chemistry. Combustion and Flame 159 (8), 2718–2741.

Christo, F., Dally, B., 2004. Application of transport PDF approach for modelling MILD combustion. In: 15th Australasian Fluid Mechanics Conference.

Christo, F. C., Dally, B. B., 2005. Modeling turbulent reacting jets issuing into a hot and diluted coflow. Combustion and Flame 142 (1), 117–129.

Chun Sang, Y., Hong, G. I., Yi, W., Arnaud, T., 2005. Interaction of turbulence, chemistry, and radiation in strained nonpremixed flames. Journal of Physics: Conference Series 16 (1), 91.

Coclite, A., Pascazio, G., De Palma, P., Cutrone, L., Ihme, M., 2015. An SMLD joint PDF model for turbulent non-premixed combustion using the flamelet progress variable approach. Flow, Turbulence and Combustion 95 (1), 97–119.

Coelho, P. J., 2007. Numerical simulation of the interaction between turbulence and radiation in reactive flows. Progress in Energy and Combustion Science 33 (4), 311–383.

Coelho, P. J., 2009. Approximate solutions of the filtered radiative transfer equation in large eddy simulations of turbulent reactive flows. Combustion and Flame 156 (5), 1099–1110.

Coelho, P. J., 2012. Turbulence-radiation interaction: From theory to application in numerical simulations. Journal of Heat Transfer 134 (3), 1–13.

Coelho, P. J., Peters, N., 2001. Numerical simulation of a MILD combustion burner. Combustion and Flame 124 (3), 503–518.

Colin, O., Michel, J.-B., 2016. A two-dimensional tabulated flamelet combustion model for furnace applications. Flow, Turbulence and Combustion.

Coppalle, A., Vervisch, P., 1983. The total emissivities of high-temperature flames. Combustion and Flame 49 (1), 101–108.

Correa, S. M., 1993. A review of $NO_x$ formation under gas-turbine combustion conditions. Combustion Science and Technology 87 (1-6), 329–362.

Dally, B. B., Karpetis, A. N., Barlow, R. S., 2002. Structure of turbulent non-premixed jet flames in a diluted hot coflow. Proceedings of the Combustion Institute 29 (1), 1147–1154.

Dally, B. B., Riesmeier, E., Peters, N., 2004. Effect of fuel mixture on moderate and intense low oxygen dilution combustion. Combustion and Flame 137 (4), 418–431.

De, A., Oldenhof, E., Sathiah, P., Roekaerts, D., 2011. Numerical simulation of Delft-Jet-in-Hot-Coflow (DJHC) flames using the eddy dissipation concept model for turbulence–chemistry interaction. Flow, Turbulence and Combustion 87 (4), 537–567.

de Joannon, M., Saponaro, A., Cavaliere, A., 2000. Zero-dimensional analysis of diluted oxidation of methane in rich conditions. Proceedings of the Combustion Institute 28 (2), 1639–1646.

Deardorff, J. W., 1970. A numerical study of three-dimensional turbulent channel flow at large reynolds numbers. Journal of Fluid Mechanics 41 (2), 453–480.

Domingo, P., Vervisch, L., Veynante, D., 2008. Large-eddy simulation of a lifted methane jet flame in a vitiated coflow. Combustion and Flame 152 (3), 415–432.

Duwig, C., Li, B., Li, Z. S., Aldén, M., 2012. High resolution imaging of flameless and distributed turbulent combustion. Combustion and Flame 159 (1), 306–316.

Eckbreth, A. C., 1978. BOXCARS: Crossed-beam phase-matched CARS generation in gases. Applied Physics Letters 32 (7), 421–423.

Eckbreth, A. C., 1981. Recent advances in laser diagnostics for temperature and species concentration in combustion. Symposium (International) on Combustion 18 (1), 1471–1488.

Eckert, E. R. G., 2004. Radiative transfer, h. c. hottel and a. f. sarofim, mcgraw-hill book company, new york, 1967. 52 pages. AIChE Journal 15 (5), 794–796.

Favre, A., 1969. Statistical equations of turbulent gases. In: Problems of hydrodynamics and continuum mechanics. pp. 231–266.

Fenimore, C. P., 1971. Formation of nitric oxide in premixed hydrocarbon flames. Symposium (International) on Combustion 13 (1), 373–380.

Fiveland, W. A., 1984. Discrete-ordinates solutions of the radiative transport equation for rectangular enclosures. ASME Transactions Journal of Heat Transfer 106, 699–706.

Flamme, M., Christian, P. B., Kremer, H., 1988. Effect of combustion air preheating on $NO_x$ emissions from gas burners in high-temperature industrial applications. Chemical Engineering & Technology 11 (1), 104–112.

Floyd, J., Kempf, A. M., Kronenburg, A., Ram, R. H., 2009. A simple model for the filtered density function for passive scalar combustion LES. Combustion Theory and Modelling 13 (4), 559–588.

Frank, G., Pfitzner, M., 2015. On the generation of non-adiabatic, non-premixed flamelet libraries with special emphasis on wall heat losses. In: Proceedings of 9th Mediterranean Combustion Symposium.

Germano, M., Piomelli, U., Moin, P., Cabot, W. H., 1991. A dynamic subgrid-scale eddy viscosity model. Physics of Fluids A: Fluid Dynamics 3 (7), 1760–1765.

Ghosh, S., Friedrich, R., 2015. Effects of radiative heat transfer on the turbulence structure in inert and reacting mixing layers. Physics of Fluids 27 (5), 311–383.

Ghosh, S., Friedrich, R., Stemmer, C., 2015. LES of turbulence-radiation interaction in plane reacting and inert mixing layers. In: Fröhlich, J., Kuerten, H., Geurts, B. J., Armenio, V. (Eds.), Direct and Large-Eddy Simulation IX. Springer International Publishing, pp. 489–495.

Giordano, P., Lentini, D., 2001. Combustion-radiation-turbulence interaction modeling in absorbing/emitting nonpremixed flames. Combustion Science and Technology 172 (1), 1–22.

Girimaji, S. S., 1992. On the modeling of scalar diffusion in isotropic turbulence. Physics of Fluids A: Fluid Dynamics 4 (11), 2529–2537.

Glassman, I., Yetter, R. A., 2008. Chapter 8-environmental combustion considerations, In: Combustion (Fourth Edition). Academic Press, Burlington, pp. 409–494.

Graça, M., Duarte, A., Coelho, P. J., Costa, M., 2013. Numerical simulation of a reversed flow small-scale combustor. Fuel Processing Technology 107, 126–137.

Habibi, A., Merci, B., Roekaerts, D., 2007. Turbulence radiation interaction in Reynolds-Averaged Navier-Stokes simulations of nonpremixed piloted turbulent laboratory-scale flames. Combustion and Flame 151 (1-2), 303–320.

Hanby, V. I., 1994. Combustion and pollution control in heating systems. Springer London, London.

Hardalupas, Y., Orain, M., 2004. Local measurements of the time-dependent heat release rate and equivalence ratio using chemiluminescent emission from a flame. Combustion and Flame 139 (3), 188–207.

Hardalupas, Y., Panoutsos, C. S., Taylor, A. M. K. P., 2010. Spatial resolution of a chemiluminescence sensor for local heat-release rate and equivalence ratio measurements in a model gas turbine combustor. Experiments in Fluids 49 (4), 883–909.

Hasegawa, T., Tanaka, R., Niioka, T., 1997. Combustion with high temperature low oxygen air in regenerative burners. In: Proc. The First Asia-Pacific Conference on Combustion. pp. 12–15.

Hosseini, S. E., Wahid, M. A., 2013. Biogas utilization: Experimental investigation on biogas flameless combustion in lab-scale furnace. Energy Conversion and Management 74, 426–432.

Ihme, M., Cha, C. M., Pitsch, H., 2005. Prediction of local extinction and re-ignition effects in non-premixed turbulent combustion using a flamelet/progress variable approach. Proceedings of the Combustion Institute 30 (1), 793–800.

Ihme, M., Pitsch, H., 2008a. Prediction of extinction and reignition in nonpremixed turbulent flames using a flamelet/progress variable model 1. A priori study and presumed pdf closure. Combustion and Flame 155 (1-2), 70–89.

Ihme, M., Pitsch, H., 2008b. Prediction of extinction and reignition in nonpremixed turbulent flames using a flamelet/progress variable model 2. Application in LES of Sandia flames D and E. Combustion and Flame 155 (1-2), 90–107.

Ihme, M., See, Y. C., 2011. LES flamelet modeling of a three-stream MILD combustor: Analysis of flame sensitivity to scalar inflow conditions. Proceedings of the Combustion Institute 33 (1), 1309–1317.

Ihme, M., Zhang, J., He, G., Dally, B., 2012. Large-eddy simulation of a jet-in-hot-coflow burner operating in the oxygen-diluted combustion regime. Flow, Turbulence and Combustion 89 (3), 449–464.

Ikeda, Y., Kojima, J., Nakajima, T., 2001. Local chemiluminescence measurements of OH*, CH* and C2* at turbulent premixed flame-fronts, In: Yoshida, A. (Ed.), Smart Control of Turbulent Combustion. Springer Japan, Tokyo, pp. 12–27.

Ishiguro, T., Tsuge, S., Furuhata, T., Kitagawa, K., Arai, N., Hasegawa, T., Tanaka, R., Gupta, A. K., 1998. Homogenization and stabilization during combustion of hydrocarbons with preheated air. Symposium (International) on Combustion 27 (2), 3205–3213.

Janicka, J., Peters, N., 1982. Prediction of turbulent jet diffusion flame lift-off using a PDF transport equation. Symposium (International) on Combustion 19 (1), 367–374.

Johansson, R., Leckner, B., Andersson, K., Johnsson, F., 2011. Account for variations in the $H_2O$ to $CO_2$ molar ratio when modelling gaseous radiative heat transfer with the weighted-sum-of-grey-gases model. Combustion and Flame 158 (5), 893–901.

Jones, W. P., Launder, B. E., 1972. The prediction of laminarization with a two-equation model of turbulence. International Journal of Heat and Mass Transfer 15 (2), 301–314.

Ju, Y., Niioka, T., 1997. Computation of $NO_x$ emission of a methane-air diffusion flame in a two-dimensional laminar jet with detailed chemistry. Combustion Theory and Modelling 1 (3), 243–258.

Kabashnikov, V. P., Kmit, G. I., 1979. Influence of turbulent fluctuations on thermal radiation. Journal of Applied Spectroscopy 31 (2), 963–967.

Katsuki, M., Hasegawa, T., 1998. The science and technology of combustion in highly preheated air. Symposium (International) on Combustion 27 (2), 3135–3146.

Kim, S. H., Huh, K. Y., Dally, B., 2005. Conditional moment closure modeling of turbulent nonpremixed combustion in diluted hot coflow. Proceedings of the Combustion Institute 30 (1), 751–757.

Kitagawa, K., Konishi, N., Arai, N., Gupta, A. K., 2003. Temporally resolved two-dimensional spectroscopic study on the effect of highly preheated and low oxygen concentration air on combustion. Journal of Engineering for Gas Turbines and Power 125 (1), 326.

Kornev, N., Hassel, E., 2007. Method of random spots for generation of synthetic inhomogeneous turbulent fields with prescribed autocorrelation functions. Communications in Numerical Methods in Engineering 23 (1), 35–43.

Kornev, N., Kröger, H., Hassel, E., 2008. Synthesis of homogeneous anisotropic turbulent fields with prescribed second-order statistics by the random spots method. Communications in Numerical Methods in Engineering 24 (10), 875–877.

Kulkarni, R. M., Polifke, W., 2013. LES of Delft-Jet-In-Hot-Coflow (DJHC) with tabulated chemistry and stochastic fields combustion model. Fuel Processing Technology 107, 138–146.

Kumar, S., Paul, P. J., Mukunda, H. S., 2002. Studies on a new high-intensity low-emission burner. Proceedings of the Combustion Institute 29 (1), 1131–1137.

Kuo, K. K., 2005. Principles of combustion, Second Edition. John Wiley & Sons.

Labahn, J. W., Devaud, C. B., 2016. Large eddy simulations (LES) including conditional source-term estimation (CSE) applied to two Delft-Jet-in-Hot-Coflow (DJHC) flames. Combustion and Flame 164, 68–84.

Labahn, J. W., Dovizio, D., Devaud, C. B., 2015. Numerical simulation of the delft-jet-in-hot-coflow (djhc) flame using conditional source-term estimation. Proceedings of the Combustion Institute 35 (3), 3547–3555.

Lallemant, N., Sayre, A., Weber, R., 1996. Evaluation of emissivity correlations for $H_2O$-$CO_2$-$N_2$/air mixtures and coupling with solution methods of the radiative transfer equation. Progress in Energy and Combustion Science 22 (6), 543–574.

Lamouroux, J., Ihme, M., Fiorina, B., Gicquel, O., 2014. Tabulated chemistry approach for diluted combustion regimes with internal recirculation and heat losses. Combustion and Flame 161 (8), 2120–2136.

Lee, J. G., Santavicca, D. A., 2003. Experimental diagnostics for the study of combustion instabilities in lean premixed combustors. Journal of Propulsion and Power 19 (5), 735–750.

Li, G., Modest, M. F., 2003. Importance of turbulence-radiation interactions in turbulent diffusion jet flames. Journal of Heat Transfer 125 (5), 831.

Li, P., Wang, F., Mi, J., Dally, B. B., Mei, Z., 2014. MILD combustion under different premixing patterns and characteristics of the reaction regime. Energy & Fuels 28 (3), 2211–2226.

Lilly, D., 1966. On the application of the eddy viscosity concept in the inertial sub-range of turbulence. NCAR Manuscript 123, 1–19.

Locci, C., Colin, O., Michel, J.-B., 2014. Large eddy simulations of a small-scale flameless combustor by means of diluted homogeneous reactors. Flow, Turbulence and Combustion 93 (2), 305–347.

Locci, C., Colin, O., Poitou, D., Mauss, F., 2015. A tabulated, flamelet based NO model for large eddy simulations of non-premixed turbulent jets with enthalpy loss. Flow, Turbulence and Combustion 94 (4), 691–729.

Lupant, D., Lybaert, P., 2015. Assessment of the EDC combustion model in MILD conditions with in-furnace experimental data. Applied Thermal Engineering 75, 93–102.

Lupant, D., Pesenti, B., Evrard, P., Lybaert, P., 2007. Numerical and experimental characterization of a self-regenerative flameless oxidation burner operation in a pilot-scale furnace. Combustion Science and Technology 179, 437–453.

Lupant, D., Pesenti, B., Lybaert, P., 2010. Influence of probe sampling on reacting species measurement in diluted combustion. Experimental Thermal and Fluid Science 34 (5), 516–522.

Ma, L., 2015. Computational modeling of turbulent spray combustion. Ph.D. thesis, Delft University of Technology.

Marques, C. S., Benvenutti, L. H., Bertran, C. A., 2001. Experimental study of OH*, CHO*, CH*, and C2* radicals in $C_2H_2/O_2$ and $C_2H_2/O_2$/Ar flames in a closed chamber. Combustion Science and Technology 167 (1), 113–129.

Marracino, B., Lentini, D., 1997. Radiation modelling in non-luminous non-premixed turbulent flames. Combustion Science and Technology 128 (1-6), 23–48.

Mastorakos, E., 2009. Ignition of turbulent non-premixed flames. Progress in Energy and Combustion Science 35 (1), 57–97.

Medwell, P. R., Kalt, P. A. M., Dally, B. B., 2007. Simultaneous imaging of oh, formaldehyde, and temperature of turbulent nonpremixed jet flames in a heated and diluted coflow. Combustion and Flame 148 (1), 48–61.

Medwell, P. R., Kalt, P. A. M., Dally, B. B., 2009. Reaction zone weakening effects under hot and diluted oxidant stream conditions. Combustion Science and Technology 181 (7), 937–953.

Mi, J., Li, P., Dally, B. B., Craig, R. A., 2009. Importance of initial momentum rate and air-fuel premixing on moderate or intense low oxygen dilution (MILD) combustion in a recuperative furnace. Energy & Fuels 23 (11), 5349–5356.

Mi, J., Li, P., Zheng, C., 2010. Numerical simulation of flameless premixed combustion with an annular nozzle in a recuperative furnace. Chinese Journal of Chemical Engineering 18 (1), 10–17.

Mi, J., Li, P., Zheng, C., 2011. Impact of injection conditions on flame characteristics from a parallel multi-jet burner. Energy 36 (11), 6583–6595.

Miller, J. A., Bowman, C. T., 1989. Mechanism and modeling of nitrogen chemistry in combustion. Progress in Energy and Combustion Science 15 (4), 287–338.

Minamoto, Y., Dunstan, T. D., Swaminathan, N., Cant, R. S., 2013. DNS of EGR-type turbulent flame in MILD condition. Proceedings of the Combustion Institute 34 (2), 3231–3238.

Minamoto, Y., Swaminathan, N., 2014. Scalar gradient behaviour in MILD combustion. Combustion and Flame 161 (4), 1063–1075.

Minamoto, Y., Swaminathan, N., Cant, R. S., Leung, T., 2014. Reaction zones and their structure in MILD combustion. Combustion Science and Technology 186 (8), 1075–1096.

Modest, M. F., 2003. Radiative heat transfer, Second Edition. McGraw-Hill, New York.

Mohamed, H., Hmaeid, B., Mohamed, S., 2012. Fundamentals and simulation of MILD combustion, In: Rasul, M. (Ed.), Thermal Power Plants. InTech, Rijeka.

Moin, P., Squires, K., Cabot, W., Lee, S., 1998. A dynamic subgrid-scale model for compressible turbulence and scalar transport. Physics of Fluids A Fluid Dynamics 3 (11), 2746–2757.

Mosca, G., 2017. Experimental and numerical study on MILD combustion of low LHV fuels. Ph.D. thesis, University of Mons.

Nishimura, M., Suzuki, T., Nakanishi, R., Kitamura, R., 1997. Low-$NO_x$ combustion under high preheated air temperature condition in an industrial furnace. Energy Conversion and Management 38 (10), 1353–1363.

Nori, V., Seitzman, J., 2008. Evaluation of chemiluminescence as a combustion diagnostic under varying operating conditions, In: 46th AIAA Aerospace Sciences Meeting and Exhibit. Aerospace Sciences Meetings. American Institute of Aeronautics and Astronautics.

Olbricht, C., Janicka, J., Kempf, A., 2010. LES as a prediction tool for lifted flames in a model gas turbine combustor (43970), 423–432, 10.1115/GT2010-22525.

Olbricht, C., Stein, O. T., Janicka, J., van Oijen, J. A., Wysocki, S., Kempf, A. M., 2012. LES of lifted flames in a gas turbine model combustor using top-hat filtered PFGM chemistry. Fuel 96, 100–107.

Oldenhof, E., Tummers, M. J., Van Veen, E. H., Roekaerts, D. J. E. M., 2010. Ignition kernel formation and lift-off behaviour of jet-in-hot-coflow flames. Combustion and Flame 157 (6), 1167–1178.

Oldenhof, E., Tummers, M. J., Van Veen, E. H., Roekaerts, D. J. E. M., 2011. Role of entrainment in the stabilisation of jet-in-hot-coflow flames. Combustion and Flame 158 (8), 1553–1563.

Oldenhof, E., Tummers, M. J., Van Veen, E. H., Roekaerts, D. J. E. M., 2013. Conditional flow field statistics of jet-in-hot-coflow flames. Combustion and Flame 160 (8), 1428–1440.

Özdemir, I. B., Peters, N., 2001. Characteristics of the reaction zone in a combustor operating at MILD combustion. Experiments in Fluids 30 (6), 683–695.

Parente, A., Malik, M. R., Contino, F., Cuoci, A., Dally, B. B., 2016. Extension of the eddy dissipation concept for turbulence/chemistry interactions to MILD combustion. Fuel 163, 98–111.

Paschereit, C. O., Gutmark, E., Weisenstein, W., 1998. Structure and control of thermoacoustic instabilities in a gas-turbine combustor. Combustion Science and Technology 138 (1-6), 213–232.

Paul, S. C., Paul, M. C., 2010. Radiative heat transfer during turbulent combustion process. International Communications in Heat and Mass Transfer 37 (1), 1–6.

Peeters, T. W., 1995. Numerical modeling of turbulent natural-gas diffusion flames. Ph.D. thesis, Delft University of Technology.

Peters, N., 1984. Laminar diffusion flamelet models in non-premixed turbulent combustion. Progress in Energy and Combustion Science 10 (3), 319–339.

Peters, N., 2004. Turbulent combustion. Cambridge University Press.

Pierce, C. D., Moin, P., 2004. Progress-variable approach for large-eddy simulation of non-premixed turbulent combustion. Journal of Fluid Mechanics 504, 73–97.

Pino Martín, M., Piomelli, U., Candler, G. V., 2000. Subgrid-scale models for compressible large-eddy simulations. Theoretical and Computational Fluid Dynamics 13 (5), 361–376.

Piomelli, U., Moin, P., Ferziger, J. H., 1988. Model consistency in large eddy simulation of turbulent channel flows. The Physics of Fluids 31 (7), 1884–1891.

Plessing, T., Peters, N., Wünning, J. G., 1998. Laseroptical investigation of highly preheated combustion with strong exhaust gas recirculation. Symposium (International) on Combustion 27 (2), 3197–3204.

Poinsot, T., Veynante, D., 2012. Theoretical and numerical combustion, Third Edition. Aquaprint.

Poitou, D., El Hafi, M., Cuenot, B., 2011. Analysis of radiation modeling for turbulent combustion: Development of a methodology to couple turbulent combustion and radiative heat transfer in LES. Journal of Heat Transfer 133 (6), 062701–062701–10, 10.1115/1.4003552.

Pope, S., 2000. Turbulent flows. Cambridge University Press.

Rebola, A., Coelho, P. J., Costa, M., 2013. Assessment of the performance of several turbulence and combustion models in the numerical simulation of a flameless combustor. Combustion Science and Technology 185 (4), 600–626.

Rittler, A., Proch, F., Kempf, A. M., 2015. LES of the Sydney piloted spray flame series with the PFGM/ATF approach and different sub-filter models. Combustion and Flame 162 (4), 1575–1598.

Roger, M., Coelho, P. J., da Silva, C. B., 2010. The influence of the non-resolved scales of thermal radiation in large eddy simulation of turbulent flows: A fundamental study. International Journal of Heat and Mass Transfer 53 (13), 2897–2907.

Ruan, J., Kobayashi, H., Niioka, T., Ju, Y., 2001. Combined effects of nongray radiation and pressure on premixed $ch_4/o_2/co_2$ flames. Combustion and Flame 124 (1), 225–230.

Sarras, G., Mahmoudi, Y., Arteaga Mendez, L. D., Van Veen, E. H., Tummers, M. J., Roekaerts, D. J. E. M., 2014. Modeling of turbulent natural gas and biogas flames of the delft jet-in-hot-coflow burner: Effects of coflow temperature, fuel temperature and fuel composition on the flame lift-off height. Flow, Turbulence and Combustion 93 (4), 607–635.

Shimada, T., Akiyama, T., Fukushima, S., Mitsui, K., Jinno, M., Kitagawa, K., Arai, N., Gupta, A. K., 2005. Time-resolved temperature profiling of flames with highly preheated/low oxygen concentration air in an industrial size furnace. Journal of Engineering for Gas Turbines and Power 127 (3), 464.

Smagorinsky, J. S., 1963. General circulation experiments with the primitive equations. Monthly Weather Review 91 (3), 99–164.

Smith, T., Shen, Z., Friedman, J., 1982. Evaluation of coefficients for the weighted-sum-of-gray-gases model. Journal of Heat Transfer 104 (4), 602–608.

Song, X., Guo, Q., Hu, C., Gong, Y., Yu, G., 2016. OH* chemiluminescence characteristics and structures of the impinging reaction region in opposed impinging diffusion flames. Energy & Fuels 30 (2), 1428–1436.

Stöllinger, M. K., Roekaerts, D., 2013. PDF modelling of soot formation in turbulent non-premixed flames using tabulated chemistry. In: Proceedings of the European Combustion Meeting. pp. 1–6.

Stojkovic, B. D., Fansler, T. D., Drake, M. C., Sick, V., 2005. High-speed imaging of OH* and soot temperature and concentration in a stratified-charge direct-injection gasoline engine. Proceedings of the Combustion Institute 30 (2), 2657–2665.

Suzukawa, Y., Sugiyama, S., Hino, Y., Ishioka, M., Mori, I., 1997. Heat transfer improvement and $NO_x$ reduction by highly preheated air combustion. Energy Conversion and Management 38 (10), 1061–1071.

Szegö, G. G., 2010. Experimental and numerical investigation of a parallel jet MILD combustion burner system in a laboratory-scale furnace. Ph.D. thesis, University of Adelaide.

Szegö, G. G., Dally, B. B., Nathan, G. J., 2008. Scaling of $NO_x$ emissions from a laboratory-scale MILD combustion furnace. Combustion and Flame 154 (1), 281–295.

Szegö, G. G., Dally, B. B., Nathan, G. J., 2009. Operational characteristics of a parallel jet MILD combustion burner system. Combustion and Flame 156 (2), 429–438.

Tabacco, D., Innarella, C., Bruno, C., 2002. Theoretical and numerical investigation on flameless combustion. Combustion Science and Technology 174 (7), 1–35.

Tolles, W. M., Nibler, J. W., McDonald, J. R., Harvey, A. B., 1977. A review of the theory and application of coherent anti-stokes raman spectroscopy (CARS). Applied Spectroscopy 31 (4), 253–271.

Tsuji, H., Gupta, A. K., Hasegawa, T., Katsuki, M., Kishimoto, K., 2003. High temperature air combustion. CRC Press.

van Oijen, J. A., de Goey, L. P. H., 2000. Modelling of premixed laminar flames using flamelet-generated manifolds. Combustion Science and Technology 161 (1), 113–137.

van Oijen, J. A., Donini, A., Bastiaans, R. J. M., ten Thije Boonkkamp, J. H. M., de Goey, L. P. H., 2016. State-of-the-art in premixed combustion modeling using flamelet generated manifolds. Progress in Energy and Combustion Science 57, 30–74.

van Veen, E. H., Roekaerts, D., 2003. On the accuracy of temperature measurements in turbulent jet diffusion flames by coherent anti-stokes-raman spectroscopy. Combustion Science and Technology 175 (10), 1893–1914.

van Veen, E. H., Roekaerts, D., 2005. Thermometry for turbulent flames by coherent anti-stokes raman spectroscopy with simultaneous referencing to the modeless excitation profile. Applied Optics 44 (32), 6995–7004.

Veríssimo, A. S., Rocha, A. M. A., Costa, M., 2011. Operational, combustion, and emission characteristics of a small-scale combustor. Energy & Fuels 25 (6), 2469–2480.

Veríssimo, A. S., Rocha, A. M. A., Costa, M., 2013a. Experimental study on the influence of the thermal input on the reaction zone under flameless oxidation conditions. Fuel Processing Technology 106, 423–428.

Veríssimo, A. S., Rocha, A. M. A., Costa, M., 2013b. Importance of the inlet air velocity on the establishment of flameless combustion in a laboratory combustor. Experimental Thermal and Fluid Science 44, 75–81.

Wang, J., Niioka, T., 2001. The effect of radiation reabsorption on NO formation in $CH_4$/air counterflow diffusion flames. Combustion Theory and Modelling 5 (3), 385–398.

Weber, R., Orsino, S., Lallemant, N., Verlaan, A., 2000. Combustion of natural gas with high-temperature air and large quantities of flue gas. Proceedings of the Combustion Institute 28 (1), 1315–1321.

Weinberg, F. J., 1971. Combustion temperatures: The future? Nature 233, 239–241.

Wünning, J. A., Wünning, J. G., 1997. Flameless oxidation to reduce thermal no-formation. Progress in Energy and Combustion Science 23 (1), 81–94.

WS. www.flox.com.

Zeldovich, J., 1946. The oxidation of nitrogen in combustion and explosions. European Physical Journal A. Hadrons and Nuclei 21, 577–628.

Zhou, B., Costa, M., Li, Z., Aldén, M., Bai, X.-S., 2017. Characterization of the reaction zone structures in a laboratory combustor using optical diagnostics: from flame to flameless combustion. Proceedings of the Combustion Institute 36 (3), 4305–4312.

# ACKNOWLEDGEMENTS

I am deeply grateful to my promotor Prof. Dirk Roekaerts. Thanks for the guidance and support you has provided during my PhD study. You let me explore my research topic in a free way, but you are always ready to give supports and advices. You provided every possible opportunity for me to present my work to the public, which helped me build self-confidence. Your carefulness and integrity in science have made a deep impression on me. It has been a great pleasure working with you and thank you for all moments we shared.

I also grateful to my copromoter Dr. Mark Tummers for the guidance and support for the experiments. It has been a great time working with you in the lab, seeking every possible way to build the LDA system for our measurements. I am always impressed by your persistence in pursuing the best solutions for problems. I would like to express my gratitude to you for your patience and generosity in our discussions.

I would like to appreciate the great help from Eric van Veen for the generous assistance during the experimental campaigns. Thanks for you spending weeks working in the lab during retirement time. Thanks for the conversations we had about the CARS setup and for providing the detailed information on the experiments.

Mr Bart Hoek, my deep gratitude is also for you. You are the most experienced technician that I have ever met. I appreciate your kindness and patience for the repeating discussion on the experimental setup design. I thank you for creating a safe and efficient lab environment which makes stable progresses during the experiments. I have learned new aspects of a laboratory life from you.

Special thanks to my Master supervisor–Prof. Zhixun Xia. I gained my first experience on scientific research under your supervision. Thanks very much for your great help providing the opportunity for me to study abroad.

It was a nice experience to closely work with Likun Ma, MengMeng Ren, Hesheng Bao, Christos Panagopoulos, Mohamed EI Abbassi, Johan Steimes, Valentina Valori and Miloš Birvalski. Discussions with you guys were enlightening for my research. It was a enjoyable journey studying and living in the Netherlands with friends like Qi Wang, Wuyuan Zhang, Xu Xie, Shilong Sun, Shanshan Ren, Yu Xin, Peng Wei and the whole Chinese group in the department P&E. Thanks to you guys.

Many thanks to my family. Without your support, none of this would have been possible. It was an unforgettable journey with you–Xiaoxia. I appreciate your company, this journey will absolutely be on of the best memory in our life. Our little boys, you bring a totally different life to us and make the journey complete.

No doubt there are many people that I will regret not personally thanking here. I thank all the people who have helped me.

***Xu Huang***
***June, 2018, Changsha***

# ABOUT THE AUTHOR

## Xu HUANG (黄序)

| | |
|---|---|
| 19-02-1988 | Born in Beibei, Chongqing, China. |

## EDUCATION

| | |
|---|---|
| 09-2006–06-2010 | Bachelor of Engineering in Aerospace Engineering<br>National University of Defense Technology<br>Changsha, China |
| 09-2010–12-2012 | MSc. in Aeronautic and Astronautic Science and Technology<br>National University of Defense Technology<br>Changsha, China<br>*Thesis:* Experimental and theoretical study on the ignition and combustion characteristics of a magnesium particle in water vapor |
| 02-2013–09-2013 | PhD student<br>National University of Defense Technology<br>Changsha, China |
| 09-2013–now | PhD student<br>Delft University of Technology<br>Delft, The Netherlands<br>*Thesis:* Measurements and Model Development for Flameless Combustion in a Lab-scale Furnace |